



**HAL**  
open science

# Polymersomes, cubosomes et hexosomes fluorescents avec émission induite par agrégation

Hui Chen

► **To cite this version:**

Hui Chen. Polymersomes, cubosomes et hexosomes fluorescents avec émission induite par agrégation. Chimie. Université Paris sciences et lettres, 2020. Français. NNT : 2020UPSLC010 . tel-04573386

**HAL Id: tel-04573386**

**<https://pastel.hal.science/tel-04573386>**

Submitted on 13 May 2024

**HAL** is a multi-disciplinary open access archive for the deposit and dissemination of scientific research documents, whether they are published or not. The documents may come from teaching and research institutions in France or abroad, or from public or private research centers.

L'archive ouverte pluridisciplinaire **HAL**, est destinée au dépôt et à la diffusion de documents scientifiques de niveau recherche, publiés ou non, émanant des établissements d'enseignement et de recherche français ou étrangers, des laboratoires publics ou privés.

**THÈSE DE DOCTORAT**  
**DE L'UNIVERSITÉ PSL**

Préparée à École Nationale Supérieure de Chimie de Paris (ENSCP)

**Fluorescent Polymersomes, Cubosomes and  
Hexosomes with Aggregation-Induced Emission**

Soutenue par

**Hui CHEN**

Le 07 Décembre 2020

Ecole doctorale n° 406

**Chimie Moléculaire de  
Paris Centre**

Spécialité

**Chimie Moléculaire**



Composition du jury :

<b>Michel Cloitre</b> Directeur de Recherche CNRS/HDR Laboratoire Matière Molle et Chimie ESPCI Paris, Université Paris Sciences & Lettres	<i>Président</i>
<b>Angelina Angelova</b> Chargée de Recherche CNRS/HDR Institut Galien Paris-Sud Université Paris-Saclay	<i>Rapportrice</i>
<b>Philippe Mésini</b> Directeur de Recherche CNRS/HDR Institut Charles Sadron Université de Strasbourg	<i>Rapporteur</i>
<b>Christophe Chassenieux</b> Professeur Institut des Molécules et des Matériaux du Mans Le Mans Université	<i>Rapporteur</i>
<b>Marianne Impéror-Clerc</b> Directrice de recherche CNRS/HDR Laboratoire de Physique des Solides Université Paris-Saclay	<i>Examinatrice</i>
<b>Annie Brûlet</b> Ingénieure de Recherche CNRS/HDR Laboratoire Léon Brillouin CEA Saclay	<i>Examinatrice</i>
<b>Sylvain Trépout</b> Ingénieur de Recherche INSERM/HDR Centre d'Imagerie Multimodale Institut Curie	<i>Examineur</i>
<b>Min-Hui Li</b> Directrice de Recherche CNRS/HDR Institut de Recherche de Chimie Paris Chimie ParisTech, Université Paris Sciences & Lettres	<i>Directrice de thèse</i>



**THÈSE DE DOCTORAT**  
DE L'UNIVERSITÉ PSL

Préparée à École Nationale Supérieure de Chimie de Paris (ENSCP)

**Fluorescent Polymersomes, Cubosomes and  
Hexosomes with Aggregation-Induced Emission**

Soutenue par

**Hui CHEN**

Le 07 Décembre 2020

Ecole doctorale n° 406

**Chimie Moléculaire de  
Paris Centre**

Spécialité

**Chimie Moléculaire**



Composition du jury :

<b>Michel Cloître</b> Directeur de Recherche CNRS/HDR Laboratoire Matière Molle et Chimie ESPCI Paris, Université Paris Sciences & Lettres	<i>Président</i>
<b>Angelina Angelova</b> Chargée de Recherche CNRS/HDR Institut Galien Paris-Sud Université Paris-Saclay	<i>Rapporteuse</i>
<b>Philippe Mésini</b> Directeur de Recherche CNRS/HDR Institut Charles Sadron Université de Strasbourg	<i>Rapporteur</i>
<b>Christophe Chassenieux</b> Professeur Institut des Molécules et des Matériaux du Mans Le Mans Université	<i>Rapporteur</i>
<b>Marianne Impéror-Clerc</b> Directrice de recherche CNRS/HDR Laboratoire de Physique des Solides Université Paris-Saclay	<i>Examinatrice</i>
<b>Annie Brûlet</b> Ingénieure de Recherche CNRS/HDR Laboratoire Léon Brillouin CEA Saclay	<i>Examinatrice</i>
<b>Sylvain Trépout</b> Ingénieur de Recherche INSERM/HDR Centre d'Imagerie Multimodale Institut Curie	<i>Examineur</i>
<b>Min-Hui Li</b> Directrice de Recherche CNRS/HDR Institut de Recherche de Chimie Paris Chimie ParisTech, Université Paris Sciences & Lettres	<i>Directrice de thèse</i>





## Acknowledgements

Studying and living in Paris is a very nice journey. I have really enjoyed it. However, now it comes to its end. I would like to express my sincerely thanks to all people throughout this journey.

I would like to give my sincere gratitude to my supervisor Mme Min-Hui Li for accepting me to do research in her group, as well as guiding me throughout the PhD study. I am very appreciated for her continuous support, assistance, patience, motivation and encouragement. I am fortunate enough to benefit a lot and then have many good results. It is really a nice experience in her lab, I have really enjoyed working here.

Besides, I would like to thank Mme Angelina Angelova and M. Philippe Mésini for agreeing to judge this research work. I want to thank Mme Marianne Impéror-Clerc, M. Michel Cloitre, Mme Annie Brûlet and M. Sylvain Trépout for their participation in my thesis jury.

The doctoral thesis is certainly not a lonely job! I have indeed benefited a lot of help from many collaborators. I would like to thank M. Sylvain Trépout, who has been of great help for the characterizations of all the polymer assemblies in this thesis with cryo-EM microscopy. Many thanks for his careful and patient training of cryo-EM microscopy operation. I would like to thank Mme Annie Brûlet for the small angle X-ray scattering characterization of polymer cubosomes and hexomes. With her help, we could know the internal structure of these colloids. The observation of giant polymersomes by fluorescence microscopy, I would like to thank M. Vincent Semetey for the help.

Many thanks to Mme Marie-Noëlle Rager for the help in the carrying out nuclear magnetic resonance measurements on all the chemical compounds. I thank M. Fan Sun for the help in scanning electron microscope measurement.

I thank my labmates and friends: Xinfeng, Yujiao, Yangwei, Dapeng, Xiang, Bin, Liang, Zhihua, Giovanni, Xingmin, Alexis, Gaoyu for their kind help and support which help me to get used to the new life quickly in Paris, for stimulating discussions on research works, for the experiment measurement support, for the all the fun we have had in the last three and a half years.

## Acknowledgements

---

I want to thank Mme Nathalie Ouvry and Mme Ikrame Benkaddour, who provide daily management of the laboratory. I also thank Mme Isabell Nicolai and Mme Fabienne Huvier from CNRS to help me to prepare my contract and residence card.

I would like to thank two members of my comité de suivi: M. Hani Amouri and Mickaël Ménand, for their good suggestions to my research work.

I acknowledge the French National Research Agency (project ANR-16-CE29-0028) for financial support.

Last but not least, I would like to thank to my girlfriend Nian for always supporting and helping me with her unconditional love, patience and encouragement during my study in Paris. I would like to thank my family. My dear mother, father and sister give their endless love, care, faith, support and understanding to me throughout my life. Thank you!

---

## Contents

Résumé de Thèse en Français .....	1
Abstract .....	25
Chapter I. Introduction .....	27
1.1 Amphiphilic block polymers and their self-assembly in aqueous solution.....	27
1.1.1 Amphiphilic block polymers.....	27
1.1.2 Self-assembly of amphiphilic block polymers in aqueous solution .....	28
1.2 Polymersomes .....	31
1.2.1 Structural and experimental conditions for polymersome formation.....	33
1.2.2 Preparation strategies of polymersomes.....	34
1.2.3 Formation mechanism of polymersomes .....	40
1.2.4 Characterization techniques of polymersomes.....	42
1.3 Polymer cubosomes and hexosomes .....	44
1.3.1 Structural and experimental conditions for inverted morphologies .....	45
1.3.2 Preparation methods of polymer cubosomes and hexosomes .....	48
1.3.3 Formation mechanism of polymer cubosomes and hexosomes .....	50
1.3.4 Characterization techniques of polymer cubosomes and hexosomes .....	53
1.4 Aggregation-induced emission (AIE) .....	55
1.4.1 Aggregation-induced quenching (ACQ) .....	55
1.4.2 Emergence of the AIE concept.....	57
1.4.3 Mechanism of AIE process .....	58
1.5 Polymersomes with aggregation-induced emission (AIE) property .....	62
1.5.1 The state of the art of AIE polymersomes.....	64

---

1.5.2. AIE amphiphilic copolymers prepared by post-modification of pre-prepared polymers with AIEgens.....	66
1.5.3 AIE amphiphilic copolymers prepared by direct polymerization of AIE monomers .....	68
1.6 Conclusion.....	76
References .....	77
Chapter II. Light-Gated Nano-Porous Polymersomes from Stereoisomer-Directed Self-Assemblies.....	91
2.1 Introduction .....	91
2.2 Experimental Sections.....	92
2.2.1 Materials.....	92
2.2.2 Synthesis.....	93
2.2.3 Instruments .....	96
2.2.4 Methods.....	97
2.3 Result and discussion .....	99
2.3.1 Synthesis and characterizations of PEG550-TPE-Chol and their stereoisomers ..	99
2.3.2 Thermal and photostability of PEG550-TPE-Chol stereoisomers .....	108
2.3.3 Self-Assembly of <i>trans</i> - and <i>cis</i> -PEG550-TPE-Chol and their mixtures: vesicles, perforated vesicles and cylindrical micelles.....	112
2.3.4 AIE and photo-responsive properties of polymersomes, perforated polymersomes, and cylindrical micelles.....	120
2.4 Conclusion.....	126
References .....	127
Chapter III. Polymersomes with Hexagonal Nano-Porous Structures in the Membrane.....	131

## Contents

---

3.1 Introduction .....	131
3.2 Experimental sections.....	132
3.2.1 Materials.....	132
3.2.2 Synthesis.....	132
3.2.3 Instruments .....	134
3.3 Results and Discussion.....	135
3.3.1 Synthesis and characterization of PEG550-SS-TPE-SS-Chol .....	135
3.3.2 Reduction-triggered degradation of PEG550-SS-TPE-SS-Chol.....	137
3.3.3 Self-assembly of PEG550-SS-TPE-SS-Chol in comparison with that of PEG550-TPE-Chol.....	138
3.3.4 Self-assembly mechanism of nanoporous structures in the membrane.....	140
3.3.5 Reduction responsive property of PEG550-SS-TPE-SS-Chol self-assemblies ..	150
3.4 Conclusion.....	151
References .....	151
Chapter IV. Fluorescent Cubosomes and Hexosomes with Aggregation-Induce Emission Characteristic.....	153
4.1 Introduction .....	153
4.2 Experimental sections.....	155
4.2.1 Materials.....	155
4.2.2 Synthesis.....	156
4.2.3 Instruments.....	156
4.3 Results and Discussion.....	158
4.3.1 Synthesis and characterizations of monomer TPEMA .....	158

## Contents

---

4.3.2 Synthesis and characterizations of PEG <sub>45</sub> - <i>b</i> -PTPEMA.....	161
4.3.4 Hexosomes, primitive cubosomes and polymersomes formed in dioxane/water system.....	164
4.3.5 Hexosomes and polymersomes formed in THF/water system.....	173
4.3.6 Effects of co-solvent on the morphology of self-assembly.....	176
4.3.7 AIE fluorescence of PEG <sub>45</sub> - <i>b</i> -PTPEMA <sub>n</sub> self-assemblies.....	180
4.4 Conclusion.....	182
4.5 References.....	183
Chapter V. General Conclusions and Perspectives.....	187
5.1 General conclusions.....	187
5.2 Perspectives.....	189
List of publications and conference abstracts.....	191

## Résumé de Thèse en Français

### **Polymersomes, Cubosomes et Hexosomes Fluorescents avec Emission Induite par l'Agrégation**

La propriété d'émission induite par l'agrégation (AIE : *aggregation-induced emission*) fait référence à un phénomène photophysique anormal présenté par un groupe de luminogènes spécifiques qui sont non émissifs en solution mais deviennent très luminescents à l'état agrégé. Elle fournit un moyen simple de s'attaquer aux problèmes d'extinction de la fluorescence causés par l'agrégation (ACQ : *aggregation-caused quench*), qui se sont produits pour la plupart des luminogènes organiques conventionnels. La combinaison des luminogènes AIE (AIEgens) avec des assemblages de polymères présente un intérêt particulier et peut ouvrir une nouvelle voie pour préparer des matériaux luminescents très efficaces avec des applications potentielles dans le domaine biomédical. Parmi les divers assemblages de polymères AIE, les polymersomes AIE et les morphologies inverses AIE (y compris les cubosomes et les hexosomes) suscitent un intérêt de recherche considérable car ils sont susceptibles d'être utilisés comme des outils de bio-imagerie en temps réel lors de l'administration de substances thérapeutiques, et utilisés dans le diagnostic et le théranostic. Des rapports sur les polymersomes AIE commencent à apparaître dans la littérature. Cependant, leur nombre reste encore très faible. En revanche, aucun cubosome ou hexosome de polymère AIE n'a été décrit dans la littérature. Dans la présente étude, une variété d'assemblages AIE comprenant des polymersomes, des polymersomes poreux, des cubosomes et des hexosomes sont construits avec succès grâce à l'auto-assemblage de copolymères amphiphiles contenant des AIEgens.

Cette thèse est divisé en cinq chapitres. Le chapitre I est une introduction générale. Le chapitre V présente la conclusion et les perspectives de cette thèse. Le contenu de la recherche est décrit dans les Chapitres II, III et IV:

### **Chapitre II. Polymersomes nanoporeux photo-sensibles issus d'auto-assemblages de stéréoisomères**

#### *Synthèse des PEG550-TPE-Chol et de ses stéréo-isomères*



Un polymère amphiphile PEG550-TPE-Chol ( $M_n = 1510$  Da) avec du tétraphényléthylène (TPE) comme stéréocentre a été synthétisé. La partie hydrophile de ce polymère est du poly(éthylène glycol) (PEG550,  $M_n = 550$  Da), et la partie hydrophobe est composée de deux noyaux rigides, le TPE et le cholestérol (Chol). Le TPE est un AIEgen emblématique. En même temps le TPE di-substitué possède deux stéréo-isomères sensibles à la photo-isomérisation.

La synthèse de PEG550-TPE-Chol sans prendre la précaution spécifique de séparation de *trans* et *cis* isomères tout de long de la synthèse, comme le montre le Schéma 1, mène à l'obtention d'un mélange d'isomères *trans* et *cis* dans le produit final. Le PEG550-TPE-Chol ainsi obtenu contenait un taux presque équivalent d'isomères, *trans/cis* = 60/40.

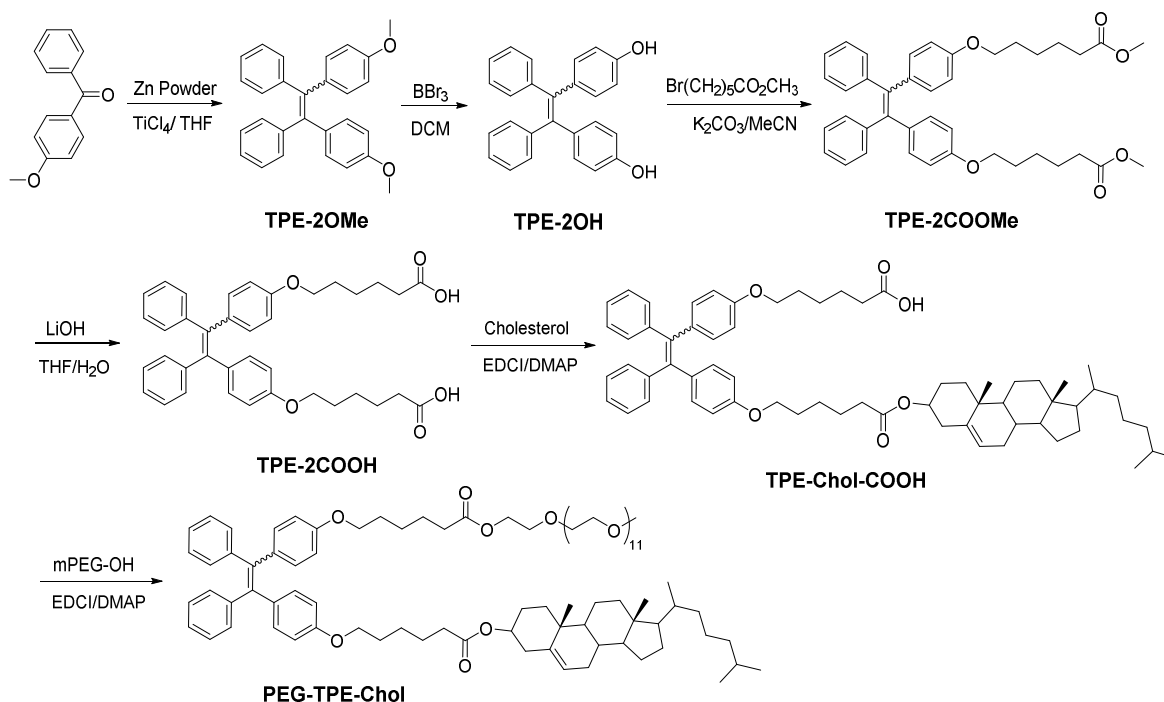


**Schéma 1.** Voie synthétique vers le polymère amphiphile PEG-TPE-Chol.

Les stéréoisomères, le *trans*- et le *cis*-PEG550-TPE-Chol, ont été préparés avec les dérivés intermédiaires séparés *trans*-TPE-2COOMe et *cis*-TPE-2COOMe (Schéma 2). Les deux isomères du TPE-2COOMe ont montré des facteurs de rétention ( $R_f$ ) suffisamment différents, 0,52 et 0,44, sur la CCM en utilisant l'éther de pétrole et l'acétate d'éthyle (rapport en volume de 10 :1) comme solvants d'éluion, ce qui nous ont permis de les séparer avec la technique de

chromatographie sur colonne (Figure 1A). Le monocristal de l'isomère pur avec  $R_f = 0,52$  (celui du haut sur la CCM) a été obtenu par l'évaporation lente des solvants. Sa structure cristalline a été caractérisée par la diffraction des rayons X (Figure 1B). Les résultats ont indiqué que l'isomère recueilli en premier lieu dans l'expérience de chromatographie sur colonne avec  $R_f = 0,52$  correspondait au *trans*-TPE-2COOMe. L'isomère collecté ensuite avec  $R_f = 0,44$  était le *cis*-TPE-2COOMe. La Figure 2A montre les spectres RMN de ces deux isomères. La différence des déplacements chimiques entre  $H_a$  ( $H_b$ ) pour le *trans*-TPE-2COOMe et  $H_a'$  ( $H_b'$ ) pour le *cis*-TPE-2COOMe a été observée sur le site  $\delta$  à environ 6.6 ppm (6.9 ppm), ce qui nous permet d'utiliser les spectres RMN pour distinguer les isomères *trans* et *cis* du TPE. Ensuite, les stéréo-isomères amphiphiles finaux *trans*-PEG-TPE-Chol et *cis*-PEG550-TPE-Chol ont été synthétisés avec le *trans*- et le *cis*-TPE-2COOMe comme matériaux de départ, respectivement.

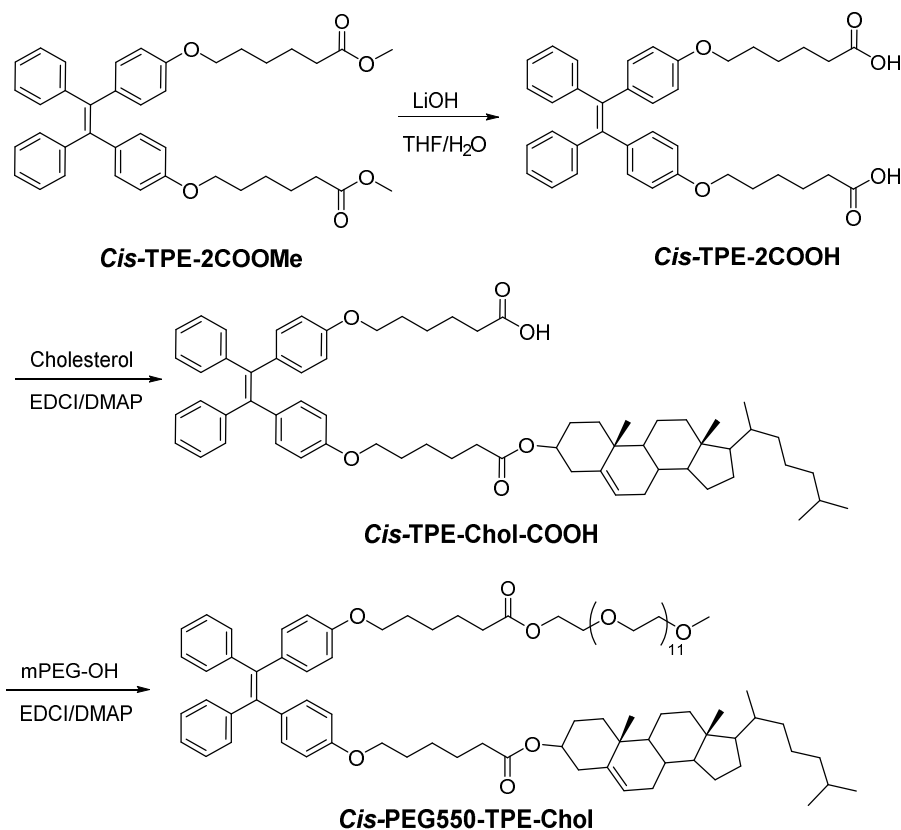


**Schéma 2.** Voie synthétique vers le *cis*-PEG550-TPE-Chol.

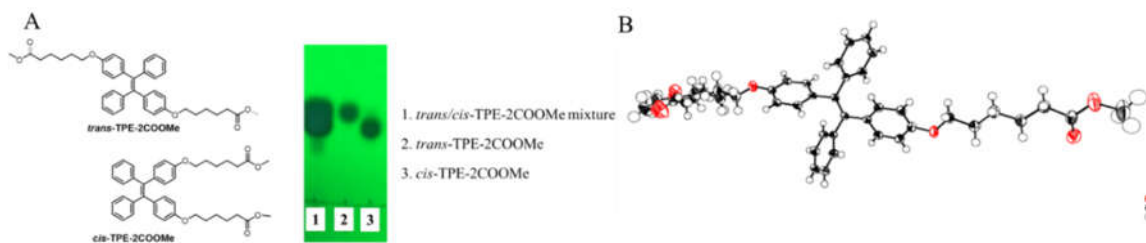


**Figure 1.** (A) Image CCM du mélange *trans/cis*-TPE-2COOMe et *trans*- et *cis*-TPE-2COOMe. (B) la structure cristalline du *trans*-TPE-2COOMe.

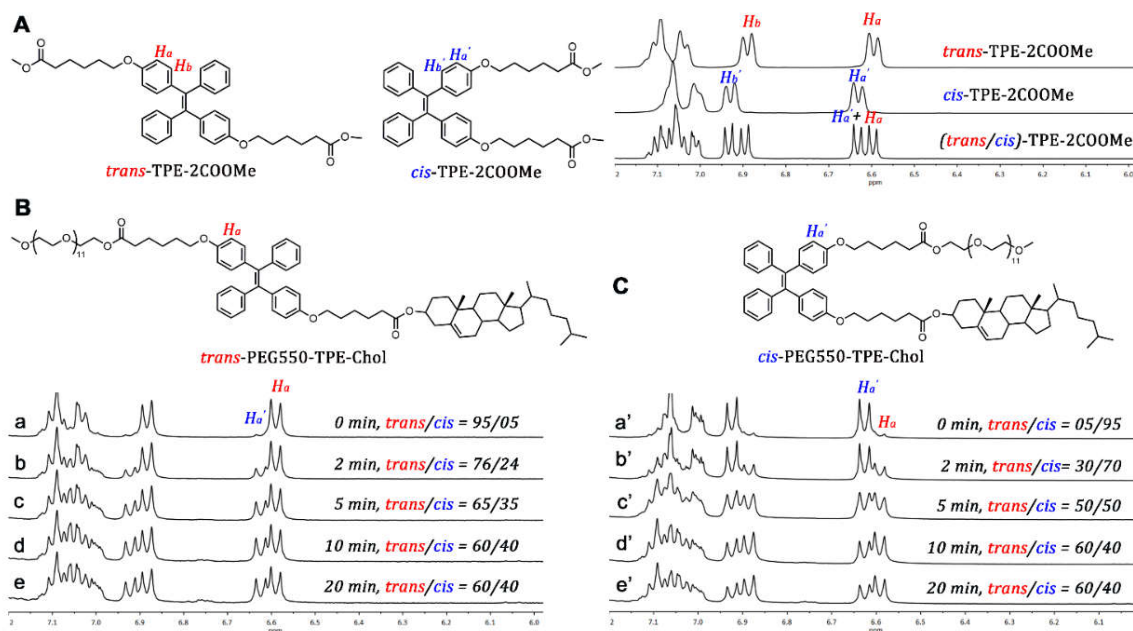


**Figure 2.** (A) Structure chimique du *trans*-TPE-2COOMe et du *cis*-TPE-2COOMe et les spectres RMN  $^1H$  partiels du mélange *trans*-TPE-2COOMe, *cis*-TPE-2COOMe et (*trans/cis*)-TPE-2COOMe (400 MHz,  $CDCl_3$ ). (B) Structure chimique du *trans*-PEG550-TPE-Chol, et spectres RMN  $^1H$  partiels du *trans*-PEG550-TPE-Chol dans le  $CDCl_3$  après irradiation UV (365 nm,  $15 \text{ mW/cm}^2$ ) de durée différente : (a)  $t = 0 \text{ min}$ , (b)  $t = 2 \text{ min}$ , (c)  $t = 5 \text{ min}$ , (d)  $t = 10 \text{ min}$ , (e)  $t = 20 \text{ min}$ . (C) Structure chimique du *cis*-PEG550-TPE-Chol, et spectres RMN  $^1H$  partiels du *cis*-PEG550-TPE-Chol dans le  $CDCl_3$  après irradiation UV (365 nm,  $15 \text{ mW/cm}^2$ ) avec différentes durées : (a')  $t = 0 \text{ min}$ , (b')  $t = 2 \text{ min}$ , (c')  $t = 5 \text{ min}$ , (d')  $t = 10 \text{ min}$ , (e')  $t = 20 \text{ min}$ . Les abscisses de tous les spectres RMN sont échelonnées de 6.0 à 7.2 ppm pour plus de clarté.

La photoisomérisation des stéréo-isomères a été vérifiée lors de l'illumination UV. Comme le montrent les Figures 2B et 2C. Le *trans* et le *cis*-PEG550-TPE-Chol exposés à la lumière UV (365 nm, 15 mW.cm<sup>-2</sup>) pendant 2 min subissent déjà 19% et 25% d'isomérisation, respectivement. Après 10 minutes d'éclairage, les isomérisations *trans*-to-*cis* et *cis*-to-*trans* atteignent un état stationnaire avec un rapport *trans/cis* de 60/40. L'isomère *trans* est légèrement supérieur à l'isomère *cis*, car le *trans*-PEG550-TPE-Chol est plus photostable que l'isomère *cis* et l'isomère *cis* a un taux d'isomérisation plus rapide que l'isomère *trans*. Aucune photo-cyclisation significative n'a été observée pour le *cis* et le *trans*-PEG550-TPE-Chol après 10 minutes d'illumination (presque aucun signal RMN <sup>1</sup>H à 6.7 -6.8 ppm).

### *Autoassemblage de trans- et cis-PEG550-TPE-Chol et de leurs mélanges*

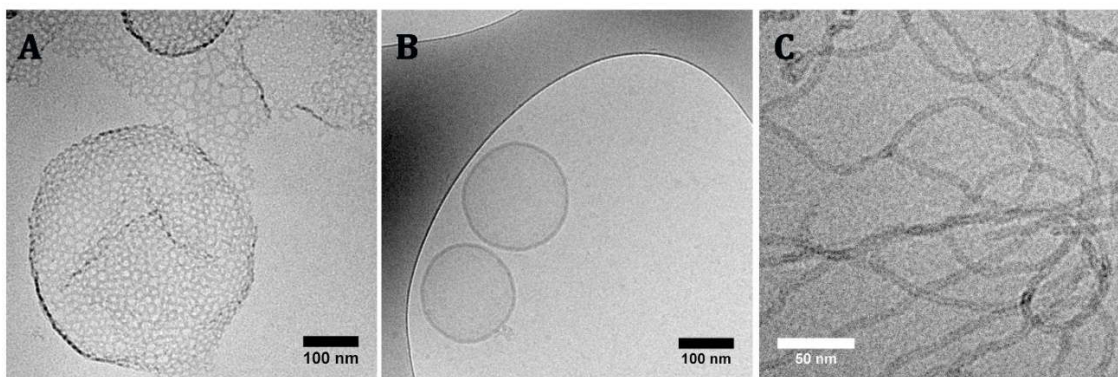


**Figure 3.** (A) Image Cryo-EM de vésicules poreuses formées par le PEG550-TPE-Chol synthétisé avec un rapport inhérent de *trans/cis* = 60/40 sans séparation des isomères. (B) Image Cryo-EM de vésicules classiques formées par du *trans*-PEG550-TPE-Chol. (C) Image Cryo-EM de micelles cylindriques formées par le *cis*-PEG550-TPE-Chol.

Compte tenu du poids moléculaire ( $M_n = 1510$  Da) du PEG550-TPE-Chol, qui est supérieur aux petites molécules amphiphiles traditionnelles comme les phospholipides, nous avons préparé les vésicules en utilisant une méthode d'hydratation en couche mince à haute température ( $T = 65$  °C) pour accélérer l'hydratation de l'échantillon et l'auto-organisation du polymère. Généralement, la solution de chloroforme du PEG550-TPE-Chol ou de son stéréoisomère (0,5 % en poids) est déposée uniformément sur la surface d'une plaque de téflon rugueuse, puis séchée sous vide pour éliminer tout solvant et obtenir un film polymère mince. Ensuite, l'échantillon de film mince est hydraté avec de l'eau déionisée à 65 °C pendant 48 heures dans une bouteille scellée. Les morphologies et les tailles des autoassemblages sont

caractérisées par la Cryo-microscopie électronique (Cryo-EM). Ces deux stéréo-isomères amphiphiles ont présenté des comportements d'autoassemblage distincts : le *trans*-PEG550-TPE-Chol préfère à former des vésicules normales, le *cis*-PEG550-TPE-Chol tend à construire les micelles cylindriques. Il est intéressant de noter que le PEG550-TPE-Chol synthétisé sans séparation des isomères (*trans/cis* = 60/40) a formé des vésicules et membranes perforées dont la taille des pores varie de 9 à 27 nm (Figure 3).

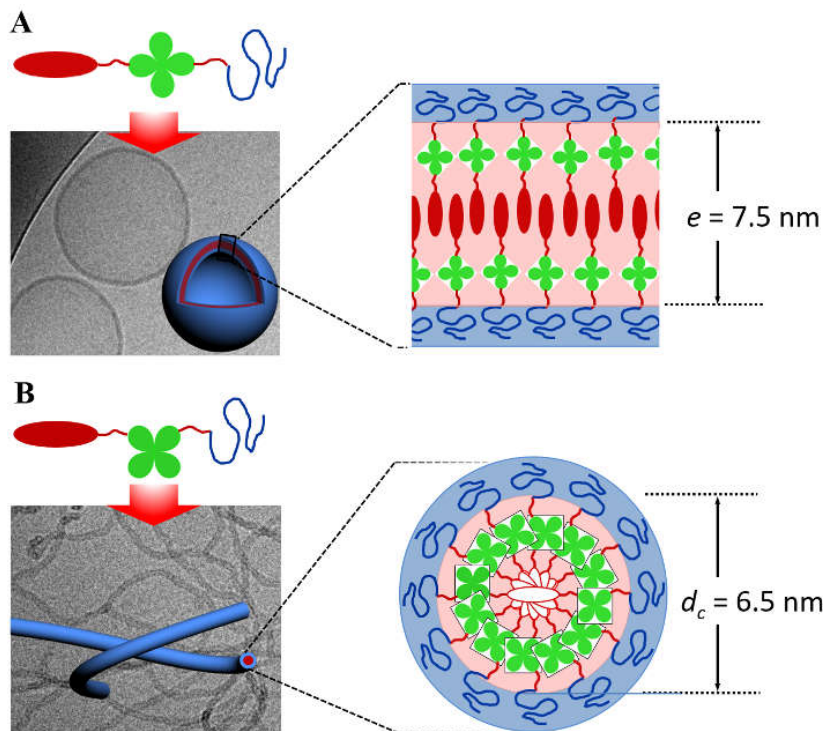


**Figure 4.** Les modèles de morphologies des polymersomes (A) et des micelles cylindriques (B) formés respectivement par l'isomère *trans* et l'isomère *cis*. L'ellipsoïde rouge représente le cholestérol, et le trèfle vert le TPE. La ligne rouge représente l'espaceur aliphatique, et la ligne bleue la chaîne PEG550. Dans le modèle de la micelle cylindrique, des ellipsoïdes rouges vides sont utilisés pour représenter le cholestérol afin de mettre en évidence l'organisation moléculaire le long de l'axe longitudinal du cylindre.

Lorsque la stéréo-structure passe du type *trans* au type *cis*, la transition morphologique des auto-assemblages des vésicules aux micelles cylindriques doit être guidée par la minimisation de l'énergie interfaciale. Suivant qualitativement la théorie d'Israelachvili *et al*, le paramètre d'assemblage  $p = v/al$  du *trans*-PEG550-TPE-Chol en solution aqueuse devrait être autour de

1 pour la formation de vésicules, tandis que la valeur  $p$  du *cis*-PEG550-TPE-Chol devrait être plus petite et approcher de 1/2 pour la formation de micelles cylindriques (où  $v$  est le volume hydrophobe,  $a$  la zone interfaciale optimale, et  $l$  la longueur du bloc hydrophobe normal à l'interface).

Ici, les structures chimiques sont les mêmes pour les deux isomères. Donc ce sont leurs formes stériques qui dictent leur paramètre d'assemblage. Une représentation schématique de leur auto-assemblage est donnée dans à la Figure 4. La longueur moléculaire de la partie hydrophobe pour le *trans*- et le *cis*-PEG-TPE-Chol à l'état étendu est  $l_{trans} = 4,54$  nm et  $l_{cis} = 4,05$  nm, respectivement. L'épaisseur de la membrane vésiculaire et le diamètre des micelles cylindriques ont été mesurés d'après les images Cryo-EM collectées. L'épaisseur de la membrane vésiculaire ( $e = 7,5$  nm) se situe entre  $l_{trans}$  (4,54 nm) et  $2l_{trans}$  (9,08 nm), le diamètre des micelles cylindriques ( $d_c = 6,5$  nm) se situe également entre  $l_{cis}$  (4,05) et  $2l_{cis}$  (8,10 nm). Par conséquent, le *trans*- et *cis*-PEG-TPE-Chol dans la membrane bicouche et dans les micelles cylindriques doivent être organisés de manière interdigitée, comme le montre la Figure 4. Le cholestérol est un élément de construction polyvalent qui favorise la formation de membranes bicouches et de structures fibrillaires en raison de sa rigidité moléculaire, de sa nature d'auto-organisation, de ses carbones asymétriques, etc. Pour les micelles cylindriques formées par le *cis*-PEG-TPE-Chol, le long de l'axe cylindrique, les motifs de cholestérol tournent autour de cet axe pour former les micelles cylindriques.

Le scénario de formation d'une membrane poreuse à partir du mélange *trans* et *cis* du PEG550-TPE-Chol peut être expliqué comme suit (Figure 5). Les isomères *cis* formant des micelles dans une membrane bicouche tentent d'imposer une courbure positive aux monocouches constitutives (feuilletts). Les monocouches ne peuvent rester unies à une bicouche plate que jusqu'à une concentration critique des isomères *cis* formant des micelles. Au-delà de ce point critique, des bords peuvent se former, qui contiendraient principalement les isomères *cis* formant des micelles et s'assembleraient en structures hémicylindriques à courbure négative (les trous). Avec un rapport *trans/cis* de 60/40, la partie trou et la partie bicouche ont des proportions similaires dans la membrane en forme de maille.

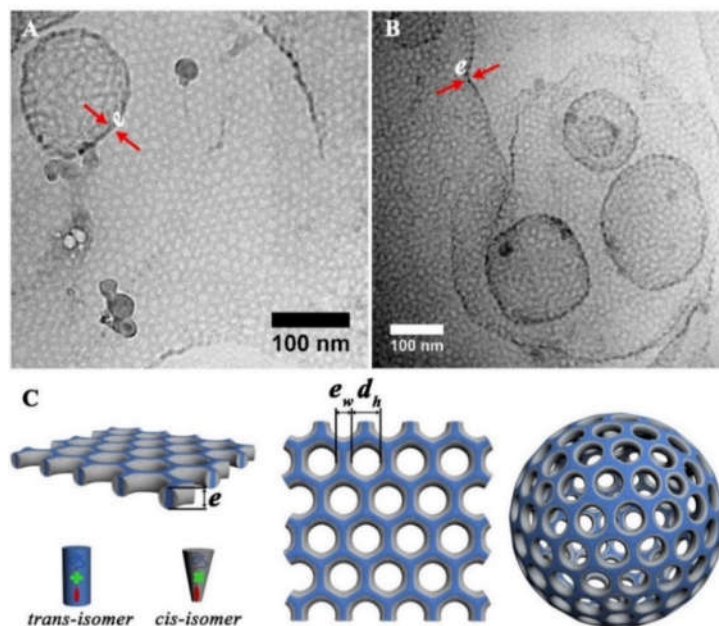


**Figure 5.** (A, B) Images Cryo-EM d'autoassemblages obtenus à partir du mélange des *trans*- et *cis*-PEG550-TPE-Chol préparés intentionnellement selon le rapport *trans/cis* = 60/40. (C) Représentation schématique de membranes et polymersomes perforées. Le cylindre bleu représente la forme du *trans*-PEG550-TPE-Chol formant la membrane, qui sont de préférence assemblés dans des zones plus plates. Le cône tronqué gris représente la forme du *cis*-PEG550-TPE-Chol formant des micelles qui sont probablement agrégées de façon prédominante aux bords des trous ayant une courbure plus élevée.

### ***Propriétés AIE des autoassemblages et leur propriétés photosensibles***

Tous les autoassemblages des *trans*- et *cis*-PEG550-TPE-Chol, ainsi que de leurs mélanges, sont fluorescents sous la lumière UV en raison de la présence de TPE (Figure 6B). Les rendements quantiques sont de 0,12 et 0,15 pour les assemblages *trans*- et *cis*-PEG550-TPE-Chol, respectivement.

Sous une intensité UV plus forte ( $15 \text{ mW/cm}^2$ ) et un temps d'éclairage plus long (2 à 30 min), des caractéristiques photosensibles ont été enregistrées en raison de la photo-isomérisation *trans*-to-*cis* et *cis*-to-*trans*. Des vésicules lisses de *trans*-PEG550-TPE-Chol ont été perforées par les isomères *cis* issus de la photo-isomérisation, tandis que des micelles cylindriques de *cis*-PEG550-TPE-Chol se sont entrelacées pour former des mailles et des membranes perforées (Figure 6C et D). Par contre, les vésicules nanoporeuses du PEG550-TPE-Chol



synthétisé tel quel sans séparation des isomères, lors de son exposition à une forte lumière UV, n'ont pas montré de changement significatif à l'échelle nanométrique, mais une fluctuation de la membrane à l'échelle micrométrique a été observée par microscopie à épifluorescence, probablement dû aux photo-isomérisations *trans*-to-*cis* et *cis*-to-*trans* simultanées (Figure 7).

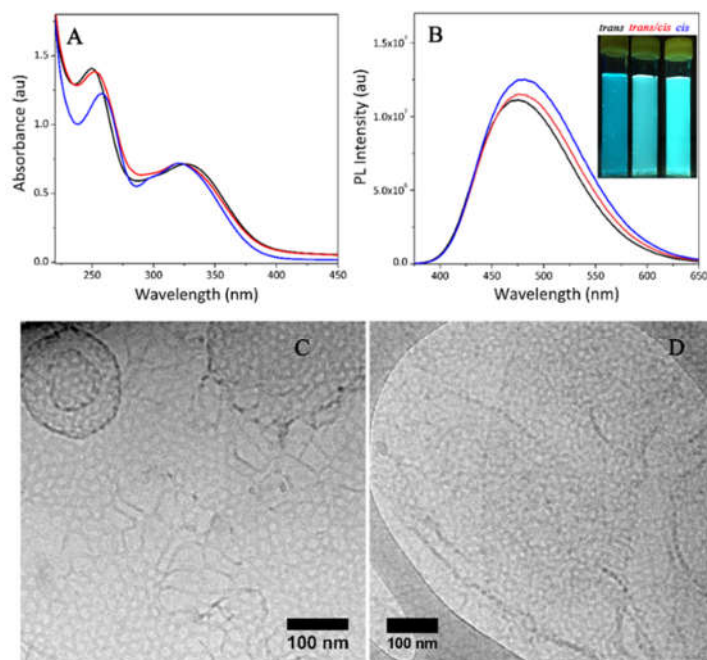


**Figure 6.** (A) Les spectres d'absorption UV-visible des assemblages de l'isomère *trans* (ligne noire), de l'isomère *cis* (ligne bleue) et du mélange *trans/cis* (*trans/cis* = 60/40) (ligne rouge). (Concentration :  $6,7 \times 10^{-2}$  mg/ml). (B) Les spectres de photoluminescence (PL) des assemblages de l'isomère *trans* (trait noir), de l'isomère *cis* (trait bleu) et du mélanges *trans/cis* (*trans/cis* = 60/40) (trait rouge). (Concentration :  $6,7 \times 10^{-2}$  mg/ml ; longueur d'onde d'excitation : 352 nm,  $0,5 \text{ mW/cm}^2$ ). Les photos insérées sont les dispersions d'autoassemblages prises sous une lumière UV de 365 nm ( $0,5 \text{ mW/cm}^2$ ). (C) et (D) Images Cryo-EM de membranes et vésicules perforées obtenues, par irradiation par la lumière UV (365 nm,  $15 \text{ mW/cm}^2$ ) pendant 30 min, à partir des vésicules de *trans*-PEG550-TPE-Chol (C) et des micelles cylindriques de *cis*-PEG550-TPE-Chol (D).



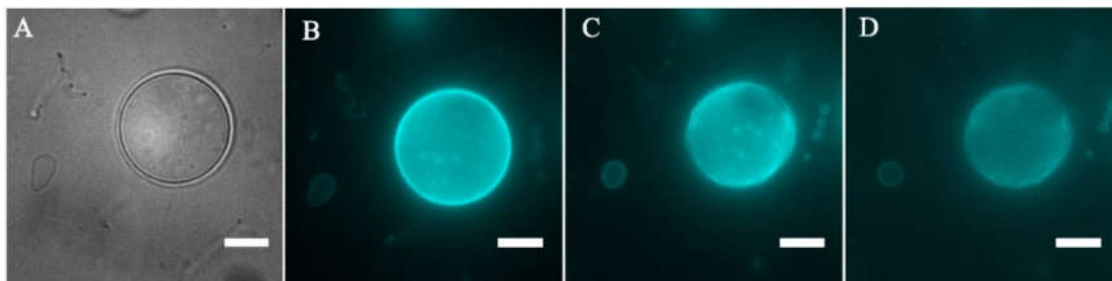


**Figure 7.** Images microscopiques optiques d'épifluorescence de vésicules géantes de PEG550-TPE-Chol. (A) Champ blanc. (B-D) Images de fluorescence sous illumination UV continue à  $t = 0$  (B),  $t = 40$  sec (C) et  $t = 60$  sec (D). Le temps d'exposition de chaque image était de 300  $\mu$ sec. Barre d'échelle = 10  $\mu$ m. L'éclairage était assuré par une lampe LED-UV (365 nm). L'intensité focalisée sur l'échantillon était de 15  $\text{mW}/\text{cm}^2$ .

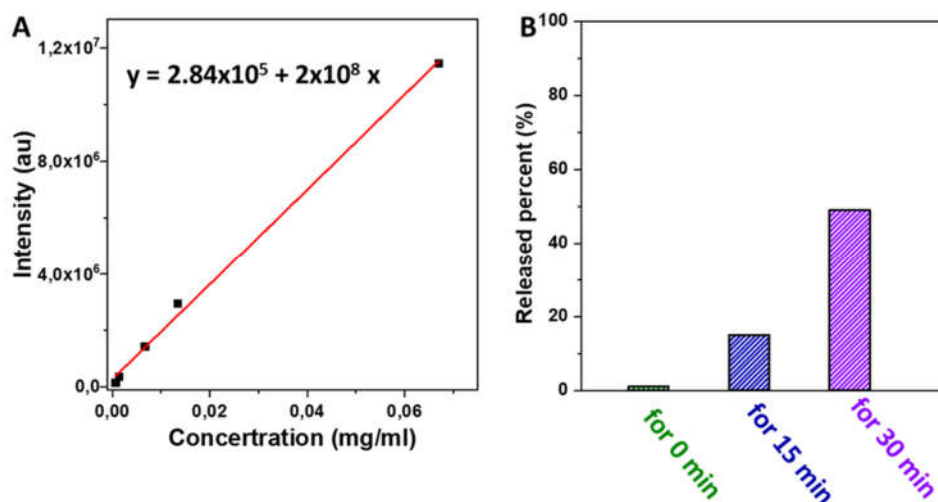


**Figure 8.** (A) L'intensité de la fluorescence des solutions aqueuses de TRITC-Dextran à 570 nm (longueur d'onde d'excitation = 490 nm) en fonction de la concentration de TRITC-Dextran. (B) Le pourcentage de libération de TRITC-Dextran à partir des polymersomes de *trans*-PEG550-TPE-Chol en fonction du temps d'irradiation.

Le passage de l'état fermé à l'état ouvert (avec des pores de 9-27 nm de diamètre) pour les polymersomes formés par le *trans*-PEG550-TPE-Chol, déclenché par la lumière UV, peut être utilisé pour encapsuler des molécules de grande taille et les libérer de manière contrôlée. L'isothiocyanate-dextran de tétraméthylrhodamine (TRITC-Dextran, MW = 4400 Da) a été utilisé comme molécule modèle pour le test. La Figure 8 montre les pourcentages de libération

après 0, 15 et 30 min d'irradiation UV, 50 % du TRITC-Dextran étant libéré après 30 min d'irradiation.

## Chapitres II. Polymersomes avec des structures nano-poreuses hexagonales dans la membrane

### Synthèse du PEG550-SS-TPE-SS-Chol

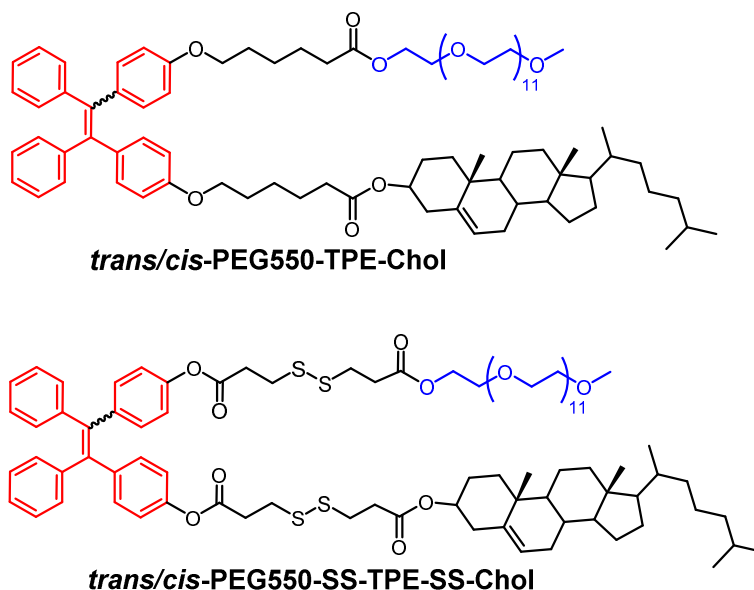


**Figure 9.** La structure chimique du mélange *trans* et *cis* du PEG550-TPE-Chol et du PEG550-SS-TPE-SS-Chol.

Dans cette partie, nous faisons état des nanopores de l'AIE, qui sont structurés en un réseau hexagonal. Ils sont auto-assemblés à partir du copolymère amphiphile PEG550-SS-TPE-SS-Chol, qui est légèrement différent du PEG550-TPE-Chol décrit dans le premier travail (Figure 9). Dans le PEG550-SS-TPE-SS-Chol, les espaceurs flexibles entre le PEG et le TPE, et entre le Chol et le TPE ont une liaison disulfure supplémentaire -S-S-, respectivement. De plus, le PEG550-SS-TPE-SS-Chol synthétisé naturellement sans séparation des stéréo-isomères contient des isomères *trans* et *cis* dans un rapport molaire presque équivalent. La synthèse des molécules amphiphiles PEG550-SS-TPE-SS-Chol a été réalisée par la voie synthétique, comme le montre le Schéma 3.

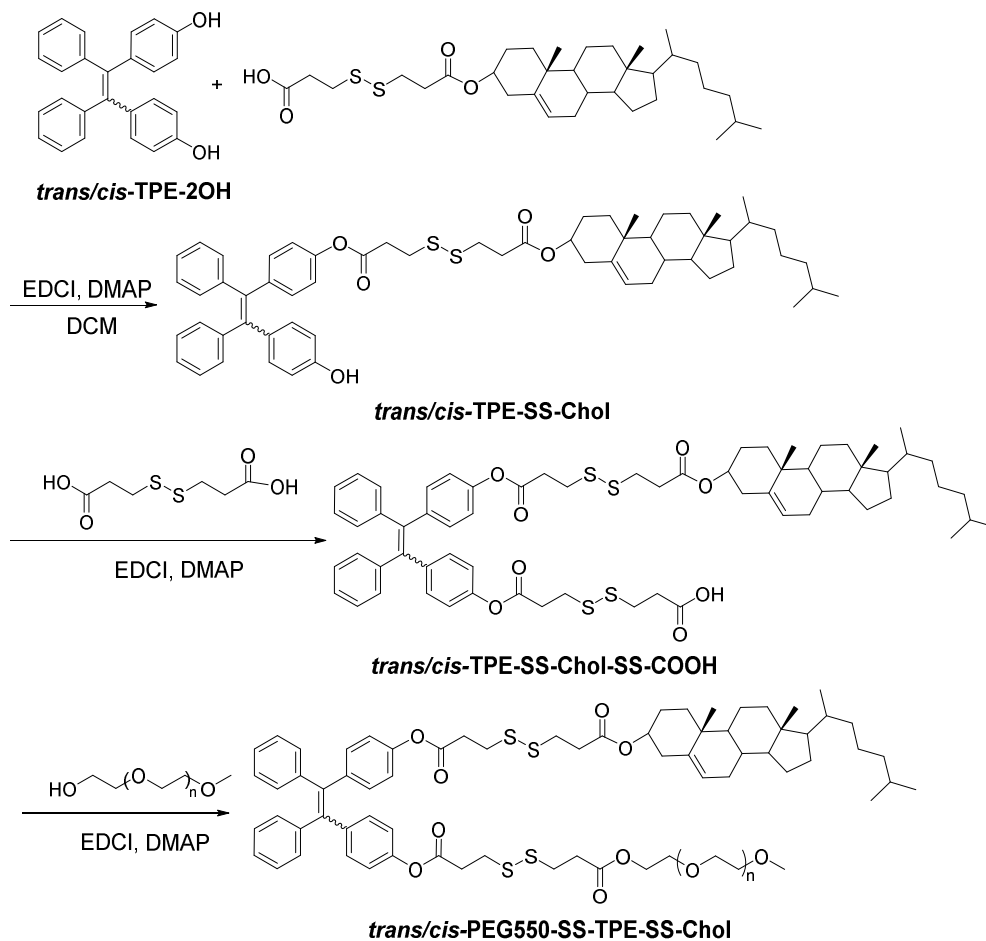


**Schéma 3.** La voie synthétique vers le PEG550-SS-TPE-SS-Chol.

### ***Autoassemblage de PEG550-TPE-Chol et PEG-SS-TPE-SS-Chol***

Compte tenu des poids moléculaires ( $M_n = 1510$  et  $1650$  Da) des oligomères amphiphiles, qui sont supérieurs aux petites molécules amphiphiles traditionnelles, nous avons préparé les vésicules en utilisant la méthode d'hydratation en couche mince à haute température ( $T = 65$  °C) pour accélérer l'hydratation de l'échantillon et l'auto-organisation moléculaire, comme décrit dans le chapitre II ci-dessus. Ces produits avec des mélanges *trans/cis*, appelés simplement PEG550-TPE-Chol et PEG550-SS-TPE-SS-Chol ci-après, forment spontanément des vésicules avec des nanopores dans la membrane (Figure 10). Il est très intéressant de noter que l'organisation des pores semble aléatoire dans le cas du PEG550-TPE-Chol avec seulement quelques motifs hexagonaux locaux (Figure 10 a et b, à l'intérieur du cadre rouge), tandis que les pores s'autoorganisent en grande partie en superstructure hexagonale dans la membrane dans le cas du PEG550-SS-TPE-SS-Chol (Figures 10c et d).

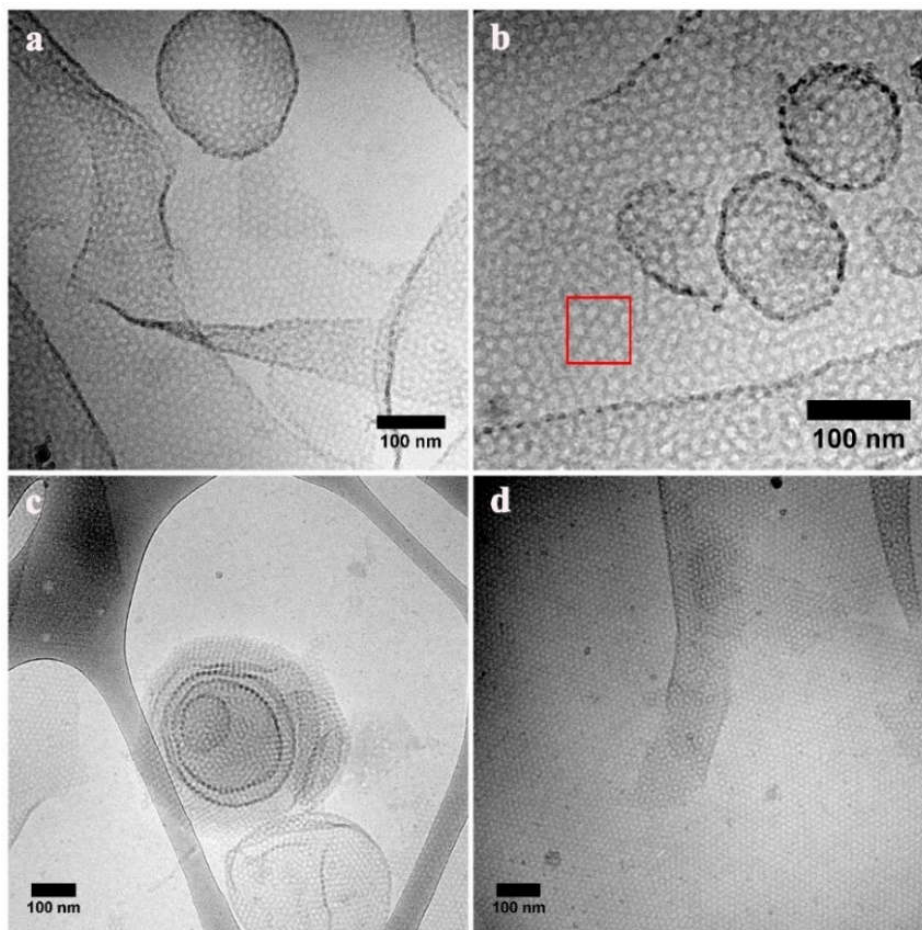


**Figure 10.** Images Cryo-EM des membranes et des vésicules formées par le PEG550-TPE-Chol (a-b) et le PEG550-SS-TPE-SS-Chol (c-d). La méthode d'hydratation en couche mince a été utilisée pour réaliser l'autoassemblage. (PEG550-TPE-Chol: *trans/cis* = 50/50; PEG550-SS-TPE-SS-Chol: *trans/cis* = 50/50).

Pour comprendre le mécanisme de formation de la membrane perforée, nous avons également étudié les comportements d'auto-assemblage des mélanges d'isomères *trans*- et *cis* du PEG550-TPE-Chol, intentionnellement préparés avec différents rapports relatifs (25/75, 40/60, 50/50, 60/40, 75/25). Les morphologies et les tailles des auto-assemblages ont été caractérisées par la Cryo-EM. Fondamentalement, le *trans*-PEG550-TPE-Chol s'est auto-assemblé en vésicules normales et le *cis*-PEG550-TPE-Chol en micelles cylindriques selon le résultat décrit dans le Chapitre II précédent. La Figure 11 montre les morphologies les plus représentatives des autoassemblages observés par Cryo-EM des cinq mélanges I-V préparés à partir du *trans*-PEG550-TPE-Chol et du *cis*-PEG550-TPE-Chol : I (*trans/cis* = 75/25), II

(*trans/cis* = 60/40), III (*trans/cis* = 50/50, voir ci-dessus), IV (*trans/cis* = 40/60), V (*trans/cis* = 25/75). Comme le montrent les Figures 11I-1 et I-2, la teneur en 25% de l'isomère *cis* est déjà suffisante pour introduire des nanopores dans les membranes et les vésicules, mais la taille des pores n'est pas homogène. 20% des pores ont un diamètre < 7,0 nm, 55% des pores ont un diamètre compris entre 7,0 et 15 nm et 25% des pores ont un diamètre > 15 nm. Il est intéressant de noter que des rubans plats au lieu de micelles cylindriques et des objets ressemblent aux pieuvres composées de bras de ruban rayonnant à partir d'une seule bicouche sont visibles dans les parties libres des mailles (voir Figure 11I-2).

Notez que les rubans dont le grand côté est perpendiculaire à la plaque d'image apparaissent plus noirs que ceux dont le grand côté est parallèle à la plaque d'image (voir la Figure 11I-2 et son encart). Il est clair que dans le mélange *trans/cis* = 75/25, des domaines riches en *cis* apparaissent, qui forment les structures hémicylindriques des bords des rubans entrelacés et des trous des vésicules poreuses (Figure 12). Lorsque les contenus des isomères *trans*- et *cis* sont plus équilibrés, comme *trans/cis* = 60/40, 50/50 et 40/60, les membranes et vésicules perforées (y compris les petites et les géantes) sont les principales morphologies. On souligne que dans le cas de *trans/cis* = 50/50, les trous de la membrane ont tendance à s'organiser localement en structure hexagonale (voir la structure à l'intérieur des cadres rouges sur la Figure 11III-2). Lorsque les isomères *cis* deviennent dominants comme *trans/cis* = 25/75, nous avons observé beaucoup de micelles cylindriques et quelques rubans (mailles) entrelacés (Figure 11V et Figure 12). Enfin, dans l'isomère *cis*, seules des micelles cylindriques ont été observées.

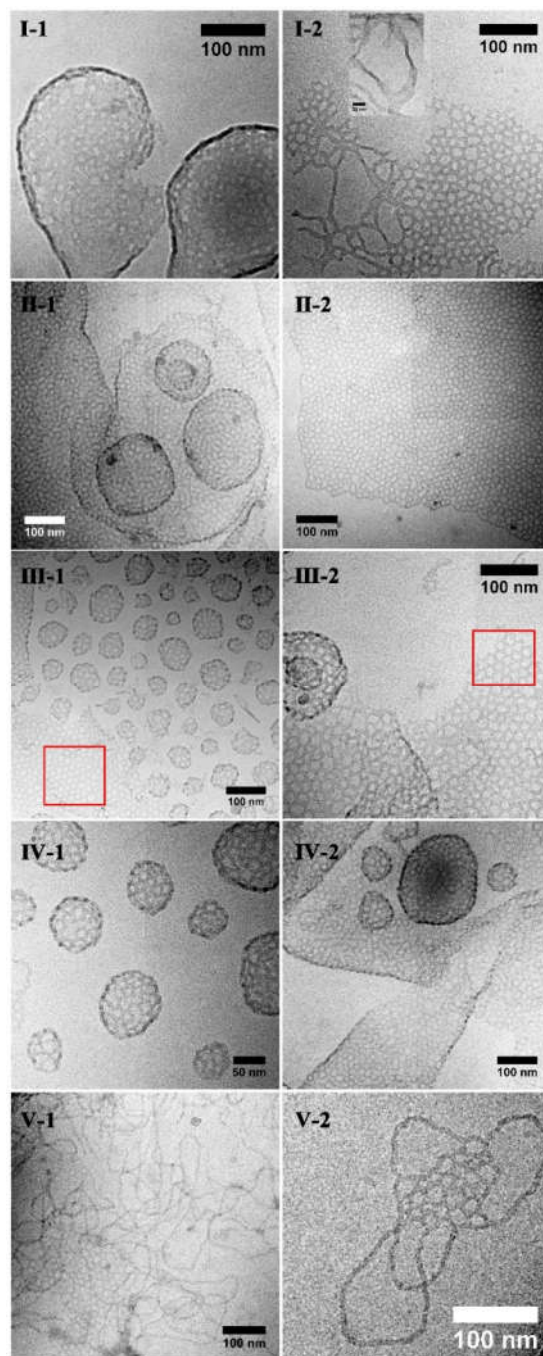


**Figure 11.** Images par Cryo-EM d'autoassemblages obtenus à partir de cinq mélanges I-V de *trans*- et *cis*-PEG550-TPE-Chol. I-1 et I-2 (*trans/cis* = 75/25), II-1 et II-2 (*trans/cis* = 60/40), III (*trans/cis* = 50/50, mentionné ci-dessus), IV-1 et IV-2 (*trans/cis* = 40/60), V-1 et V-2 (*trans/cis* = 25/75).

L'ensemble du scénario des transitions morphologiques ci-dessus peut être expliqué comme suit (Figure 12). Des isomères *cis* formant des micelles ajoutés à une membrane bicouche tentent d'imposer une courbure positive aux monocouches constitutives (feuillet). Les monocouches ne peuvent rester unies à une bicouche plate que jusqu'à une concentration critique des isomères *cis* formant des micelles. Au-delà de ce point critique, des bords peuvent se former, qui contiendraient principalement les isomères *cis* formant des micelles et s'assembleraient en structures hémicylindriques à courbure négative (les trous). Avec l'augmentation des *cis*-isomères micellaires, les bords hémicylindriques s'agrandissent et les zones bicouches plates se rétrécissent. Par conséquent, la séquence de transformation a été observée des bicouches, aux bicouches avec des trous croissants, aux rubans entrelacés, jusqu'aux micelles cylindriques.

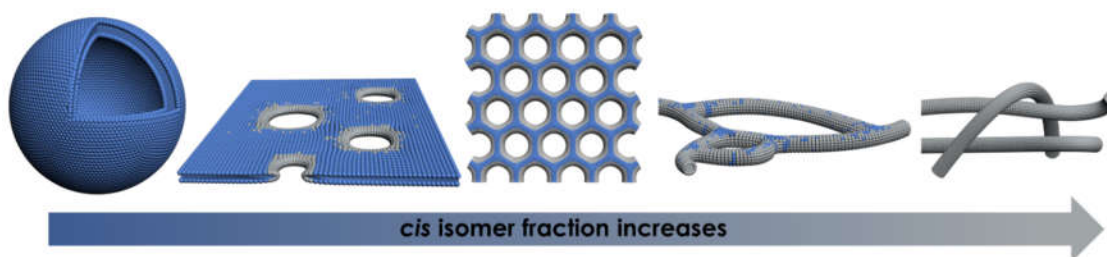


**Figure 12.** Représentation schématique de l'évolution morphologique représentative du PEG550-TPE-Chol en fonction de la fraction *cis*. Les points bleus représentent la forme du *trans*-PEG550-TPE-Chol formant la membrane, qui est de préférence assemblée dans des zones plus plates. Les points gris représentent la forme du *cis*-PEG550-TPE-Chol formant des micelles, qui sont probablement agrégées aux bords des trous ayant une courbure plus élevée.

A la fin, nous tentons d'expliquer du point de vue de la flexibilité moléculaire pourquoi les nanopores dans la membrane du PEG550-SS-TPE-SS-Chol (*trans/cis* = 50/50) s'auto-organise en superstructure hexagonale, tandis que les nanopores dans la membrane du PEG550-TPE-Chol (*trans/cis* = 50/50) ont une structure plutôt aléatoire et ne présentent une organisation hexagonale très localement.

#### **Chapitre IV. Cubosomes et hexosomes polymères fluorescents présentant les caractéristiques de l'AIE**

##### ***Synthèse des PEG-b-PTPEMA***



Dans ce chapitre, nous avons développé des cubosomes et hexosomes AIE à partir des nouveaux copolymères séquencés amphiphiles PEG-*b*-PTPEMA, dans lesquels le bloc hydrophobe PTPEMA était un polyméthacrylate avec le TPE comme groupe latéral (Schéma 4). Quatre copolymères séquencés hautement asymétriques avec un bloc hydrophobe beaucoup plus grand que son bloc hydrophile ont été synthétisés par transfert de chaîne réversible par addition-fragmentation, conduisant à des copolymères avec  $f_{\text{PEG}}$  (% en poids) = 20, 12.3, 8.9, 3.3 %, respectivement.

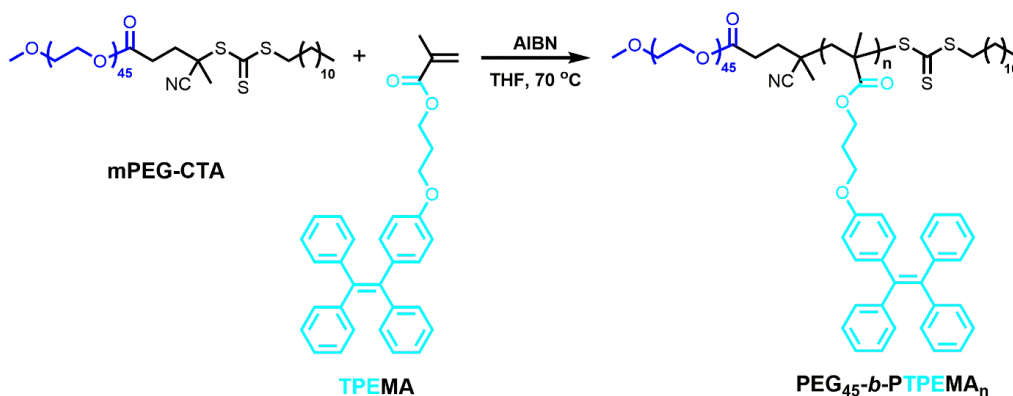


**Schéma 4.** La voie synthétique vers le PEG<sub>45</sub>-*b*-PTPEMA<sub>n</sub>.

#### *Hexosomes, cubosomes primitifs et polymersomes formés dans le système dioxane/eau*

L'autoassemblage du PEG<sub>45</sub>-*b*-PTPEMA<sub>n</sub> a été réalisé par la méthode de nano-précipitation en utilisant d'abord le dioxane comme co-solvant. Typiquement, une solution de copolymère à une concentration de 0.25 % en poids a été préparée dans du dioxane, puis de l'eau a été ajoutée progressivement à la solution jusqu'à ce que la teneur en volume d'eau atteigne 83 %. Les autoassemblages finaux étaient obtenus par dialyse du mélange contre un grand volume d'eau pour éliminer tout solvant organique. Leurs morphologies ont été étudiées par Cryo-EM, MET et MEB. Comme le montre la Figure 13, les PEG<sub>45</sub>-*b*-PTPEMA<sub>n</sub> avec  $n = 16, 29, 42$  et  $122$  ont formé des polymersomes, des structures spongieuses, des cubosomes et des hexosomes, respectivement. Les polymersomes sphériques du PEG<sub>45</sub>-*b*-PTPEMA<sub>16</sub> sont clairement révélés par l'image Cryo-EM (Figure 13A) et confirmés par l'image MEB montrant des sphères vides brisées (Figure 13E). Lorsque la longueur du bloc hydrophobe PTPEMA<sub>n</sub> augmente jusqu'à  $n = 29$ , des nanoparticules spongieuses à structure poreuse désordonnée, ainsi que des polymersomes, apparaissent comme le montrent les images MET et MEB (Figure



13B, 13F). En augmentant encore la longueur du bloc hydrophobe à  $n = 42$  et  $122$ , les PEG<sub>45</sub>-*b*-PTPEMA<sub>42</sub> et PEG<sub>45</sub>-*b*-PTPEMA<sub>122</sub> s'auto-assemblent en cubosomes (Figure 13C, 13G) et hexosomes (Figure 13D, 13H), respectivement. L'encart de la Figure 13G (MEB) montre que le cubosome présente des pores tétraogonaux à sa surface. La Figure 13D (Cryo-EM) montre les cylindres courbés typiques des hexosomes, tandis que la Figure 13H (MEB) présente une morphologie non sphérique avec des cylindres tassés.

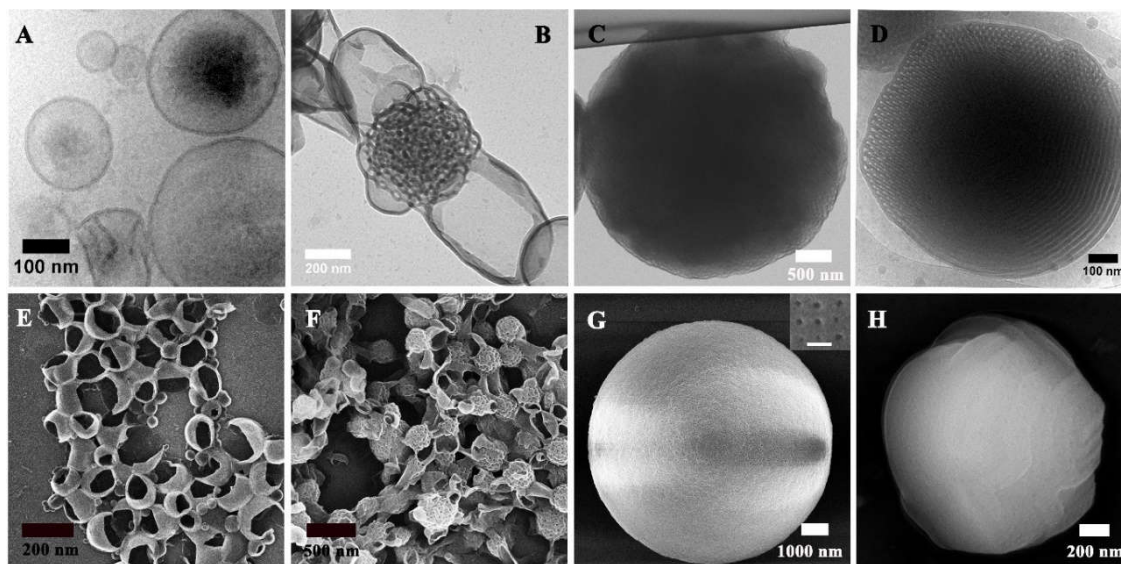


**Figure 13.** Auto-assemblages formés par le PEG<sub>45</sub>-*b*-PTPEMA<sub>n</sub> utilisant le dioxane comme cosolvant avec une concentration initiale de 0.25 % en poids. (A, E) Polymersomes du PEG<sub>45</sub>-*b*-PTPEMA<sub>16</sub>. (B, F) Morphologies mixtes de structures d'éponge et de polymersomes de PEG<sub>45</sub>-*b*-PTPEMA<sub>29</sub>. (C, G) Cubosomes primitifs de PEG<sub>45</sub>-*b*-PTPEMA<sub>42</sub> (l'encadré en G montre les images amplifiées d'une partie de la surface. Barre d'échelle : 100 nm). (D, H) Hexosomes de PEG<sub>45</sub>-*b*-PTPEMA<sub>122</sub>. (A, D) Cryo-EM, (B, C) MET, (E-H) MEB.

D'autres images MEB et Cryo-EM de cubosomes et d'hexosomes, ainsi que des courbes de diffusion des rayons X aux petits angles (SAXS), sont données dans la Figure 14. Le profil SAXS des cubosomes PEG<sub>45</sub>-*b*-PTPEMA<sub>42</sub> (Figure 14A) présente des rapports caractéristiques de 2:4:32 pour le carré du vecteur de diffusion ( $q^2$ ), qui correspondent à (110), (200) et (440) réflexions de la structure cubique primitive  $Im\bar{3}m$ . Le profil SAXS des hexosomes PEG<sub>45</sub>-*b*-PTPEMA<sub>122</sub> (Figure 14D) donne des rapports  $q^2$  de 1:3:4 correspondant à (10), (11), et (20) réflexions de la structure hexagonale  $P6mm$ . Les paramètres du réseau

déduits de ces profils SAXS étaient  $a_p = 46$  nm pour les cubosomes  $Im\bar{3}m$  et  $a_H = 25$  nm pour la structure hexagonale  $P6mm$ .

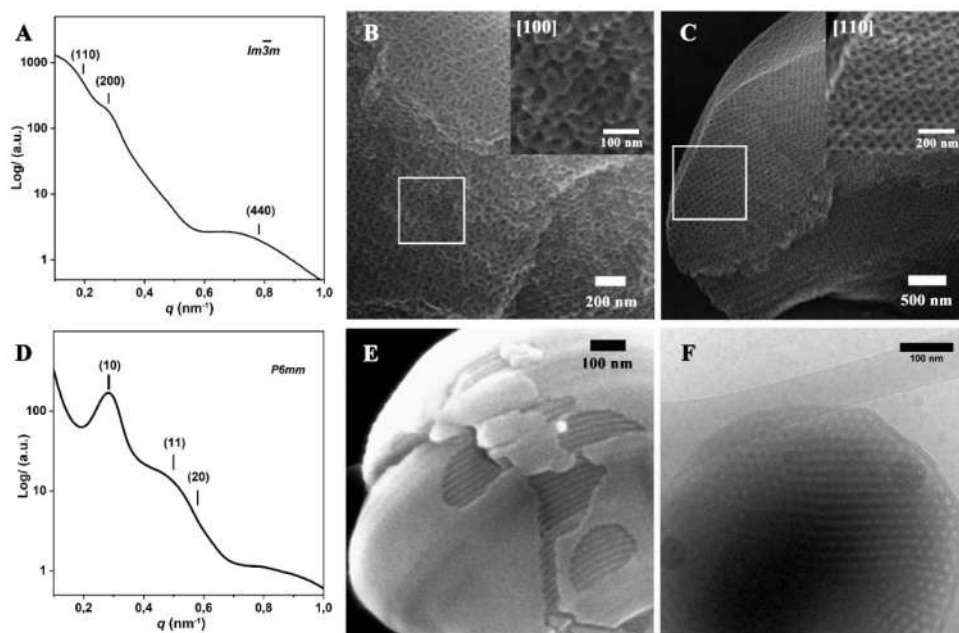


**Figure 14.** Caractérisation structurale des cubosomes et hexosomes de PEG-*b*-PTPEMA formés avec le dioxane comme co-solvant. Profil SAXS (A) et images MEB (B et C) des cubosomes  $Im\bar{3}m$  de PEG<sub>45</sub>-*b*-PTPEMA<sub>42</sub>. Profil SAXS (D), images MEB (E) et Cryo-EM (F) des hexosomes de PEG<sub>45</sub>-*b*-PTPEMA<sub>122</sub>. Les encadrés dans B et C sont les images MEB des cubosomes  $Im\bar{3}m$  dans les directions [100] et [110], respectivement.

Les Figures 14B et 14C montrent des images MEB de cubosomes de PEG<sub>45</sub>-*b*-PTPEMA<sub>42</sub> brisés par la congélation à l'azote liquide pendant la préparation de l'échantillon, où leurs domaines internes ordonnés le long de la direction [100] et [110] sont exposés (encarts dans les Figures 14B et 14C respectivement). Le MET a également été appliqué pour examiner la structure interne des cubosomes (Figure 13C). La taille moyenne des cellules unitaires de la structure cubique primitive a été mesurée comme  $a_p = 45$  nm de l'image MET, ce qui est en bon accord avec celle évaluée par SAXS. Les Figures 14E et 14F montrent des images MEB et Cryo-EM des hexosomes du PEG<sub>45</sub>-*b*-PTPEMA<sub>122</sub>. L'image MEB de la Figure 14E montre un hexosome présentant des défauts de surface, ce qui révèle clairement les canaux cylindriques très serrés. Le tassement hexagonal de ces cylindres est visible sur les images Cryo-EM (Figure 14F) dans les régions des coupes transversales. Le paramètre unitaire moyen

des cellules de la structure  $P6mm$  a été mesuré comme  $a_H = 24$  nm de l'image Cryo-EM, ce qui est également en bon accord avec celui évalué par SAXS. La tendance de la formation de polymersomes, cubosomes et hexosomes avec la diminution progressive du rapport hydrophile  $f_{PEG}$  (de 20% à 3,3%) et l'augmentation de la longueur du bloc hydrophobe est en accord avec le diagramme de phase classique selon le paramètre d'assemblage  $p$  passant de  $p \leq 1$  pour les structures vésiculaires normales à  $p > 1$  pour les phases inverses (cubique et hexagonale).

### ***Hexosomes et polymersomes formés dans le système THF/eau***

L'effet du co-solvant sur l'autoassemblage a également été étudié. Au lieu du dioxane, le tétrahydrofurane (THF) a ensuite été utilisé comme co-solvant pour préparer des particules de  $PEG_{45}-b-PTPEMA_n$  avec une concentration initiale de 0.25 % en poids. La Figure 15 montre des images Cryo-EM, MET et MEB

Comme dans le cas du système dioxane/eau, le  $PEG_{45}-b-PTPEMA_{16}$  forme également des vésicules sphériques, comme le montre l'image Cryo-EM (Figure 15A) et confirmé par l'image MEB montrant des capsules ouvertes (Figure 15E). En augmentant la longueur du bloc hydrophobe à  $n = 29$ , les polymersomes sont toujours l'espèce dominante d'après les images MEB et MET (Figure 15B et 15F). Cependant, dans les systèmes THF/eau, la structure spongieuse et la phase cubique inverse n'existent plus. Les hexosomes semblent directement coexister avec les polymersomes (voir les Figures 15B, 15F). En augmentant encore la longueur du bloc hydrophobe jusqu'à  $n = 42$ , les hexosomes deviennent la structure principale (Figure 15C, 15G). Les images Cryo-EM (Figure 15C) révèlent leurs structures internes avec une section transversale hexagonale. Le paramètre moyen des cellules unitaires de la structure  $P6mm$  a été mesuré comme  $a_H = 26$  nm sur la base des images Cryo-EM. Cette structure hexagonale du  $PEG_{45}-b-PTPEMA_{42}$ , lorsqu'il est préparé dans du THF/eau, a été confirmée par l'analyse du profil SAXS, montrant des pics avec des rapports  $q^2$  de 1:3:7, attribués aux réflexions (10), (11) et (21) de la structure hexagonale avec  $a_H = 29$  nm comme paramètre de réseau (Figure 16). Enfin, lorsque la longueur du bloc hydrophobe augmente à  $n = 122$ , on obtient des particules solides à structure dense selon leurs images Cryo-EM et MEB (Figure 15D, 15H).

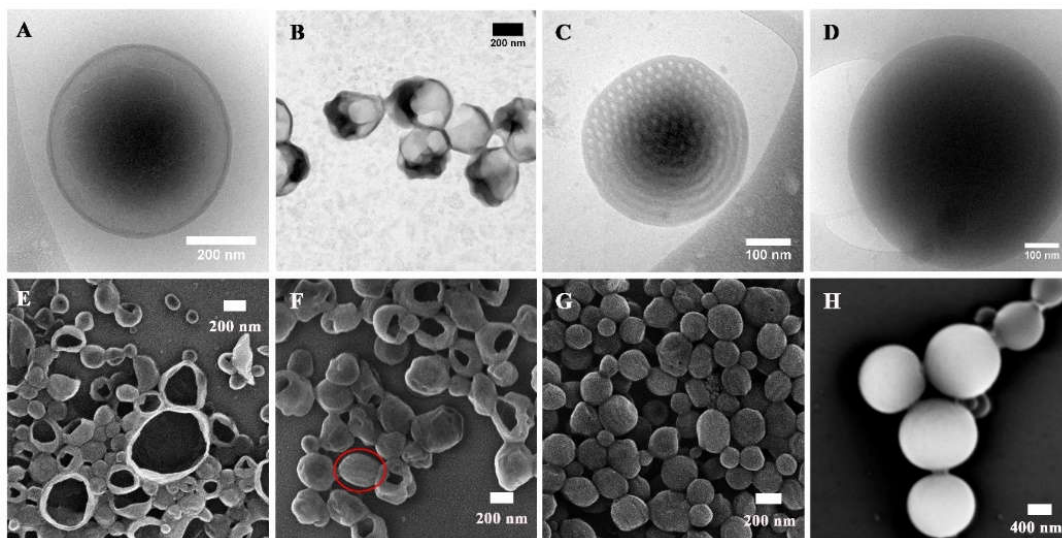


**Figure 15.** Auto-assemblages formés par le  $\text{PEG}_{45}\text{-}b\text{-PTPEMA}_n$  utilisant le THF comme cosolvant avec une concentration initiale de 0.25 % en poids. (A, E) Polymersomes du  $\text{PEG}_{45}\text{-}b\text{-PTPEMA}_{16}$ . (B, F) Polymersomes et hexosomes du  $\text{PEG}_{45}\text{-}b\text{-PTPEMA}_{29}$  (l'hexosome est indiqué par le cercle rouge). (C, G) Hexosomes du  $\text{PEG}_{45}\text{-}b\text{-PTPEMA}_{42}$ . (D, H) Sphères solides de  $\text{PEG}_{45}\text{-}b\text{-PTPEMA}_{122}$ . (A, C, D) Images Cryo-EM, (B) MET, et (E-H) MEB.

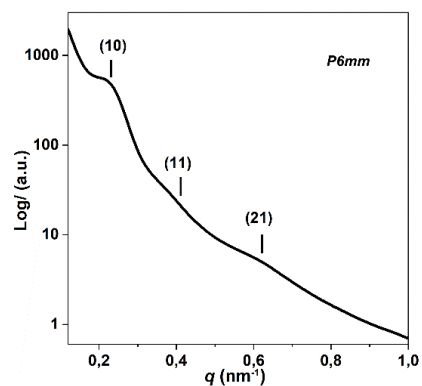


**Figure 16.** Le profil SAXS des hexosomes formés par le  $\text{PEG}_{45}\text{-}b\text{-PTPEMA}_{42}$  en utilisant le THF comme cosolvant avec une concentration initiale de 0.25 % en poids.

### *Effets du co-solvant sur la morphologie de l'autoassemblage*

Les résultats évoqués ci-dessus suggèrent que la nature du co-solvant a une influence significative sur la nanostructure des particules colloïdales. Cela est prévisible car le co-solvant avec un paramètre de solubilité différent affecte directement les dimensions des

domaines hydrophile et hydrophobe au cours du processus d'auto-assemblage. Les paramètres de solubilité ( $\delta$ ) du THF, du dioxane et de l'unité répétitive du PEG sont respectivement  $\delta_{\text{THF}} = 18.6$ ,  $\delta_{\text{dioxane}} = 20,5$  et  $\delta_{\text{PEG}} = 20.2 \text{ MPa}^{1/2}$ . Pour le bloc PTPEMA,  $\delta_{\text{PTPEMA}} = 18,9 \text{ MPa}^{1/2}$  est calculé en utilisant une méthode de contribution de groupe. En général, plus les valeurs  $\delta$  du polymère et du solvant sont proches, meilleure est la solubilité du polymère dans le solvant. Par conséquent, le PEG est plus soluble dans le dioxane que dans le THF, tandis que le PTPEMA est plus soluble dans le THF que dans le dioxane. Les formes initiales du PEG<sub>45</sub>-*b*-PTPEMA<sub>42</sub>, par exemple, sont différentes dans les systèmes dioxane/eau et THF/eau, comme le montre la Figure 17. Ainsi, la courbure inverse vers l'interface PEG est plus élevée dans le cas du THF que dans celui du dioxane. En effet, le PEG<sub>45</sub>-*b*-PTPEMA<sub>42</sub> s'est auto-assemblé en cubosomes avec une courbure négative d'interface plus faible dans le cas du dioxane/eau, mais en hexosomes avec une courbure négative plus élevée dans le cas du système THF/eau. En outre, pour le bloc PTPEMA plus court, le PEG<sub>45</sub>-*b*-PTPEMA<sub>29</sub> a formé une structure spongieuse avec des polymersomes dans le système dioxane/eau, tandis qu'il a formé des hexosomes à forte courbure négative avec des polymersomes dans le système THF/eau. Comme le solvant de la partie PEG est progressivement remplacé par l'eau (un bon solvant pour le PEG mais pas du tout miscible avec la PTPEMA), la forme gonflée de la PTPEMA dans le THF ou dans le dioxane est le paramètre clé du processus d'autoassemblage.

L'évolution de la fluorescence au cours du processus d'autoassemblage par nano-précipitation a été ensuite étudiée en prenant comme exemple le PEG<sub>45</sub>-*b*-PTPEMA<sub>42</sub> dans le dioxane/eau. Comme le montre la Figure 17A, une légère augmentation de l'intensité de la fluorescence est observée après l'ajout d'eau à  $f_{\text{water}} = 15 \%$ , ce qui indique que le PEG<sub>45</sub>-*b*-PTPEMA<sub>42</sub> commence à former des assemblages. Ensuite, l'intensité de la fluorescence conserve un taux d'augmentation lent jusqu'à  $\sim 50\%$  de la teneur en eau. À ce stade, la mobilité des chaînes hydrophobes et des fragments de TPE dans les agrégats est encore élevée en raison de l'effet plastifiant du solvant organique, ce qui entraîne un faible taux de croissance de la fluorescence. En augmentant encore la teneur en eau, on observe une augmentation exponentielle de l'intensité de la fluorescence, probablement due à l'élimination du solvant organique des domaines hydrophobes sous l'effet de la forte pression osmotique entre l'extérieur et l'intérieur de ces domaines. Cette élimination du solvant réduit efficacement la mobilité de la chaîne PTPEMA et bloque la rotation intermoléculaire des unités TPE, ce qui entraîne une croissance

rapide de l'intensité de la fluorescence. Ces observations montrent clairement la propriété AIE des autoassemblages (les inserts de la Figure 18A).

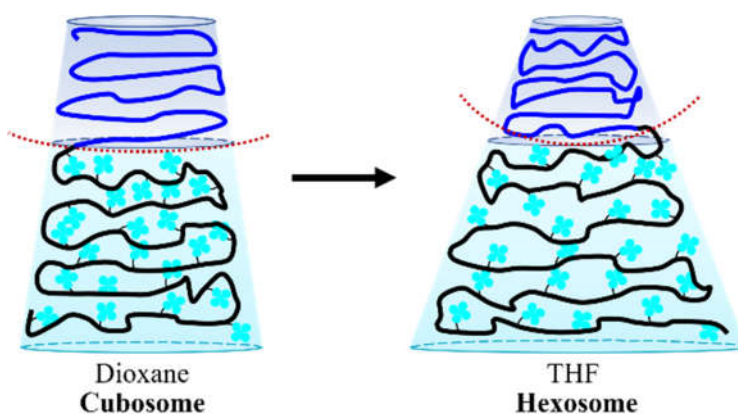


**Figure 17.** (a) Représentation schématique des formes moléculaires du  $\text{PEG}_{45}\text{-}b\text{-PTPEMA}_{42}$  dans le système dioxane/eau et THF/eau, qui donnent respectivement un cubosome et un hexosome.

#### ***Fluorescence AIE des autoassemblages $\text{PEG}_{45}\text{-}b\text{-PTPEMA}_n$***

Les dispersions colloïdales finales du  $\text{PEG}_{45}\text{-}b\text{-PTPEMA}_{42}$  et du  $\text{PEG}_{45}\text{-}b\text{-PTPEMA}_{122}$  dans l'eau ont ensuite été caractérisées par fluorospectromètre et microscopie à fluorescence. Les cubosomes de  $\text{PEG}_{45}\text{-}b\text{-PTPEMA}_{42}$  et les hexosomes de  $\text{PEG}_{45}\text{-}b\text{-PTPEMA}_{122}$  présentent une fluorescence élevée (Figure 18B) avec une émission maximale aux longueurs d'onde de 468 nm et 469 nm, respectivement, sous l'excitation à la longueur d'onde de 370 nm. Observés par microscopie à épifluorescence, les colloïdes (cubosomes et hexosomes) émettent une fluorescence cyan brillante sous l'éclairage de la lumière UV ( $\lambda = 365$  nm) comme le montre la Figure 18C-D. Les rendements quantiques des cubosomes  $\text{PEG}_{45}\text{-}b\text{-PTPEMA}_{42}$  et des hexosomes  $\text{PEG}_{45}\text{-}b\text{-PTPEMA}_{122}$  ont été mesurés à 17 % et 23 %, respectivement, en utilisant la méthode de la sphère intégrante.

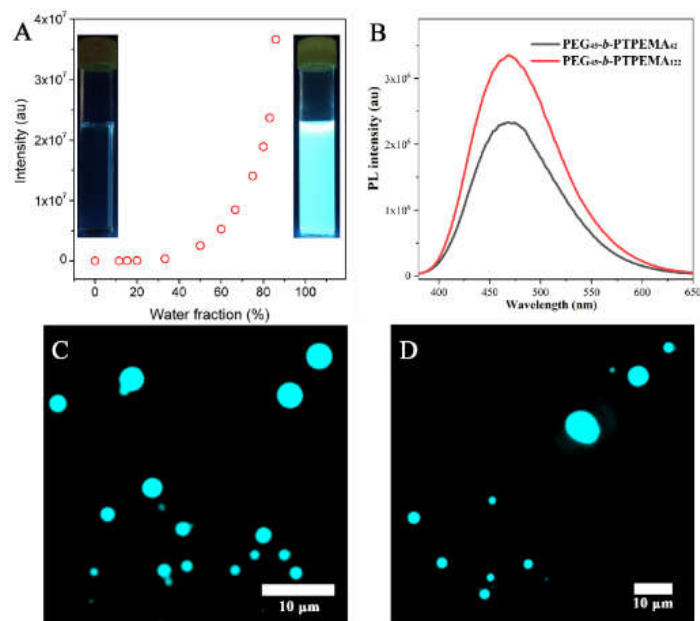


**Figure 18.** (A) L'évolution de l'intensité de la fluorescence en fonction de la teneur en eau pendant la nanopréciipitation du PEG<sub>45</sub>-*b*-PTPEMA<sub>42</sub> dans le système dioxane/eau. Les photos sont prises sous une lumière UV de 365 nm pour le PEG<sub>45</sub>-*b*-PTPEMA<sub>42</sub> en solution de dioxane (à gauche) et ses cubosomes dans l'eau après dialyse (à droite). (B) Spectres de photoluminescence des cubosomes du PEG<sub>45</sub>-*b*-PTPEMA<sub>42</sub> et des hexosomes du PEG<sub>45</sub>-*b*-PTPEMA<sub>122</sub> (concentration : 0,4 mg mL<sup>-1</sup> ; longueur d'onde d'excitation :  $\lambda = 370$  nm). (C, D) Les images des cubosomes (C) de PEG<sub>45</sub>-*b*-PTPEMA<sub>42</sub> et des hexosomes (D) de PEG<sub>45</sub>-*b*-PTPEMA<sub>122</sub> prises au microscope à épifluorescence (longueur d'onde d'illumination :  $\lambda = 365$  nm). L'auto-assemblage a été réalisé dans un système dioxane/eau.



## Abstract

Aggregation-induced emission (AIE) property refers to an unnormal photophysical phenomenon shown by a group of specific luminogens that are non-emissive in solution but become highly luminescent in aggregated state. The combination of AIE luminogens (AIEgens) with polymer assemblies presents particular interest and may open a novel way to prepare highly efficient luminescent materials with potential applications in bio-medical field. In the present study, a variety of AIE polymer assemblies including polymersomes, porous polymersomes, cubosomes and hexosomes are constructed through the self-assembly of different families of AIEgen-containing amphiphilic copolymers. The thesis manuscript consists of five chapters, in which the first chapter is “Introduction”, and the fifth chapter is “General conclusion and perspectives”. The main research contents can be divided into three parts and are described in the chapters II, III and IV.

In the first research part (Chapter II), AIE polymersomes and AIE porous polymersomes are discussed. They were obtained from the self-assembly of the amphiphilic copolymers PEG550-TPE-Chol with tetraphenylene (TPE) and cholesterol (Chol) as the hydrophobic component, and polyethylene glycol (PEG550) as the hydrophilic block. TPE in its center is an emblematic fluorescent AIEgen, meanwhile the disubstituted TPE possesses two stereoisomers which are sensitive to UV illumination. With stereoisomers separation, two amphiphilic stereoisomers, namely *trans*-PEG550-TPE-Chol and *cis*-PEG550-TPE-Chol were obtained. These two amphiphilic stereoisomers exhibited distinct self-assembling behaviors: *trans*-isomer of the polymer formed classical vesicles, *cis*-isomer formed cylindrical micelles, while *trans/cis* mixtures constructed perforated polymersomes with nanopores in the membrane. All these assemblies were highly fluorescent. The smooth vesicles of *trans*-isomer were perforated upon UV illumination due to the generation of its *cis* counterpart. The polymersomes from “closed” to “open” state allowed to release the encapsulated substance in a controlled way by light. In addition, the cylindrical micelles of *cis* isomer interweaved to construct perforated membranes upon UV illumination due to the generation of its *trans* counterpart. There was no significant morphological change for porous polymersomes self-assembled by *trans/cis* mixture of PEG550-TPE-chol upon UV illumination, but membrane fluctuation in micrometer scale was observed by epifluorescence microscopy.



In the Chapter III, AIE polymersomes with hexagonal packed nanopores on its membrane are presented. They were prepared from a *trans* and *cis* isomers' mixture of amphiphilic copolymer PEG550-SS-TPE-SS-Chol obtained naturally from synthesis without isomers separation. Compared to PEG550-TPE-Chol described above, PEG550-SS-TPE-SS-Chol possess two disulfide bonds -S-S- inserted in the spacers between PEG and TPE, and between Chol and TPE. The PEG550-SS-TPE-SS-Chol formed vesicles with hexagonal packed nanopores in the membrane, while the PEG550-TPE-Chol formed vesicles with randomly packed nanopores in the membrane. Moreover, the hexagonal nano-porous vesicles exhibited reduction-responsive property due to the presence of disulfide bonds. To understand the formation mechanism of perforated membrane by *trans/cis* mixtures and the structuration of nanopores, both situations of PEG550-SS-TPE-SS-Chol and PEG550-TPE-Chol are compared. Especially, morphological evolution of *trans/cis* mixture of PEG550-TPE-Chol as function of the *cis* proportion was studied in detail.

In the Chapter IV, AIE polymer cubosomes and hexosomes are described. They were prepared from amphiphilic block copolymers PEG-*b*-PTPEMA where the hydrophobic block PTPEMA was a polymethacrylate with TPE as side group. Four highly asymmetric block copolymers with hydrophilic block weight ratio  $f_{\text{PEG}} \leq 20\%$  were synthesized. Cubosomes and hexosomes with strong fluorescence emission were obtained by nanoprecipitation of polymers with  $f_{\text{PEG}} < 9\%$  in dioxane/water and THF/water systems. Their ordered internal structures were studied by cryogenic-electron microscopy (cryo-EM), scanning electron microscopy (SEM) and transmission electron microscopy (TEM), X-ray scattering technique (SAXS). To elucidate the formation mechanisms of these inverted colloids, other parameters influencing the morphologies, like the water content during self-assembly and the organic solvent composition, were also investigated. This study not only inspires people to design novel building blocks for the preparation of functional cubosomes and hexosomes, but also present the first AIE fluorescent polymer cubosomes and hexosomes with potential applications in bio-related fields.

## Chapter I. Introduction

### 1.1 Amphiphilic block polymers and their self-assembly in aqueous solution

#### 1.1.1 Amphiphilic block polymers

Small amphiphilic molecules are compounds of low molar masses (typically  $< 500 \text{ g}\cdot\text{mol}^{-1}$ ), which are composed of hydrophobic and hydrophilic components, such as lipids. Among lipids, the phospholipids are the essential building segments of the bilayers of cell membranes. By analogy, small amphiphilic molecules have macromolecular counterparts with higher molar masses, for instance, amphiphilic block copolymers that are made of hydrophobic block (*e.g.* polybutadiene, polystyrene...) and hydrophilic block (*e.g.* polyethylene oxide, polyacrylic acid...). Amphiphilic block copolymers have some special properties in comparison to small amphiphiles. For example, the polymer chemistry allows much more flexibility to design the amphiphilic block copolymers. This design flexibility includes the variety of the number of polymer blocks, of their chemical structures and molar masses, and of their functionalities and architectures.<sup>1</sup> Consequently, almost an infinite number of possible amphiphilic block copolymers are accessible through rational design.<sup>2</sup>

In general, there are two main approaches for the synthesis of amphiphilic block copolymers.<sup>3</sup> In the first approach, the desired amphiphilic block copolymers are synthesized by end group connection of pre-prepared polymer block(s). Such an approach is advantageous when it is convenient to attach suitable functional end group to a pre-prepared block. The second and also the most popular approach is based on the sequential polymerization of different monomers using anionic, cationic, radical, or ring-opening polymerization techniques.<sup>2</sup> Among them, the controlled/ “living” radical polymerization (CRP) are the most used techniques to prepare amphiphilic block copolymers with low molecular weight distribution. There are three fundamental CRP techniques, *i.e.*, atom-transfer radical polymerization (ATRP),<sup>4</sup> reversible addition fragmentation transfer (RAFT) polymerization,<sup>5,6</sup> and nitroxide-mediated polymerization (NMP).<sup>7,8</sup> These techniques present exceptional advantages compared to ionic living polymerizations: the requirements of polymerization conditions are less strict and the tolerance for functional groups are higher. A broad range of vinyl monomers with various functional groups could be utilized for CRP. Polymers with functional end groups are readily obtained *via* CRPs, which can be further used to yield new block polymers with more complicated architectures. The CRP can even be carried out in aqueous medium. Due to

these advantages, tremendous amphiphilic block copolymers have been created through CRP. Additionally, ring-opening metathesis polymerization (ROMP), chain growth polycondensation, is also applied to synthesize amphiphilic block copolymers.<sup>9</sup>

Amphiphilic polymers have attracted much attention due to their great potential in various applications. The application areas include drug delivery,<sup>10-14</sup> lithographic technique,<sup>15,16</sup> fabrication of thin films and ordered porous membrane,<sup>17-21</sup> biomolecular separation,<sup>22,23</sup> virus filtration,<sup>24</sup> gas delivery,<sup>25</sup> and water purification.<sup>26</sup> In fact, the potential application areas of amphiphilic block copolymers are still expanding, with lots of opportunities in the fields of physics, chemistry, biological and materials sciences.

### 1.1.2 Self-assembly of amphiphilic block polymers in aqueous solution

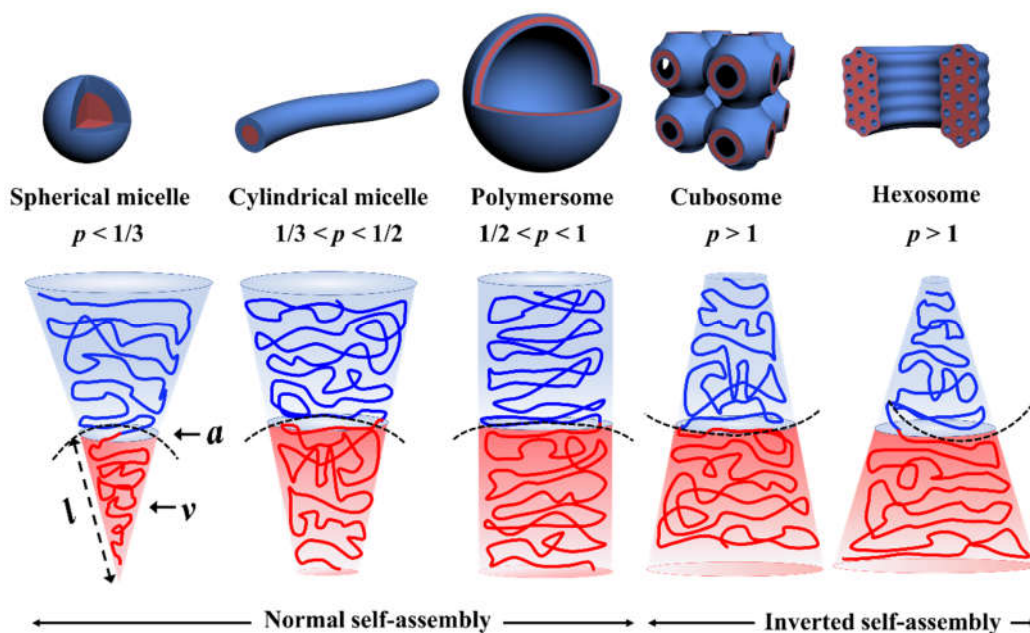


**Figure 1.1.** Self-assembly structures of amphiphilic block copolymers: spherical micelles, cylindrical micelles, polymer vesicles, cubosomes and hexosomes with corresponding packing parameters.

When dissolved in aqueous solution at fixed temperature, above the critical micelle concentration (CMC), the amphiphilic block copolymer can self-assemble into various morphologies, such as spherical micelles, cylindrical micelles, vesicles, lamellas and inverted structures, depending on their shape in solution.<sup>27,28</sup> The geometrical packing parameters  $p$ ,

originally developed for small amphiphiles in water, can be used to explain empirically the morphologies formed by block copolymers. The  $p$  is defined as  $p=v/al$ , where  $v$  is the volume of the hydrophobic part,  $a$  is the optimal area of the hydrophilic part at the interface and  $l$  is the length of the hydrophobic component. Typically, amphiphilic block copolymers form spherical micelles when  $p \leq 1/3$ , cylindrical micelles are favored for copolymers with  $1/3 \leq p \leq 1/2$ , and for the copolymers with  $1/2 \leq p \leq 1$ , polymer vesicles (or bilayers) are generated (Figure 1.1). All these structures belong to the normal assemblies with positive curvature. Inverted structures (also called inverse structure) with negative curvature including polymer cubosomes and hexosomes are obtained when  $p > 1$ .<sup>29</sup>

The packing parameter suggests the inherent curvature and favorable conformation of a block copolymer in aqueous solution, which is determined by its molecular properties including chemical structure, molecular weight, hydrophilic/hydrophobic ratio, chain rigidity and intermolecular interactions, *etc.* In thermodynamic view, the self-assembly of amphiphilic block copolymers is driven by the minimization of the total free energy of the system. The packing parameter method is useful to predict the assembled morphology when the aggregate is in the global equilibrium state. Nevertheless, the relatively high molecular weight sets barriers for the polymer to adjust its conformation and position towards global equilibrium state. It is often found that the self-assembled structures of polymer stop at a (meta)stable stage, which is called “kinetically frozen” structures.<sup>30</sup> As a result, the self-assembly of block copolymers presents nonergodic properties.<sup>31</sup> This nonergodicity endows the copolymer with the potential ability to form a large diversity of morphologies, which could be controlled by different preparation conditions including concentration variation,<sup>32</sup> temperature variation,<sup>33</sup> polarity of solvents,<sup>34</sup> crystallization,<sup>35</sup> addition of surfactant,<sup>36</sup> emulsification,<sup>37</sup> applying of electric field,<sup>38</sup> *etc.*

For example, with the kinetic control, Pochan *et al.*, reported the preparation of cylindrical micelles and worm-like micelles with an alternating structure by controlling the cosolvent in self-assembly (Figure 1.2).<sup>39</sup> As shown in Figure 1.2A, poly(acrylic acid)-*b*-poly(methyl acrylate)-*b*-polystyrene (PAA-*b*-PMA-*b*-PS) firstly self-assembled into spherical micelles in the presence of 2,2'-(ethylenedioxy)diethylamine (EDDA) in THF/water mixture (THF/water = 1:4). In this case, the PMA and PS block accumulated inside the spherical core, while the PPA localized at the corona of the spherical micelles (Figure 1.2C). Then, THF was pipetted into the solution quickly to get a final volumetric ratio of THF/water= 2/1. TEM demonstrated

that all the micelles polymerized along a preferred growth axis since the PAA-diamine pairs in the corona were immiscible in THF (Figure 1.2B). Further aging for several hours allowed additional one-dimensional growth of the structure into long structure with uniform widths (Figure 1.2D). In the late stage of growth, branches were formed when two disks pack to one end of the worm (Figure 1.2E-F).

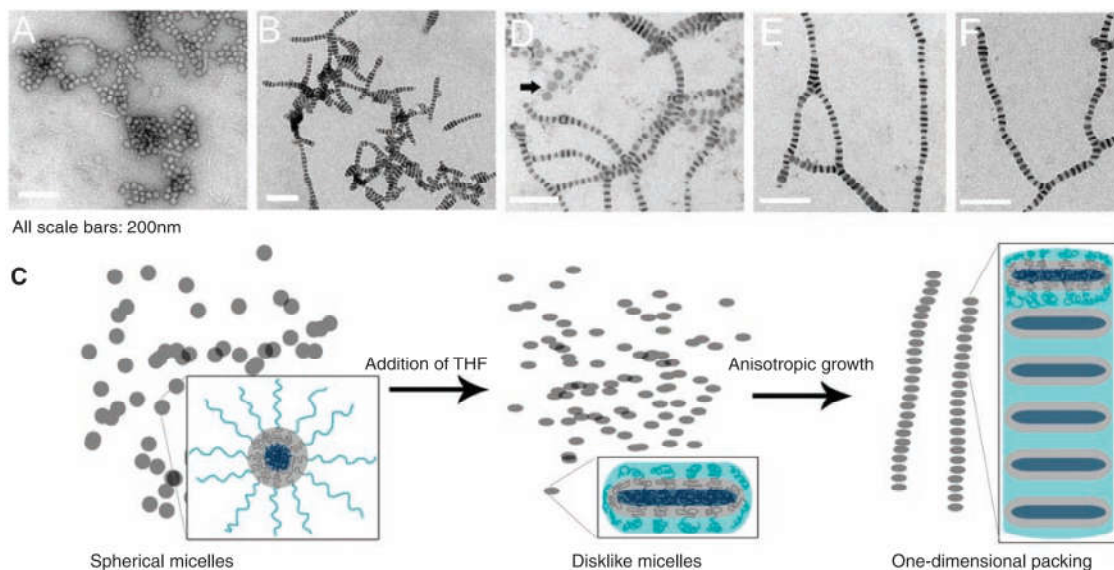


**Figure 1.2.** (A) The spherical micelles formed by triblock copolymer PAA<sub>94</sub>-*b*-PMA<sub>103</sub>-*b*-PS<sub>44</sub> and EDDA (polymer : EDDA = 1 : 1) in the mixture of THF : H<sub>2</sub>O = 1 : 4; (B) Cylinders resulted from the quick introduction of THF; (C) The schematic illustration on the growth mechanism of ribbon-like structures; (D) Worm-like micelles and separate disk-like micelles marked by black arrows; (E and F) Branched structures formed in the late stage of growth. Scale bar = 200 nm.<sup>39</sup>

By combining the inherent molecular property and the external preparation condition, a variety of structures with high complexity can be obtained.<sup>40</sup> So far, more than 20 morphologies have been reported such as spherical micelles,<sup>41</sup> rods,<sup>42</sup> cyclic micelles,<sup>43</sup> lamellae,<sup>44</sup> polymer vesicles,<sup>45</sup> faceted vesicles,<sup>46</sup> networks,<sup>47</sup> large compound micelles (LCMs),<sup>48</sup> large compound vesicles (LCVs),<sup>49</sup> tubules,<sup>33</sup> “onions”,<sup>50</sup> pincushions,<sup>51</sup> “eggshells”,<sup>50</sup> bicontinuous structures,<sup>52</sup> hexosomes,<sup>52</sup> *etc.* Some of which are thermodynamically induced, while others are kinetically controlled.<sup>53</sup>

Among various morphologies, we are interested in development of polymersomes (normal self-assembly), as well as polymer cubosomes and hexosomes (inverted assembly). The detail introduction of these assemblies will be discussed in following section.

## 1.2 Polymersomes

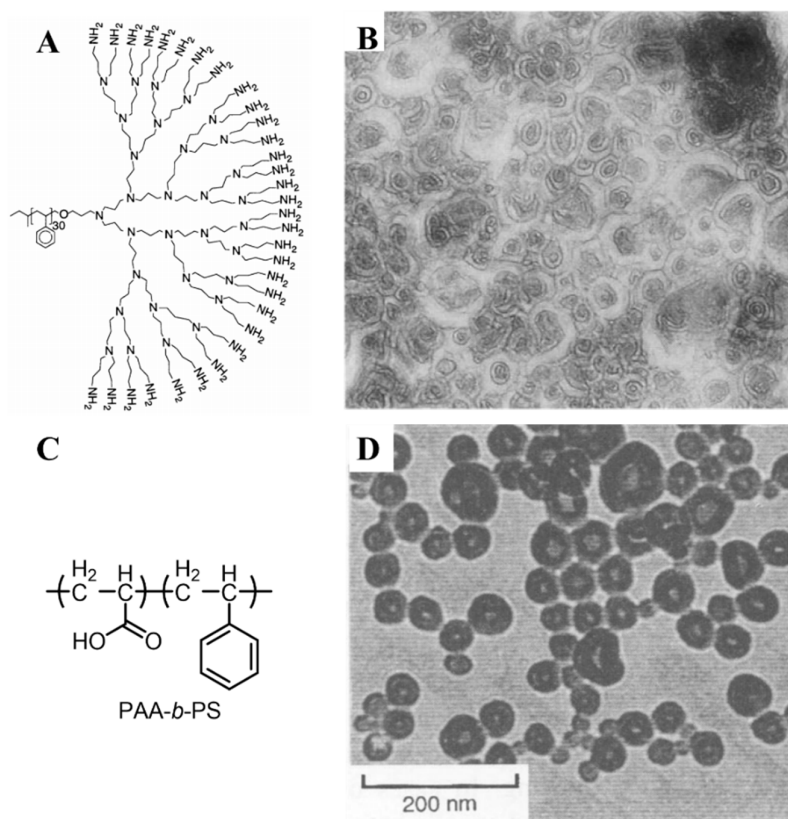


**Figure 1.3.** (A) The chemical structure of PS-*b*-poly(propylene imine) dendrimer. (B) The TEM images of the polymer vesicles formed by PS-*b*-poly(propylene imine) dendrimer.<sup>54</sup> (C) The chemical structure of PAA-*b*-PS. (D) The TEM images of the polymer vesicles formed PAA<sub>8</sub>-*b*-PS<sub>200</sub>.<sup>48</sup>

Polymersomes (also called polymer vesicles) have been an attractive research object since the end of last century. In 1995, Meijer *et al.*<sup>54</sup> and Eisenberg *et al.*<sup>48</sup> initially described polymer vesicles in two seminal publications. Meijer *et al.* reported polymer vesicle from amphiphilic polymers composed of a poly(styrene) (PS) block and a poly(propylene imine) dendrimer (Figure 1.3A-B). Eisenberg *et al.* studied self-assembly behavior of poly(acrylic acid)-*b*-PS (PAA-*b*-PS) diblock copolymers in the N,N-dimethylformamide (DMF)/water mixture. Transmission electron microscopy (TEM) images revealed a transition from spherical

(PAA<sub>21</sub>-*b*-PS<sub>200</sub>), to rod-like micelles (PAA<sub>15</sub>-*b*-PS<sub>200</sub>) and polymer vesicles (PAA<sub>8</sub>-*b*-PS<sub>200</sub>, Figure 1.3D) with the decrease of the PAA block length. These initial studies revealed that amphiphilic copolymers were able to form vesicular structures with rational molecular design.

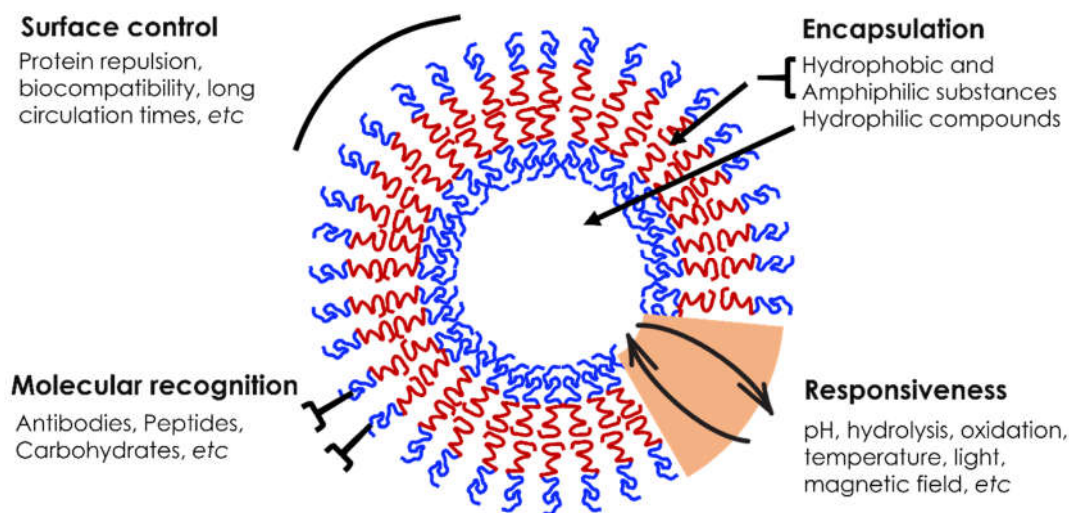


**Figure 1.4.** Different properties that can be integrated into the molecular design of polymersomes.

Basically, polymer vesicles are macromolecular homologues of liposomes (lipid vesicles). They have shell structures where an inner aqueous cavity is enclosed by a bilayer membrane composed of amphiphilic copolymers (block, dendronized, or graft copolymers). Because of the high molecular weight of the copolymers, the polymer bilayer has a higher thickness (5-50 nm) than that of the lipid bilayer (3-5 nm), and polymersomes have lower CMC and lower molecular exchange rates than liposomes. The polymersomes can entrap not only many hydrophilic molecules in the large volume of the inner aqueous compartment, but also a considerable quantity of hydrophobic molecules in the membrane of high molecular weight polymer (big hydrophobic pockets) (Figure 1.4). These characteristics are promising for the development of a new generation of vesicular drug delivery systems that are superior to liposomes in terms of stability, circulation time, and drug loading capacity. Moreover, polymer chemistry enables unlimited molecular design of polymersomes (Figure 1.4). An impressive library of polymersomes with diverse sizes, architectures, surface properties, membrane properties such as permeability and chemical functionalities has been constructed.<sup>40,55</sup> In the last decade, the research focuses involve the construction of “smart” polymersomes that can recognize environmental stimuli, such as pH, hydrolysis, oxidation, temperature, light,



magnetic field, *etc.*<sup>56-61</sup> In response to specific stimuli, the “smart” polymersomes are then capable of physical and chemical changes, such as swelling, membrane fusion and vesicle structural destruction, leading to drug release in dose-, spatial-, and temporal-controlled manners. Targeted transport can be achieved by surface modification of polymersomes with target-specific ligands such as antibodies,<sup>62,63</sup> proteins,<sup>64,65</sup> carbohydrates,<sup>66,67</sup> *etc.* In addition, fluorescent polymersomes that are liable to be used as bioimaging tools for real-time imaging of therapeutic substances delivery, diagnostic and theranostics.<sup>68,69</sup>

### 1.2.1 Structural and experimental conditions for polymersome formation

According to packing parameter model, the amphiphilic block copolymers with  $p$  in the range from 1/2 to 1 preferentially self-assemble into polymersomes. However, the value of  $p$  for an amphiphilic polymer is not easy to evaluate. It is more convenient to predict empirically the preferred morphology through hydrophilic fraction ( $f$ ). A liposome-forming hydrophilic to total mass ratio  $f$  for phospholipids ( $f \sim 35\%$ ) is often used as a practical guide for designing the polymersome-forming block copolymers. For example, vesicles were formed directly in water by PEO-*b*-PBD as its hydrophilic to total mass ratio  $f$  was around 35% (a phospholipids-like ratio).<sup>45,70,71</sup> Kinetic aspect and additional intermolecular interactions *etc.* should also be taken into consideration. As a rule of thumb, an amphiphilic block copolymer with  $f$  approximately  $35 \pm 10\%$  yields polymersomes. The vesicles were also obtained by PAA-*b*-PS with a very short hydrophilic block (e.g.  $f < 20\%$ , even at 4%) in the mixture of water and dioxane because of kinetical freezing.<sup>50,72,73</sup> If the organization in the hydrophobic core and/or in the hydrophilic shell is not isotropic fluidlike, but crystalline or strongly bound by hydrogen bonding or  $\pi$ - $\pi$  stacking *etc.*, considerable changes will take place in their self-assemblies.<sup>27</sup> In the case of coil-rod block copolymers, the shape anisotropy and additional interactions (introduced, for example, by secondary peptide structures such as  $\alpha$  helices or  $\beta$  sheets, liquid crystalline or crystalline structures) in the rod-like block also influences considerably the self-assembly.<sup>74-81</sup> In brief, both the chemical and physical structure of the block copolymers determine the formation of polymersomes.

In addition, external conditions such as concentration of amphiphilic block copolymers, temperature, nature of the common solvent, water content in the solution and presence of additives also affect the formation of polymersomes.<sup>40</sup> For instance, as shown in the phase diagram of PS<sub>310</sub>-*b*-PAA<sub>52</sub> in dioxane-water mixture, spherical micelles, cylindrical micelles



and polymer vesicles are accessible with the same copolymer (Figure 1.5).<sup>82</sup> The polymersomes could be obtained by adjusting the copolymer concentration and water content in dioxane/water system.

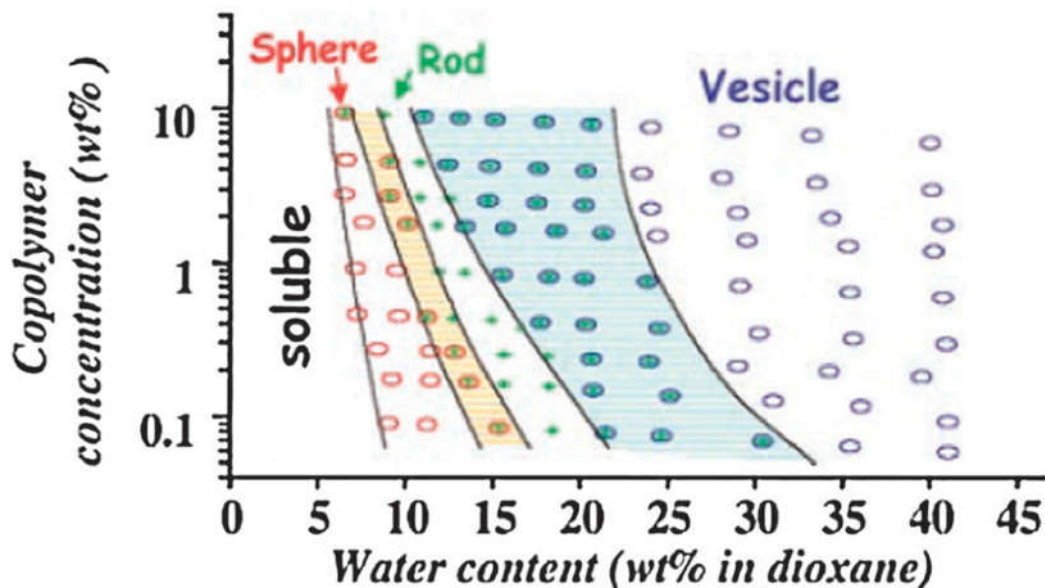


**Figure 1.5.** Phase diagram of PS<sub>310</sub>-*b*-PAA<sub>52</sub> block copolymer in dioxane/water mixture as functions of copolymer concentration and water content. The colorful regions between sphere and rod phases and between rod and vesicle phases correspond to the coexistence regions.<sup>82</sup>

### 1.2.2 Preparation strategies of polymersomes

Nevertheless, the block copolymers with appropriate hydrophilic/hydrophobic ratios cannot self-assemble automatically into polymersomes by simply mixing them with water. Various methods have been developed for polymersomes preparation. The most important methods include organic solvent free strategy and solvent displacement strategy (also called co-solvent technique) for pre-prepared amphiphilic block copolymers. Apart from these strategies, polymerization-induced self-assembly (PISA) has recently developed as an interesting approach for the *in-situ* preparation of polymer vesicles along with the synthesis of amphiphilic block copolymers.<sup>83</sup>

**Table 1.1.** Preparation methods of polymersomes with pre-prepared amphiphilic block copolymer.

Type	Method	Size	Polydispersity	Ref
Organic solvent free strategy	Solid hydration	SUV, MLV	Large	84,85
	Thin-film hydration	SUV, GUV, MLV	Large	86,87
	Electroformation	GUV	Low	86,88,89
	Gel-assistant hydration	GUV	Low	89-91
Solvent displacement strategy	Nanoprecipitation	SUV	Large	51,92,93
	Solvent injection	SUV	Large	94-96
	Emulsion-solvent evaporation	GUV	Large	97-99
	Inverted emulsion	GUV	Low	100-102
	Microfluidics	SUV, GUV	Low	103,104

SUV/GUV: small/giant unilamellar vesicles; MLV: multilamellar vesicles.

### ***Organic solvent free strategy***

In the solvent free strategy, the amphiphilic copolymer in dry state was directly hydrated by water to yield polymersomes. Four representative methods including solid hydration, thin-film hydration method, electro-formation method and gel-assisted hydration method based on organic solvent free strategy are listed in Table 1. Among them, thin-film hydration method is widely used. As shown in Figure 1.6, the amphiphilic block copolymer is firstly dissolved in a suitable organic solvent, leading to polymer solution with a concentration ranging from 5 to 10 mg/ml.<sup>105</sup> Then the solution is deposited on the surface of vial or roughened Teflon plate. A thin polymer film will be formed on glass or Teflon plate after evaporation of the volatile organic solvent. Subsequently, deposited surface is immersed in water or an apt buffer system to hydrate the polymer to yield vesicles. In general, the thin-film hydration method is effective when the hydrophobic block of the copolymer has a low glass transition temperature ( $T_g$ ). For instance, the PBD block in PEO-*b*-PBD possess the  $T_g$  in the range from  $-90^\circ\text{C}$  to  $-8^\circ\text{C}$  depending on their relative 1,4- and 1,2- content, and their polymersomes have been successfully prepared by thin-film hydration method.<sup>106</sup> Nevertheless, if the hydrophobic block has high  $T_g$  or very high molecular weight, external energy source such as heating and/or sonicating is required during the hydration process. With this method, the time span for

production of the polymersomes is quite wide (from hours to weeks), depending on the type of polymer and the conditions used (*e.g.*, with or without sonication aid, heating temperature).<sup>38,107-109</sup> On average, nanometer or micron-sized spherical vesicles are obtained, even though metastable tubular vesicles could also be isolated if the process is stopped at an adequate timepoint.<sup>110-112</sup>

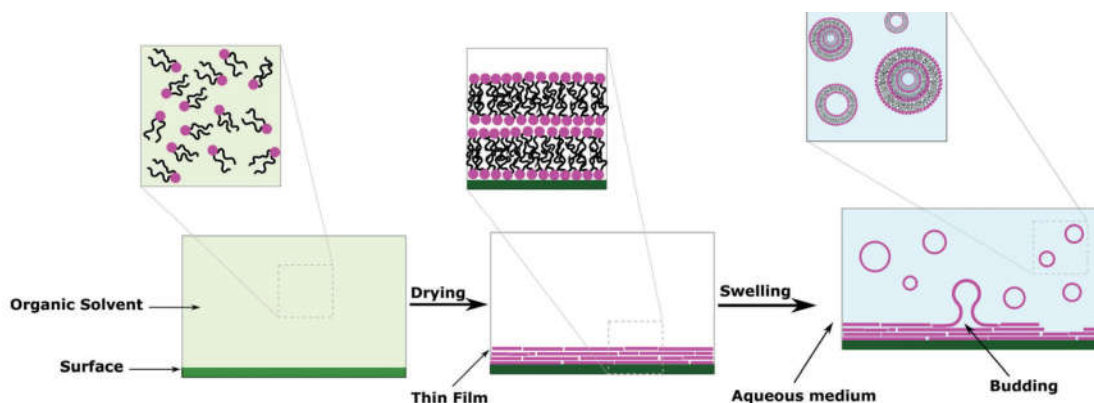


**Figure 1.6.** Schematic illustration of thin film hydration method.<sup>105</sup>

Giant polymersomes with a diameter about tens of micrometers obtained through thin-film hydration method are well visible under optical microscopy, which allow their direct observation and manipulation. Moreover, giant polymer vesicles have sizes like those of cells, which makes them good candidate for cell-mimic. It should be noted that the polymersomes obtained from film hydration method often present broad size distribution, and a coexistence of unilamellar and multilamellar structures.<sup>113,114</sup> Further processes like extrusion and freeze-thaw cycles after film hydration are necessary to obtain mono-disperse and/or small vesicles.<sup>115,116</sup>

### ***Solvent displacement strategy***

In solvent displacement strategy, the formation of polymersomes starts with the preparation of a polymer solution where the amphiphilic block copolymer is fully solubilized and molecularly dispersed in an organic solvent, and is then followed by the gradual exchange of the organic solvent by water. The solvent displacement by water drives the hydrophobic block to accumulate together, eventually resulting in the formation of polymersomes. At the end, all organic solvent was removed by dialysis or evaporation. This strategy has been widely used to prepare polymersomes of amphiphilic block copolymer since most amphiphilic block

copolymers have poor solubility and chain flexibility in water. There are five variants in this strategy as shown in Table 1. Among them, nanoprecipitation is the most frequently employed method to perform the self-assembly of amphiphilic block copolymers (Figure 1.7). In nanoprecipitation, the amphiphilic copolymers are firstly dissolved in a water-miscible organic solvent (THF, Dioxane, DMF, *etc.*) which is good solvent for both hydrophobic and hydrophilic blocks. Then the water is slowly added to the copolymer solution (or the polymer solution is slowly added to water). The hydrophobic chains tend to aggregate together to form hydrophobic parts of the membranes in order to avoid the contact with water. The hydrophilic chains tend to face the water to form the inner and outer surfaces of the membranes, thus maintaining the stability of polymersomes.

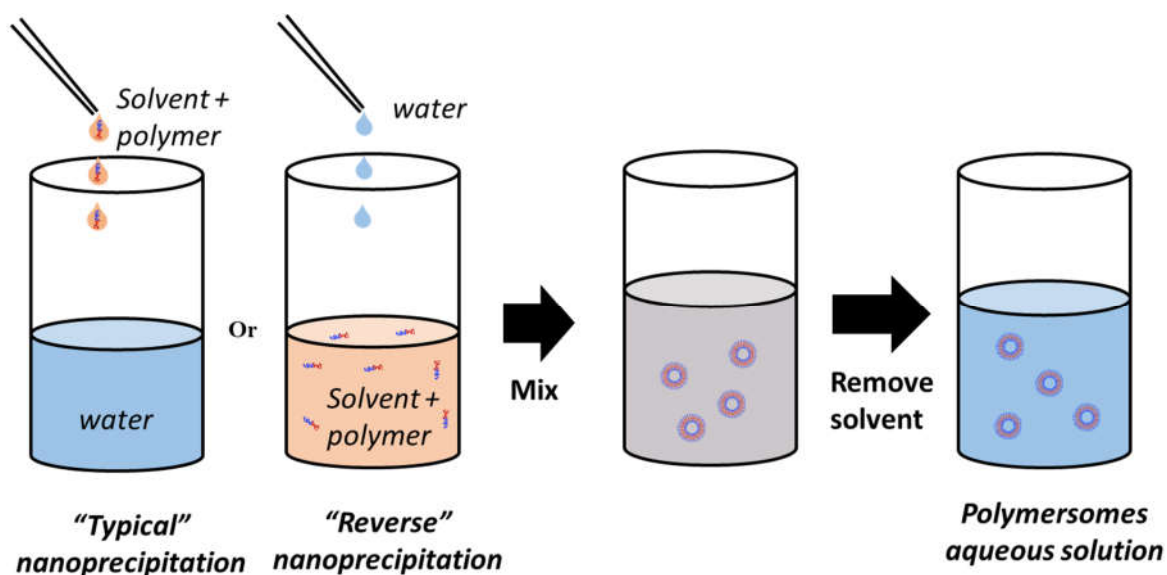


**Figure 1.7.** Schematic illustration of nanoprecipitation. Light blue represents water, and light orange refers to polymer organic solution. Grey color represents organic solvent/water mixtures.

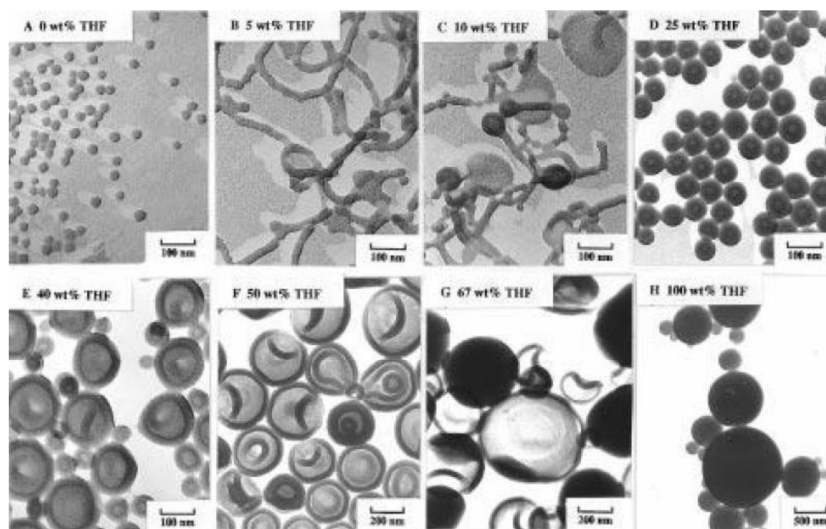


**Figure 1.8.** TEM images of self-assemblies of PS<sub>200</sub>-*b*-PAA<sub>18</sub> using DMF/THF mixture as cosolvent: (A) 0 wt% THF (B) 5 wt% THF; (C) 10 wt% THF; (D) 25 wt% THF; (E) 40 wt% THF; (F) 50 wt% THF; (G) 67 wt% THF; (H) 100% THF. <sup>117</sup>

With nanoprecipitation, the preparation conditions such as the concentration of copolymers, nature of the common solvent, water content in the system *etc.*, could affect considerably the formation of polymersomes. For example, early in 1997, Eisenberg *et al* have prepared the polymersomes from PS-*b*-PAA through nanoprecipitation with the control of the organic solvents (Figure 1.8).<sup>117</sup> Spherical micelles of PS<sub>200</sub>-*b*-PAA<sub>18</sub> were formed with DMF as cosolvent, while worm-like micelles were observed using DMF/THF (weight ratio 95/5) mixture as the cosolvent. Increasing the THF content to 10 wt% in DMF/THF, a mixture of worm-like micelles, lamellae and vesicles were formed by PS<sub>200</sub>-*b*-PAA<sub>18</sub>. Only polymersomes were obtained when the THF proportion in the range from 25% to 67%. The diameter of polymersomes increases with the increase of THF ratio. However, only large compound micelles were formed with pure THF as organic solvent.

### ***Polymerization-induced self-assembly (PISA)***

Recently, PISA has been employed for preparation of polymersomes.<sup>118</sup> With PISA, a soluble homopolymer or copolymer as the stabilizing block is chain-extended in a suitable polymerization medium that is a good solvent for the stabilizing building block and the monomer, but a poor solvent for the growing block. Amphiphilic copolymer forms and self-assembles *in-situ* into different morphologies during the polymerization. Blanazs *et al.*

obtained polymer vesicles during the PISA process of PGMA-*b*-PHPMA. RAFT polymerization was applied to polymerize the (2-hydroxyl)propyl methacrylate (HPMA) using poly(glycerol methacrylate) as the macromolecular chain transfer agent.<sup>83</sup> As HPMA is consumed, a series of self-assembly structures are observed during the polymerization. The mixture of spherical micelles and worm-like micelles are captured from the system with monomer conversion at 55-68%, while for the system with conversion at 72-82%, octopus- and jelly-fish-like structures emerge. Eventually spherical vesicles were obtained when the reaction completes with 100% conversion (Figure 1.9).

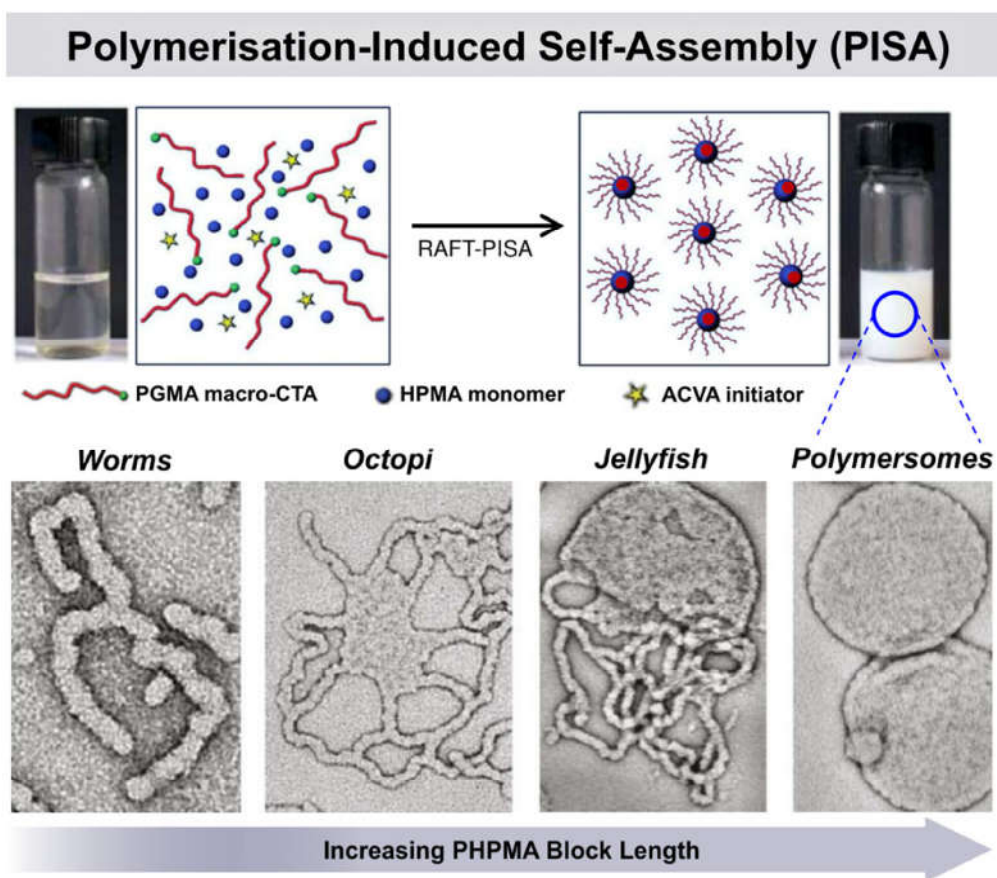


**Figure 1.9.** Synthesis of the PGMA-*b*-PHPMA block copolymers *via* the RAFT-PISA process and the polymerization-induced worm-to-polymersome transition during the chain extension polymerization of HPMA in water using PGMA as a macro-chain transfer agent.<sup>83</sup>

### 1.2.3 Formation mechanism of polymersomes

Polymersomes are self-assembled by the block copolymers with packing parameter  $1/2 \leq p \leq 1$ . While their formation mechanism, which involves both thermodynamic and kinetic aspects, is still not fully understood. Two main pathways were put forward to understand the polymersomes formation process.<sup>119</sup>

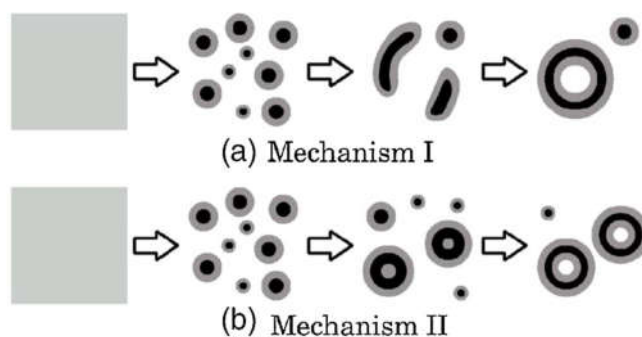


**Figure 1.10.** A Schematic representation of two most probable formation mechanisms of polymersomes.<sup>120</sup>

In Mechanism I, the spherical micelles are firstly formed from the homogenous amphiphilic block copolymers (Figure 1.10). Those objects would then fuse to generate cylindrical micelles and in further open lamellae. Driven by minimization of edge energy, the lamellae close to form vesicles.<sup>121</sup> This pathway was proved by the work from Du *et al* (Figure 1.11).<sup>122</sup> They studied the self-assembly behavior of poly(ethylene oxide)-*b*-poly(3-(trimethoxysilyl) propyl methacrylate) (PEO-*b*-PTMSPMA). PEO-*b*-PTMSPMA is firstly dissolve in methanol. Water was then gradually added to the solution. At  $f_w = 31.3 \text{ wt}\%$ , spherical micelles together with a small number of rod-like micelles occur. Further increasing the water fraction to 33 wt%. Lamellae with protruding rod-like morphologies were formed and vesicles began to appear at the same time. The polymer vesicle structure began to be the major morphologies at water content of  $f_w = 48.7 \text{ wt}\%$ , probably due to the lamellae closure to vesicles. Polymer vesicles were observed exclusively when water content was over than 50%. The PISA process discussed above also helps to understand the whole procedure of vesicle formation through Mechanism I (Figure 1.9).



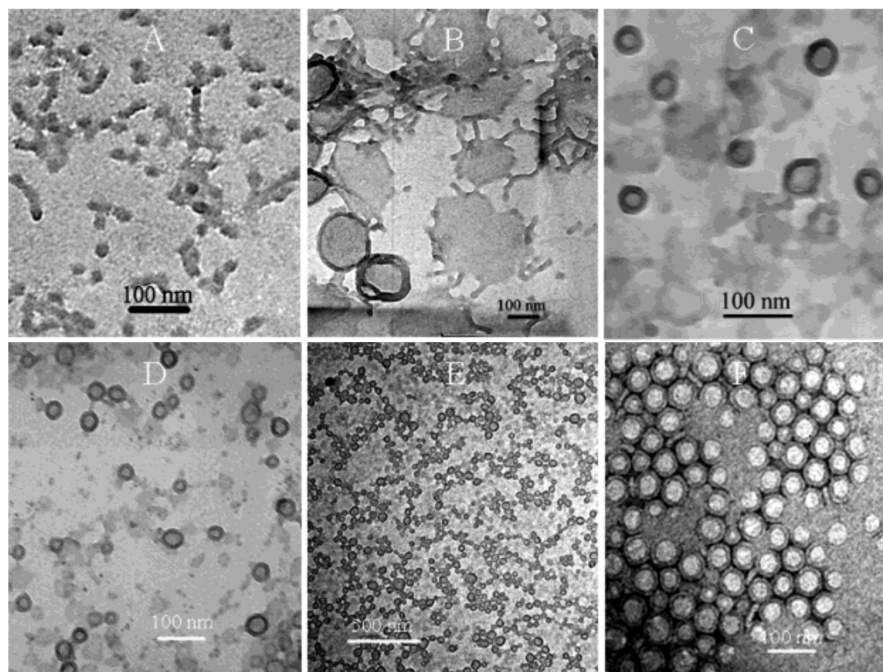


**Figure 1.11.** TEM images of self-assemblies from PEO<sub>45</sub>-*b*-PTMSPMA<sub>42</sub> at different water fraction ( $f_w$ ) in the water-methanol mixture: (A) spheres, coexisted with few rods,  $f_w = 31.3$  wt%; (B) lamellae with protruding rods and a few vesicles,  $f_w = 33.6$  wt%; (C) vesicles and lamellae,  $f_w = 38.7$  wt%; (D) vesicles,  $f_w = 48.7$  wt%; (E) vesicles,  $f_w = 55.8$  wt%; (F) vesicles in (E) stained with uranyl acetate.<sup>122</sup>

The Mechanism II also starts with the formation of spherical micelles (Figure 1.10). However, instead of transforming into cylinder and lamella, these micelles increase their sizes by integrating the free copolymer. Then, the solvent would diffuse into the core of the large micelles, leading to formation of vesicles.<sup>123</sup> This proposal was supported by work of Adams and coworkers.<sup>119</sup> The PEG-*b*-poly((2-N,N-diethyl)aminoethyl methacrylate) (PEG-*b*-PDEAMA) is amphiphilic polymer, in which PEG acts the hydrophilic block and PDEAMA serves as the hydrophobic block. It could be dissolved in water with pH = 2 due to the protonation of PDEAMA block. Then, the NaOH was added to deprotonate PDEAMA, driving copolymer to self-assemble. The results of dynamic light scattering (DLS) and cryo-EM suggest that neither cylindrical micelles nor lamella appear during the self-assembly process. Instead, spheres with loose cores are observed, which are supposed to be the intermediate morphology in Mechanism II. Interestingly, they found the vesicles cannot efficiently encapsulate the hydrophilic fluorescent molecules, which further prove that the vesicles are formed *via* Mechanism II. This is because the inner aqueous cavity is formed by the diffusion



of water molecules from outside to inside across polymer bilayer, and consequently, it is difficult for water-soluble fluorescent molecules with rather high MW to diffuse across this barrier. If these polymersomes were formed by Mechanism I, they can trap hydrophilic molecules during the closing of disk-like micelles.

#### **1.2.4 Characterization techniques of polymersomes**

The typical characterization methods of polymersomes include optical microscopy, electron microscopies and light scattering methods.

##### ***Optical microscopy***

Optical microscopy is a technique to directly visualize polymeric vesicles under real or “physiological” conditions after fast and easy sample preparation. It is suitable for the visualization of giant polymersomes (diameter > 1000 nm). Nevertheless, the membrane thickness (< 50 nm) is below the resolution of optical microscopy, so it cannot be measured. Moreover, as the contrast of specimens is rather limited, it is difficult to distinguish vesicles from emulsions in bright-field mode. Therefore, labelling the membrane with a fluorescent dye is a necessary and fluorescence microscopy is used to clarify polymersomes morphology<sup>124</sup>. Fluorescence microscopy has other benefits. For example, specific labeling of parts of the polymersomes with fluorochromes gives information about their position in the polymersomes, and multiple staining with different probes allows the visualization of the presence of individual molecules in compartments of the polymersomes. One of the interesting possibilities of fluorescence technique is to study the dynamics such as diffusion, rotational mobility, and fluorescence lifetime of fluorophores in polymersomes by time-resolved measurements. Confocal laser scanning microscopy (CLSM) can take the images slice by slice along the z-direction and then provide a 3D vesicular image by reconstruction.<sup>125</sup>

##### ***Electron microscopies***

Electron microscopies including scanning electron microscopy (SEM), classical transmission electron microscopy (TEM) and cryogenic electron microscopy (cryo-EM) are commonly used for visualization of polymersomes. Compared to optical microscopes, the theoretical resolution of electron microscopies is about hundred thousand times higher. Small polymersomes (diameter < 1000 nm) could be visualized. However, with SEM and TEM, the specimens need to be dried and optionally stained to enhance the contrast.<sup>126</sup> Polymersomes

are frequently broken during the specimen preparation.<sup>127,128</sup> Therefore, we can only confirm the vesicular nature on observing crashed empty spheres through SEM and TEM. The diameter and membrane thickness cannot be measured with precision. In contrast, the cryo-EM technique allows the polymersomes to be visualized in a frozen hydrated state. Since specimens are frozen and viewed in vitreous ice, they are seen in a natural hydrated state, which is the same as their natural state. Cryo-EM eliminates common sample preparation artefacts, like collapsing of the polymersomes structure, particle shrinkage due to dehydration of the polymersomes corona, difficulty in determining membrane thickness, which are associated with the drying process involved in conventional SEM and TEM sample preparation.

With cryo-EM, a copper grid is firstly treated with plasma to make them highly hydrophilic. The samples aqueous solution is then deposited on it. The excessive aqueous is blotted by a filter paper, leaving a thin film of the polymersomes dispersion on the grid. Then the film on the grid is vitrified by plunging the grid into liquid ethane ( $T = -175^{\circ}\text{C}$ ). After that, the vitrified specimen can be stored in a cryo-box and then cryo-transferred into an electron microscope and imaged under cryogenic conditions. Cryo-EM is the only technique to characterize unambiguously and precisely the size, shape and membrane thickness of small and large polymersomes.<sup>129</sup>

### ***Light Scattering Methods***

Although light and electron microscopy provide straightforward visualization of polymersomes, the observable number is limited by the sample volume on the microscopic grid ( $\sim 1 \mu\text{L}$ ). We may not have an overall view of the size distribution of polymersomes. Another type of techniques like dynamic and static light scattering that probe the sample in larger volume ( $\sim 1 \text{ mL}$ ) in reciprocal space can determine polymersomes size and size distribution (polydispersity index).<sup>130</sup> The zeta potential of polymersomes can also be determined through dynamic light scattering by measuring their electrophoretic mobility in a capillary cell.<sup>131</sup> Note that the dynamic light scattering allows to estimate the hydrodynamic radius ( $R_h$ ) of particles dispersed in water, while the static light scattering allows to measure their radius of gyration ( $R_g$ ). In the case of hollow spherical structures like polymersomes, the ratio  $R_g/R_h$  is close to 1.<sup>132-134</sup> Therefore, when light and electron microscopes are not available,

the combination of dynamic and static light scattering also enable the confirmation of hollow structure of spherical polymersomes.

### 1.3 Polymer cubosomes and hexosomes

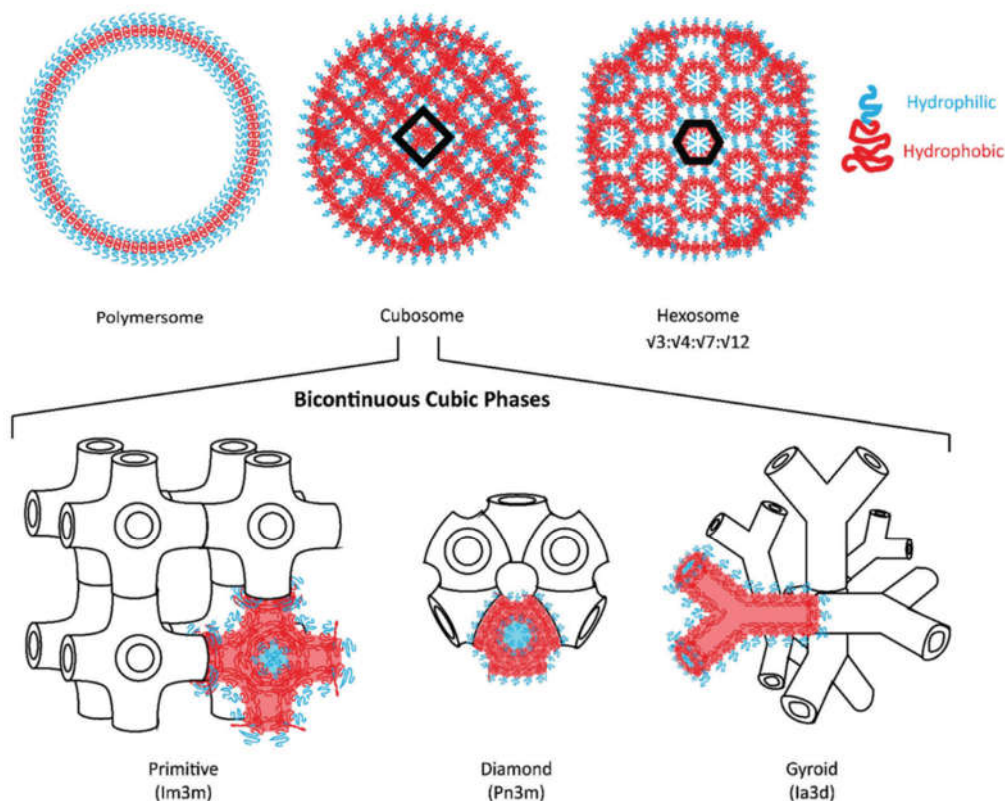


**Figure 1.12.** Scheme illustration of cubosome and hexosome with a polymersome shown for comparison. Blue regions are hydrophilic, while red regions are hydrophobic. Schematic representations of the different bicontinuous cubic phases are included.<sup>52</sup>

Most efforts have long since been dedicated to exploring polymer micelles, polymer cylindrical micelles and polymer vesicles from the amphiphilic copolymer with  $p < 1$ , which belong to the normal (oil-in-water) self-assembled nanostructures. Very recently, polymer cubosomes including  $Ia\bar{3}d$ ,  $Im\bar{3}m$  and  $Pn\bar{3}m$  cubosomes, and hexosomes constructed from the amphiphilic copolymers with  $p > 1$ , which belong to the inverted (water-in-oil) self-assembled nanostructures, have attracted more and more attention (Figure 1.12).<sup>52</sup> The early work on polymer inverted nanostructures was reported by Eisenberg *et al.*<sup>135</sup> They captured several “exotic” micron-sized morphologies including the large compound vesicles (LCV) and hexagonally-packed hollow hoops (HHH) from the self-assembling of polystyrene-*b*-

poly(acrylic acid) (PS-*b*-PAA) in water. The latter is very reminiscent of what we today describe as a hexosome ( $P6mm$ ). However, only very recently polymer cubosomes and hexosomes are rationalized as part of morphological diagram of amphiphilic block copolymers in the selective solvent. The inverted morphologies present numerous advantages due to their uniform, tunable and highly ordered porous structure, such as higher loading volume for both hydrophilic and hydrophobic substances, larger specific surface areas, and much better colloidal, chemical and mechanical stability. Their pore size can be adjusted from  $10^1$  to  $10^2$  nm by regulating the molecular weight of polymers. Therefore, these inverted structures are interesting candidates as functional materials for gated uptake, release, separation, catalysts, electrodes, and photonics, *etc.*<sup>52,136,137</sup>

### 1.3.1 Structural and experimental conditions for inverted morphologies

Inverted morphologies occur when  $p > 1$  based on the classical packing parameter model. Nevertheless, the hydrophilic content of the copolymer is more often used to predict the formation of these structures. According to the examples in the literature, amphiphilic block copolymers that could self-assemble into inverted structures generally possess the hydrophilic block weight ratio  $f_{\text{hydrophilic}}$  below 25%, but this limit of  $f_{\text{hydrophilic}}$  depended also on the detailed chemical structures. For instance, Mai *et al.* prepared cubosomes and hexosomes from the linear diblock copolymers PEO-*b*-PS (Figure 1.13).<sup>138</sup> They gradually increase the length of the PS block and synthesized a series of linear diblock copolymers PEO-*b*-PS that exhibited hydrophilic PEG content ( $f_{\text{PEO}}$ ) ranging from 9.7 to 5.1%. At  $f_{\text{PEO}} = 9.7\%$ , the PEO-*b*-PS prefer to form polymer vesicle. When the  $f_{\text{PEG}}$  decrease to 7.9%,  $Im\bar{3}m$  cubosomes occurs. Further decreasing the  $f_{\text{PEO}}$  to 7.0 %,  $Pn\bar{3}m$  cubosomes was constructed from PEO-*b*-PS. The hexosome was obtained when  $f_{\text{PEO}}$  reaches 5.1%. The result suggested that PEO-*b*-PS with  $f_{\text{PEO}}$  in the range of 7.9 –5.1% preferentially self-organized into inverse structures. Nevertheless, Sommerdijk *et al.* have prepared polymer inverse structures with PEO-*b*-poly(octadecyl methacrylate) (PEO<sub>39</sub>-*b*-PODMA<sub>17</sub>) with  $f_{\text{PEO}} = 25\%$ .<sup>139</sup>

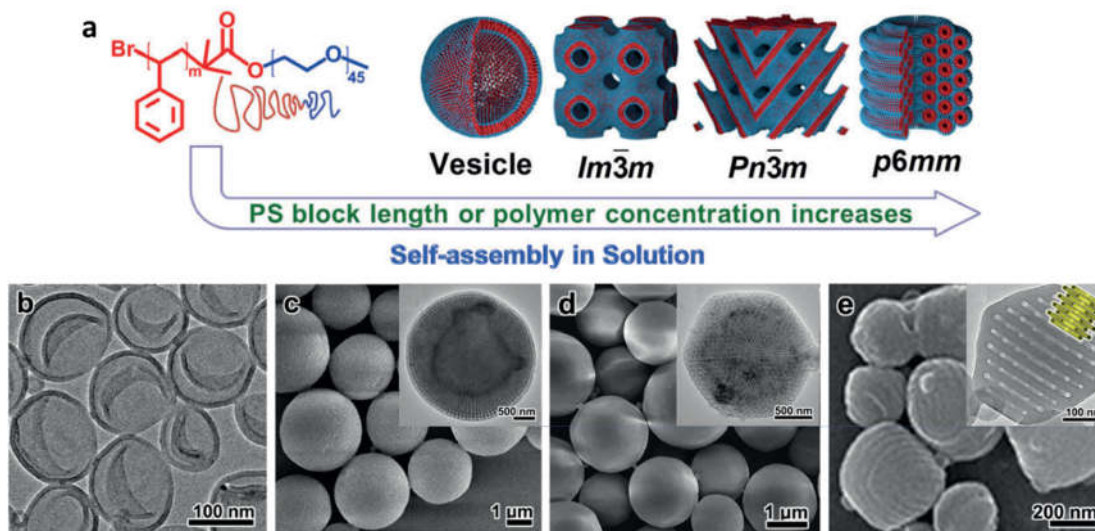


**Figure 1.13.** a) The scheme illustration of the self-assembly of PEO-*b*-PS into vesicles, cubosomes, and hexosomes by increasing its PS block length (decreasing the hydrophilic block ratio:  $f_{\text{PEO}}$ ). The red color highlights the hydrophobic PS block and the PS domain in the assemblies, while the hydrophilic PEG block and the hydrophilic domain of the assemblies are shown in blue. b) The TEM images of vesicles formed by PEO<sub>45</sub>-*b*-PS<sub>185</sub> ( $f_{\text{PEO}} = 8.8\%$ ). c) The SEM images of  $Im\bar{3}m$  cubosomes self-assembled from PEO<sub>45</sub>-*b*-PS<sub>209</sub> ( $f_{\text{PEO}} = 7.9\%$ ). d) The SEM images of  $Pn\bar{3}m$  cubosomes constructed from PEO<sub>45</sub>-*b*-PS<sub>236</sub> ( $f_{\text{PEO}} = 7.0\%$ ). e) The SEM images of Hexasomes formed by PEO<sub>45</sub>-*b*-PS<sub>334</sub> ( $f_{\text{PEO}} = 5.1\%$ ). The insets in (c), (d) and (e) present the corresponding TEM images, showing their internal structures.<sup>138</sup>

Apart from the consideration of polymer architecture, the preparation condition also needs to be taken into consideration for formation of inverse morphologies. According to the work of McKenzie *et al.* shifting the cosolvent used in nanoprecipitation from dioxane to THF was sufficient to alter the aggregate morphology from vesicles to inverse morphology, probably due to their distinct solubility parameters which affect the dimensions of both hydrophilic and hydrophobic domains during the self-assembling.<sup>34</sup> Similarly, La *et al.* found that the branched PEG-*b*-PS only self-assembled into polymer vesicle when either the pure dioxane or THF were used as cosolvent.<sup>140</sup> However, when a dioxane/DMF mixture was used as cosolvent, the inverse structure was formed from the same copolymer. Moreover, Matyjaszewski *et al.* found that in their systems cubosomes were only obtained with the initial concentrations in the range from 2 to 5 mg. L<sup>-1</sup>.<sup>141</sup> When the concentrations were 20, 10, 1 or 0.5 mg. L<sup>-1</sup>, no cubosomes were observed. In addition, the particles with cubic phase were obtained only at an appropriate

rate of addition of water (1.6 ml in 20 s). A faster or slower addition rate of water failed to lead to the formation of cubosomes.

In brief, one of the prerequisites for the preparation of inverse structures is constructing highly asymmetric amphiphilic copolymer with a hydrophobic block much larger than its corresponding hydrophilic block, which could be linear diblock, side chain diblock and block copolymers with dendrimers as blocks. Of equal importance for consideration is preparation conditions. Table 1.2 summarize the polymers and corresponding formulation parameters for formation of the inverse structures.

**Table 1.2.** Representative polymers and corresponding formulation parameters.

Polymer	Chemical structure	$f_{\text{hydrophilic}}$ (wt %)	Preparation method	Solvents System	Ref.
linear diblock copolymers	PEO <sub>45</sub> - <i>b</i> -PTMSPMA <sub>180</sub> <sup>a</sup>	$f_{\text{PEO}} = 4.3\%$	nanoprecipitation	methanol/water	142
	PEO <sub>52</sub> - <i>b</i> -PBMA <sub>110</sub> or <sub>86</sub> <sup>b</sup>	$f_{\text{PEO}} = 14\%$ or 17%	nanoprecipitation	THF/water	143
	PAA <sub>22</sub> - <i>b</i> -PS <sub>144</sub> <sup>c</sup>	$f_{\text{PAA}} = 9.50\%$	nanoprecipitation	toluene/methanol	144
	PDMAEMA <sub>37</sub> - <i>b</i> -PS <sub>934</sub> - <sub>1190</sub> <sup>d</sup>	$f_{\text{PDMAEMA}} = 5.9\%$ -4.9%	PISA	ethanol	145
	PEG <sub>45</sub> - <i>b</i> -PS <sub>324</sub> <sup>e</sup>	$f_{\text{PEG}} = 5.60\%$	PISA	ethanol/water	146
	P4VP- <i>b</i> -PS <sup>f</sup>	$f_{\text{P4VP}} < 32\%$	oil-in-water emulsion	toluene-in water	36
	PTFEPPS <sub>35</sub> - <i>b</i> -PS <sub>35</sub> <sup>g</sup>	$f_{\text{PS}} = 29\%$	dispersed in THF		147
	PAA <sub>45</sub> - <i>b</i> -P(ionic-liquid) <sub>23</sub> <sup>h</sup>	$f_{\text{PIL}} = 79.7\%$	nanoprecipitation	THF/water	141
	PEO <sub>45</sub> - <i>b</i> -PS <sub>m</sub> <sup>i</sup>	$f_{\text{PEO}} < 8\%$	nanoprecipitation	dioxane/water	138
PEG <sub>17</sub> - <i>b</i> -PPS <sub>75</sub> <sup>j</sup>	$f_{\text{PEG}} < 12\%$	nanoprecipitation	THF/water	148	
side-chain block copolymers	PNOEG <sub>50</sub> - <i>b</i> -PNGLF <sub>50</sub> <sup>k</sup>	33%	nanoprecipitation	DMSO/water	149
	PEO <sub>39</sub> - <i>b</i> -PODMA <sub>17</sub> <sup>l</sup>	25%	nanoprecipitation	THF/water	139,150
	PEO <sub>52</sub> - <i>b</i> -PODMA <sub>26</sub> <sup>l</sup>	17,30%	nanoprecipitation	THF/water	151
	PEO <sub>45</sub> - <i>b</i> -(PODMA- <i>co</i> -PDSMA) <sub>m</sub> <sup>m</sup>	$f_{\text{PEO}} = 15\text{-}25\%$	nanoprecipitation	THF/water	152
	POEGMA <sub>70</sub> - <i>b</i> -PTMAm <sup>n</sup>	43%	nanoprecipitation	DMSO/water	153
	PEO <sub>3</sub> - <i>b</i> -PS <sub>70</sub> <sup>i</sup> and PEO <sub>120</sub> - <i>b</i> -PDMAEMA <sub>120</sub> <sup>o</sup>	12%	nanoprecipitation	DMSO/water	154

	PEO <sub>45</sub> - <i>b</i> -PMPCSm <sup>p</sup>	7-13 %	nanoprecipitation	THF/water	155
dendritic-linear block copolymers	(PEG <sub>7</sub> ) <sub>6</sub> - <i>b</i> -PS <sub>180-240</sub> <sup>q</sup>	8-11%	nanoprecipitation	dioxane/water	156
	(PEG <sub>7</sub> ) <sub>3</sub> - <i>b</i> -PS <sub>217</sub> or <sub>213</sub> <sup>q</sup>	9.3-9.4%	solvent diffusion-evaporation mediated self-assembly	dioxane/water	157
	(PEG <sub>m</sub> ) <sub>3</sub> - <i>b</i> -PS <sub>n</sub> <sup>q</sup>	m=12 (7.8%, 7.1%) ; m=17 (5.7%, 5.4%)	nanoprecipitation	dioxane/water	158
	(PEG <sub>m</sub> ) <sub>3</sub> - <i>b</i> -(PS <sub>n</sub> ) <sub>2</sub> <sup>r</sup>	19.7%	nanoprecipitation	dioxane/water	158
	A: (PEG <sub>12</sub> ) <sub>3</sub> - <i>b</i> -PS <sub>42</sub> <sup>q</sup> B: (PEG <sub>12</sub> ) <sub>3</sub> - <i>b</i> -PS <sub>42</sub> <sup>q</sup>	A: $f_{\text{PEG}}=37\%$ , B: $f_{\text{PEG}}=7\%$ ; A/B = 15/85, 5/95, 0/100	nanoprecipitation	dioxane/water	159
	(PEG <sub>m</sub> ) <sub>3</sub> - <i>b</i> -(P <sub>x-co</sub> -PS <sub>y</sub> ) <sup>s</sup>	$f_{\text{PEG}}=10\%$	nanoprecipitation	THF/water, dioxane/water	160
	(PEG <sub>m</sub> ) <sub>3</sub> - <i>b</i> -PS <sub>n</sub> <sup>q</sup>	$f_{\text{PEG}}=10.6\%$ , 9.4%, 2.7%	nanoprecipitation	dioxane/water	161

<sup>a</sup> Poly(ethylene oxide)-*b*-poly(3-(trimethoxysilyl)propyl methacrylate). <sup>b</sup> Poly-(ethylene oxide) -*b*- poly(*n*-butyl methacrylate). <sup>c</sup> Poly(acrylic acid)-*b*-polystyrene. <sup>d</sup> Poly(2-(diethylamino)ethyl methacrylate)-*b*-polystyrene. <sup>e</sup> poly(ethylene glycol)-*b*-polystyrene. <sup>f</sup> poly(4-vinylpyridine)-*b*-polystyrene. <sup>g</sup> poly[bis(trifluoroethoxy)phosphazene]-*b*-polystyrene. <sup>h</sup> poly(acrylic acid)-*b*-poly(4-vinylbenzyl)-3-butyl imidazolium bis(trifluoromethylsulfonyl)imide. <sup>i</sup> Poly(ethylene oxide)-*b*-polystyrene. <sup>j</sup> Poly(ethylene glycol)-*b*-poly(propylene sulfide). <sup>k</sup> Poly-(norbornene-oligo(ethylene glycol))-*b*-poly(norbornene-lysine-leucine-phenylalanine). <sup>l</sup> Poly(ethylene oxide)-*b*-poly(octadecyl methacrylate). <sup>m</sup> Poly(ethylene oxide)-*b*-poly(octadecyl methacrylate)- poly(*n*-docosyl methacrylate). <sup>n</sup> Poly(oligo(ethylene glycol) methyl ether methacrylate)-*b*-poly (3-(thymine-1-yl)propyl methacrylate). <sup>o</sup> Poly(ethylene oxide)-*b*-poly(2-(diethylamino) ethyl methacrylate). <sup>p</sup> Poly(ethylene oxide)-*b*-Poly(2,5-bis((4-methoxyphenyl)-oxycarbonyl)styrene). <sup>q</sup> Branched poly(ethylene glycol)-*b*-polystyrene. <sup>r</sup> Branched poly(ethylene glycol)-*b*-branched polystyrene. <sup>s</sup> Branched poly(ethylene glycol)-*b*-poly(2-(4-vinylphenyl))-1H-indene-*b*-polystyrene.

### 1.3.2 Preparation methods of polymer cubosomes and hexosomes

The amphiphilic block copolymer employed for formation of inverse morphologies possess a hydrophobic block with relatively high molecular weight. The organic solvent is necessary to facilitate the copolymers to adjust their conformation towards the global equilibrium state. To date, nearly all inverse morphologies have been formed by using solvent-displacement

strategy including (flash) nanoprecipitation and emulsion-solvent evaporation.<sup>52</sup> Among them, the most employed method for inverse morphologies formation is nanoprecipitation. The flash nanoprecipitation has been previously restricted to the formation of solid-core and micellar nanoparticle formulations are also employed for inverse morphologies formation. It involves the rapid impingement and controlled microsecond mixing of the polymer/solvent and non-solvent, followed by dilution of the solvent in a non-solvent reservoir. Compared to traditional nanoprecipitation techniques, flash nanoprecipitation promotes uniform nucleation and growth of these precipitating solutes through rapid and thorough mixing of the nonsolvent and solvent. It is rapid and scalable, which may allow the scalable preparation of inverse morphologies in quantities necessary for clinical evaluation of new drug formulations.

In addition to nanoprecipitation, the polymerization-induced self-assembly (PISA) was also exploited to investigate the formation of polymer cubosomes/hexosomes.<sup>145,146,162</sup> In 2019, Wu *et al* report scalable preparation of inverse bicontinuous mesophases *via* PISA. Styrene (St) and pentafluorostyrene (PFS) were copolymerized using a poly(N,N-dimethylacrylamide) macro-RAFT agent (PDMA<sub>29</sub>-CTA) in 2 % toluene/ethanol with a targeted degree of polymerization, DP = 800.<sup>162</sup> When a 1:1 monomer feed is used, the polymerization affords an alternating copolymer PDMA<sub>29</sub>-*b*-P(St-*alt*-PFS), in which PDMA is a solvophilic block and P(St-*alt*-PFS) block is solvophobic part (Figure 1.14). At low conversions with the DP<sub>P(S-*alt*-PFS)</sub> in the range from 97 to 294, conventional morphologies such as spherical micelles, worm-like micelles and vesicles were afforded (Figure 1.14A-C). At around DP<sub>P(S-*alt*-PFS)</sub> = 388, large compound vesicles (LCVs) were formed (Figure 1.14D). As shown in Figure 1.14E, the LCVs will transform to *Im* $\bar{3}m$  polymer cubosome with further polymerization (DP<sub>P(S-*alt*-PFS)</sub> = 428). When the DP<sub>P(S-*alt*-PFS)</sub> reaches 582, a “hybrid” structure composed of both *Im* $\bar{3}m$  and *P6mm* hexosomes were obtained (Figure 1.14F).



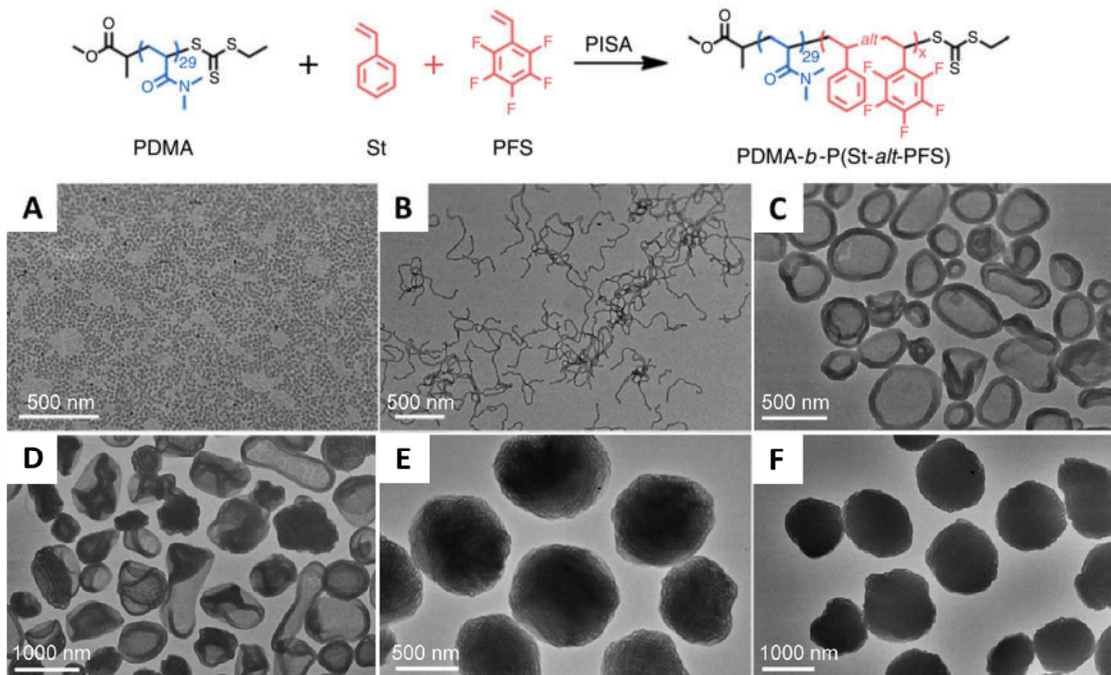


**Figure 1.14.** TEM images of PDMA<sub>29</sub>-*b*-P(S-*alt*-PFS)<sub>y</sub> particles prepared by PISA with increasing length of the hydrophobic P(S-*alt*-PFS)<sub>y</sub>. A) DP<sub>P(S-*alt*-PFS)</sub> = 89, Spherical micelles; B) DP<sub>P(S-*alt*-PFS)</sub> = 108, worm-like micelles; C) DP<sub>P(S-*alt*-PFS)</sub> = 191, vesicles; D) DP<sub>P(S-*alt*-PFS)</sub> = 388, LCVs; E) DP<sub>P(S-*alt*-PFS)</sub> = 428, *Im* $\bar{3}m$  cubosomes; F) DP<sub>P(S-*alt*-PFS)</sub> = 428, “hybrid” *Im* $\bar{3}m$  + *P6mm* structure.<sup>162</sup>

### 1.3.3 Formation mechanism of polymer cubosomes and hexosomes

In the past decade, efforts have been also devoted to understanding how polymer cubosomes and hexosomes spontaneously form in solution. Although currently there exists no well-established theory for their formation mechanism, several studies have shown vaguely similar self-assembly pathways as follows: at the beginning of the self-assembly process, the polymer vesicles are formed; then these vesicles tend to fuse to form large compound vesicles (LCVs) or sponge-like particles; these intermediate eventually reorganizes into colloids with ordered internal structures.

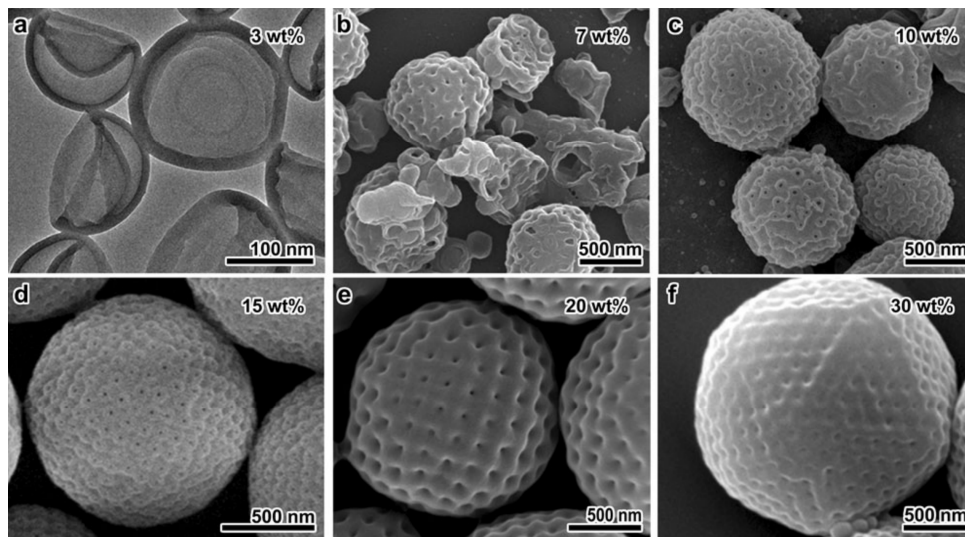


**Figure 1.15.** TEM (a) and SEM (b-f) images of intermediate assemblies trapped at different water fraction, showing the formation pathway of PEO<sub>45</sub>-*b*-PS<sub>236</sub> cubosomes. (a) vesicles, (b) large-compound vesicles (LCVs), (c) sponge-like particles, (d) sponge-like particles with ordered surfaces, (e)  $Im\bar{3}m$  cubosomes, and (f)  $Pn\bar{3}m$  cubosomes.<sup>138</sup>

Since most of cubosomes/hexosome are formed by nanoprecipitation, the intermediate morphologies preceding the formation of the final cubosome/hexosome structures can be kinetically frozen by controlling the preparation condition. Firstly, small aliquots (10- 20  $\mu$ L) are removed from the self-assembly mixture at different water content addition, and then immediately put into a large excess of water to freeze the self-assembly process. Thus, the kinetically frozen intermediate morphologies could be preserved. Figure 1.15 presents the captured intermediate structures of the highly asymmetric PEO<sub>45</sub>-*b*-PS<sub>236</sub>, which precede the formation of  $Im\bar{3}m$  and  $Pn\bar{3}m$  cubosomes.<sup>138</sup> PEO<sub>45</sub>-*b*-PS<sub>236</sub> underwent a morphological evolution from polymersomes, LCVs, sponge-like structures,  $Im\bar{3}m$  cubosomes to final  $Pn\bar{3}m$  cubosomes with the increase of water addition. Specifically, when the amount of water was relatively low (3 wt%), polymersomes were observed (Figure 1.15a). An increase in the amount of water (7 wt%) resulted in the formation of large compound vesicles (LCVs) presumably due to coalescence of the vesicles. At around 10 wt% water content, these LCVs underwent structural refinement, forming sponge-like particles (Figure 1.15d). Further increasing water content from 10 to 30 wt%, intraparticle phase separation phenomenon is found, where the sponge-like particles first rearranged into  $Im\bar{3}m$  cubosomes (Figure 1.15e) before transforming into  $Pn\bar{3}m$  cubosomes (Figure 1.15f).

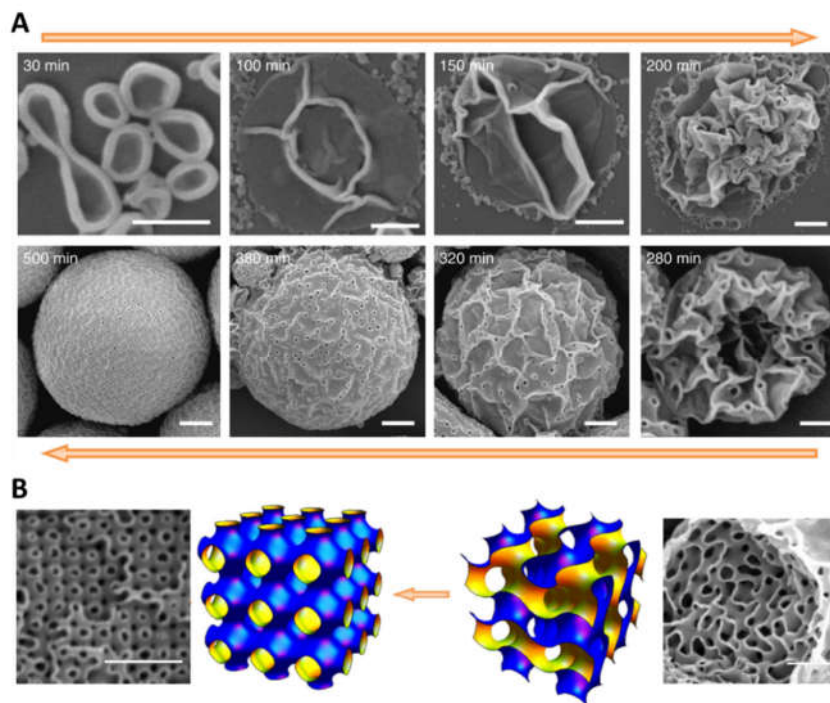


**Figure 1.16.** A) SEM images of intermediate structures of PS<sub>144</sub>-*b*-PAA<sub>22</sub> obtained with different incubation times. B) The cross-sectional SEM images and schematic depicting the transition of a Schoen gyroid ( $Ia\bar{3}d$ ) structure (right) into a Schwarz primitive ( $Im\bar{3}m$ ) structure (left).<sup>144</sup>

In another work, the formation process of  $Im\bar{3}m$  cubosomes of asymmetric polystyrene-*b*-poly(acrylic acid) (PS<sub>144</sub>-*b*-PAA<sub>22</sub>) were studied (Figure 1.16).<sup>144</sup> Authors have taken an uncommon way to prepare  $Im\bar{3}m$  cubosomes. An excess of non-solvent ( $\sim 3$ -fold) is added directly in one portion (instead of dropwise) into a polymer solution. Nevertheless, the self-assemblies of PS<sub>144</sub>-*b*-PAA<sub>22</sub> in this solvent mixture need time to achieve the global equilibrium at room temperature under stirring, during which a series of morphological transformations occurs. The intermediate morphologies that formed over time were quenched in a further 5-fold excess of non-solvent and imaged using either TEM or SEM. Similar to example of PEO<sub>45</sub>-*b*-PS<sub>236</sub> discussed above, here polymer vesicles are also formed at the beginning of the self-assembly process (30 min after non-solvent addition, Figure 1.16A). These vesicles eventually fuse to form sponge-like particles at  $t = 280$  min. Further equilibration beyond the 280 min, the irregular sponge structure reorganizes into an ordered gyroid network ( $Ia\bar{3}d$  cubosomes). At the end of the self-assembly process, these  $Ia\bar{3}d$

cubosomes transform into  $Im\bar{3}m$  cubosomes, presumably due to the  $Im\bar{3}m$  structure has less surface area than an  $Ia\bar{3}d$  structure.

### 1.3.4 Characterization techniques of polymer cubosomes and hexosomes

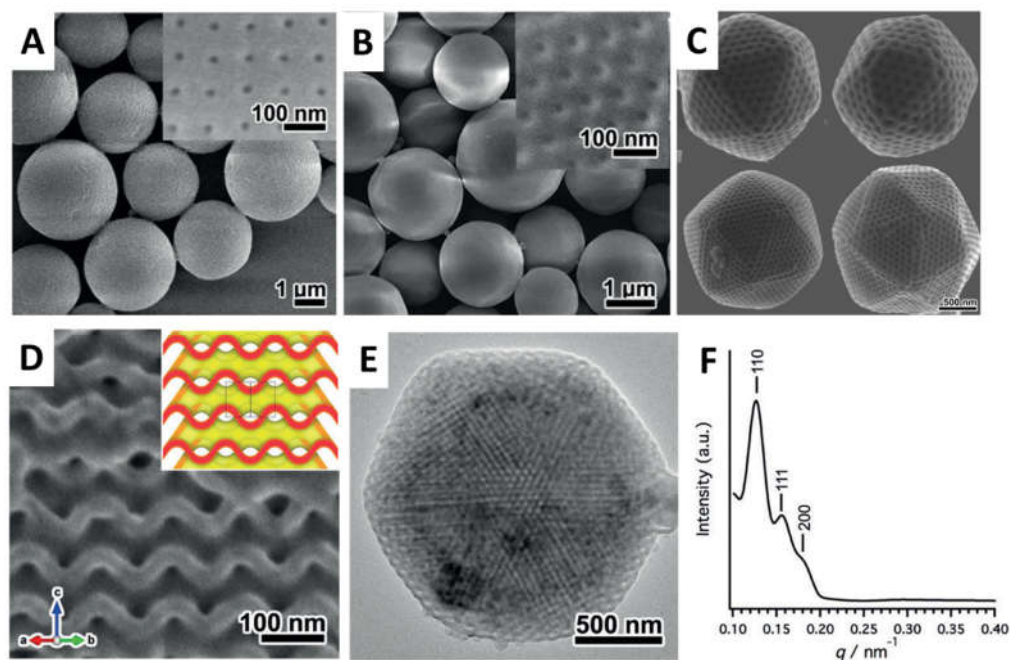


**Figure 1.17.** Examples of different characterization techniques for polymer inverse morphologies. (A) SEM image of  $Im\bar{3}m$  polymer cubosomes, the inset shows the tetragonally packed pores on their spherical surface. (B) SEM image of  $Pn\bar{3}m$  polymer cubosomes, the inset indicates hexagonally packed pores on the surfaces. (C) SEM images of  $Pn\bar{3}m$  cubosomes exhibiting polyhedral surfaces. (D) High resolution SEM image show the internal structure of a broken  $Pn\bar{3}m$  cubosomes. (E) TEM images of  $Pn\bar{3}m$  cubosomes. (F) SAXS scattering of cubosomes in (E), validating the  $Pn\bar{3}m$  structure.<sup>138</sup>

The typical characterization techniques of polymer cubosomes and hexosomes include electron microscopies, radiation scattering techniques and nitrogen adsorption–desorption isotherm analysis. They can measure characteristic parameters like the size, shape, space symmetry, internal organization, surface area and porosity.

#### Electron microscopies

SEM, TEM and cryo-EM used for visualization of polymersomes are also applied to visualize the shape and internal organization of polymer cubosomes/hexosomes. Thanks to the high stability of polymer cubosomes/hexosomes, their morphologies could often be maintained after dehydration during sample preparation of SEM and TEM.

Nearly intact structures could be visualized in most case by the SEM technique. Regular packed pores on the surface of cubosomes could be observed by SEM, from which some characteristic information could be obtained for these colloids. For example, the  $Im\bar{3}m$  polymer cubosomes typically have uniform tetragonal pores on their spherical surface, while the  $Pn\bar{3}m$  cubosomes exhibit hexagonally packed pores on the polyhedral surfaces (Figure 1.17). On the other hand, nearly ellipsoidal or conical morphology with tightly packed channels winding around the surface of hexosomes could also be identified by SEM (Figure 1.13e). Using high-resolution SEM, it was possible to showcase the bicontinuous internal structure of the broken cubosomes (Figure 1.17D).

TEM also allows the visualization of the internal structures of cubosomes and hexosomes (Figure 1.17E). In particular, cryo-EM gives visualization and measurement of internal aqueous channels of polymer cubosomes/hexosomes in a natural hydrated state. McKenzie *et al.* studied internal pore connectivity of poly(ethylene oxide)-*b*-poly(octadecyl methacrylate) (PEO-*b*-PODMA) inverse morphology using cryo-electron tomography (3D-cryoEM).<sup>34</sup> In this study, slices of inverse structure captured at different tilt angles were used to construct a 3D tomogram to analyze the internal channels. Nevertheless, the cryo-EM is not suitable to visualize the internal structure of the large inverse morphologies with diameter in micro scale.

### ***Radiation scattering techniques***

Light and synchrotron or X-ray scattering techniques can give more quantitative assessment of the internal structures of cubosomes and hexosomes. Dynamic light scattering (DLS) can be utilized to study the size and polydispersity as well as zeta potential of nano- and micro-particles including colloids with inverse morphologies. For assigning the type of internal symmetry within inverse morphologies, small angle X-ray scattering (SAXS) is an important tool (Figure 1.17F). In SAXS experiments, an X-ray beam is passed through the colloidal sample and the resulting scattering intensity is recorded at smaller scattering angles (typically  $0.1\text{--}10^\circ$ ). The modulus of the scattering vector ( $q$ ) is defined as  $q = 4\pi\sin(\theta/2)/\lambda$ , where  $\theta$  and

$\lambda$  are the scattering angle and X-ray wavelength, respectively. The internal geometries ( $Im\bar{3}m$ ,  $Pn\bar{3}m$  and  $Ia\bar{3}d$ ) of bicontinuous cubic structures are assigned using characteristic Bragg peak spacing ratios in Table 1.3. This characteristic diffraction patterns are generated from an ordered microstructure due to specific repeat distances of the associated interlayer spacings  $d$ . Its value can be calculated using  $d = 2\pi/q$  and the mean lattice parameter,  $a$ , can be calculated from  $d$ . In addition, SAXS can also allow calculation of the radii of aqueous channels within inverse morphologies.

**Table 1.3.** Selected mesophases and their corresponding peak ratios observed using SAXS.

Mesophase	Descriptor	Peak spacing ratio in q space
Bicontinuous cubic	$Im\bar{3}m$	1: $\sqrt{2}$ : $\sqrt{4}$ : $\sqrt{6}$ : $\sqrt{8}$ : $\sqrt{10}$ : $\sqrt{12}$ ...
	$Pn\bar{3}m$	1: $\sqrt{2}$ : $\sqrt{3}$ : $\sqrt{4}$ : $\sqrt{6}$ : $\sqrt{8}$ : $\sqrt{9}$ ...
	$Ia\bar{3}d$	1: $\sqrt{6}$ : $\sqrt{8}$ : $\sqrt{14}$ : $\sqrt{16}$ : $\sqrt{20}$ : $\sqrt{22}$ ...
Inverse hexagonal	$P6mn$	1: $\sqrt{3}$ : $\sqrt{4}$ : $\sqrt{7}$ : $\sqrt{9}$ : $\sqrt{12}$ : $\sqrt{13}$ ...

### ***Nitrogen adsorption-desorption isotherm analysis***

Nitrogen adsorption-desorption isotherm analysis has been applied to characterize bicontinuous cubic colloids surface area and pore size distributions. For example, Kim *et al.* have analyzed the nitrogen adsorption-desorption isotherms for dried  $Pn\bar{3}m$  cubosomes, giving a large surface area ( $73 \text{ m}^2 \text{ g}^{-1}$ ) and pore volume ( $0.45 \text{ cm}^3 \text{ g}^{-1}$ ).<sup>163</sup> The nitrogen adsorption-desorption isotherm analysis may allow routine estimation of the loading and release kinetics of bicontinuous cubic colloids payloads.

## **1.4 Aggregation-induced emission (AIE)**

### **1.4.1 Aggregation-induced quenching (ACQ)**

The development of luminescent materials has allowed to gain enormous knowledge that has undoubtedly promoted high-tech innovations and benefited the whole world. For example, the development of green fluorescent proteins (GFP), which has enabled to “see” the biochemical structures and processes to gain extraordinary knowledge and insights into biological pathways. Fluorescent probes have been used as sensors to detect the movement and

concentration of drugs or biological molecules *in vitro* and *in vivo*. The luminescent materials have also been widely used as organic light-emitting diodes (OLEDs) and organic field-effect transistors (OFETs) for display. So far, research on luminescent materials remains a hot topic.

Nevertheless, most conventional luminophores experience emission quenching, partially or completely, when aggregated or used in high concentration. Since the main reason is mechanistically related to the “formation of aggregates”, the quenching effect of conventional organic dyes is frequently referred to as “aggregation-caused quenching” (ACQ). According to Birks’s book “Photophysics of Aromatic Molecules in 1970”, it is commonly recognized that many aromatic luminophores suffer from the ACQ effect.<sup>164</sup> They often emit strongly in solution but meet the ACQ effect to some extent when they aggregated. These aromatic luminophores typically possess planar aromatic rings in their molecular structures. Once the dyes aggregated, the aromatic luminophores tend to stay together *via* intense intermolecular  $\pi$ - $\pi$  stacking interaction, which may prompt the formation of such detrimental species as excimers, leading to the emission quenching of the luminophores. As a matter of fact, luminophores often happen to be in aggregates state. For example, in biomedical research, luminescent probes are often used in aqueous media. Although the incorporation of hydrophilic moiety into chemical structures of the luminophores enhance their miscibility with water, the intrinsic hydrophobicity of their aromatic parts will still result in the formation of aggregates, resulting in decrease of fluorescence intensity. It will hamper their efficiency in detecting or monitoring biological activities. From the viewpoint of practical applications, the ACQ effect is considered detrimental in most case. Therefore, how to tackle the ACQ effect is a crucial research subject and has gained a lot of research interests. Obviously, an alternative way is to prevent the aggregation of luminophore molecules. Bulky cycles, spiral kinks and dendritic wedges have been covalently connected to luminophore cores to hamper aggregate formation of the luminophore moieties.<sup>165-168</sup> These approaches, however, can only partially or temporarily hamper the aggregation to certain extents. As aggregate formation of luminogen molecules is an inevitable process for practical applications. The ideal solution for tackling ACQ effect may be in finding a novel luminogen system, where the aggregation may work constructively rather than destructively compared to conventional fluorescent system.

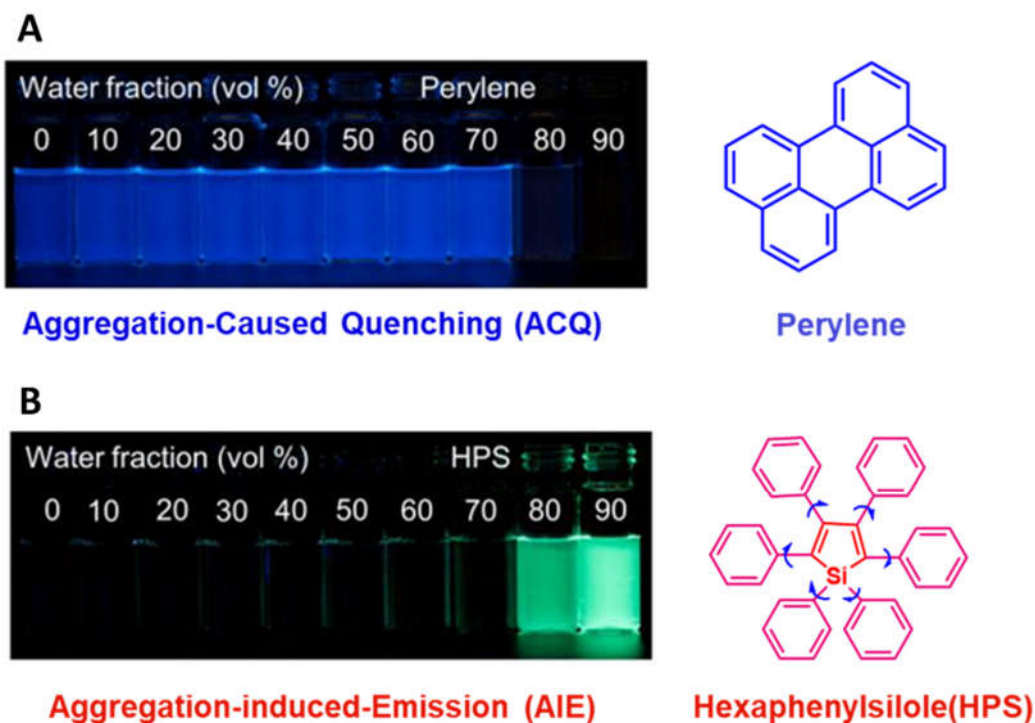
### 1.4.2 Emergence of the AIE concept

Early in 1921, Gerhard C. Schmidt found that some compounds fluoresce in solidified solutions but are quenched in the respective fluid solvents.<sup>169</sup> Later, scientists observed that solution of luminogen molecules with flexible  $\pi$ -systems exhibited enhanced fluorescence in solvent of high viscosity or at low temperature. In 1996, Oelkrug and co-workers described a series of oligophenylenevinyls that showed an increase in fluorescence quantum yield from nearly zero in solution to 60% in nanoparticle suspensions and in thin films.<sup>170</sup> This fluorescence enhancement phenomena after aggregation were also observed by other groups.<sup>171</sup> However, they only focused on preparing highly emissive materials in bulk state and did not pay much attention to the question of whether the individual molecule is emissive in solution. They did not make systematic studies on mechanism for this unnormal photophysical process to broaden the application of these novel luminogen systems.

In 2001, Tang and coworkers discovered serendipitously an unusual luminogen system, a silole derivative, 1-methyl-1,2,3,4,5-pentaphenylsilole.<sup>172</sup> This compound was non-emissive when it was molecularly dissolved in a good solvent, but became highly luminescent when it aggregated in the poor solvent. Since the light emission was induced by aggregate formation, the authors termed the phenomenon as “aggregation-induced emission” (AIE). Since then, the research on AIE has been blooming and became a hot topic as witnessed by a remarkable number of reviews.<sup>173-177</sup> For AIE luminogens (AIEgens), the aggregates are brighter than the parts, presenting opposite photophysical property to ACQ luminogens. To better clarify this difference, the representative luminogens, perylene, with ACQ effect and AIEgen, hexaphenylsilole (HPS), were taken as the examples. Figure 1.18 shows their chemical structure and fluorescent property as function of water fraction under UV light. As shown in Figure 1.18A, the perylene solution shows strong fluorescence when it was dissolved in a good solvent such as tetrahydrofuran (THF). Poor solvent such as water was then added to induce the formation of perylene aggregates. Consequently, the fluorescence was partially quenched when the water fraction reached 80%. Further increasing the water fraction to 90%, the fluorescence disappeared completely. The reason is that, to some extent of water fraction, the  $\pi$ - $\pi$  stacking interactions between the perylene molecules in the aggregates effectively promote the formation of excimers, resulting in the observation of ACQ phenomenon. In contrast, the AIE phenomenon is clearly depicted in Figure 1.18B. No fluorescence was observed when the HPS was well-dissolved in the THF. Interestingly, the solution began to be



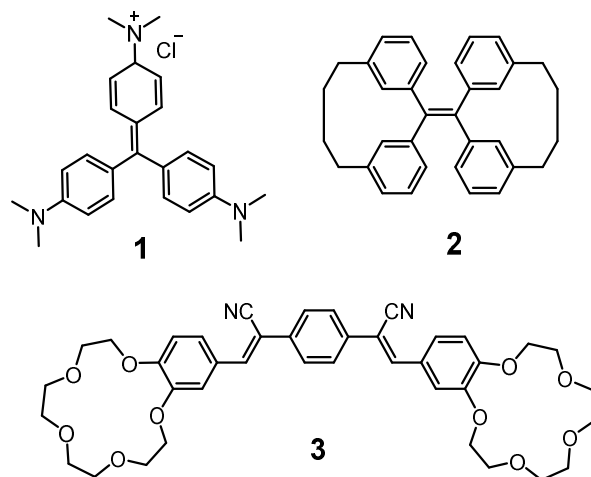
fluorescent when the water fraction reached 80% due to the formation of HPS aggregates in THF/water mixtures. Their fluorescence brightness further increased after addition of 90% water. The working mechanism of this AIE effect will be described in following section.



**Figure 1.18.** Fluorescence photographs of perylene solution (20  $\mu\text{M}$ ) (up) and hexaphenylsilole solution (20  $\mu\text{M}$ ) (down) in THF/water mixtures with different content of water (vol %).<sup>178</sup>

### 1.4.3 Mechanism of AIE process

The systematic decipherment of the mechanism of AIE property is of great importance to fully understand the essence of AIE property, to create new AIE systems, and to explore potential applications of AIE systems. A number of hypotheses of the mechanism of AIE process have been proposed, including restriction of intramolecular rotations (RIR),<sup>179</sup> restriction of intramolecular vibrations (RIV),<sup>180</sup> excited state intramolecular proton transfer (ESIPT),<sup>181</sup> *J*-aggregate formation (JAF),<sup>164</sup> and distorted intramolecular charge transfer (TICT).<sup>182</sup> Excellent review by Tang *et al.* has discussed in detail the working mechanism of AIE process.<sup>183</sup> Here, we will focus on the introduction of the RIR and RIV, which are main mechanistic causes for the observation of AIE property.

**Restriction of intramolecular rotations (RIR)****Scheme 1.1.** The chemical structure of different molecules.

It is generally acknowledged that molecular motion, including rotations and vibrations, consumes energy. In 1956, Nishijima *et al.* reported on the relationship between fluorescence and internal rotation.<sup>184</sup> In 1971, Forster found that the fluorescence of triphenylmethane derivative 1 (Scheme 1.1) increases in more viscous solvents or the solid state compared to that in fluid solutions.<sup>185</sup> They interpreted that the decrease in fluorescence intensity in fluid solution originates from the rotation of the phenyl groups. In contrast, fluorescence increase was observed through restriction of internal rotation of luminogen molecules. In 1989, Fox *et al.* synthesized a series of torsion-restricted tri- and tetraphenylethylenes (TPEs) as shown in Scheme 1.1 (molecule 2).<sup>186</sup> Its fluorescence quantum yields was measured as 53%, while quantum yields of the parent TPE was less than 0.1%. They proposed that phenyl ring torsional motion plays a significant role in the photochemistry of TPEs. In 1999, Xia *et al.* presented a fluorescent probe (molecule 3) for alkali metal ions (Scheme 1.1).<sup>187</sup> A strong fluorescence enhancement was observed upon the metal ion binding. The author proposed that the rotation of aromatic rings in molecule 3 are blocked in double-decker complexes upon complexation with a metal ion. However, systematic studies on mechanism of this unnormal photophysical process were rare until the coinage of the AIE concept in 2001 by Tang group.

Since 2001, researchers have made a great effort to study systematically AIE process and to decipher its mechanism.<sup>183</sup> Tang group found that these AIEgens have some similarities in chemical structure. They have a conjugate center (stator) linking with multiple aromatic rings

(rotors) through the single bond. As stated above, the HPS is an emblematic AIEgen, in which six phenyl peripheries (rotors) are tethered to the silole stator. In TPE, four phenyl rings (rotors) are connected to the central ethene stator through single bonds. Based on these discoveries, Tang group proposed the RIR mechanism for the AIE process.<sup>188</sup>

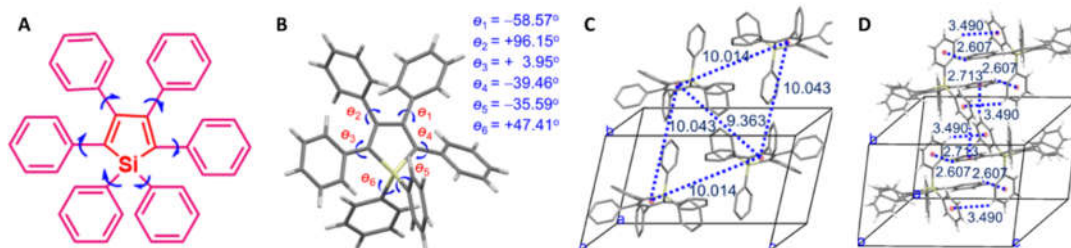


**Figure 1.19.** The chemical structure (A) and crystal conformation (B-D) of HPS. The blue dotted line in C indicate the distance between two HPS molecules. The blue dotted in D show the multiple intermolecular C–H··· $\pi$  interaction between the adjacent HPS molecules.

Here, we take HPS as an example to explain the RIR mechanism. In dilute solution, the bulky aromatic rotors in HPS have great freedom to rotate against the central silole through the single bond axes (Figure 1.19A). The nonradiative decay in solution occurs due to the unhindered intramolecular rotations. In aggregate state, however, the intramolecular rotations are basically restricted due to the physical constraint. Figure 1.19B shows the crystalline lattice of HPS. The HPS take a propeller-like conformation, in which six peripheral phenyl rings are highly twisted from the central silole plane. Such a propeller-like conformation efficiently prevents intermolecular  $\pi$ – $\pi$  stacking interaction between the neighboring phenyl rings that lead to the emission quenching frequently observed in aggregates of conventional luminophores. The long distances (9.363–10.043 Å) between the central silole in the unit cell of HPS crystal further verified it (Figure 1.19C). Meanwhile, multiple intermolecular C–H··· $\pi$  hydrogen bond between the adjacent HPS molecules will stabilize and reinforce the propeller-like conformation (Figure 1.19D). All these works collectively to induce the emission of HPS in aggregated state by RIR.

The rationality of the RIR mechanism has been verified by a string of control experiments through modulating the intramolecular rotation both externally and internally. The experiments show that the HPS emits more efficiently at lower temperature, in more viscous solvent and higher pressure.<sup>179,189</sup> The emission enhancement indicated the RIR is

undoubtedly responsible for AIE process of HPS. Besides the control of external environment factors, fluorescence enhancement is also expected when the intramolecular rotations of the aromatic rings are blocked by introducing sterically bulk group in the aromatic rings and cross-locked with tethering units.<sup>190</sup> In addition, the RIR mechanism is also supported by theoretical calculations and simulations of low-frequency intramolecular motion.<sup>191,192</sup>

### *Restriction of intramolecular vibrations (RIV)*

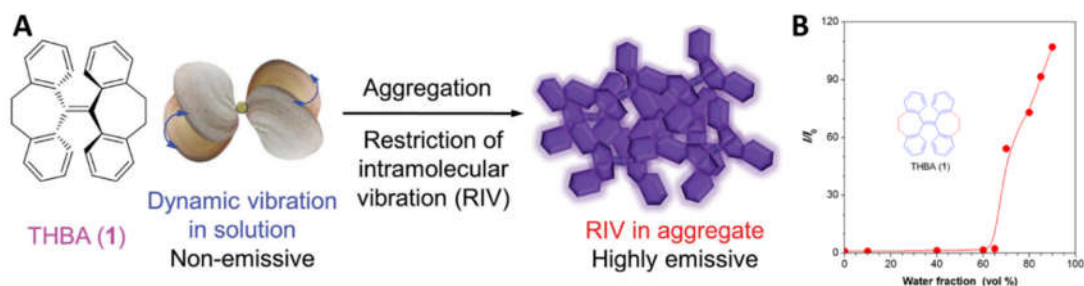


**Figure 1.20.** (A) Chemical structure and schematic depicting of RIV of THBA. (B) Fluorescence evolution of THBA as function of water fraction ( $[1] = 20 \mu\text{M}$ ).<sup>193</sup>

As the AIE study advances, more and more AIEgens have been discovered. The AIE process for some AIEgens cannot be interpreted by the RIR mechanism. Taking shell-like luminogen of 10,10',11,11'-tetrahydro-5,5'-bidibenzo[a,d][7]annulenyliene (THBA, Figure 1.20A) for example, it is non-emissive in solution, while the fluorescence intensity increases about 110 times when the fraction of water reaches 90% (Figure 1.20B).<sup>178</sup> It suggests the THBA is an AIEgen. However, the THBA has no rotatable element. The two flexible parts are locked by a pair of ethylene tethers instead of single bond. In 2014, Tang and coworkers proposed the mechanism of RIV to interpret the AIE process of THBA.<sup>180</sup> As shown in Figure 1.20A, two flexible part of THBA are non-coplanar, in which two phenyl rings are connected by a bendable flexure. The flexibility of the flexure allows the phenyl rings to bend or vibrate, which prompt the nonradiative decay pathway in the solution. The cartoon shown in Figure 1.20A illustrated the intramolecular vibration of THBA that like the breathing movement of a clam. In aggregated state, the intramolecular vibration will be blocked due to the physical constraint and the radiative decay pathway is opened. At the same time, which results in the strong fluorescence for THBA.

With the discovery of more AIEgens over years, a lot of works have been simultaneously carried out to decipher and understand the mechanisms of AIE processes, which validate and further establish the AIE concept. The systematic decipherment of the mechanism has laid the groundwork for navigating AIE research in developing the novel AIE materials and exploring their potential application in various fields, ranging from bioimaging, chemosensing, optoelectronics to stimuli-responsive systems. We are interested in development of novel fluorescent polymersomes system with AIE characteristic.

### 1.5 Polymersomes with aggregation-induced emission (AIE) property

Fluorescent polymersomes are interesting bioimaging tools for real-time imaging of therapeutic substances delivery, diagnostic and theranostics. Fluorescent polymersomes are normally obtained *via* two strategies (see Figure 1.21), *i.e.*, either by engineering fluorophores into the chemical structure of polymers<sup>194-196</sup> or by simply encapsulating the fluorophores into polymersomes membrane<sup>197-199</sup>. For example, rhodamine-labelled PMPC-*b*-PDPA polymersomes were employed for imaging of tumor and its environment (PMPC-*b*-PDPA: poly(2-methacryloxyethylphosphorylcholine)-*b*-poly(2-(diisopropylamino)ethyl methacrylate)).<sup>195</sup> The rhodamine fluorophore was first linked chemically to amphiphilic block copolymer chains, and 5% of these rhodamine-labelled polymers were then self-assembled together with PMPC-*b*-PDPA to form fluorescent polymersomes. These fluorescent polymersomes were successfully employed for real-time tracking of the internalization rates, retention and biodistribution of the polymersomes in oral squamous cell carcinoma cells *in vitro* and *in vivo*. Another example is the near infra-red (NIR) emissive polymersomes generated through cooperative self-assembly of block copolymers and conjugated multi(porphyrin)-based NIR fluorophores (NIRFs).<sup>197-199</sup> The block copolymers are PEO-*b*-PBD (polyethylene oxide-*b*-polybutadiene), PEO-*b*-PCL (PCL: poly( $\epsilon$ -caprolactone), or PEO-*b*-PMCL (PMCL: poly( $\gamma$ -methyl- $\epsilon$ -caprolactone). Polymersomes could incorporate and uniformly distribute a number of large hydrophobic NIR fluorophores exclusively in their hydrophobic membranes (up to 10 mol%, beyond that limit polymersomes destabilized). The prepared polymersomes presented a good colloidal stability in physiological condition for 1 week, indicating their effectiveness for biomedical applications. By controlling the number of NIR fluorophores (NIRF) in the membrane, these NIRF-polymersomes manifested photophysical properties similar to those in organic solvents, and the total fluorescence emanating from the assemblies gave rise to a localized optical signal of sufficient intensity to

penetrate through the dense tumor tissue of a live animal. The *in vitro* 3D scanning of the tumor tissue has been performed with these NIRF-polymersomes.

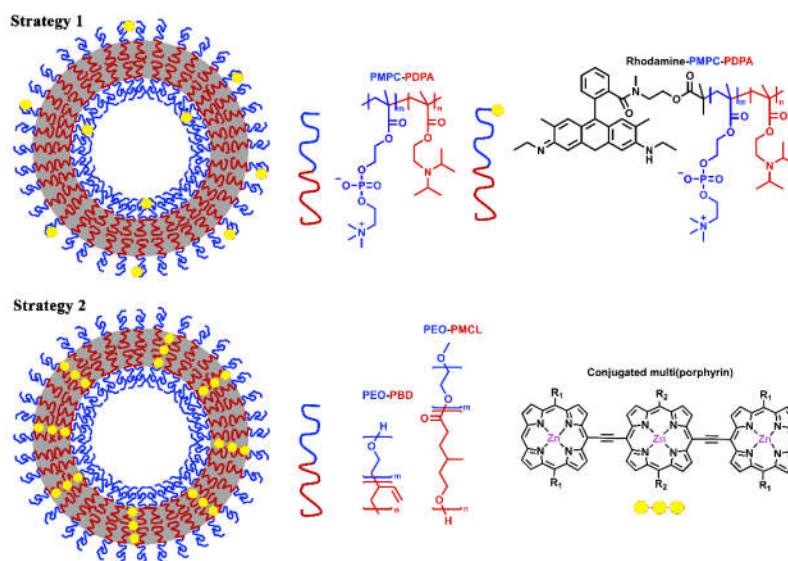


**Figure 1.21.** Two strategies to construct the fluorescent polymersomes.

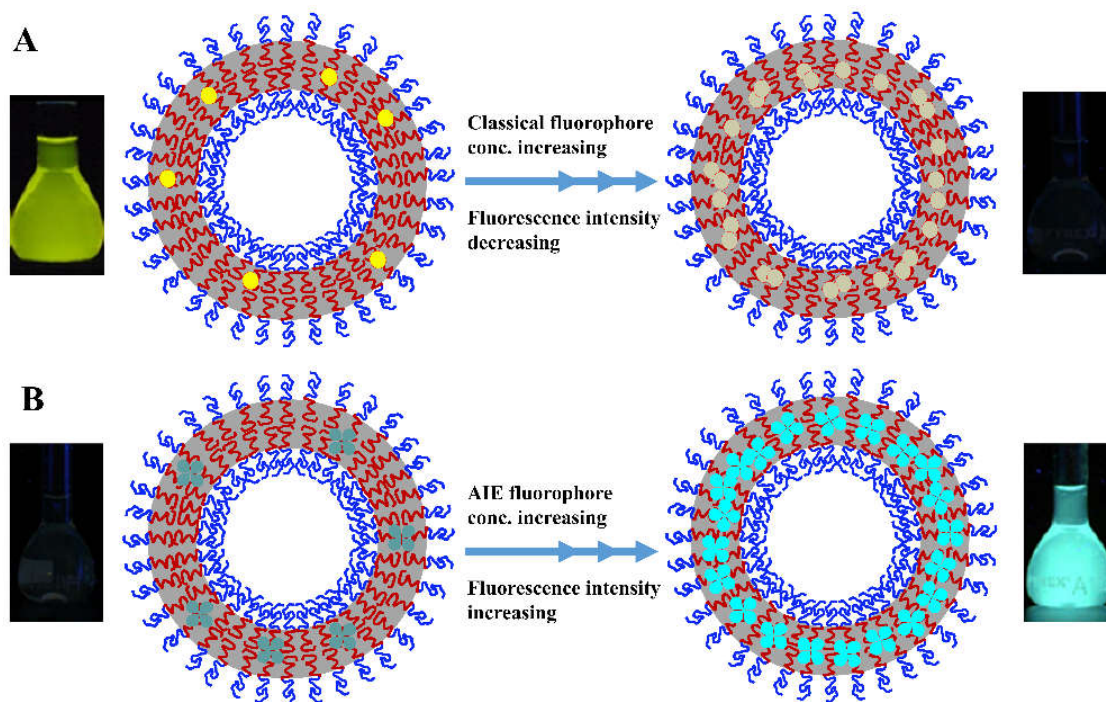


**Figure 1.22.** Comparison between fluorescent polymersomes with ACQ and AIE luminogens.

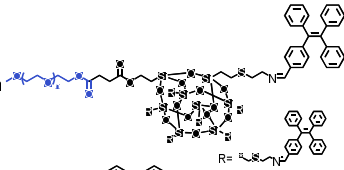
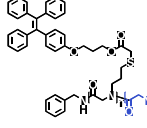
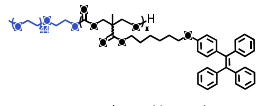
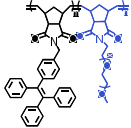
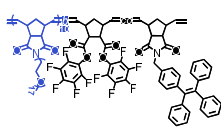
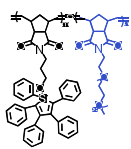
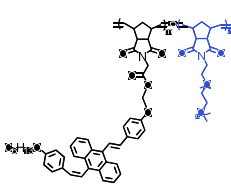
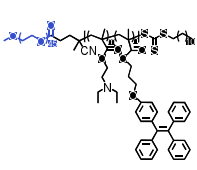
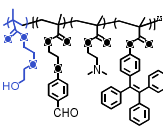
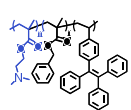


Despite the efforts, the examples of fluorescent polymersomes are still relatively rare in the literature.<sup>194-199</sup> The classical fluorophores usually contain planar and multiple conjugated aromatic rings and tend to aggregate at high concentration in the hydrophobic domain of nanostructures. It is well-known that these organic aromatic dyes always suffer from the ACQ. Their fluorescence emissions are usually weak or completely negligible in the aggregated state because of the short-range molecular interactions such as  $\pi$ - $\pi$  stacking originating from the planarity of the molecular skeleton.<sup>200</sup> In order to avoid the ACQ in the fluorescent polymersomes, fluorophore-labelled polymers always need to co-self-assemble with a large quantity of non-labelled polymers (with a molar ratio 5:95) in the first strategy above-discussed, while in the second strategy the number of the hydrophobic dye molecules incorporated in the membrane should also be limited (only 1-10% mol of dye can be used). Moreover, the local segregation of fluorophore-labelled polymers or of hydrophobic dye molecules need to be avoided during the co-assembling process.<sup>197</sup> The mean fluorophore-fluorophore interspatial separation is thus regulated to minimize the subsequent loss of fluorescence efficiency. It seems that there is an intrinsic obstacle to construct luminescent polymersomes of high efficiency with conventional fluorophores (Figure 1.22). Thus, the combination of AIEgens and polymer vesicle structures provide an alternative way to prepare highly efficient luminescent polymersomes with extended potential for applications in drug delivery, bioimaging, diagnostics, and theranostics.<sup>201</sup>

### 1.5.1 The state of the art of AIE polymersomes

So far, AIE Polymersomes are formed through strategy 1 by engineering AIEgens into the chemical structure of polymers (Figure 1.21). The most used AIEgen is TPE, other AIEgens like distyrylanthracene and 1,2,3,4,5-pentaphenylisole are also employed. AIEgens can be integrated in the amphiphilic block copolymer by post-modification of a pre-polymer.<sup>202-205</sup> They can also be attached first to the monomers to get AIE-monomers which further are polymerized to form the hydrophobic block of amphiphilic AIE copolymers. Various polymerization techniques including polymerization, ring-opening polymerization (ROP),<sup>206</sup> ROMP,<sup>207-209</sup> and RAFT polymerization<sup>210-213</sup> are chosen to prepare different polymer backbones with interesting properties, such as ROP to obtain biocompatible and biodegradable polypeptoids and polycarbonates, ROMP to get rigid polynorbornenes and RAFT polymerization to get polymethacrylates and polystyrene-type backbones.

**Table 1.4.** Polymers and corresponding formulation parameters for AIE polymersomes.

Name	Synthetic strategy	Chemical structure	Vesicle-forming hydrophilic/total mass ratio	Vesicle-formation method	Ref
PEG- <i>b</i> -POSS(TPE) <sub>7</sub>	Post-modification		$f_{\text{PEG}} = 8.7\%, 17\%$	Nanoprecipitation	202-204
P(TPE-NAG)- <i>b</i> -PSar	Post-modification		$f_{\text{PSar}} = 18\%$	Nanoprecipitation	205
PEG <sub>45</sub> - <i>b</i> -P(TPE-TMC) <sub>n</sub>	ROP polymerization		$f_{\text{PEG}} = 17\%, 21\%, 27\%, 33\%$	Nanoprecipitation	206
poly(M1)- <i>b</i> -poly(M2)	ROMP polymerization		$f_{\text{Poly(M2)}} = 26\%$	Nanoprecipitation	207
Poly(M2)- <i>b</i> -poly(M1-co-M3)	ROMP polymerization		$f_{\text{Poly(M2)}} = 14\%$	Nanoprecipitation	208
Poly(N-PPSiol)- <i>b</i> -Poly(N-PEG)	ROMP polymerization		$f_{\text{Poly(N-PEG)}} = 12\%$	Nanoprecipitation	209
Poly(N-DSAnthracene)- <i>b</i> -Poly(N-PEG)	ROMP polymerization		$f_{\text{Poly(N-PEG)}} = 11\%$	Nanoprecipitation	209
PEG <sub>45</sub> - <i>b</i> -P(DEAEMA-co-TPEMA)	RAFT polymerization		$f_{\text{PEG}} = 17\%, 23\%, 26\%, 30\%$	Nanoprecipitation	210
PHEO <sub>2</sub> MA- <i>b</i> -P(MAEBADMAEMA-TPEMA)	RAFT polymerization		$f_{\text{PHEO2MA}} = 13\%, 11\%, 7.5\%$	PISA	211
PDMA- <i>b</i> -P(BzMA-TPE)	RAFT polymerization		$f_{\text{PDMA}} = 10\%$	PISA	210

Depending on the chemical structures, the vesicle-forming copolymers have hydrophilic to total mass ratios from 8% to 33% (Table 1.4). In all the examples, nanoprecipitation is the



major method employed to perform the self-assembly. PISA is an interesting method for preparation of AIE polymerosomes. In the following part we will briefly introduce the reported AIE polymersomes in the literature according to their synthetic methods and chemical structures of the AIE amphiphilic copolymers.

### 1.5.2. AIE amphiphilic copolymers prepared by post-modification of pre-prepared polymers with AIEgens

A simple strategy to generate amphiphilic AIE block copolymer is to post-functionalize AIEgens with one or several blocks of block copolymers.

Polypeptoids have a protein-mimicking structure with *N*-substituted glycine as repeating units but lack intramolecular and intermolecular hydrogen bonding along the amino acid backbone. Therefore, polypeptoids show better solubility, thermal processability, cell permeability and proteolytic stability compared to polypeptides. Recently, our group reported a series of amphiphilic polypeptoids with TPE as the side group in the hydrophobic block by the post-modification of poly(*N*-allylglycine)-*b*-polysarcosine (PNAG-*b*-PSar).<sup>205</sup> Here the polymer PNAG is an excellent platform for post-modification to produce different functional polypeptoids. PSar (also called poly(*N*-methyl glycine)) is a hydrophilic block that shows resistance to protein adsorption and low toxicity, similar to PEG. A series of diblock copolypeptoids PNAG-*b*-PSar with different chain lengths and narrow molecular weight distribution ( $M_w/M_n \sim 1.1$ ) were first synthesized by ring opening polymerization (ROP) using primary amine as the initiator and sequential feeding of NAG-NTA and Sar-NTA (Figure 1.23A). TPE-functionalized P(TPE-NAG)<sub>10</sub>-*b*-PSar<sub>53</sub> ( $f_{\text{PSar}} = 38\%$ ), P(TPE-NAG)<sub>15</sub>-*b*-PSar<sub>54</sub> ( $f_{\text{PSar}} = 30\%$ ) and P(TPE-NAG)<sub>25</sub>-*b*-PSar<sub>46</sub> ( $f_{\text{PSar}} = 18\%$ ) were prepared by post-polymerization reaction as shown in Figure 1.21A. Self-assembling was performed by nanoprecipitation method using DMF/water as co-solvents. Micelles, micelles/polymersomes and polymersomes are obtained for P(TPE-NAG)<sub>10</sub>-*b*-PSar<sub>53</sub>, P(TPE-NAG)<sub>15</sub>-*b*-PSar<sub>54</sub> and P(TPE-NAG)<sub>25</sub>-*b*-PSar<sub>46</sub>, respectively (Figure 1.23B). The vesicle structure in the last two cases has unambiguously been proved by the cryo-EM. For example, only polymersomes are formed by PNAG<sub>25</sub>-*b*-PSar<sub>46</sub> ( $f_{\text{PSar}} = 18\%$ ), according to cryo-EM images. The thickness of the hydrophobic part of membrane is measured as  $10 \pm 1$  nm that corresponds to the value of unilamellar bilayer membrane, in which P(TPE-NAG) chains might not be totally extended or

might be interdigitated between the two leaflets (the contour lengths of P(TPE-NAG)<sub>25</sub> is about 7.3 nm).

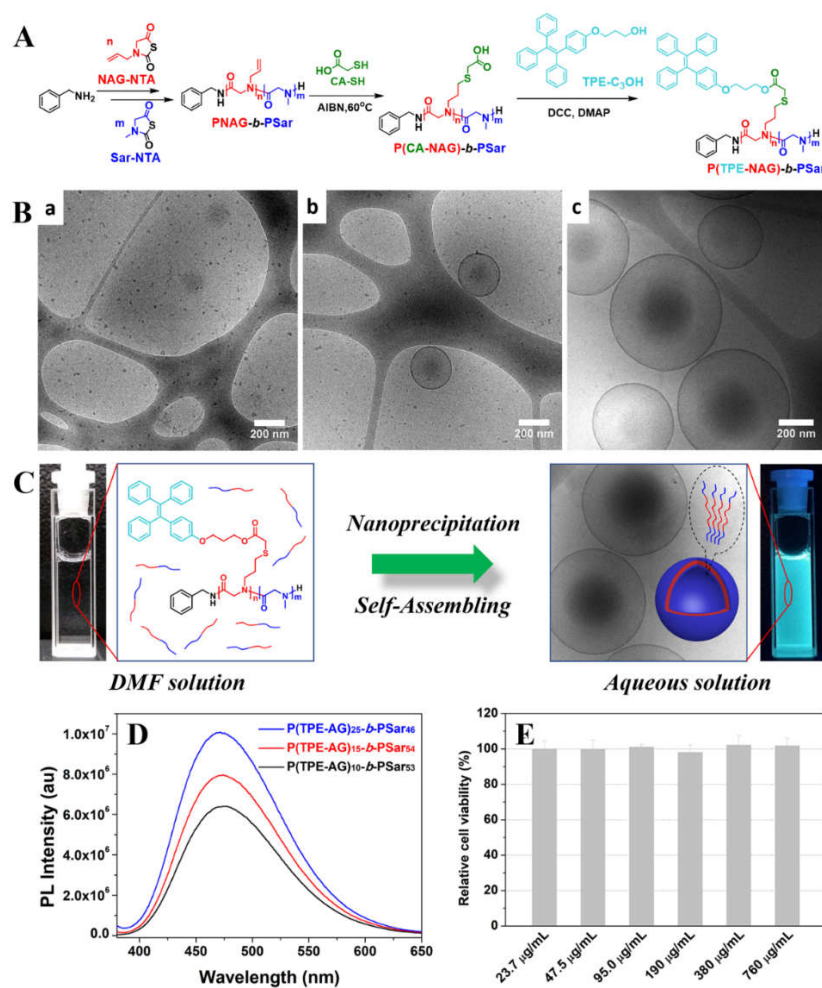


**Figure 1.23.** (A) Synthetic route to P(TPE-NAG)-b-PSar. (B) Cryo-EM images of nanoparticles formed by P(TPE-NAG)<sub>10</sub>-b-PSar<sub>53</sub> (a), P(TPE-NAG)<sub>15</sub>-b-PSar<sub>54</sub> (b) and P(TPE-NAG)<sub>25</sub>-b-PSar<sub>46</sub> (c). (C) Schematic presentation of self-assembly of P(TPE-NAG)-b-PSar in aqueous solution and the AIE phenomenon of the polymersome dispersion. (D) Fluorescence spectra of different nanoparticles (concentration: 0.4 mg. mL<sup>-1</sup>; excitation wavelength: 370 nm). (E) Relative cell viability of P(TPE-NAG)<sub>25</sub>-b-PSar<sub>46</sub> polymersomes incubated with human vein endothelial cells for 24 h at various polymer concentrations.<sup>205</sup>

The three copolypeptoids are not fluorescent in solution in DMF, while in aqueous solution their self-assembled nanoparticles show all strong fluorescence with emission peak at around 474 nm (Figure 1.23C-1.23D). High quantum yields of 26%, 29% and 34% were measured

for P(TPE-NAG)<sub>10</sub>-*b*-PSar<sub>53</sub>, P(TPE-NAG)<sub>15</sub>-*b*-PSar<sub>54</sub> and P(TPE-NAG)<sub>25</sub>-*b*-PSar<sub>46</sub> nanoparticles, respectively, using the integrating sphere method. Human vein endothelial cells were incubated with these AIE nanoparticles for 24 h at different concentrations. The result shows that these AIE polymer nanoparticles are non-cytotoxic (Figure 1.23E), which guarantee their safety in potential applications in bio-related field such as bio-imaging and drug delivery.

### 1.5.3 AIE amphiphilic copolymers prepared by direct polymerization of AIE monomers

Instead of the post-modification of pre-polymers, another strategy to prepare AIE amphiphilic block copolymers is to copolymerize the AIEgen-containing monomers by living or controlled polymerization, such as ROP of cyclic carbonates, ROMP and RAFT.

#### *ROP polymerization*

Our group synthesized a series of amphiphilic diblock copolymers PEG-*b*-Poly(trimethylene carbonate) (PTMC) with TPE as side chain, by ROP.<sup>206</sup> The hydrophobic polymers based on PTMC are extensively studied for biomedical applications because of their special degradation behavior such as resistance to non-enzymatic hydrolysis, generation of non-acidic degradation products, and enzymatic degradation with a surface erosion mechanism. A cyclic trimethylene carbonate monomer with TPE pendant (TPE-TMC) was first designed and then polymerized by ROP using mPEG<sub>45</sub>-OH as the macroinitiator and N-(3,5-trifluoromethyl)phenyl-N'-cyclohexylthiourea (TU)/1,8-diazabicyclo[5.4.0]undec-7-ene (DBU) (TU/DBU) as catalysts (Figure 1.24A). Block copolymers PEG<sub>45</sub>-*b*-P(TPE-TMC)<sub>n</sub> with different degrees of polymerization (n = 16, 13, 9, and 7) and narrow molecular weight distribution ( $M_w/M_n \sim 1.3$ ) were obtained. All these copolymers PEG<sub>45</sub>-*b*-P(TPETMC)<sub>n</sub> could form polymersomes by nanoprecipitation method using THF as cosolvent (Figure 1.24B-1.24E). The diameter of polymersomes decrease with the decrease of the chain length of hydrophobic block P(TPE-TMC). The polymersomes of PEG<sub>45</sub>-*b*-P(TPE-TMC)<sub>16</sub> ( $f_{\text{PEG}} = 17\%$ ) have an average hydrodynamic diameter ( $D_h$ ) of 450 nm, while those of PEG<sub>45</sub>-*b*-P(TPE-TMC)<sub>13</sub> ( $f_{\text{PEG}} = 21\%$ ), PEG<sub>45</sub>-*b*-P(TPE-TMC)<sub>9</sub> ( $f_{\text{PEG}} = 27\%$ ) and PEG<sub>45</sub>-*b*-P(TPE-TMC)<sub>7</sub> ( $f_{\text{PEG}} = 33\%$ ) have  $D_h$  of 250, 90 and 70 nm, respectively. In addition, the whole size of the polymersomes depends also on the organic solvent used in nanoprecipitation (Figure 1.24C and 1.24F). For example, PEG<sub>45</sub>-*b*-P(TPE-TMC)<sub>13</sub> polymersomes formed in THF/water have the  $D_h$  value around 250 nm, while those formed in dioxane/water have  $D_h$  around 650 nm (Figure 1.24G). This is

probably because the solubility of hydrophobic polymers P(TPE-TMC) in THF is better than in dioxane. Upon water addition in THF/water system, the content of THF in the membrane may be higher and the polymer membrane more plasticized to lead more flexible membrane that close to form smaller vesicles. Therefore, the control of the polymersomes size can be achieved by the choice of co-solvent (THF or dioxane) or by altering the hydrophilic/hydrophobic ratio of block copolymers. This size adjustment is of great importance for the control of the cell uptake of polymersomes in biotechnological applications.

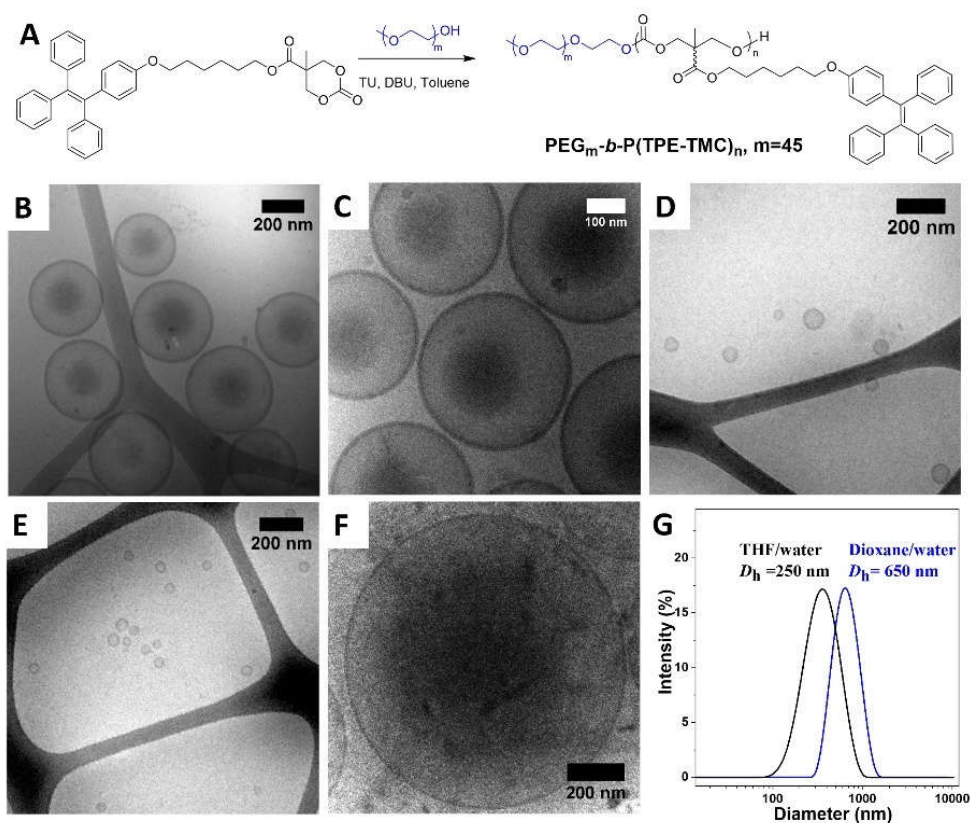


**Figure 1.24.** (A) Synthetic route of  $\text{PEG}_{45}\text{-}b\text{-P(TPE-TMC)}_n$ . (B-E) Cryo-EM images of polymersomes formed by  $\text{PEG}_{45}\text{-}b\text{-P(TPE-TMC)}_{16}$  (B),  $\text{PEG}_{45}\text{-}b\text{-P(TPE-TMC)}_{13}$  (C),  $\text{PEG}_{45}\text{-}b\text{-P(TPE-TMC)}_9$  (D) and  $\text{PEG}_{45}\text{-}b\text{-P(TPE-TMC)}_7$  (E) using THF/water as cosolvents. (F) Cryo-EM images of polymersomes formed by  $\text{PEG}_{45}\text{-}b\text{-P(TPE-TMC)}_{13}$  using dioxane/water as cosolvents. (G) DLS profile of polymersomes formed by  $\text{PEG}_{45}\text{-}b\text{-P(TPE-TMC)}_{13}$  using THF or dioxane as cosolvent.<sup>206</sup>

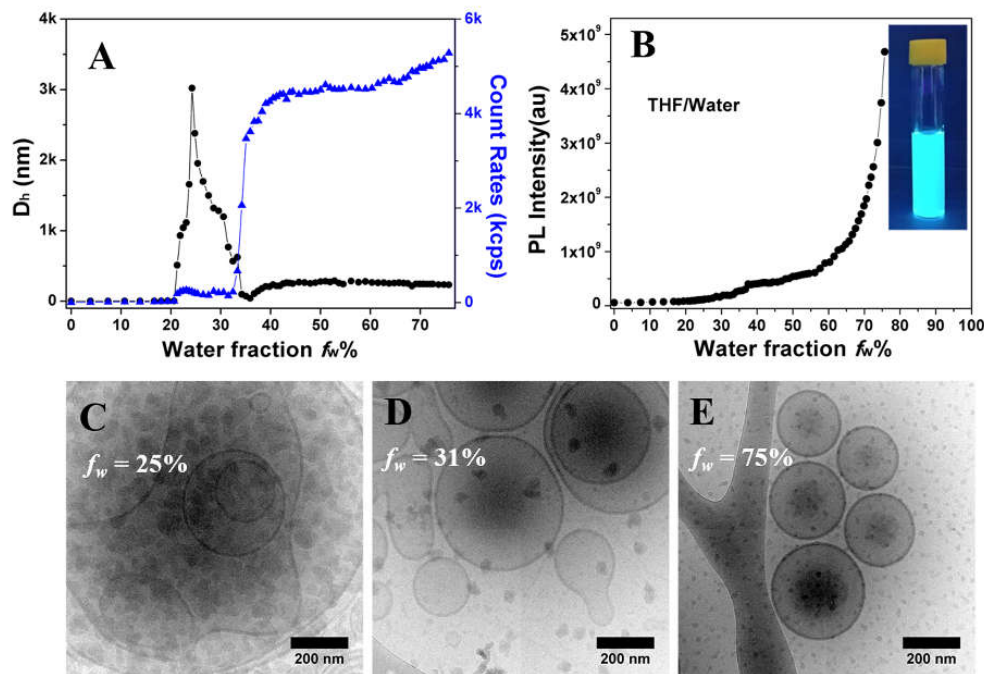


**Figure 1.25.** (A) Evolution of hydrodynamic diameter  $D_h$  and counts rates of polymersomes as a function of water content during the self-assembly. (B) Evolution of fluorescence intensity as a function of water content during the self-assembly. (C-D) Morphologies of PEG<sub>45</sub>-*b*-P(TPE-TMC)<sub>13</sub> self-assemblies in THF/water mixture with water content of (C)  $f_w = 25\%$ , (D)  $f_w = 31\%$ , and (E)  $f_w = 75\%$ .

The membrane of all polymersomes here has an unilamellar bilayer structure with a thickness of 10-15 nm. This affords a nanosized aggregation environment for the TPE AIEgens. For the first time, we examined the appearance of AIE fluorescence along the whole self-assembling process taking PEG<sub>45</sub>-*b*-P(TPE-TMC)<sub>16</sub> as an example (Figure 1.25A-E). Two main stage can be distinguished in the increase of fluorescence intensity upon the water addition in the polymer solution of THF (Figure 1.25B): a slow increase of fluorescence intensity at the water contents  $f_w < 60\%$  followed by an abrupt increase of fluorescence intensity at  $f_w > 60\%$ . In the first stage, the PEG<sub>45</sub>-*b*-P(TPE-TMC)<sub>16</sub> self-assemble to form membranes, big polymersomes, and finally polymersomes of optimal size and distribution. The initially fluorescence increase attributes to the aggregation of hydrophobic blocks P(TPE-TMC) (Figure 1.25C and 1.25D), because the intramolecular motion of TPE moieties start to be restricted in the membrane. However, the content of solvent in the membrane is still high at this stage which “lubricate” the intramolecular motion in a certain extent, and the restriction of intramolecular motions of

TPE moieties remain limited. Therefore, the growth of fluorescence intensity is moderate. When water content goes beyond 60%, due to the high osmotic pressure, the removal of the organic solvent from the membrane accelerates, and fewer and fewer of organic solvent present in the hydrophobic part of the membrane. This results in the effective restriction of intramolecular motions of TPE moieties that gives rise to the abrupt increase of fluorescence intensity (Figure 1.25B). The quantum yield of the final polymersomes dispersed in pure water is measured as 12.7%.

### ***ROMP polymerization***

Besides the cyclic trimethylene carbonate discussed above, monomers based on norbornene or cyclooctadiene are also popular for the synthesis of AIE amphiphilic polymers with narrow molecular weight distribution by ROMP using Grubbs catalysts. Zhang *et al.* have prepared amphiphilic diblock polynorbornene poly(M1)-*b*-poly(M2) by ring-opening metathesis polymerization (ROMP) of M1 and M2 as shown in Figure 1.26A, where M1 is a TPE-functionalized norbornene (hydrophobic monomer) and M2 a norbornene with PEG750 ( $M_n = 750$  Da) as side chains (hydrophilic monomer)<sup>207</sup>. Three amphiphilic diblock copolymers with narrow molecular weight distribution ( $M_w/M_n \sim 1.05$ ) and different hydrophilic to total mass ratio  $f_{M2}$  were prepared by ROMP on varying the hydrophobic block length and self-assembled using nanoprecipitation method with THF/water as co-solvents. Poly(M1)<sub>50</sub>-*b*-poly(M2)<sub>10</sub> ( $f_{M2} = 5.6\%$ ), poly(M1)<sub>100</sub>-*b*-poly(M2)<sub>10</sub> ( $f_{M2} = 15\%$ ) and poly(M1)<sub>300</sub>-*b*-poly(M2)<sub>10</sub> ( $f_{M2} = 26\%$ ) self-assemble into spherical micelles, cylindrical micelles and polymersomes, respectively (Figure 1.26B-D). The insets in Figure 1.26B-D are fluorescence microscope image showing all the nanoparticles exhibit strong green fluorescence. Note that only classical TEM with sample dried on copper grid was used to characterize the nanostructures. However, the membrane structure of the polymersomes was effectively revealed here. This can be explained probably as follows: the aromatic TPE groups are attached to the rigid polynorbornene backbone with very short spacer and the hydrophobic blocks may be stacked tightly, consequently the polymersomes are tough enough to resist the crack during sample drying and the membrane has high electron density leading to high contrast in TEM image.

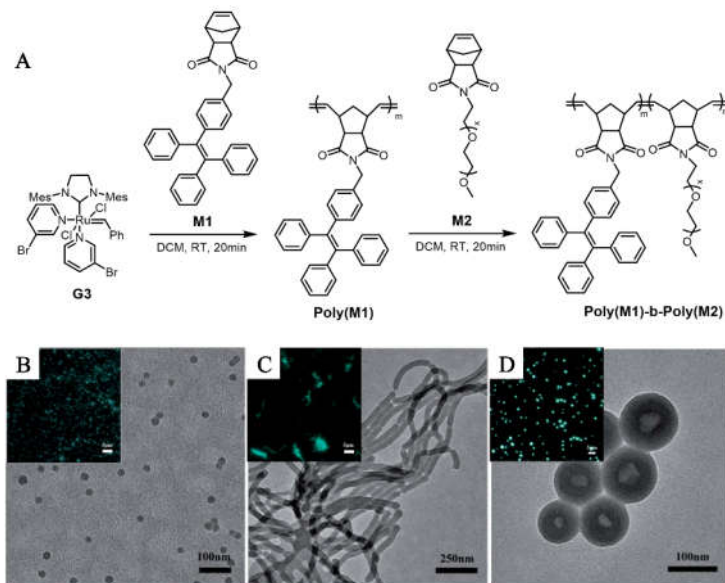


**Figure 1.26.** (A) Synthetic route to poly(M1)-*b*-poly(M2). (B-D) TEM image of nanoparticles formed by poly(M1)<sub>50</sub>-*b*-poly(M2)<sub>10</sub> (B), poly(M1)<sub>100</sub>-*b*-poly(M2)<sub>10</sub> (C) and poly(M1)<sub>300</sub>-*b*-poly(M2)<sub>10</sub> (D). Inserted pictures in (B-D) are fluorescence microscope images of nanoparticles.

### ***RAFT polymerization***

RAFT polymerization is a very popular technique to construct AIE amphiphilic block copolymers with backbone such as polymethacrylate and polystyrene. Recently, our group has prepared AIE block copolymethacrylates PEG-*b*-P(DEAEMA-*co*-TPEMA) containing TPE as the side groups by RAFT polymerization.<sup>210</sup> TPE functionalized methacrylate TPEMA and 2-(diethylamino)ethyl methacrylate (DEAEMA) were first synthesized and then polymerized using a macro-chain transfer agent (macro-CTA), mPEG<sub>45</sub>-CTA (M<sub>n</sub> = 2000 Da), and a traditional initiator, 2,2'-azobis(isobutyronitrile) (Figure 1.27A). The hydrophobic block P(DEAEMA-*co*-TPEMA) was a copolymer made of TPEMA and DEAEMA with unspecified sequence arrangement. The role of DEAEMA is to introduce CO<sub>2</sub> responsive property in the polymer. Four block copolymers with different hydrophilic/hydrophobic ratios, namely PEG<sub>45</sub>-*b*-P(DEAEMA<sub>7</sub>-*co*-TPEMA<sub>6</sub>) ( $f_{\text{PEG}} = 30\%$ ), PEG<sub>45</sub>-*b*-P(DEAEMA<sub>13</sub>-*co*-TPEMA<sub>6</sub>) ( $f_{\text{PEG}} = 26\%$ ), PEG<sub>45</sub>-*b*-P(DEAEMA<sub>18</sub>-*co*-TPEMA<sub>6</sub>) ( $f_{\text{PEG}} = 23\%$ ) and PEG<sub>45</sub>-*b*-P(DEAEMA<sub>36</sub>-*co*-TPEMA<sub>6</sub>) ( $f_{\text{PEG}} = 17\%$ ) were synthesized, and self-assembled in water by the nanoprecipitation method using THF as co-solvent. All four copolymers PEG-*b*-



P(DEAEMA-*co*-TPEMA) form AIE polymersomes (Figure 1.27B-E), and their quantum yields are measured as 6%.

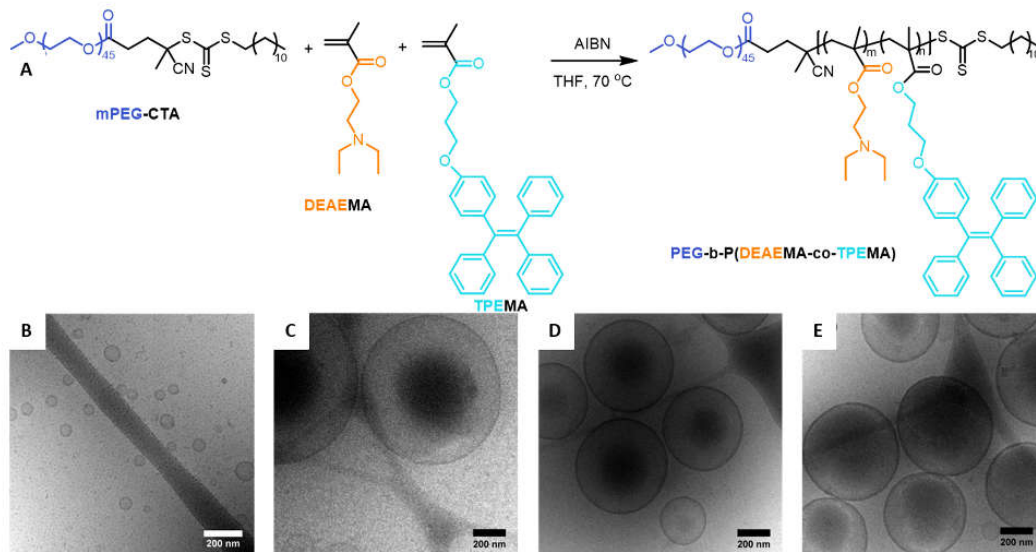


**Figure 1.27.** (A) Synthesis of CO<sub>2</sub>-responsive AIE amphiphilic block copolymer PEG-*b*-P(DEAEMA-*co*-TPEMA) by RAFT polymerization. (B-E) Cryo-EM images of the polymersomes formed by PEG<sub>45</sub>-*b*-(PDEAEMA<sub>7</sub>-*co*-PTPEMA<sub>6</sub>) (B), PEG<sub>45</sub>-*b*-(PDEAEMA<sub>13</sub>-*co*-PTPEMA<sub>6</sub>) (C), PEG<sub>45</sub>-*b*-(PDEAEMA<sub>18</sub>-*co*-PTPEMA<sub>6</sub>) (D) and PEG<sub>45</sub>-*b*-(PDEAEMA<sub>36</sub>-*co*-PTPEMA<sub>6</sub>) (E) in THF/water system.

PDEAEMA in the hydrophobic block P(DEAEMA-*co*-TPEMA) endows the polymersomes with CO<sub>2</sub>-responsive property (Figure 1.28a). Taking PEG<sub>45</sub>-*b*-P(DEAEMA<sub>36</sub>-*co*-TPEMA<sub>6</sub>) as an example, the CO<sub>2</sub>-activated reversible polymersomes–micelles transition is observed: polymersomes are transformed to small spherical micelles upon CO<sub>2</sub> bubbling (Figure 1.28c). Upon subsequent argon (Ar) bubbling, the micelles return to vesicular structures coexisting with a few intermediate morphologies (Figure 1.28d-e). Briefly, bubbling CO<sub>2</sub> into the polymersomes aqueous dispersion induces the protonation of the amine groups in DEAEMA block (Figure 1.28a). Consequently, hydrophobic DEAEMA<sub>36</sub> block changes to the hydrophilic one, resulting the decrease of the interfacial tension. Therefore, the pathway of unimer exchange between the aggregates will “turn on” and the frozen polymersomes tend to re-organize dynamically. As the core-forming block becomes smaller and the hydrophilic volume becomes bigger, the protonated polymer with higher interfacial curvature



preferentially forms micelles according to the classic packing parameter model. Upon the subsequent Ar bubbling, an inverse hydrophilic–hydrophobic transition of protonated DEAEMA<sub>36</sub> takes place and the core-forming block goes back to its original state comprising the blocks of TPMA<sub>6</sub> and DEAEMA<sub>36</sub>. As a result, the amphiphilic block copolymer with original hydrophilic/hydrophobic balance preferentially forms polymersomes. Both polymersomes and micelles show AIE fluorescence under illumination of UV light ( $\lambda = 365$  nm), while the transmittances detected at the wavelength of 620 nm are substantially different as shown in Figure 1.28f.

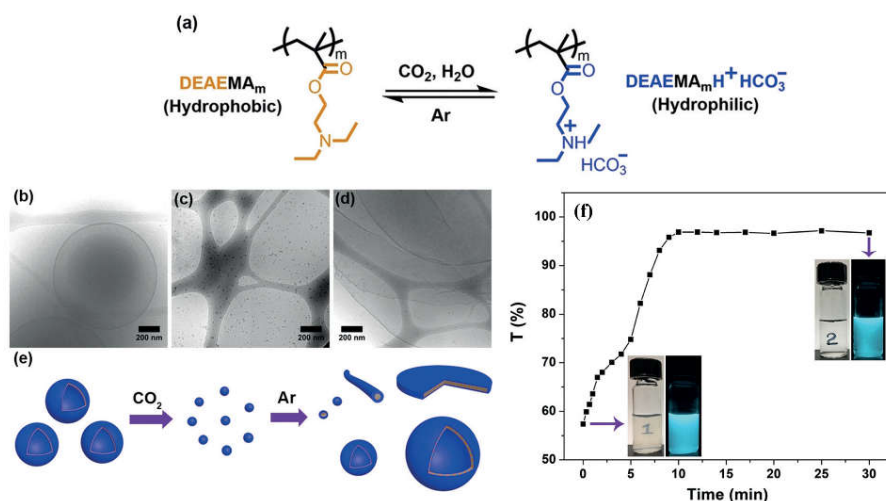


**Figure 1.28.** (a) Reversible protonation and deprotonation processes of DEAEMA block with CO<sub>2</sub> and Ar treatment in aqueous solution. (b–d) Cryo-EM images of PEG<sub>45</sub>-*b*-P(DEAEMA<sub>36</sub>-*co*-TPMA<sub>6</sub>) polymersomes dispersion without any treatment (b), treated by bubbling CO<sub>2</sub> for 20 min (c) and then treated by Ar bubbling for 40 min (d). (e) Illustration of the transformation from polymersomes to micelles after CO<sub>2</sub> treatment, and of the return to polymersomes along with a few of intermediate morphologies after Ar treatment. (f) The variation of transmittance of PEG<sub>45</sub>-*b*-P(DEAEMA<sub>36</sub>-*co*-TPMA<sub>6</sub>) self-assembly solution (1 mg/mL) during bubbling CO<sub>2</sub> to the solution. The transmittance was detected at the wavelength of 620 nm. The photographs taken under natural light show the solution changes from turbid to transparent. Their pictures under UV light ( $\lambda = 365$  nm) show fluorescence in both cases.

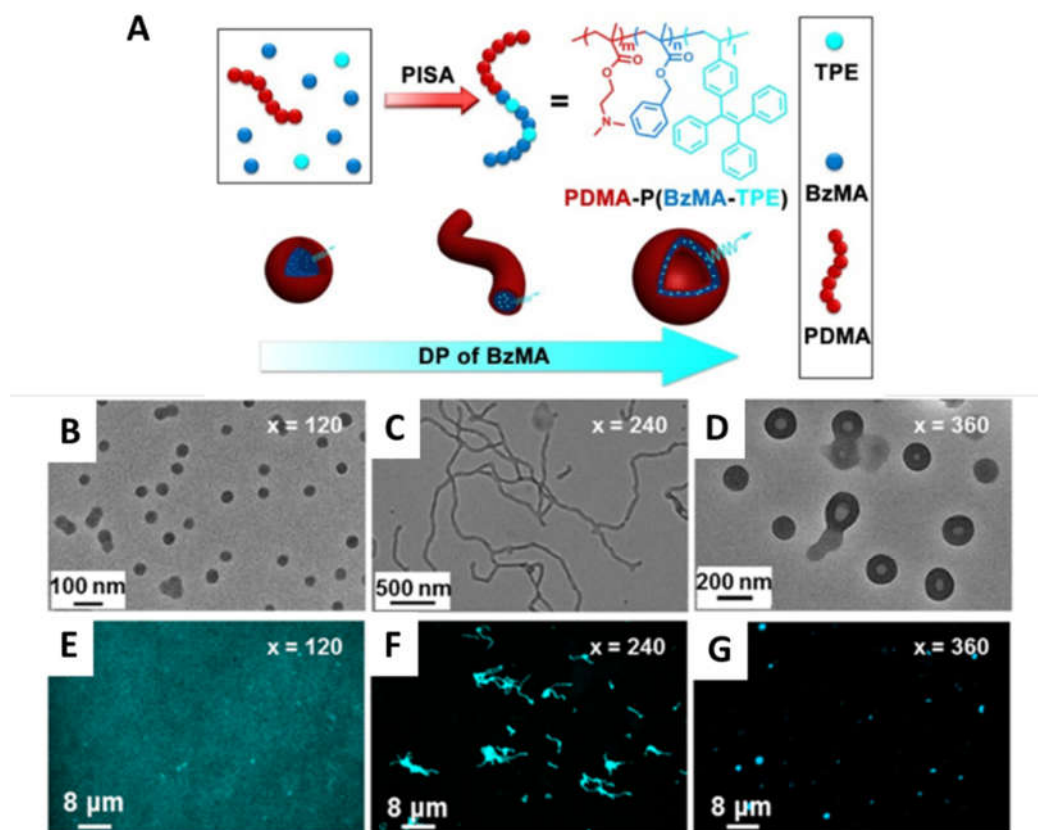


**Figure 1.29.** (a) Schematic representation of the preparation of AIE-nanostructures by PISA. TEM (B-D) and CLSM (E-G) images for PDMA<sub>39</sub>-*b*-P(BzMA-TPE)-*x* assemblies (*x* = 120, 240, 360).<sup>213</sup>

RAFT-PISA technique that combine the polymerization and the self-assembly in one pot also used to prepare AIE polymersomes. Yuan *et al.* have obtained AIE spherical micelles, cylindrical micelles and polymersomes of PDMA-*b*-P(BzMA-TPE) (poly(*N,N*-dimethylaminoethyl methacrylate)-*b*-poly(benzylmethacrylate-*co*-1-ethenyl-4-(1,2,2-triphenylethenyl)benzene) *via* PISA by RAFT polymerization using ethanol as the solvent (Figure 1.29A).<sup>213</sup> The PDMA is the solvent-soluble part synthesized by RAFT beforehand, and acts as the macro-CTA. P(BzMA-TPE) is the solvent-insoluble polymer obtained by dispersed RAFT polymerization of a mixture of benzylmethacrylate and 1-ethenyl-4-(1,2,2-triphenylethenyl)benzene (a styrene-type TPE monomer). Typically, with PDMA<sub>39</sub> as the macro-CTA, the mole ratio of TPE/PDMA<sub>39</sub> was fixed at 20, while the mole ratio of BzMA/PDMA<sub>39</sub> was varied from 120, 240, 360. All the experiments were performed at 14.5% solid content. With the increase of the feed ratios of BzMA/PDMA<sub>39</sub>, spherical micelles,

worm-like micelles, polymersomes were formed *in-situ* as the final morphologies in ethanol (Figure 1.29B-D). The hydrophilic ratio  $f_{\text{PDMA}}$  of the final PDMA<sub>39</sub>-*b*-P(BzMA-TPE)-*x* ( $x = 120, 240, 360$ ) are 21%, 16% and 10%, respectively. All nanoparticles show strong AIE fluorescence with emission peak around 480 nm (Figure 1.29E-F). The fluorescent quantum yield increases in the order of polymersomes > wormlike micelles > spherical micelles, and for polymersomes the quantum yield increases with the increase of the membrane thickness. High quantum yields of 25-35% are measured for AIE polymersomes.

## 1.6 Conclusion

The emergence of AIE concept has significantly stimulated the development of luminescent self-assembled materials, which offer a straightforward solution to ACQ problem. It is interesting to combine the AIE luminogens with polymersomes and inverse morphologies to prepare highly efficient luminescent materials for potential bio-related application, such as real-time imaging of therapeutic substances delivery, diagnostic and theranostics.

Our group is one of the first groups who have reported AIE polymersomes. However, the number of research reports on AIE polymersomes is still limited. On the other hand, there is no published research on AIE polymer cubosomes and hexosomes.

This PhD thesis aims to synthesize new AIE amphiphilic block copolymers, and to prepare novel AIE self-assembled materials, especially AIE polymer cubosomes and hexosomes, and stimuli responsive AIE polymersomes. The research works could be divided into three chapters. In each chapter, I will describe the synthesis of the amphiphilic block copolymer and their characterizations firstly. Then I studied their self-assembly behavior. After self-assembling, I will use the various characterization techniques, such as cryo-EM, SEM and TEM (characterized by myself), to study the self-assembled morphologies.

My first work (Chapter 2 of this dissertation) is focused on the preparation of photo-responsive AIE polymersomes and nano-porous polymersomes from TPE-containing amphiphilic stereoisomer prepared by post-modification of PEG. The Chapter 3 is dedicated to reductive-responsive polymersomes with hexagonally packed nano-pores on their membrane. In Chapter 4, we describe the first examples of AIE polymer cubosomes and hexosomes constructed from a series of AIE amphiphilic block copolymers synthesized by RAFT polymerization.

---

**References**

- 1 Bates, F. S. *et al.* Multiblock polymers: panacea or Pandora's box? *Science* **336**, 434-440 (2012).
- 2 Hadjichristidis, N., Pitsikalis, M. & Iatrou, H. in *Block Copolymers I* 1-124 (Springer, 2005).
- 3 Feng, H., Lu, X., Wang, W., Kang, N.-G. & Mays, J. W. Block copolymers: Synthesis, self-assembly, and applications. *Polymers* **9**, 494 (2017).
- 4 Matyjaszewski, K. & Xia, J. Atom transfer radical polymerization. *Chem. Rev.* **101**, 2921-2990 (2001).
- 5 Lowe, A. B. & McCormick, C. L. Reversible addition-fragmentation chain transfer (RAFT) radical polymerization and the synthesis of water-soluble (co)polymers under homogeneous conditions in organic and aqueous media. *Prog. Polym. Sci.* **32**, 283-351 (2007).
- 6 Keddie, D. J. A guide to the synthesis of block copolymers using reversible-addition fragmentation chain transfer (RAFT) polymerization. *Chem. Soc. Rev.* **43**, 496-505 (2014).
- 7 Hawker, C. J., Bosman, A. W. & Harth, E. New polymer synthesis by nitroxide mediated living radical polymerizations. *Chem. Rev.* **101**, 3661-3688 (2001).
- 8 Matyjaszewski, K. *Controlled/Living Radical Polymerization: Progress in RAFT, DT, NMP & OMRP*. Vol. 1024 (American Chemical Society, 2009).
- 9 Bielawski, C. W. & Grubbs, R. H. Living ring-opening metathesis polymerization. *Prog. Polym. Sci.* **32**, 1-29 (2007).
- 10 Mura, S., Nicolas, J. & Couvreur, P. Stimuli-responsive nanocarriers for drug delivery. *Nat. Mater.* **12**, 991-1003 (2013).
- 11 Kamaly, N., Xiao, Z., Valencia, P. M., Radovic-Moreno, A. F. & Farokhzad, O. C. Targeted polymeric therapeutic nanoparticles: design, development and clinical translation. *Chem. Soc. Rev.* **41**, 2971-3010 (2012).
- 12 Jokerst, J. V., Lobovkina, T., Zare, R. N. & Gambhir, S. S. Nanoparticle PEGylation for imaging and therapy. *Nanomedicine* **6**, 715-728 (2011).
- 13 Ge, Z. & Liu, S. Functional block copolymer assemblies responsive to tumor and intracellular microenvironments for site-specific drug delivery and enhanced imaging performance. *Chem. Soc. Rev.* **42**, 7289-7325 (2013).
- 14 Karimi, M. *et al.* Smart micro/nanoparticles in stimulus-responsive drug/gene delivery systems. *Chem. Soc. Rev.* **45**, 1457-1501 (2016).
- 15 Kwak, J. *et al.* Fabrication of Sub-3 nm Feature Size Based on Block Copolymer Self-Assembly for Next-Generation Nanolithography. *Macromolecules* **50**, 6813-6818 (2017).
- 16 Bang, B. M., Kim, H., Lee, J.-P., Cho, J. & Park, S. Mass production of uniform-sized nanoporous silicon nanowire anodes via block copolymer lithography. *Energy Environ. Sci.* **4**, 3395 (2011).
- 17 Acikbas, Y. *et al.* An Optical Vapor Sensor Based on Amphiphilic Block Copolymer Langmuir-Blodgett Films. *IEEE Sens. J.* **18**, 5313-5320 (2018).

- 18 Beattie, D. *et al.* Honeycomb-structured porous films from polypyrrole-containing block copolymers prepared via RAFT polymerization as a scaffold for cell growth. *Biomater. Sci.* **7**, 1072-1082 (2006).
- 19 Yabu, H., Tanaka, M., Ijio, K. & Shimomura, M. Preparation of Honeycomb-Patterned Polyimide Films by Self-Organization. *Langmuir* **19**, 6297-6300 (2003).
- 20 Hernández-Guerrero, M. & Stenzel, M. H. Honeycomb structured polymer films via breath figures. *Polym. Chem.* **3**, 563-577 (2012).
- 21 Zhang, A., Bai, H. & Li, L. Breath Figure: A Nature-Inspired Preparation Method for Ordered Porous Films. *Chem. Rev.* **115**, 9801-9868 (2015).
- 22 Yang, S. Y. *et al.* Single-file diffusion of protein drugs through cylindrical nanochannels. *ACS Nano* **4**, 3817-3822 (2010).
- 23 Qiu, X. *et al.* Selective separation of similarly sized proteins with tunable nanoporous block copolymer membranes. *ACS Nano* **7**, 768-776 (2013).
- 24 Yang, S. Y. *et al.* Nanoporous Membranes with Ultrahigh Selectivity and Flux for the Filtration of Viruses. *Adv. Mater.* **18**, 709-712 (2006).
- 25 Greil, S., Rahman, A., Liu, M. & Black, C. T. Gas Transport Selectivity of Ultrathin, Nanoporous, Inorganic Membranes Made from Block Copolymer Templates. *Chem.Mater.* **29**, 9572-9578 (2017).
- 26 Cooney, D. T., Hillmyer, M. A., Cussler, E. L. & Moggridge, G. D. Diffusion in nanoporous materials made from block copolymers. *Crystallogr. Rev.* **12**, 13-24 (2006).
- 27 Antonietti, M. & Förster, S. Vesicles and Liposomes: A Self-Assembly Principle Beyond Lipids. *Adv. Mater.* **15**, 1323-1333 (2003).
- 28 Blanz, A., Armes, S. P. & Ryan, A. J. Self-assembled block copolymer aggregates: From micelles to vesicles and their biological applications. *Macromol Rapid Commun* **30**, 267-277 (2009).
- 29 Gröschel, A. H. & Walther, A. Block copolymer micelles with inverted morphologies. *Angew. Chem. Int. Ed.* **56**, 10992-10994 (2017).
- 30 Denkova, A. G., Mendes, E. & Coppens, M.-O. Non-equilibrium dynamics of block copolymer micelles in solution: recent insights and open questions. *Soft Matter* **6**, 2351-2357 (2010).
- 31 Jain, S. & Bates, F. S. Consequences of nonergodicity in aqueous binary PEO– PB micellar dispersions. *Macromolecules* **37**, 1511-1523 (2004).
- 32 Shen, H. & Eisenberg, A. Block length dependence of morphological phase diagrams of the ternary system of PS-*b*-PAA/dioxane/H<sub>2</sub>O. *Macromolecules* **33**, 2561-2572 (2000).
- 33 Jia, L. *et al.* Smectic polymer micellar aggregates with temperature-controlled morphologies. *Soft Matter* **7**, 7395-7403 (2011).
- 34 McKenzie, B. E. *et al.* Bicontinuous nanospheres from simple amorphous amphiphilic diblock copolymers. *Macromolecules* **46**, 9845-9848 (2013).
- 35 Rizis, G., van de Ven, T. G. & Eisenberg, A. “Raft” Formation by Two-Dimensional Self-Assembly of Block Copolymer Rod Micelles in Aqueous Solution. *Angew. Chem. Int. Ed.* **126**, 9146-9149 (2014).

- 
- 36 Ku, K. H. *et al.* Particles with tunable porosity and morphology by controlling interfacial instability in block copolymer emulsions. *ACS nano* **10**, 5243-5251 (2016).
- 37 Wang, X. *et al.* Dual-Phase Separation in a Semiconfined System: Monodispersed Heterogeneous Block-Copolymer Membranes for Cell Encoding and Patterning. *Adv. Mater.* **29**, 1605932 (2017).
- 38 Battaglia, G. & Ryan, A. J. Pathways of polymeric vesicle formation. *J. Phys.* **110**, 10272-10279 (2006).
- 39 Cui, H., Chen, Z., Zhong, S., Wooley, K. L. & Pochan, D. J. Block copolymer assembly via kinetic control. *Science* **317**, 647-650 (2007).
- 40 Mai, Y. & Eisenberg, A. Self-assembly of block copolymers. *Chem. Soc. Rev.* **41**, 5969-5985 (2012).
- 41 Gao, Z., Varshney, S. K., Wong, S. & Eisenberg, A. Block copolymer "crew-cut" micelles in water. *Macromolecules* **27**, 7923-7927 (1994).
- 42 Zhang, L. & Eisenberg, A. Multiple morphologies and characteristics of "crew-cut" micelle-like aggregates of polystyrene-*b*-poly (acrylic acid) diblock copolymers in aqueous solutions. *J. Am. Chem. Soc.* **118**, 3168-3181 (1996).
- 43 Cui, H., Chen, Z., Wooley, K. L. & Pochan, D. J. Origins of toroidal micelle formation through charged triblock copolymer self-assembly. *Soft Matter* **5**, 1269-1278 (2009).
- 44 Rizis, G., van de Ven, T. G. M. & Eisenberg, A. "Raft" Formation by Two-Dimensional Self-Assembly of Block Copolymer Rod Micelles in Aqueous Solution. *Angew. Chem. Int. Ed.* **53**, 9000-9003 (2014).
- 45 Discher, D. & Eisenberg, A. Polymer vesicles. *Science* **297**, 967 (2002).
- 46 Xu, B. *et al.* Self-assembly of liquid crystal block copolymer PEG-*b*-smectic polymer in pure state and in dilute aqueous solution. *Faraday Discuss.* **143**, 235-250 (2009).
- 47 Jain, S. & Bates, F. S. On the Origins of Morphological Complexity in Block Copolymer Surfactants. *Science* **300**, 460-464 (2003).
- 48 Zhang, L. & Eisenberg, A. Multiple morphologies of "crew-cut" aggregates of polystyrene-*b*-poly (acrylic acid) block copolymers. *Science* **268**, 1728-1731 (1995).
- 49 Wang, L.-H. *et al.* Biodegradable large compound vesicles with controlled size prepared via the self-assembly of branched polymers in nanodroplet templates. *Chem. Commun.* **50**, 9676-9678 (2014).
- 50 Yu, K. & Eisenberg, A. Bilayer morphologies of self-assembled crew-cut aggregates of amphiphilic PS-*b*-PEO diblock copolymers in solution. *Macromolecules* **31**, 3509-3518 (1998).
- 51 Yu, K., Zhang, L. & Eisenberg, A. Novel morphologies of "crew-cut" aggregates of amphiphilic diblock copolymers in dilute solution. *Langmuir* **12**, 5980-5984 (1996).
- 52 Allen, S. D., Bobbala, S., Karabin, N. B. & Scott, E. A. On the advancement of polymeric bicontinuous nanospheres toward biomedical applications. *Nanoscale Horiz.* **4**, 258-272 (2019).
- 53 Cameron, N. S., Corbierre, M. K. & Eisenberg, A. 1998 EWR Steacie Award Lecture Asymmetric amphiphilic block copolymers in solution: a morphological wonderland. *Can. J. Chem.* **77**, 1311-1326 (1999).

- 54 Van Hest, J., Delnoye, D., Baars, M., Van Genderen, M. & Meijer, E. Polystyrene-dendrimer amphiphilic block copolymers with a generation-dependent aggregation. *Science* **268**, 1592-1595 (1995).
- 55 Bleul, R., Thiermann, R. & Maskos, M. Techniques to control polymersome size. *Macromolecules* **48**, 7396-7409 (2015).
- 56 Deng, Y., Ling, J. & Li, M.-H. Physical stimuli-responsive liposomes and polymersomes as drug delivery vehicles based on phase transitions in the membrane. *Nanoscale* **10**, 6781-6800 (2018).
- 57 Hocine, S. & Li, M.-H. Thermoresponsive self-assembled polymer colloids in water. *Soft Matter* **9**, 5839-5861 (2013).
- 58 Meng, F., Zhong, Z. & Feijen, J. Stimuli-responsive polymersomes for programmed drug delivery. *Biomater. Sci.* **10**, 197-209 (2009).
- 59 Hu, X. *et al.* Stimuli-responsive polymersomes for biomedical applications. *Biomater. Sci.* **18**, 649-673 (2017).
- 60 Onaca, O., Enea, R., Hughes, D. W. & Meier, W. Stimuli-responsive polymersomes as nanocarriers for drug and gene delivery. *Macromol. Biosci.* **9**, 129-139 (2009).
- 61 Li, M.-H. & Keller, P. Stimuli-responsive polymer vesicles. *Soft Matter* **5**, 927-937 (2009).
- 62 Lin, J. J., Ghoroghchian, P. P., Zhang, Y. & Hammer, D. A. Adhesion of Antibody-Functionalized Polymersomes. *Langmuir* **22**, 3975-3979 (2006).
- 63 Pang, Z. *et al.* Preparation and brain delivery property of biodegradable polymersomes conjugated with OX26. *J. Control. Release* **128**, 120-127 (2008).
- 64 Zhang, Y. *et al.* Targeted delivery of Tet1 peptide functionalized polymersomes to the rat cochlear nerve. *Int. J. Nanomedicine* **7**, 1015 (2012).
- 65 Petersen, M. A., Yin, L., Kokkoli, E. & Hillmyer, M. A. Synthesis and characterization of reactive PEO-PMCL polymersomes. *Polym. Chem.* **1**, 1281-1290 (2010).
- 66 Kim, B.-S., Hong, D.-J., Bae, J. & Lee, M. Controlled self-assembly of carbohydrate conjugate rod-coil amphiphiles for supramolecular multivalent ligands. *J. Am. Chem. Soc.* **127**, 16333-16337 (2005).
- 67 You, L. & Schlaad, H. An easy way to sugar-containing polymer vesicles or glycosomes. *J. Am. Chem. Soc.* **128**, 13336-13337 (2006).
- 68 Thambi, T., Park, J. H. & Lee, D. S. Stimuli-responsive polymersomes for cancer therapy. *Biomater. Sci.* **4**, 55-69 (2016).
- 69 Rifaie-Graham, O., Apebende, E. A. & Bruns, N. Bio-inspired polymersome nanoreactors. *CHIMIA* **73**, 21-24 (2019).
- 70 Won, Y. Y., Davis, H. T. & Bates, F. S. Giant wormlike rubber micelles. *Science* **283**, 960-963 (1999).
- 71 Jain, S. & Bates, F. S. On the origins of morphological complexity in block copolymer surfactants. *Science* **300**, 460-464 (2003).
- 72 Bhargava, P. *et al.* Self-assembled polystyrene-block-poly(ethylene oxide) micelle morphologies in solution. *Macromolecules* **39**, 4880-4888 (2006).

- 
- 73 Cameron, N. S., Corbierre, M. K. & Eisenberg, A. 1998 E.W.R. Steacie Award Lecture asymmetric amphiphilic block copolymers in solution: a morphological wonderland. *Can. J. Chem.* **77**, 1311-1326 (1999).
- 74 Pinol, R. *et al.* Self-assembly of PEG-b-Liquid crystal polymer: The role of smectic order in the formation of nanofibers. *Macromolecules* **40**, 5625-5627 (2007).
- 75 Jia, L. *et al.* Smectic polymer vesicles. *Soft Matter* **5**, 3446-3451 (2009).
- 76 Jenekhe, S. & Chen, X. Self-assembled aggregates of rod-coil block copolymers and their solubilization and encapsulation of fullerenes. *Science* **279**, 1903 (1998).
- 77 Kukula, H., Schlaad, H., Antonietti, M. & Förster, S. The formation of polymer vesicles or "peptosomes" by polybutadiene-block-poly(L-glutamate)s in dilute aqueous solution. *J. Am. Chem. Soc.* **124**, 1658-1663 (2002).
- 78 Bellomo, E., Wyrsta, M., Pakstis, L., Pochan, D. & Deming, T. Stimuli-responsive polypeptide vesicles by conformation-specific assembly. *Nat. Mater.* **3**, 244-248 (2004).
- 79 Jiang, H. Z., Guler, M. O. & Stupp, S. I. The internal structure of self-assembled peptide amphiphiles nanofibers. *Soft Matter* **3**, 454-462 (2007).
- 80 Burkoth, T. S. *et al.* Structure of the  $\beta$ -Amyloid(10-35) Fibril. *J. Am. Chem. Soc.* **122**, 7883-7889 (2000).
- 81 Massey, J. A. *et al.* Self-Assembly of Organometallic Block Copolymers: The Role of Crystallinity of the Core-Forming Polyferrocene Block in the Micellar Morphologies Formed by Poly(ferrocenylsilane-b-dimethylsiloxane) in n-Alkane Solvents. *J. Am. Chem. Soc.* **122**, 11577-11584 (2000).
- 82 Shen, H. & Eisenberg, A. Morphological Phase Diagram for a Ternary System of Block Copolymer PS310-b-PAA52/Dioxane/H<sub>2</sub>O. *J. Phys.* **103**, 9473-9487 (1999).
- 83 Blanzas, A., Madsen, J., Battaglia, G., Ryan, A. J. & Armes, S. P. Mechanistic Insights for Block Copolymer Morphologies: How Do Worms Form Vesicles? *J. Am. Chem. Soc.* **133**, 16581-16587 (2011).
- 84 Lee, J. C. *et al.* Preparation, stability, and in vitro performance of vesicles made with diblock copolymers. *Biotechnol. Bioeng.* **73**, 135-145 (2001).
- 85 Kukula, H., Schlaad, H., Antonietti, M. & Förster, S. The Formation of Polymer Vesicles or "Peptosomes" by Polybutadiene-block-poly(l-glutamate)s in Dilute Aqueous Solution. *J. Am. Chem. Soc.* **124**, 1658-1663 (2002).
- 86 Dionzou, M. *et al.* Comparison of methods for the fabrication and the characterization of polymer self-assemblies: what are the important parameters? *Soft Matter* **12**, 2166-2176 (2016).
- 87 Kita-Tokarczyk, K., Grumelard, J., Haefele, T. & Meier, W. Block copolymer vesicles—using concepts from polymer chemistry to mimic biomembranes. *Polymer* **46**, 3540-3563 (2005).
- 88 Discher, B. M. Polymersomes: Tough Vesicles Made from Diblock Copolymers. *Science* **284**, 1143-1146 (1999).



- 89 Dao, T. P. T. *et al.* Membrane properties of giant polymer and lipid vesicles obtained by electroformation and pva gel-assisted hydration methods. *Colloids. Surf.* **533**, 347-353 (2017).
- 90 Greene, A. C., Sasaki, D. Y. & Bachand, G. D. Forming Giant-sized Polymersomes Using Gel-assisted Rehydration. *J. Vis. Exp.*, e54051 (2016).
- 91 Weinberger, A. *et al.* Gel-assisted formation of giant unilamellar vesicles. *Biophys. J.* **105**, 154-164 (2013).
- 92 Zhang, L. & Eisenberg, A. Multiple Morphologies of "Crew-Cut" Aggregates of Polystyrene-*b*-poly(acrylic acid) Block Copolymers. *Science* **268**, 1728-1731 (1995).
- 93 Jia, L., Albouy, P. A., Di Cicco, A., Cao, A. & Li, M. H. Self-assembly of amphiphilic liquid crystal block copolymers containing a cholesteryl mesogen: Effects of block ratio and solvent. *Polymer* **52**, 2565-2575 (2011).
- 94 Zhou, W., Meng, F., Engbers, G. H. M. & Feijen, J. Biodegradable polymersomes for targeted ultrasound imaging. *J. Control. Release* **116**, e62-e64 (2006).
- 95 Meng, F., Engbers, G. H. M. & Feijen, J. Biodegradable polymersomes as a basis for artificial cells: encapsulation, release and targeting. *J. Control. Release* **101**, 187-198 (2005).
- 96 Zhang, L. & Eisenberg, A. Multiple Morphologies of "Crew-Cut" Aggregates of Polystyrene-*b*-poly(acrylic acid) Block Copolymers. *Science* **268**, 1728-1731 (1995).
- 97 Zhou, S., Deng, X. & Yang, H. Biodegradable poly( $\epsilon$ -caprolactone)-poly(ethylene glycol) block copolymers: characterization and their use as drug carriers for a controlled delivery system. *Biomaterials* **24**, 3563-3570 (2003).
- 98 Kim, J. H. & Bae, Y. H. Albumin loaded microsphere of amphiphilic poly(ethylene glycol)/ poly(alpha-ester) multiblock copolymer. *Eur. J. Pharm. Sci.* **23**, 245-251 (2004).
- 99 Giri, T. K. *et al.* Prospects of pharmaceuticals and biopharmaceuticals loaded microparticles prepared by double emulsion technique for controlled delivery. *Saudi Pharm. J.* **21**, 125-141 (2013).
- 100 Mabrouk, E. *et al.* Formation and material properties of giant liquid crystal polymersomes. *Soft Matter* **5**, 1870 (2009).
- 101 Marguet, M., Sandre, O. & Lecommandoux, S. Polymersomes in "gelly" polymersomes: toward structural cell mimicry. *Langmuir* **28**, 2035-2043 (2012).
- 102 Marguet, M., Edembe, L. & Lecommandoux, S. Polymersomes in polymersomes: multiple loading and permeability control. *Angew. Chem. Int. Ed.* **51**, 1173-1176 (2012).
- 103 Shum, H. C., Kim, J. W. & Weitz, D. A. Microfluidic fabrication of monodisperse biocompatible and biodegradable polymersomes with controlled permeability. *J. Am. Chem. Soc.* **130**, 9543-9549 (2008).
- 104 Lorenceau, E. *et al.* Generation of polymersomes from double-emulsions. *Langmuir* **21**, 9183-9186 (2005).

- 
- 105 Rideau, E., Dimova, R., Schwille, P., Wurm, F. R. & Landfester, K. Liposomes and polymersomes: a comparative review towards cell mimicking. *Chem. Soc. Rev.* **47**, 8572-8610 (2018).
- 106 Dimova, R., Seifert, U., Pouligny, B., Förster, S. & Döbereiner, H. G. Hyperviscous diblock copolymer vesicles. *Eur. Phys. J. E* **7**, 241-250 (2002).
- 107 Robertson, J. D. *et al.* pH-sensitive tubular polymersomes: formation and applications in cellular delivery. *ACS nano* **8**, 4650-4661 (2014).
- 108 Battaglia, G., Tomas, S. & Ryan, A. J. Lamellarsomes: metastable polymeric multilamellar aggregates. *Soft Matter* **3**, 470-475 (2007).
- 109 Parnell, A. *et al.* The efficiency of encapsulation within surface rehydrated polymersomes. *Faraday Discuss.* **143**, 29-46 (2009).
- 110 Grumelard, J., Taubert, A. & Meier, W. Soft nanotubes from amphiphilic ABA triblock macromonomers. *Chem. Commun.*, 1462-1463 (2004).
- 111 Robertson, J. D. *et al.* Purification of nanoparticles by size and shape. *Sci. Rep.* **6**, 1-9 (2016).
- 112 Battaglia, G. & Ryan, A. J. Neuron-Like Tubular Membranes Made of Diblock Copolymer Amphiphiles. *Angew. Chem. Int. Ed.* **118**, 2106-2110 (2006).
- 113 Battaglia, G. & Ryan, A. J. Effect of amphiphile size on the transformation from a lyotropic gel to a vesicular dispersion. *Macromolecules* **39**, 798-805 (2006).
- 114 Battaglia, G. & Ryan, A. J. The evolution of vesicles from bulk lamellar gels. *Nat. Mater.* **4**, 869-876 (2005).
- 115 Photos, P. J., Bacakova, L., Discher, B., Bates, F. S. & Discher, D. E. Polymer vesicles in vivo: correlations with PEG molecular weight. *J. Control. Release* **90**, 323-334 (2003).
- 116 Ghoroghchian, P. P. *et al.* Bioresorbable vesicles formed through spontaneous self-assembly of amphiphilic poly(ethylene oxide)-block-polycaprolactone. *Macromolecules* **39**, 1673-1675 (2006).
- 117 Yu, Y., Zhang, L. & Eisenberg, A. Morphogenic Effect of Solvent on Crew-Cut Aggregates of Amphiphilic Diblock Copolymers. *Macromolecules* **31**, 1144-1154 (1998).
- 118 Zhang, W.-J., Hong, C.-Y. & Pan, C.-Y. Polymerization-Induced Self-Assembly of Functionalized Block Copolymer Nanoparticles and Their Application in Drug Delivery. *Macromol. Rapid Commun.* **40**, 1800279 (2019).
- 119 Adams, D. J., Adams, S., Atkins, D., Butler, M. F. & Furzeland, S. Impact of mechanism of formation on encapsulation in block copolymer vesicles. *J. Control. Release* **128**, 165-170 (2008).
- 120 Uneyama, T. Density functional simulation of spontaneous formation of vesicle in block copolymer solutions. *J. Chem. Phys.* **126**, 114902 (2007).
- 121 Zhou, L., Zhang, D., Hocine, S., Pilone, A., Trépout, S., Marco, S., Christophe, T., Guo, J., & Li, M. H. Transition from smectic nanofibers to smectic vesicles in the self-assemblies of PEG-*b*-liquid crystal polycarbonates. *Poly. Chem.* **8**, 4776-4780 (2017).

- 122 Adams, D. J., Adams, S., Atkins, D., Butler, M. F. & Furzeland, S. Impact of mechanism of formation on encapsulation in block copolymer vesicles. *J Control Release* **128**, 165-170 (2008).
- 123 He, X. & Schmid, F. Dynamics of spontaneous vesicle formation in dilute solutions of amphiphilic diblock copolymers. *Macromolecules* **39**, 2654-2662 (2006).
- 124 Meng, F., Hiemstra, C., Engbers, G. H. M. & Feijen, J. Biodegradable polymersomes. *Macromolecules* **36**, 3004-3006 (2003).
- 125 Ghoroghchian, P. P. *et al.* Near-infrared-emissive polymersomes: Self-assembled soft matter for in vivo optical imaging. *PNAS* **102**, 2922-2927 (2005).
- 126 Clarke, D. transmission scanning electron microscopy. *J. Mater. Sci.* **8**, 279-285 (1973).
- 127 Hocine, S. *et al.* Structural changes in liquid crystal polymer vesicles induced by temperature variation and magnetic fields. *Soft Matter* **7**, 2613-2623 (2011).
- 128 Yang, J. *et al.* Formation of polymer vesicles by liquid crystal amphiphilic block copolymers. *Langmuir* **22**, 7907-7911 (2006).
- 129 Yang, J., Lévy, D., Deng, W., Keller, P. & Li, M.-H. Polymer vesicles formed by amphiphilic diblock copolymers containing a thermotropic liquid crystalline polymer block. *Chem. Commun.*, 4345-4347 (2005).
- 130 Robinson, N. Molecular size and shape. *J. Pharm. Pharmacol.* **12**, 129-149 (1960).
- 131 Lee, J. S. *et al.* Circulation kinetics and biodistribution of dual-labeled polymersomes with modulated surface charge in tumor-bearing mice: Comparison with stealth liposomes. *J. Control. Release* **155**, 282-288 (2011).
- 132 Stauch, O., Schubert, R., Savin, G. & Burchard, W. Structure of artificial cytoskeleton containing liposomes in aqueous solution studied by static and dynamic light scattering. *Biomater. Sci.* **3**, 565-578 (2002).
- 133 Houga, C. *et al.* Micelles and polymersomes obtained by self-assembly of dextran and polystyrene based block copolymers. *Biomater. Sci.* **10**, 32-40 (2009).
- 134 Ferji, K. *et al.* Polymersomes from amphiphilic glycopolymers containing polymeric liquid crystal grafts. *ACS Macro Lett.* **4**, 1119-1122 (2015).
- 135 Zhang, L., Bartels, C., Yu, Y., Shen, H. & Eisenberg, A. Mesosized Crystal-like Structure of Hexagonally Packed Hollow Hoops by Solution Self-Assembly of Diblock Copolymers. *Phys. Rev. Lett.* **79**, 5034-5037 (1997).
- 136 Li, C. *et al.* Self-assembly of block copolymers towards mesoporous materials for energy storage and conversion systems. *Chem. Soc. Rev.* **49**, 4681-4736 (2020).
- 137 Barriga, H. M. G., Holme, M. N. & Stevens, M. M. Cubosomes: The Next Generation of Smart Lipid Nanoparticles? *Angew. Chem. Int. Ed.* **58**, 2958-2978 (2019).
- 138 Lin, Z. *et al.* Tunable Self-Assembly of Diblock Copolymers into Colloidal Particles with Triply Periodic Minimal Surfaces. *Angew. Chem. Int. Ed.* **129**, 7241-7246 (2017).
- 139 McKenzie, B. E., Nudelman, F., Bomans, P. H., Holder, S. J. & Sommerdijk, N. A. Temperature-responsive nanospheres with bicontinuous internal structures from a semicrystalline amphiphilic block copolymer. *J. Am. Chem. Soc.* **132**, 10256-10259 (2010).

- 
- 140 La, Y., An, T. H., Shin, T. J., Park, C. & Kim, K. T. A Morphological Transition of Inverse Mesophases of a Branched-Linear Block Copolymer Guided by Using Cosolvents. *Angewandte Chemie (International ed. in English)* **54**, 10483-10487 (2015).
- 141 He, H. *et al.* Cubosomes from hierarchical self-assembly of poly (ionic liquid) block copolymers. *Nat. Commun.* **8**, 1-8 (2017).
- 142 Chen, Y. *et al.* Perforated block copolymer vesicles with a highly folded membrane. *Macromolecules* **40**, 4389-4392 (2007).
- 143 McKenzie, B. E. *et al.* Bicontinuous Nanospheres from Simple Amorphous Amphiphilic Diblock Copolymers. *Macromolecules* **46**, 9845-9848 (2013).
- 144 Yu, H., Qiu, X., Nunes, S. P. & Peinemann, K.-V. Biomimetic block copolymer particles with gated nanopores and ultrahigh protein sorption capacity. *Nat. Commun.* **5**, 4110 (2014).
- 145 Zhang, W. J., Hong, C. Y. & Pan, C. Y. Formation of hexagonally packed hollow hoops and morphology transition in RAFT ethanol dispersion polymerization. *Macromol. Rapid Commun.* **36**, 1428-1436 (2015).
- 146 Ding, Z., Gao, C., Wang, S., Liu, H. & Zhang, W. Macro-RAFT agent mediated dispersion polymerization: the monomer concentration effect on the morphology of the in situ synthesized block copolymer nano-objects. *Polym. Chem.* **6**, 8003-8011 (2015).
- 147 Presa-Soto, D., Carriedo, G. A., de la Campa, R. & Presa Soto, A. Formation and Reversible Morphological Transition of Bicontinuous Nanospheres and Toroidal Micelles by the Self-Assembly of a Crystalline-b-Coil Diblock Copolymer. *Angew. Chem. Int. Ed.* **128**, 10256-10261 (2016).
- 148 Allen, S. D., Bobbala, S., Karabin, N. B., Modak, M. & Scott, E. A. Benchmarking Bicontinuous Nanospheres against Polymersomes for in Vivo Biodistribution and Dual Intracellular Delivery of Lipophilic and Water-Soluble Payloads. *ACS Appl. Mater.* **10**, 33857-33866 (2018).
- 149 Parry, A. L., Bomans, P. H., Holder, S. J., Sommerdijk, N. A. & Biagini, S. C. Cryo electron tomography reveals confined complex morphologies of tripeptide-containing amphiphilic double-comb diblock copolymers. *Angew. Chem. Int. Ed.* **120**, 8991-8994 (2008).
- 150 McKenzie, B. E. *et al.* Controlling internal pore sizes in bicontinuous polymeric nanospheres. *Angew. Chem. Int. Ed.* **127**, 2487-2491 (2015).
- 151 áde Visser, J. The evolution of bicontinuous polymeric nanospheres in aqueous solution. *Soft Matter* **12**, 4113-4122 (2016).
- 152 Monaghan, O., Bomans, P., Sommerdijk, N. A. & Holder, S. J. Controlling the melting transition of semi-crystalline self-assembled block copolymer aggregates: controlling release rates of ibuprofen. *Polym. Chem.* **8**, 5303-5316 (2017).
- 153 Kang, Y. *et al.* Use of complementary nucleobase-containing synthetic polymers to prepare complex self-assembled morphologies in water. *Polym. Chem.* **7**, 2836-2846 (2016).

- 154 Vanderkooy, A., Pfefferkorn, P. & Taylor, M. S. Self-assembly of polymer nanostructures through halogen bonding interactions of an iodoperfluoroarene-functionalized polystyrene derivative. *Macromolecules* **50**, 3807-3817 (2017).
- 155 Lyu, X. *et al.* Head-tail asymmetry as the determining factor in the formation of polymer cubosomes or hexosomes in a rod-coil amphiphilic block copolymer. *Angew. Chem. Int. Ed.* **57**, 10132-10136 (2018).
- 156 La, Y. *et al.* Colloidal inverse bicontinuous cubic membranes of block copolymers with tunable surface functional groups. *Nat. Chem.* **6**, 534-541 (2014).
- 157 Park, C. *et al.* Mesoporous monoliths of inverse bicontinuous cubic phases of block copolymer bilayers. *Nat. Commun.* **6**, 1-9 (2015).
- 158 An, T. H. *et al.* Solution self-assembly of block copolymers containing a branched hydrophilic block into inverse bicontinuous cubic mesophases. *ACS nano* **9**, 3084-3096 (2015).
- 159 Cho, A. *et al.* Mix-and-match assembly of block copolymer blends in solution. *Macromolecules* **50**, 3234-3243 (2017).
- 160 Jeong, M. G. & Kim, K. T. Covalent Stabilization of Inverse Bicontinuous Cubic Structures of Block Copolymer Bilayers by Photodimerization of Indene Pendant Groups of Polystyrene Hydrophobic Blocks. *Macromolecules* **50**, 223-234 (2017).
- 161 La, Y. *et al.* Templated synthesis of cubic crystalline single networks having large open-space lattices by polymer cubosomes. *Nat. Commun.* **9**, 1-9 (2018).
- 162 Lv, F., An, Z. & Wu, P. Scalable preparation of alternating block copolymer particles with inverse bicontinuous mesophases. *Nat. Commun.* **10**, 1397 (2019).
- 163 Park, C. *et al.* Mesoporous monoliths of inverse bicontinuous cubic phases of block copolymer bilayers. *Nat. Commun.* **6**, 6392 (2015).
- 164 Birks, J. B. *Photophysics of aromatic molecules*. (London, New York, Wiley-Interscience [1970], 1970).
- 165 Wang, J. *et al.* Alkyl and dendron substituted quinacridones: synthesis, structures, and luminescent properties. *J. Phys. Chem. B* **111**, 5082-5089 (2007).
- 166 Nguyen, B. T. *et al.* Enhancing the photoluminescence intensity of conjugated polycationic polymers by using quantum dots as antiaggregation reagents. *Langmuir* **22**, 4799-4803 (2006).
- 167 Chen, L., Xu, S., McBranch, D. & Whitten, D. Tuning the Properties of Conjugated Polyelectrolytes through Surfactant Complexation. *J. Am. Chem. Soc.* **122**, 9302-9303 (2000).
- 168 Hecht, S. & Frechet, J. M. Dendritic Encapsulation of Function: Applying Nature's Site Isolation Principle from Biomimetics to Materials Science. *Angew. Chem. Int. Ed.* **40**, 74-91 (2001).
- 169 Schmidt, G. C. Über Lumineszenz von festen Lösungen. *Annalen der Physik* **370**, 247-256 (1921).
- 170 Oelkrug, D. *et al.* Towards highly luminescent phenylene vinylene films. *Synth. Met.* **83**, 231-237 (1996).

- 
- 171 Würthner, F., Sens, R., Etzbach, K. H. & Seybold, G. Design, Synthesis, and Evaluation of a Dye Library: Glass-Forming and Solid-State Luminescent Merocyanines for Functional Materials. *Angew. Chem. Int. Ed.* **38**, 1649-1652 (1999).
- 172 Luo, J. *et al.* Aggregation-induced emission of 1-methyl-1, 2, 3, 4, 5-pentaphenylsilole. *Chem. Commun.*, 1740-1741 (2001).
- 173 Mei, J., Leung, N. L., Kwok, R. T., Lam, J. W. & Tang, B. Z. Aggregation-induced emission: together we shine, united we soar! *Chem. Rev.* **115**, 11718-11940 (2015).
- 174 Zhao, Z., Zhang, H., Lam, J. W. & Tang, B. Z. Aggregation-Induced Emission: New Vistas at the Aggregate Level. *Angew. Chem. Int. Ed.*
- 175 Kwok, R. T. K., Liu, B. & Tang, B. Z. 20 Years of Aggregation-Induced Emission Research. *Adv. Opt. Mater.* **8**, 2000855 (2020).
- 176 Cai, X. & Liu, B. Aggregation-Induced Emission: Recent Advances in Materials and Biomedical Applications. *Angew. Chem. Int. Ed.* **59**, 9868-9886 (2020).
- 177 Kenry, Tang, B. Z. & Liu, B. Catalyst: Aggregation-Induced Emission—How Far Have We Come, and Where Are We Going Next? *Chem* **6**, 1195-1198 (2020).
- 178 Mei, J., Leung, N. L., Kwok, R. T., Lam, J. W. & Tang, B. Z. Aggregation-Induced Emission: Together We Shine, United We Soar! *Chem. Rev.* **115**, 11718-11940 (2015).
- 179 Chen, J. *et al.* Synthesis, Light Emission, Nanoaggregation, and Restricted Intramolecular Rotation of 1,1-Substituted 2,3,4,5-Tetraphenylsiloles. *Chem. Mater.* **15**, 1535-1546 (2003).
- 180 Leung, N. L. *et al.* Restriction of intramolecular motions: the general mechanism behind aggregation-induced emission. *Chemistry* **20**, 15349-15353 (2014).
- 181 Liu, J., Lam, J. W. Y. & Tang, B. Z. Aggregation-induced Emission of Silole Molecules and Polymers: Fundamental and Applications. *J. Inorg. Organomet. Polym.* **19**, 249-285 (2009).
- 182 Hong, Y., Lam, J. W. & Tang, B. Z. Aggregation-induced emission. *Chem. Soc. Rev.* **40**, 5361-5388 (2011).
- 183 Mei, J. *et al.* Aggregation-Induced Emission: The Whole Is More Brilliant than the Parts. *Adv. Mater.* **26**, 5429-5479 (2014).
- 184 Oster, G. & Nishijima, Y. Fluorescence and internal rotation: Their dependence on viscosity of the medium. *J. Am. Chem. Soc.* **78**, 1581-1584 (1956).
- 185 Th, F. & Hoffmann, G. Die Viskositätsabhängigkeit der Fluoreszenzquantenausbeuten einiger Farbstoffsysteme. *Zeitschrift für Physikalische Chemie* **75**, 63-76 (1971).
- 186 Shultz, D. A. & Fox, M. A. Effect of phenyl ring torsional rigidity on the photophysical behavior of tetraphenylethylenes. *J. Am. Chem. Soc.* **111**, 6311-6320 (1989).
- 187 Xia, W.-S., Schmehl, R. H. & Li, C.-J. A highly selective fluorescent chemosensor for K<sup>+</sup> from a bis-15-crown-5 derivative. *J. Am. Chem. Soc.* **121**, 5599-5600 (1999).
- 188 Hong, Y., Lam, J. W. & Tang, B. Z. Aggregation-induced emission: phenomenon, mechanism and applications. *Chem. Commun.*, 4332-4353 (2009).
- 189 Fan, X. *et al.* Photoluminescence and electroluminescence of hexaphenylsilole are enhanced by pressurization in the solid state. *Chem. Commun.*, 2989-2991 (2008).

- 190 Li, Z. *et al.* Structural Control of the Photoluminescence of Silole Regioisomers and Their Utility as Sensitive Regiodiscriminating Chemosensors and Efficient Electroluminescent Materials. *J. Phys.* **109**, 10061-10066 (2005).
- 191 Peng, Q., Yi, Y., Shuai, Z. & Shao, J. Toward quantitative prediction of molecular fluorescence quantum efficiency: role of duschinsky rotation. *J. Am. Chem. Soc.* **129**, 9333-9339 (2007).
- 192 Chen, J., Xie, Z., Lam, J. W. Y., Law, C. C. W. & Tang, B. Z. Silole-Containing Polyacetylenes. Synthesis, Thermal Stability, Light Emission, Nanodimensional Aggregation, and Restricted Intramolecular Rotation. *Macromolecules* **36**, 1108-1117 (2003).
- 193 Mei, J. *et al.* Aggregation-induced emission: the whole is more brilliant than the parts. *Adv. Mater.* **26**, 5429-5479 (2014).
- 194 Ghoroghchian, P. P., Therien, M. J. & Hammer, D. A. In vivo fluorescence imaging: a personal perspective. *Wiley Interdiscip. Rev. Nanomed. Nanobiotechnol.* **1**, 156-167 (2009).
- 195 Murdoch, C. *et al.* Internalization and biodistribution of polymersomes into oral squamous cell carcinoma cells in vitro and in vivo. *Nanomedicine* **5**, 1025-1036 (2010).
- 196 Lai, M.-H., Lee, S., Smith, C. E., Kim, K. & Kong, H. Tailoring polymersome bilayer permeability improves enhanced permeability and retention effect for bioimaging. *ACS Appl. Mater. Interfaces* **6**, 10821-10829 (2014).
- 197 Ghoroghchian, P. P. *et al.* Quantitative membrane loading of polymer vesicles. *Soft Matter* **2**, 973-980 (2006).
- 198 Duncan, T. V., Ghoroghchian, P. P., Rubtsov, I. V., Hammer, D. A. & Therien, M. J. Ultrafast excited-state dynamics of nanoscale near-infrared emissive polymersomes. *J. Am. Chem. Soc.* **130**, 9773-9784 (2008).
- 199 Ghoroghchian, P. P. *et al.* Controlling bulk optical properties of emissive polymersomes through intramembranous polymer-fluorophore interactions. *Chem. Mater.* **19**, 1309-1318 (2007).
- 200 Birks, J. B. *Aromatic molecules*. Vol. 704 (Wiley, 1970).
- 201 Chen, H. & Li, M.-H. Recent progress in fluorescent vesicles with aggregation-induced emission. *Chin. J. of Polym. Sci.* **37**, 352-371 (2019).
- 202 Wang, X., Yang, Y., Yang, F., Shen, H. & Wu, D. pH-triggered decomposition of polymeric fluorescent vesicles to induce growth of tetraphenylethylene nanoparticles for long-term live cell imaging. *Polymer* **118**, 75-84 (2017).
- 203 Wang, X. *et al.* Fabrication of pH-responsive nanoparticles with an AIE feature for imaging intracellular drug delivery. *Biomater. Sci.* **17**, 2920-2929 (2016).
- 204 Wang, X. *et al.* Facile creation of FRET systems from a pH-responsive AIE fluorescent vesicle. *Chem. Commun.* **52**, 5320-5323 (2016).
- 205 Tao, X. *et al.* Polymersomes with aggregation-induced emission based on amphiphilic block copolypeptoids. *Chem. Commun.* **55**, 13530-13533 (2019).
- 206 Zhang, N. *et al.* Fluorescent Polymersomes with Aggregation-Induced Emission. *ACS Nano* **12**, 4025-4035 (2018).

- 
- 207 Zhao, Y., Wu, Y., Yan, G. & Zhang, K. Aggregation-induced emission block copolymers based on ring-opening metathesis polymerization. *RSC Adv.* **4**, 51194-51200 (2014).
- 208 Zhao, Y., Zhu, W., Ren, L. & Zhang, K. Aggregation-induced emission polymer nanoparticles with pH-responsive fluorescence. *Polym. Chem.* **7**, 5386-5395 (2016).
- 209 Wu, Y., Qu, L., Li, J., Huang, L. & Liu, Z. A versatile method for preparing well-defined polymers with aggregation-induced emission property. *Polymer* **158**, 297-307 (2018).
- 210 Zhang, D., Fan, Y., Chen, H., Trepout, S. & Li, M. H. CO<sub>2</sub>-Activated Reversible Transition between Polymersomes and Micelles with AIE Fluorescence. *Angew. Chem. Int. Ed.* **58**, 10260-10265 (2019).
- 211 Qiu, L. *et al.* CO<sub>2</sub>-responsive nano-objects with assembly-related aggregation-induced emission and tunable morphologies. *ACS Appl. Mater. Interfaces* **12**, 1348-1358 (2020).
- 212 He, X., Wang, B., Li, X. & Dong, J. Converse transitions between the micelles and the vesicles of pyrrolidone-based AIE amphiphilic copolymers in polar and apolar solvents. *RSC Adv.* **9**, 28102-28111 (2019).
- 213 Huo, M. *et al.* Polymer Assemblies with Nanostructure-Correlated Aggregation-Induced Emission. *Macromolecules* **50**, 1126-1133 (2017).





## Chapter II. Light-Gated Nano-Porous Polymersomes from Stereoisomer-Directed Self-Assemblies

### 2.1 Introduction

Capsules with regularly spaced holes in the walls exist in Nature. For example, many virus capsids have such a structure, where protein units form a rigid frame with holes.<sup>1</sup> In the biomimetic systems like ISCOM (immune-stimulating complexes) vaccines, cage-like structures exhibit also regular holes, but they are formed from small amphiphilic molecules including saponins, phospholipids and cholesterol.<sup>2</sup> Perforated vesicles (also called stomatosomes) made from small amphiphilic molecules were then clearly identified in two-amphiphiles mixtures,<sup>3,4,5,6</sup> such as in cetyltrimethylammonium chloride/egg phosphatidylcholines (C16TAC/EPC) in NaCl aqueous solution. All these two-amphiphiles systems have a common feature: the amphiphile 1 tends to form micelles, whereas the amphiphile 2 favors vesicle formation. The perforated vesicles are evidenced as intermediate structures in the transition from bilayer vesicles to cylindrical micelles with the increase of the ratio of amphiphile 1 over amphiphile 2.<sup>4</sup> Later, supramolecular capsules with nanopores were reported in dumbbell-shaped amphiphiles containing rod-core<sup>7</sup> and in dendritic amphiphiles containing fluorinated-core.<sup>8</sup> In contrast to the multicomponent systems of small amphiphilic molecules, only one amphiphilic dendrimer is necessary to form porous membrane in these systems. The mechanism of their pore formation is more complicated and seems to be closely related to the membrane rigidity.<sup>7,8</sup> It was possible to change the pore size or pore opening/closing in supramolecular capsules by external stimuli like temperature variation.<sup>7</sup> Structuring pores into stable membrane of capsules and controlling their opening are extremely useful for applications that require nano-pores as channels for material exchange and transportation, such as organ-on-chip tissue engineering.<sup>9,10</sup> However, the number of experimental and theoretical researches in perforated vesicles is still limited.

This chapter, we report on the perforated polymersomes with nanopores formed from a mixture of *trans*- and *cis*-stereoisomers of an amphiphilic polymer PEG550-TPE-Chol ( $M_n = 1510$  Da) with tetraphenylethene (TPE) as the stereocenter. The hydrophilic part of the polymer is poly(ethylene glycol) (PEG550,  $M_n = 550$  Da), and the hydrophobic part is composed of two rigid cores including the TPE and the cholesterol (Chol) moiety. From the point of view of materials, capsules with higher molecular weight and rigid cores are more

stable and robust than those made from small molecular amphiphiles. The cholesterol moiety is introduced because it is a biocompatible and bio-sourced lipophilic molecule very popular for the core-construction of self-assemblies<sup>11,12</sup>. The role of TPE is three-fold. Firstly, TPE core is a stilbene-type moiety which has structurally distinct and stable *trans* and *cis* stereoisomers.<sup>13,14</sup> These TPE-based isomers exhibit different properties and have been reported as chemical probes for ions and biospecimens.<sup>13</sup> However, the influence of *trans* and *cis* configuration of TPE molecules on their self-assembly behavior was seldomly investigated.<sup>14,15</sup> Thanks to the shape difference between the *trans* and *cis* isomers, their packing parameter is different and stereoisomer-directed self-assembly has been realized: normal vesicles for *trans*-PEG550-TPE-Chol, cylindrical micelles for *cis*-PEG550-TPE-Chol, and perforated vesicles for *trans/cis* mixture. Secondly, the stilbene-type TPE can undergo *trans-cis* photo-activated isomerization under UV illumination.<sup>16</sup> This photo-isomerization can make the self-assembly photo-responsive. Under UV illumination of high intensity (15 mW/cm<sup>2</sup>), both normal vesicles and cylindrical micelles tend to transform into porous vesicles, and the design of smart nanostructures is possible. Finally, TPE is a typical aggregation-induced emission (AIE) fluorophore and highly emissive in aggregate states.<sup>17,18</sup> The self-assembled nanomaterials containing TPE exhibit tuneable brightness, high sensitivity and photostability.<sup>19-21</sup> All PEG550-TPE-Chol self-assemblies in this work are highly fluorescent under normal intensity of UV for observation and imaging (typically < 0.5 mW/cm<sup>2</sup>). In brief, the porous polymersomes reported here can provide a deeper insight in this intriguing membrane structure. This stilbene-type photo-sensitive system enrich the examples of photo-responsive vesicles and polymersomes, mostly based on azobenzene.<sup>22-26</sup> The AIE fluorescence polymersomes and cylindrical polymer micelles may also be advantageous fluorescent systems to be explored in the future as bio-imaging tools.

## 2.2 Experimental Sections

### 2.2.1 Materials

4-Methoxybenzophenone ( $\geq 98\%$ ), Titanium tetrachloride (TiCl<sub>4</sub>, >98%), Boron tribromide (BBr<sub>3</sub>, >98%), 4-dimethylaminopyridine (DMAP, >99%), Zn Powder (2.5 cm, >99%), 1-(3-Dimethylaminopropyl)-3-ethylcarbodiimide hydrochloride (EDCI, >98%), Lithium hydroxide (LiOH,  $\geq 98\%$ ), Cholesterol (Chol, >95%), Poly (ethylene glycol) methyl ether (MeO-PEG<sub>n</sub>-OH, n = 12,  $M_n = 550$  Da,  $M_w/M_n = 1.01$ ) were purchased from Alfa Aesar. Tetramethylrhodamine isothiocyanate–Dextran (TRITC-Dextran, MW = 4400) were

purchased from Sigma-Aldrich. Tetrahydrofuran (THF) was distilled from sodium-benzophenone ketyl under argon. Dichloromethane (DCM) was distilled with calcium hydride under argon. Other chemical reagents were used as purchased without further purification.

### 2.2.2 Synthesis

The amphiphilic polymers (PEG550-TPE-Chol) with tetraphenylethene (TPE) at core were synthesized as shown in Scheme 2.1, without stereoisomers separation.

**Synthesis of TPE-2OMe:** A two-necked flask equipped with a magnetic stirrer was charged with *p*-methoxybenzophenone (8.07 g, 38.1 mmol), Zn powder (12.3 g, 190.0 mmol) and THF were stirred at 0 °C under an argon atmosphere. Then TiCl<sub>4</sub> (29.20 g, 190.0 mmol) was dropped into the reaction mixture with rapidly stirring over 30 min. The mixture was heated to 80 °C for 24 h. The reaction mixture was cooled to room temperature and then filtered. The filtrates were evaporated, and the crude product was purified by a silica gel column using hexane as eluent. The final product was white solid (6.27 g, 84%). <sup>1</sup>H NMR (CDCl<sub>3</sub>, 400 MHz): δ = 7.15- 7.03 (m, 10H, *ArH*), 6.98- 6.93 (m, 4H, *ArH*), 6.68- 6.63 (m, 4H, *ArH*), 3.75 (m, 3H, *OCH*<sub>3</sub>). <sup>13</sup>C NMR (CDCl<sub>3</sub>, 100 MHz): δ = 158.1, 144.4, 144.3, 139.8, 136.6, 136.5, 132.7, 131.5, 127.8, 127.7, 126.3, 113.2, 113.1, 55.2. HRMS (ESI) calcd. for ([M+H]<sup>+</sup>): C<sub>28</sub>H<sub>25</sub>O<sub>2</sub> 393.18491; Found: 393.18477.

**Synthesis of TPE-2OH:** A two-necked flask containing compound TPE-2OMe (4.51 g, 11.5 mmol) and dried CH<sub>2</sub>Cl<sub>2</sub> (50 mL) was cooled to -20 °C, and 0.9 mL of BBr<sub>3</sub> (12.93 g, 51.6 mmol) was slowly added. The mixture was warmed to room temperature, allowed to stand for 4 h, and then poured into saturated aqueous sodium bicarbonate. The organic phase was dried over anhydrous MgSO<sub>4</sub>, and the crude product obtained in nearly quantitative yield. <sup>1</sup>H NMR (CDCl<sub>3</sub>, 400 MHz): δ= 7.12- 7.00 (m, 10H, *ArH*), 6.91- 6.86 (m, 4H, *ArH*), 6.59- 6.54 (m, 4H, *ArH*). <sup>13</sup>C NMR (CDCl<sub>3</sub>, 100 MHz): δ= 154.0, 144.3, 144.2, 139.8, 136.8, 136.7, 132.9, 131.5, 127.8, 127.7, 126.4, 114.8, 114.7. HRMS (ESI) calcd. for ([M-H]<sup>-</sup>): C<sub>26</sub>H<sub>19</sub>O<sub>2</sub> 363.13905; Found: 363.13865.

**Synthesis of TPE-2COOMe:** The crude product TPE-2OH (2.18 g, 6.0 mmol) was dissolved in 50 mL of CH<sub>3</sub>CN. K<sub>2</sub>CO<sub>3</sub> (2.50 g, 18.0 mmol) and methyl 6-bromohexanoate (2.75, 13.2 mol) were added, and the mixture was refluxed for 4h before cooling and filtering. The filtrate was concentrated and purified by flash chromatography to obtain random TPE-2COOMe

product (without stereoisomers separation) 1 g (81% yield). If careful chromatography on a silica gel column with an eluent of PE and EA (10:1 v/v) was performed, *trans*-TPE-2COOMe and *cis*-TPE-2COOMe were separated. The *trans*-TPE-2COOMe was obtained as white solid and *cis*-TPE-2COOMe as pale-yellow liquid. Then *Trans*- and *cis*-isomers of PEG550-TPE-Chol were synthesized from *trans*- and *cis*-TPE-2COOMe according to Scheme 2.2.

***Trans*-TPE-2COOMe:**  $^1\text{H}$  NMR ( $\text{CDCl}_3$ , 400 MHz):  $\delta = 7.10$ - 7.03 (m, 10H, ArH), 6.89 (d,  $J = 8.0$  Hz, 4H, ArH), 6.59 (d,  $J = 8.1$  Hz, 4H, ArH), 3.87 (t, 4H,  $J = 6.2$  Hz, ArOCH<sub>2</sub>CH<sub>2</sub>), 3.67 (s, 6H, OCH<sub>3</sub>), 2.34 (t,  $J = 7.3$  Hz, 4H, CH<sub>2</sub>COOCH<sub>3</sub>), 1.77- 1.65 (m, 8H, CH<sub>2</sub>CH<sub>2</sub>CH<sub>2</sub>), 1.50- 1.47 (m, 4H, CH<sub>2</sub>CH<sub>2</sub>CH<sub>2</sub>).  $^{13}\text{C}$  NMR ( $\text{CDCl}_3$ , 100 MHz):  $\delta = 174.2$ , 157.5, 144.5, 139.8, 136.4, 132.7, 131.5, 127.8, 126.3, 113.6, 67.5, 51.7, 34.1, 29.1, 25.8, 24.9. HRMS (ESI) calcd. for ( $[\text{M}+\text{Na}]^+$ ): C<sub>40</sub>H<sub>44</sub>O<sub>6</sub>Na 643.30301; Found: 643.30295. ***Cis*-TPE-2COOMe:**  $^1\text{H}$  NMR ( $\text{CDCl}_3$ , 400 MHz):  $\delta = 7.06$ - 7.02 (m, 10H, ArH), 6.93 (d,  $J = 7.8$  Hz, 4H, ArH), 6.63 (d,  $J = 7.8$  Hz, 4H, ArH), 3.89 (t, 4H,  $J = 6.1$  Hz, ArOCH<sub>2</sub>CH<sub>2</sub>), 3.67 (s, 6H, OCH<sub>3</sub>), 2.35 (t,  $J = 7.3$  Hz, 4H, CH<sub>2</sub>COOCH<sub>3</sub>), 1.78- 1.68 (m, 8H, CH<sub>2</sub>CH<sub>2</sub>CH<sub>2</sub>), 1.50- 1.47 (m, 4H, CH<sub>2</sub>CH<sub>2</sub>CH<sub>2</sub>).  $^{13}\text{C}$  NMR ( $\text{CDCl}_3$ , 100 MHz):  $\delta = 174.2$ , 157.5, 144.4, 139.7, 136.4, 132.6, 131.6, 127.7, 126.3, 113.7, 67.5, 51.6, 34.1, 29.1, 25.8, 24.9.

**Synthesis of TPE-2COOH:** TPE-2COOMe (or its *trans*- or *cis*-isomer) (1.52 g, 2.5 mmol) was dissolved in 80 mL of THF/H<sub>2</sub>O (v/v = 7:1). LiOH (0.31 g, 12.5 mmol) was then slowly added, and the mixture was stirred overnight. THF was removed under reduced pressure and CH<sub>2</sub>Cl<sub>2</sub> 100 mL added. The pH of the mixture was then adjusted to 1.0 with 1 M HCl before extracting 3 times with DCM. The organic phase was dried over anhydrous MgSO<sub>4</sub> and then concentrated to give compound TPE-2COOH (1.32 g, 91% yield) with flash chromatography.

***Trans*-TPE-2COOH:**  $^1\text{H}$  NMR ( $\text{CDCl}_3$ , 400 MHz):  $\delta = 7.12$ - 7.03 (m, 10H, ArH), 6.89 (d,  $J = 8.5$  Hz, 4H, ArH), 6.59 (d,  $J = 8.4$  Hz, 4H, ArH), 3.87 (t, 4H,  $J = 6.3$  Hz, ArOCH<sub>2</sub>CH<sub>2</sub>), 2.38 (t,  $J = 7.4$  Hz, 4H, CH<sub>2</sub>COOH), 1.79- 1.66 (m, 8H, CH<sub>2</sub>CH<sub>2</sub>CH<sub>2</sub>), 1.54- 1.46 (m, 4H, CH<sub>2</sub>CH<sub>2</sub>CH<sub>2</sub>).  $^{13}\text{C}$  NMR ( $\text{CDCl}_3$ , 100 MHz):  $\delta = 179.3$ , 157.5, 144.5, 139.8, 136.4, 132.7, 131.5, 127.8, 126.3, 113.7, 67.5, 34.0, 29.1, 25.8, 24.6. HRMS (ESI) calcd. for ( $[\text{M}-\text{H}]^-$ ): C<sub>38</sub>H<sub>39</sub>O<sub>6</sub> 591.27521; Found: 591.27569. ***Cis*-TPE-2COOH:**  $^1\text{H}$  NMR ( $\text{CDCl}_3$ , 400 MHz):  $\delta = 7.08$ - 7.01 (m, 10H, ArH), 6.91 (d,  $J = 8.1$  Hz, 4H, ArH), 6.64 (d,  $J = 8.3$  Hz, 4H, ArH), 3.89 (t, 4H,  $J = 6.1$  Hz, ArOCH<sub>2</sub>CH<sub>2</sub>), 2.40 (t,  $J = 7.1$  Hz, 4H, CH<sub>2</sub>COOH), 1.80- 1.69 (m, 8H, -CH<sub>2</sub>CH<sub>2</sub>CH<sub>2</sub>), 1.54- 1.50 (m, 4H, CH<sub>2</sub>CH<sub>2</sub>CH<sub>2</sub>).  $^{13}\text{C}$  NMR ( $\text{CDCl}_3$ , 100 MHz):  $\delta = 180.3$ , 157.6, 144.3, 139.9, 136.5, 132.6, 131.6, 127.7, 126.3, 113.8, 67.6, 34.1, 29.0, 25.7, 24.6.

**Synthesis of TPE-Chol-COOH:** TPE-2COOH (or its *trans*- or *cis*-isomer) (2.50 g, 4.2 mmol), cholesterol (1.63 g, 4.2 mmol), EDCI (0.89 g, 4.6 mmol), DMAP (0.52 g, 4.2 mmol) and dried CH<sub>2</sub>Cl<sub>2</sub> (100 mL) were introduced into a two-necked flask. The mixture was stirred overnight at room temperature. The organic layer was washed with saturated brine solution three times. The combined organic phase was dried over anhydrous Na<sub>2</sub>SO<sub>4</sub>. The filtrate was concentrated and purified on a silica gel column with an eluent of petroleum ether and ethyl acetate (10:1, *v/v*) to give white solid compound TPE-Chol-COOH (2.21 g, 54 % yield). ***Trans*-TPE-Chol-COOH:** <sup>1</sup>H NMR (CDCl<sub>3</sub>, 400 MHz): δ= 7.11- 7.00 (m, 10H, ArH), 6.89 (d, *J* = 8.0 Hz, 4H, ArH), 6.59 (d, *J* = 8.0 Hz, 4H, ArH), 5.37 (d, *J* = 4.0 Hz, 1H, C=CH), 4.65–4.57 (m, 4H, OCH), 2.40-2.30 (m, 6H, CH<sub>2</sub>), 2.02-0.85 (m, 51H, CH, CH<sub>2</sub>, CH<sub>3</sub>), 0.68 (s, 3H, CH<sub>3</sub>). <sup>13</sup>C NMR (CDCl<sub>3</sub>, 100 MHz): δ=178.6, 173.1, 157.4, 157.4, 144.3, 139.7, 139.6, 139.6, 136.3, 136.3, 132.5, 131.4, 127.6, 126.1, 122.6, 113.5, 77.3, 73.8, 67.4, 67.4, 56.7, 56.1, 50.0, 42.3, 39.8, 39.5, 38.2, 37.0, 36.6, 36.2, 35.8, 34.9, 33.7, 31.9, 31.9, 29.0, 28.3, 28.0, 27.8, 25.6, 24.8, 24.5, 24.3, 23.8, 22.8, 22.6, 21.0, 19.4, 18.7, 11.9. HRMS (ESI) calcd. for ([M-H]<sup>-</sup>): C<sub>65</sub>H<sub>83</sub>O<sub>6</sub> 959.61951; Found: 959.62004. ***Cis*-TPE-Chol-COOH:** <sup>1</sup>H NMR (CDCl<sub>3</sub>, 400 MHz): δ= 7.09-7.00 (m, 10H, ArH), 6.93 (d, *J* = 8.0 Hz, 4H, ArH), 6.63 (d, *J* = 8.4 Hz, 4H, ArH), 5.38 (d, *J* = 4.0 Hz, 1H, C=CH), 4.67–4.59 (m, 4H, OCH), 3.87 (t, 4H, *J* = 6.3 Hz, ArOCH<sub>2</sub>CH<sub>2</sub>), 2.41-2.30 (m, 6H, CH<sub>2</sub>), 2.05-0.87 (m, 51H, CH, CH<sub>2</sub>, CH<sub>3</sub>), 0.69 (s, 3H, CH<sub>3</sub>). <sup>13</sup>C NMR (CDCl<sub>3</sub>, 100 MHz): δ= 179.1, 173.2, 157.4, 144.3, 139.7, 139.7, 139.6, 136.4, 136.3, 132.5, 131.4, 127.5, 126.1, 122.7, 113.6, 73.9, 67.4, 67.4, 56.7, 56.2, 50.0, 42.3, 39.8, 39.5, 38.2, 37.0, 36.6, 36.2, 35.8, 34.6, 33.9, 31.9, 31.9, 29.0, 28.3, 28.0, 27.8, 25.7, 24.8, 24.5, 24.3, 23.9, 22.9, 22.6, 21.1, 19.4, 18.8, 11.8.

**Synthesis of PEG-TPE-Chol:** TPE-Chol-COOH (or its *trans*- or *cis*-isomer) (0.28 g, 0.30 mmol), mPEG-OH (*M*<sub>n</sub> = 550 Da, 0.13 g, 0.23 mmol), EDCI (62.2 mg, 0.33 mmol), DMAP (39.7 mg, 0.33 mmol) and dried CH<sub>2</sub>Cl<sub>2</sub> (50 mL) were introduced into two-necked flask. The mixture was stirred overnight at room temperature. The organic layer was washed with saturated brine solution 3 times. The combined organic phase was dried over anhydrous Na<sub>2</sub>SO<sub>4</sub>. The filtrate was concentrated and purified on a silica gel column with an eluent of dichloromethane and methanol (35:1, *v/v*) to give product PEG550-TPE-Chol (or *trans*-PEG550-TPE-Chol or *cis*-PEG550-TPE-Chol).

### 2.2.3 Instruments

**Nuclear Magnetic Resonance (NMR).**  $^1\text{H}$  NMR and  $^{13}\text{C}$  NMR spectra were measured on a Bruker AV 400 and Bruker AV 500 spectrometers. Chemical shifts  $\delta$  are given in ppm and referenced to tetramethylsilane (TMS) in  $\text{CDCl}_3$  (0 ppm). High-resolution mass spectra (HRMS) were recorded on a GCT premier CAB048 mass spectrometer operating in MALDI-TOF mode.

**Size Exclusion Chromatography (SEC).** Number-average molecular weights ( $M_n$ ) of polymers were calculated by  $^1\text{H}$  NMR. Molecular weight distributions ( $M_w/M_n$ ) of polymers were estimated by size exclusion chromatography (SEC) using THF as eluent at a flow rate of 1 mL/min.

**UV-vis Spectroscopy.** UV spectra were measured on a Milton Ray Spectronic 3000 Array spectrophotometer.

**Fluorescence Emission Spectroscopy.** Photoluminescence (PL) spectra were recorded on a Horiba FluoroMax Spectrofluorometers. The sample solution in THF or acetone with concentrations of  $\sim 10^{-5}$  M was put in quartz cells with a pathlength of 1 cm.

**UV-vis Detector.** UV (365 nm) intensities were measured with International Light ILT 1400-A Radiometer/Photometer equipped with SEL005 UV-Visible GaAsP detector.

**Dynamic Light Scattering (DLS).** Hydrodynamic diameters of self-assemblies and their distributions in pure water were measured at 25 °C by dynamic light scattering (DLS, Malvern zetasizer 3000HS, UK) with a 633 nm laser. A 90° scattering angle was used for all measurements.

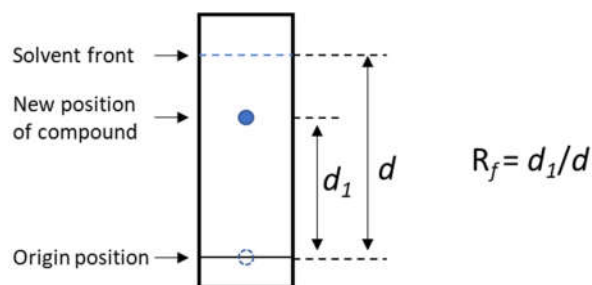
**Cryo-Electron Microscopy (Cryo-EM).** Self-assembled morphologies were studied by cryo-electron microscopy (cryo-EM). Cryo-EM images were acquired on a JEOL 2200FS energy-filtered (20 eV slit) field emission gun electron microscope operating at 200 kV using a Gatan US1000 camera. For the sample preparation, a total of 5  $\mu\text{L}$  of samples were deposited onto a 200-mesh holey copper grid (Ted Pella Inc., U.S.A.) and flash-frozen in liquid ethane cooled down at liquid nitrogen temperature using a Leica EM-CPC system.

**Epifluorescence Microscopy.** Giant polymersomes were observed by epifluorescence microscopy using a Leica DMR upright microscope equipped with a Retiga Exi CCD camera (Teledyne Technologies) and LED Lamp ( $\lambda=365$  nm). Images were acquired with Image-Pro Plus (Media Cybernetics) and processed/analyzed using ImageJ. Samples (10  $\mu\text{L}$ ) were

deposited between a glass slide and cover slip with spacers. The observations were performed with a 100x objective lens (N.A. 1.3).

## 2.2.4 Methods

**The retention factor ( $R_f$ ).**  $R_f$  is defined as the distance traveled by the compound divided by the distance traveled by the solvent.

$$R_f = \frac{\text{distance traveled by compound}}{\text{distance traveled by the solvent front}}$$


The  $R_f$  for a compound depends on the chromatography conditions including the solvent system, thickness of the adsorbent, amount of compound spotted, *etc.* Since these factors are difficult to keep constant from experiment to experiment, relative  $R_f$  value is generally considered.

**Quantum Yield Measurement.** Quantum yield was measured by a relative method using the following equation:

$$\Phi_2 = \Phi_1 \times \frac{n_2^2}{n_1^2} \times \frac{F_2}{F_1} \times \frac{A_1}{A_2}$$

$\Phi_2$  is the quantum yield of the fluorogen sample to be tested;  $\Phi_1$  is the quantum yield of a standard fluorogen;  $n_1$  and  $n_2$  are the refractive indexes of the standard solution and the sample solution;  $F_1$  and  $F_2$  are the fluorescence integral areas of fluorescence spectra of standard and sample, which are measured at the same conditions;  $A_1$  and  $A_2$  are the absorbances of standard and sample, which are measured at the same conditions and at values lower than 0.05. The refractive index of ethanol was 1.366 at room temperature; the refractive index of water was 1.333 at room temperature. The selected standard fluorogen was 9,10-diphenylanthracene and its quantum yield was 0.96 in ethanol at room temperature (1  $\mu\text{g/mL}$ ;  $\lambda_{\text{ex}}=366$  nm).

**Encapsulation of TRITC-Dextran in Polymersomes:** Typically, about 200  $\mu\text{L}$  of chloroform solution of *trans*-PEG550-TPE-Chol (5 mg/ml, 0.5 wt%) was uniformly deposited



on the surface of a roughened Teflon plate, followed by drying in vacuum to remove all solvent and to get a thin polymer film. Then the thin film sample was hydrated with 15 ml of TRITC-Dextran solution in water (0.1 mg/ml) at 65 °C for 48 h in a sealed bottle. The resultant polymersomes dispersion was then dialyzed against water for 3 days (refreshing water two times per day) to remove the free TRITC-Dextran.

To determine the quantity of TRITC-Dextran loaded in polymersomes, 10 mL tetrahydrofuran (THF) were added to 1ml of the TRITC-Dextran-loaded polymersomes dispersion to destroy the vesicular structures and dissolve all molecules. Then, the residues, after the removal of THF and water by vacuum pump, were dissolved and dispersed in water. The amount of TRITC-Dextran dissolved in water, which corresponded to those loaded in polymersomes, was determined according to the calibration curve of fluorescence intensity vs the concentration as shown in Figure 2.32A.

The loading capacity and loading efficiency of TRITC-Dextran in the polymersomes were calculated as follows:

$$\text{loading efficiency} = (\text{weight of loaded TRITC-Dextran})/(\text{weight of initial TRITC-Dextran})$$

$$\text{loading capacity} = (\text{weight of loaded TRITC-Dextran})/(\text{weight of polymer})$$

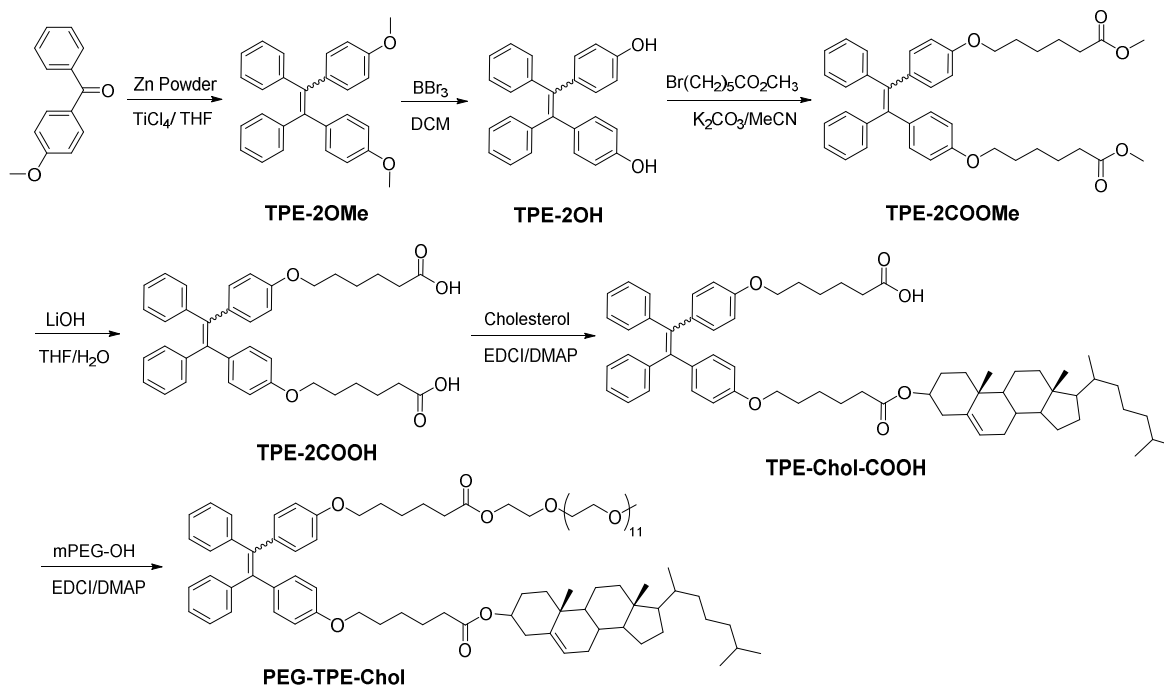
The loading efficiency is 4.8 %, and the loading capacity calculated as 7.7%.

**Release of TRITC-Dextran from polymersomes:** Taking the sample irradiated for 15 min as an example. About 4.5 mL of TRITC-Dextran-loaded polymersomes dispersion was irradiated for 15 min. Then 3.0 mL of irradiated sample was transferred to a dialysis tube (MWCO 100 KDa) and dialyzed against 40 mL water for 12 h. The fluorescence intensity of the water solution outside the dialysis tube was recorded with fluorescence spectra. The concentration of released TRITC-Dextran (*c*) was calculated according to the standard curve. The release percentage was calculated as follows:

$$\begin{aligned} \text{Release percent (\%)} &= (\text{weight of released TRITC-Dextran})/(\text{weight of loaded TRITC-Dextran}) \times 100\% \\ &= (c \times 40 \text{ ml}) / [7.7\% \times (\text{weight of polymer})] \times 100\% \\ &= (c \times 40 \text{ ml}) / [7.7\% \times 1 \text{ mg} \times (3 \text{ ml} / 15 \text{ ml})] \times 100\% \end{aligned}$$

## 2.3 Result and discussion

### 2.3.1 Synthesis and characterizations of PEG550-TPE-Chol and their stereoisomers



**Scheme 2.1.** Synthetic route to amphiphilic polymer PEG-TPE-Chol.

The synthesis of amphiphilic molecules PEG550-TPE-Chol was performed through the synthetic route as shown in Scheme 2.1. Initially, Ti-catalyzed McMurry coupling reaction was employed to provide *trans/cis* mixture of TPE-2OMe (Figure 2.1). Because *trans*- and *cis*- isomers of TPE-2OMe have nearly identical retardation factor ( $R_f$ ) on thin-layer chromatography (TLC), they cannot be separated easily by column chromatography. In addition, for TPE-2OH with phenolic hydroxyl moieties, it is difficult to get stable *trans*- and *cis*- isomers since they can undergo easily *trans-cis* isomerization, especially under acid conditions.<sup>27</sup> We supposed that the *trans-cis* conversion is ascribed to keto-enol tautomerization for TPE-2OH (Figure 2.2). If no separation between *trans*- and *cis*-isomers was made during the whole synthetic procedure, the final product PEG550-TPE-Chol contained nearly the equivalent rate of *trans*- and *cis*-isomers. The ratio of *trans/cis* was calculated as 60/40 (Figure 2.3).

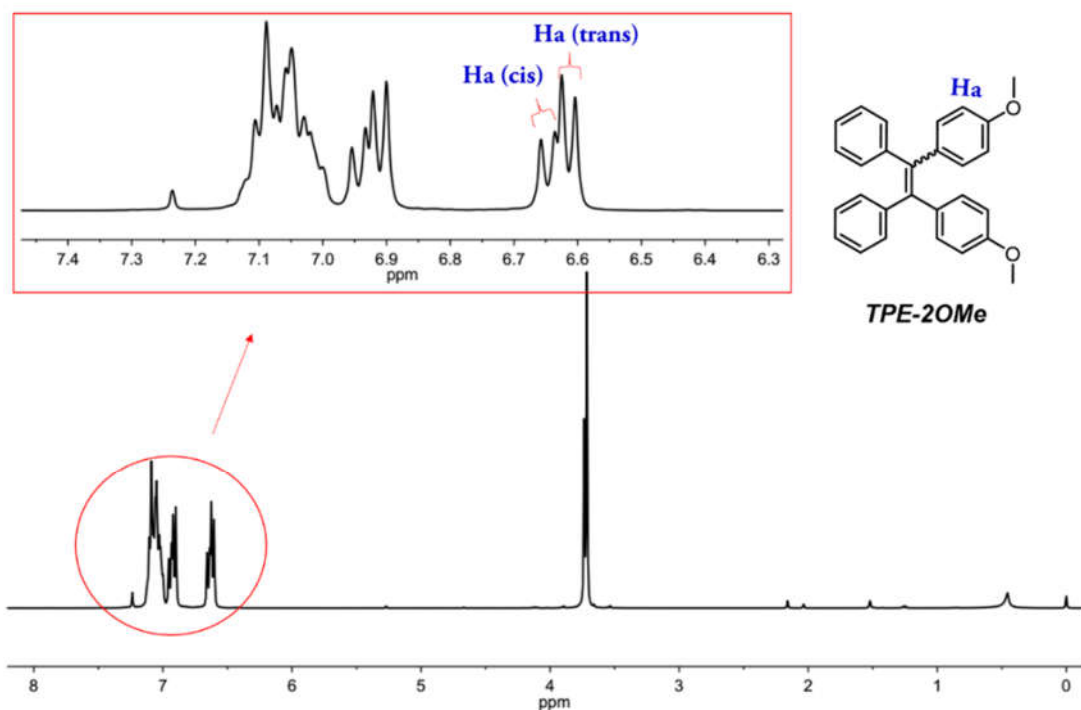


**Figure 2.1.**  $^1\text{H}$  NMR spectra of TPE-2OMe (400 MHz,  $\text{CDCl}_3$ ).

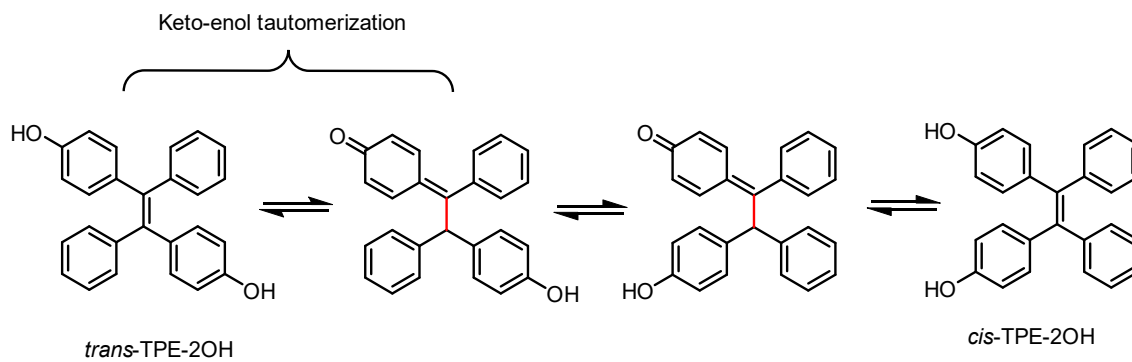


**Figure 2.2.** Potential mechanism of transformation between *trans*- and *cis*-TPE-2OH.

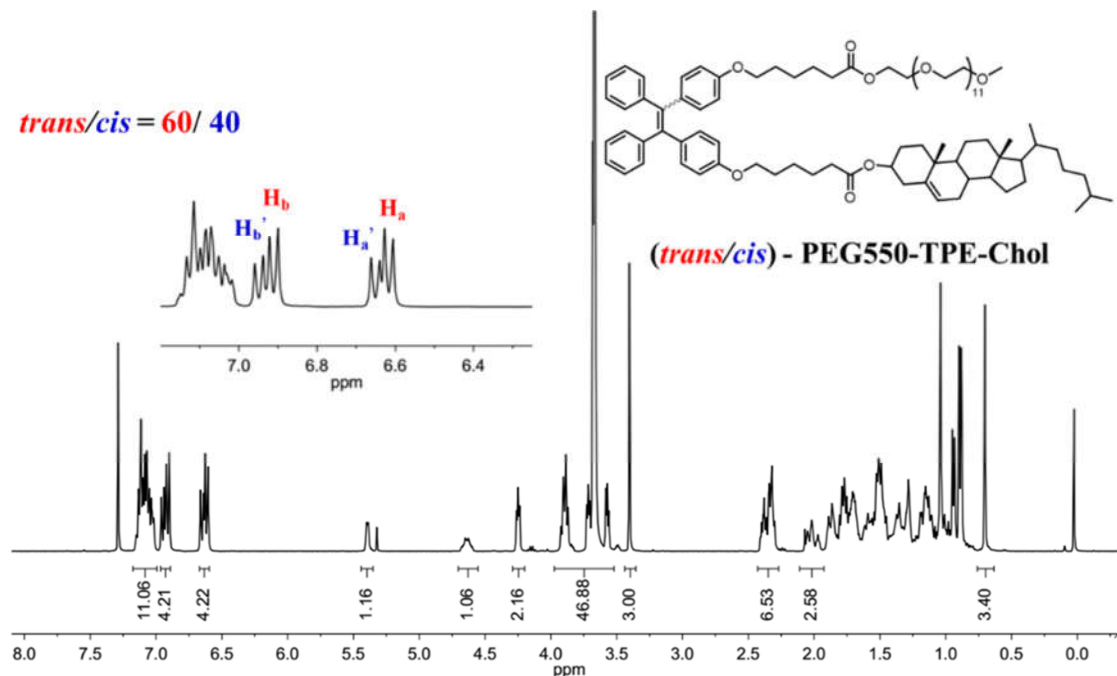


**Figure 2.3.**  $^1\text{H}$  NMR spectra of PEG550-TPE-Chol synthesized inherently without *trans/cis* stereoisomers separation (400 MHz,  $\text{CDCl}_3$ ).

We found that the separation of *trans*- and *cis*-isomers could be conducted for TPE-2COOMe derivative where two big and polar substituents methyl 6-bromohexanoate were connected to TPE-2OH by Williamson reaction. The TPE-2COOMe possess two big and polar substituents methyl 6-hexanoate, which might bring about a big enough difference in the shape and polarity of the resultant TPE derivative to enable macroscopic separation of its stereoisomers. Indeed, the two isomers of TPE-2COOMe showed different retention factor ( $R_f$ , see method for detail definition), 0.52 and 0.44, respectively, on TLC using petroleum ether and ethyl acetate (10:1 volume ratio) as eluent solvents (Figure 2.4).

Then the *trans* and *cis* isomer of TPE-2COOMe were successfully separated by careful column chromatography. The single crystal of the pure isomer with  $R_f = 0.52$  (the upper one on TLC) was acquired by slow evaporation of solvents. Its crystal structure was acquired through X-rays diffraction (see Figure 2.5). The results clearly show that the functionalized phenyl groups are located on the opposite sides of the central double bond. Unambiguously, the isomer collected firstly in column chromatographic experiment with  $R_f = 0.52$  corresponded to the *trans*-TPE-2COOMe. The isomer collected later with  $R_f = 0.44$  was *cis*-TPE-2COOMe. Both isomers are very stable and can be stored at room temperature.

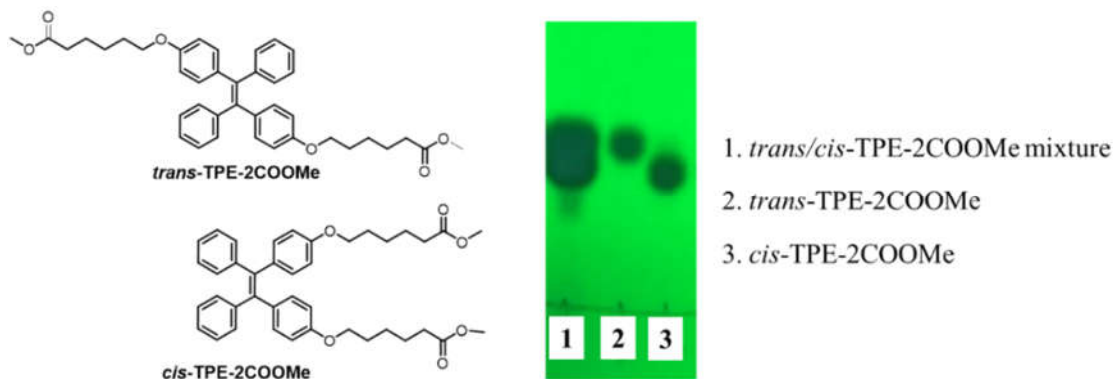


**Figure 2.4.** TLC picture of *trans/cis*-TPE-2COOMe mixture and *trans*- and *cis*-TPE-2COOMe.

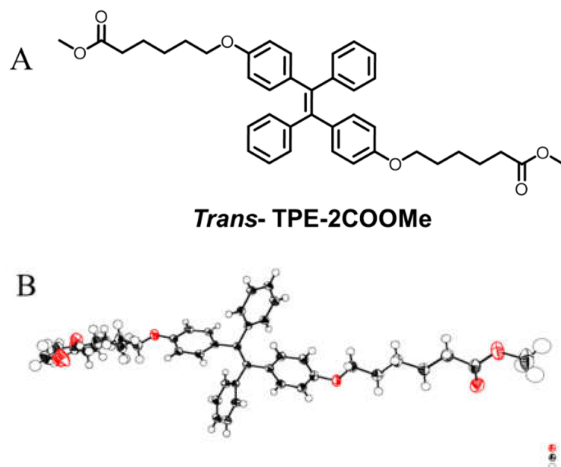


**Figure 2.5.** The chemical structure (A) and the crystal structure of *trans*-TPE-2COOMe.

Figure 2.6 shows the COSY-NMR of *trans*-TPE-2COOMe. The double peaks at  $\delta = 6.59$  ppm correspond to  $H_a$  protons in *trans*-TPE-2COOMe due to the electron-donating property of the neighboring ester group. The double peaks at  $\delta = 6.89$  ppm ascribe to  $H_b$  because of their strong correlation with  $H_a$  in the COSY spectra. Similarly, for its *cis* counterpart, the resonances at  $\delta = 6.63$  are assigned to  $H_a'$ , showing the downfield shift compared to those of its *trans* counterpart (Figure 2.7). Different resonances of the characteristic proton  $H_a$  and  $H_a'$  allow us to use the NMR spectra to distinguish the *trans* and *cis* geometry of TPE molecules. Figure 2.7 shows clearly the difference of chemical shifts between  $H_a$  ( $H_b$ ) for *trans*-isomer and  $H_a'$  ( $H_b'$ ) for *cis*-isomer at  $\delta$  around 6.6 ppm (6.9 ppm).

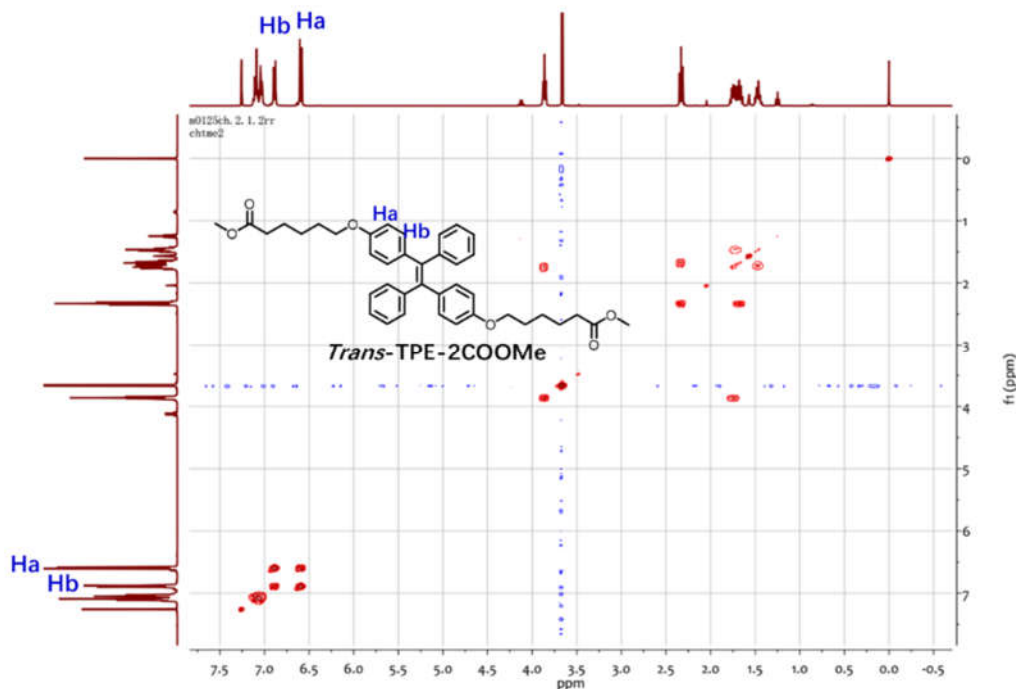


**Figure 2.6.** COSY-NMR of *trans*-TPE-2COOMe (400 MHz, CDCl<sub>3</sub>)

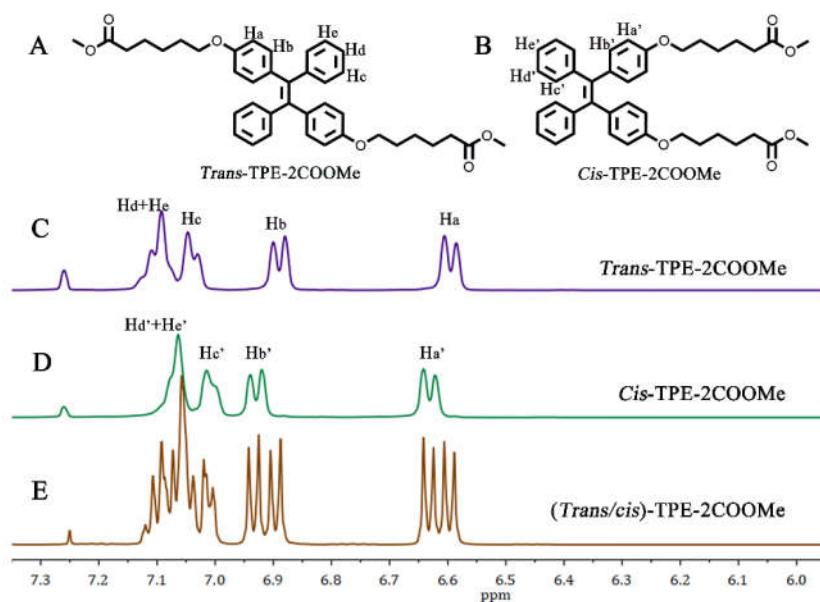
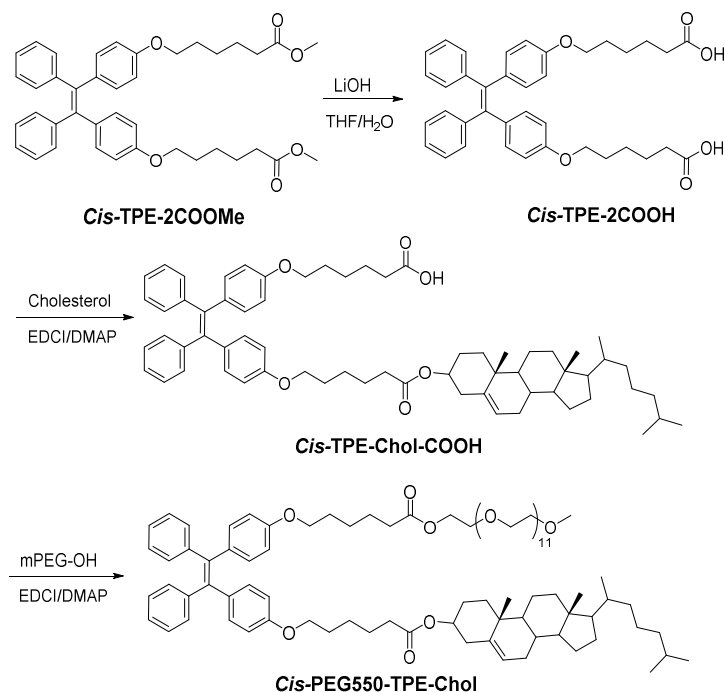


**Figure 2.7.** Chemical structure of *trans*-TPE-2COOMe (A) and *cis*-TPE-2COOMe (B). The partial <sup>1</sup>H NMR spectra of the *trans*-TPE-2COOMe (C), *cis*-TPE-2COOMe (D) and (*trans/cis*)-TPE-2COOMe mixture (E) (400 MHz, CDCl<sub>3</sub>).



**Scheme 2.2.** Synthetic route to *cis*-PEG550-TPE-Chol.

The *trans*- and *cis*-TPE-2COOMe were then used as starting materials to synthesize corresponding amphiphilic stereoisomers, respectively (Scheme 2.2), *via* hydrolysis reaction to get *trans* and *cis*-TPE-2COOH followed by a first esterification reaction with cholesterol and a second esterification with methoxy-poly(ethylene glycol) (mPEG550-OH). The structures of all the compounds were confirmed by  $^1\text{H}$  NMR,  $^{13}\text{C}$  NMR and high-resolution mass spectrometry (see experimental section). *Trans*- and *cis*- isomers were stable and maintained their geometry along the synthetic process from TPE-2COOMe to PEG550-TPE-Chol according to NMR results (see Figure 2.7 and Figure 2.8). For example, signal  $\text{H}_a$  belong to *trans* derivatives did not show any change after reaction (Figure 2.8). For the final amphiphilic stereoisomer *trans*-PEG550-TPE-Chol, the  $^1\text{H}$  NMR analysis detected tiny *cis*-signals of  $\text{H}_a'$  next to the main *trans*-signals of  $\text{H}_a$  (Figure 2.8 and Figure 2.10). Careful peak integration revealed that the *trans*-PEG550-TPE-Chol contained around 5% of *cis* isomer. The same result was also observed for the *cis*-PEG550-TPE-Chol (Figure 2.9 and Figure 2.10), which contained about 5% of *trans* isomer. This small imperfection can be explained as follows. In order to obtain enough final compounds of *trans*- and *cis*-PEG550-TPE-Chol, TPE-2COOMe have been synthesized in great quantity. The large-scale separation of *trans*- and *cis*-TPE-2COOMe by manual column chromatography are not perfect because their  $R_f$  values are too close (Figure 2.4) and it is difficult to separate them completely. Nevertheless,

we will show hereinafter that this trace impurity will not influence the self-assembly behaviors of both *trans*- and *cis*- PEG550-TPE-Chol.

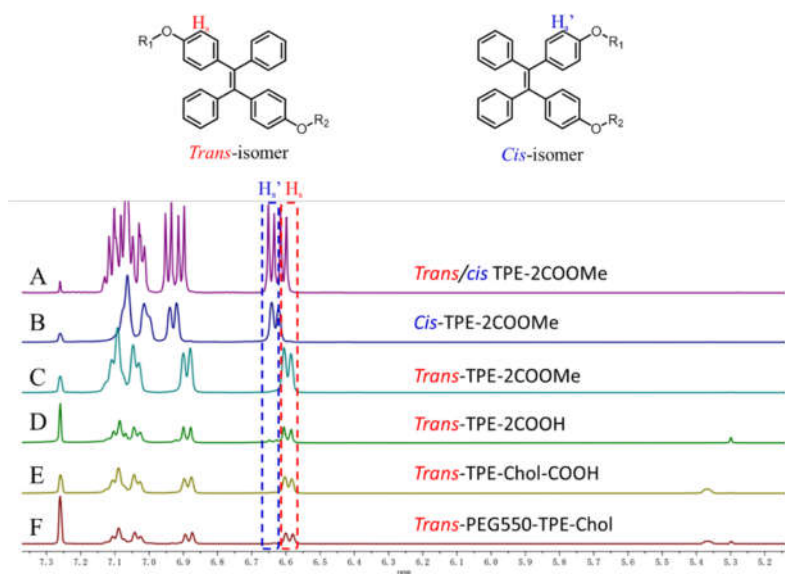


**Figure 2.8.** Partial <sup>1</sup>H NMR spectra of synthesized *trans* derivatives (400 MHz, CDCl<sub>3</sub>). The characteristic proton H<sub>a</sub> of *trans*-TPE-COOMe and other derivatives have the same chemical shift at δ = 6.59 ppm. The results indicated that the geometry of purified isomers would not be changed by the reactions.

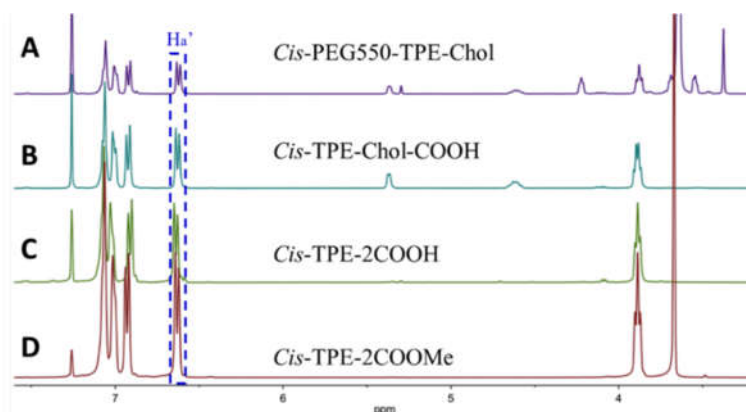


**Figure 2.9.** Partial <sup>1</sup>H NMR spectra of synthesized *cis* derivatives (400 MHz, CDCl<sub>3</sub>). The protons H<sub>a'</sub> of *cis*-TPE-COOMe and other derivatives also gave the identical chemical shift at δ = 6.63 ppm. The results indicated that the geometry of purified isomers would not be changed by the reactions.



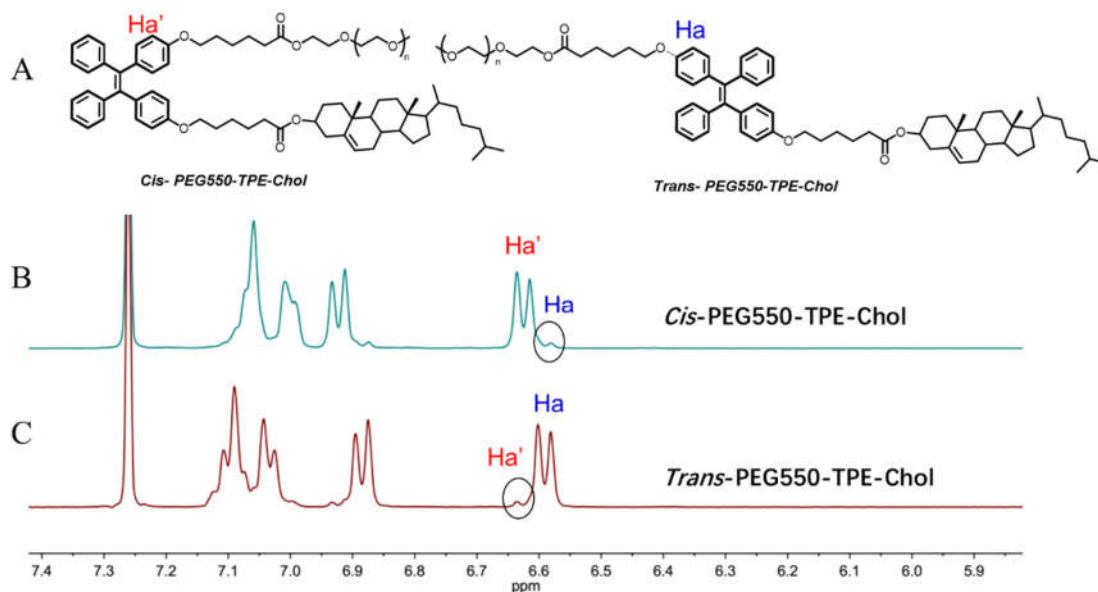


**Figure 2.10.** Chemical structure (A) and partial  $^1\text{H}$  NMR spectra of *trans*- and *cis*-PEG550-TPE-Chol (B and C) (400 MHz,  $\text{CDCl}_3$ ).

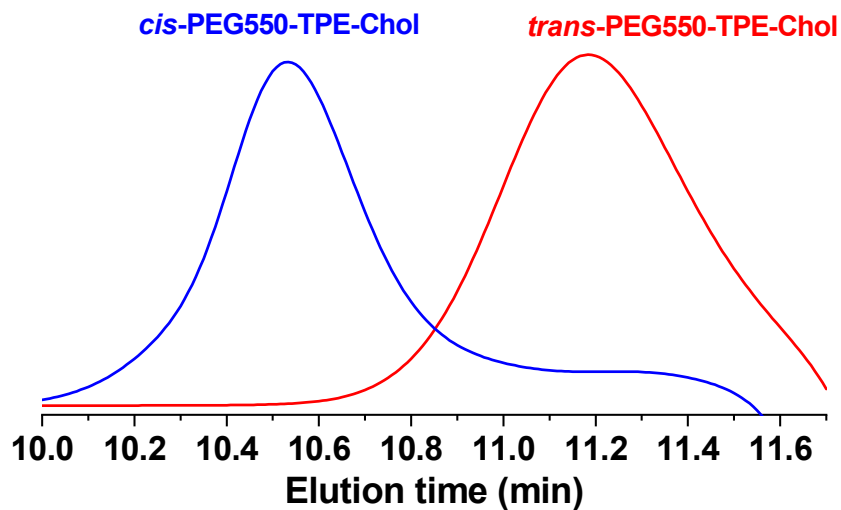


**Figure 2.11.** SEC curves of *trans*- and *cis*-PEG550-TPE-Chol with THF eluent at rate of 1 mL/min (by refractometer).

The molecular weight of *trans*- and *cis*-PEG550-TPE-Chol were then analyzed by size exclusion chromatography (SEC) (Figure 2.11). Their SEC peaks are well separated, and the elution time of *trans*-isomer is longer than that of its *cis* counterpart. This observation is

completely coherent with the fact that the shapes of *trans*- and *cis*- PEG550-TPE-Chol are quite different, even though their molecular weight are the same ( $M_n = 1510$  Da).

The *trans*- and *cis*- PEG550-TPE-Chol also exhibit differences in their fluorescence spectra. As shown in Figure 2.12A, a large absorption peak with a maximum around 318 nm was recorded for *trans* and *cis*-PEG550-TPE-Chol, which is characteristic absorbance peak of TPE moiety. However, the maximum emission peak of *trans*-PEG550-TPE-Chol is located at 487 nm, showing a blue shift ( $\Delta\lambda_{\max} = 8$  nm) compare with that of its *cis* counterpart (Figure 2.12D). The reason may be that the *cis* isomers may take a more planar conformation when they performed self-assembly in water and show a redder fluorescence.

Figure 2.12B shows the fluorescence evolution of *trans*-PEG550-TPE-Chol as function of water fraction. At  $f_w = 0$ , the *trans*-PEG550-TPE-Chol in acetone solution is non-emissive because it is perfectly soluble and the intramolecular rotation of TPE leads to non-radiative decay after UV illumination. At  $f_w = 60\%$ , the molecules start to assemble and light up the fluorescence because of the restriction of the intramolecular motion of TPE moieties. Nevertheless, at this stage, the content of acetone in the hydrophobic domain of assemblies is still high, which could “lubricate” the intramolecular motion in a certain extent. As a result, the increase of fluorescent intensity is not so significant. Further, the fluorescence intensity increases significantly as water fraction reaching at 90%. In this stage, due to the high osmotic pressure, the removal of the acetone from the hydrophobic domain of assemblies accelerates, and fewer and fewer of acetone present in the hydrophobic domain. This leads to the effective restriction of intramolecular motions of TPE moieties. Consequently, fluorescence intensity increases significantly. In nearly pure water ( $f_w = 99\%$ ), the assemblies of *trans*-PEG550-TPE-Chol exhibit bright AIE fluorescence (inset in Figure 2.12B). The similar trend for fluorescence increase was observed for *cis*-PEG550-TPE-Chol with the increase of water fraction (Figure 2.12C). However, fluorescence intensity of *cis*-PEG550-TPE-Chol begins to exceed that of *trans*-PEG550-TPE-Chol when water fraction over 60%. The more planar conformation would lead to more restriction of intramolecular motions (RIM) for *trans* isomers than that of *cis* isomers, showing a stronger fluorescence.

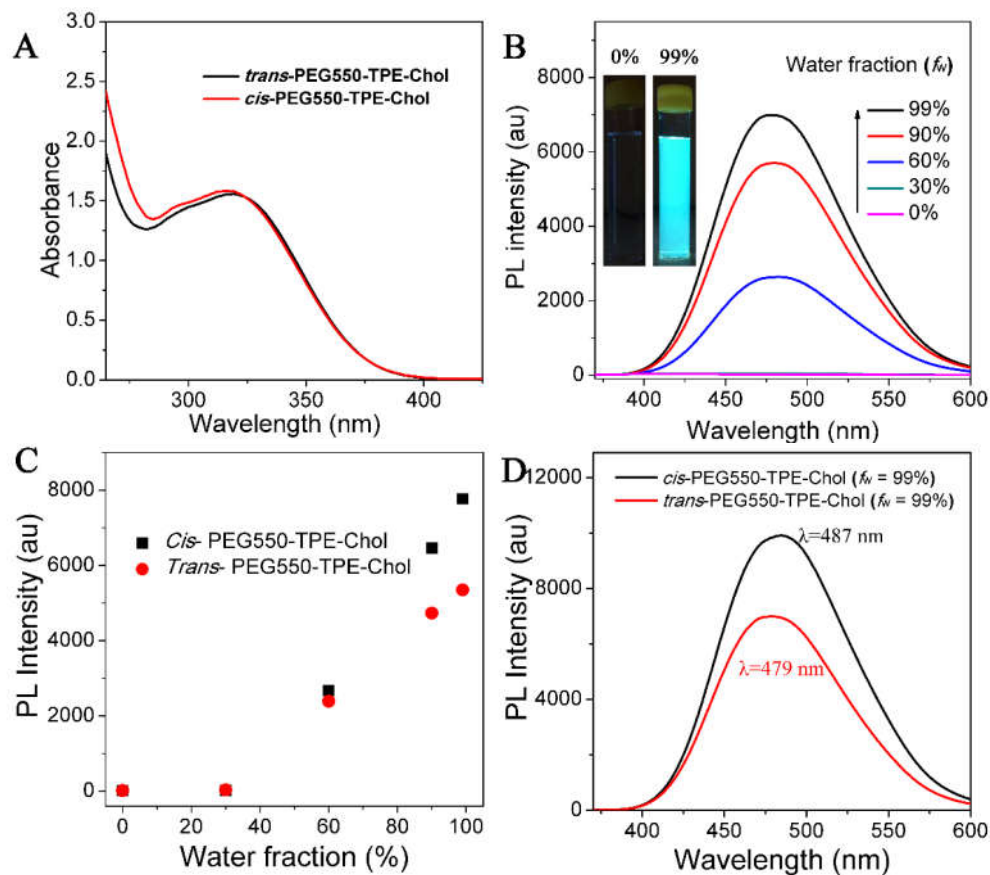


**Figure 2.12.** (A) UV-*vis* absorption spectra of *trans*- and *cis*-PEG550-TPE-Chol in acetone (concentration of polymer =  $1 \times 10^{-4}$  M). (B) Photoluminescence (PL) spectra of *trans*-PEG550-TPE-Chol in acetone/H<sub>2</sub>O with different water fractions (concentration:  $1 \times 10^{-5}$  M; excitation wavelength: 352 nm). (C) Evolution of fluorescence intensity of *trans*- and *cis*-PEG550-TPE-Chol as a function of water content  $f_w$ . (D) PL spectra of *trans*-PEG550-TPE-Chol and *cis*-PEG550-TPE-Chol in acetone/H<sub>2</sub>O with  $f_w = 99%$ .

### 2.3.2 Thermal and photostability of PEG550-TPE-Chol stereoisomers

The possibility to activate the isomerization between two stereoisomers by heating and by UV illumination has been examined. Both isomers are rather thermally stable as shown by <sup>1</sup>H NMR spectra in Figure 2.13 and Figure 2.14. Heating their DMSO-*d*<sub>6</sub> solution up to 70°C cannot induce *trans*-to-*cis* or *cis*-to-*trans* isomerization. When heating at 120°C for 24h, only 12-14% of isomerization occurs.

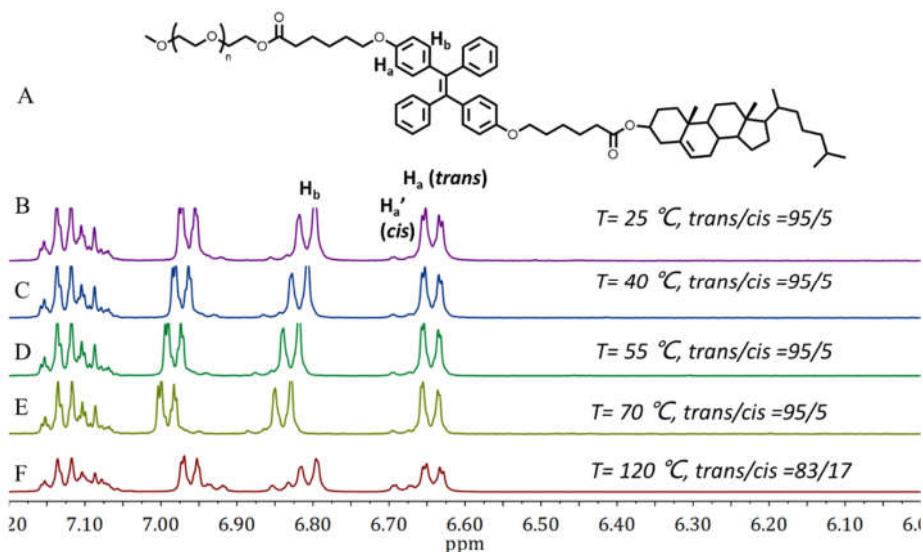


**Figure 2.13.** Chemical structure (A) of *trans*-PEG550-TPE-Chol, and its partial  $^1\text{H}$  NMR spectra of in  $\text{DMSO-}d_6$  recorded at different temperatures: (B)  $T=25^\circ\text{C}$ . (C)  $T=40^\circ\text{C}$ . (D)  $T=55^\circ\text{C}$ . (E)  $T=70^\circ\text{C}$ . (F)  $T=120^\circ\text{C}$ . (B-E) were recorded at temperature  $T$  after keeping at it for 30 min, while (F) was recorded at  $25^\circ\text{C}$  after heating at  $120^\circ\text{C}$  for 24h and cooled down to room temperature.

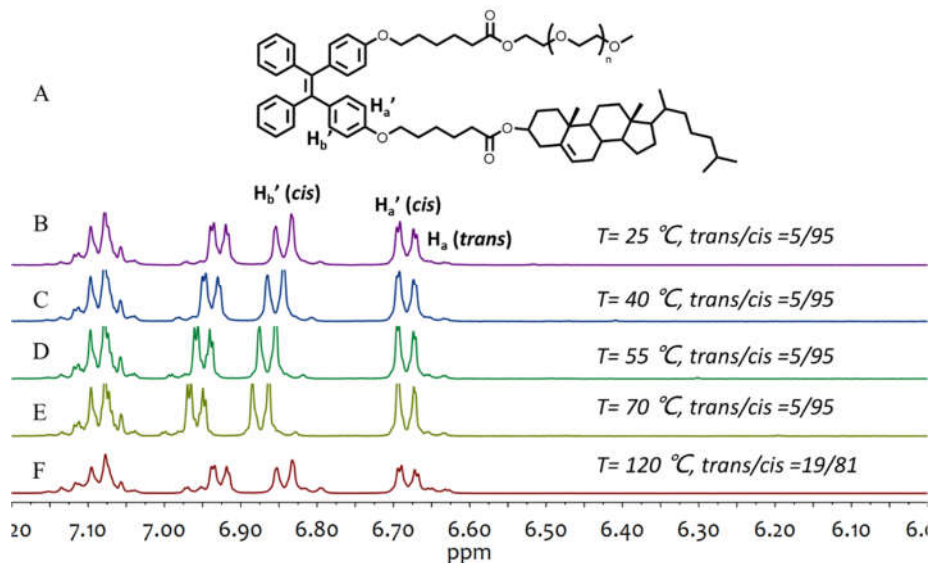


**Figure 2.14.** Chemical structure of *cis*-PEG550-TPE-Chol (A), and its partial  $^1\text{H}$  NMR spectra in  $\text{DMSO-}d_6$  recorded at different temperatures: (B)  $T=25^\circ\text{C}$ . (C)  $T=40^\circ\text{C}$ . (D)  $T=55^\circ\text{C}$ . (E)  $T=70^\circ\text{C}$ . (F)  $T=120^\circ\text{C}$ . (B-E) were recorded at temperature  $T$  after keeping at it for 30 min, while (F) was recorded at  $25^\circ\text{C}$  after heating at  $120^\circ\text{C}$  for 24h and cooled down to room temperature.

Under weak UV light (365 nm,  $< 0.5 \text{ mW/cm}^2$ ), both isomers in solution are also stable during normal observation time (in the order of minutes), as shown by  $^1\text{H}$  NMR spectra in Figure 2.15 and Figure 2.16. Typically, the UV light (365 nm) for TLC revealing is less than  $0.5 \text{ mW/cm}^2$ , and that in Spectrofluorometer is  $0.25 \text{ mW/cm}^2$ . After 2 min of illumination by UV light (365 nm,  $0.5 \text{ mW/cm}^2$ ), no photoisomerization can be detected for both the *trans* and *cis* isomers (Figure 2.15 and Figure 2.16). In contrast, photo-isomerization of isomers in solution takes place readily under high UV light as shown by  $^1\text{H}$  NMR spectra in Figure 2.17 and 2.18. *Trans* and *cis*-PEG550-TPE-Chol exposed to UV light (365 nm,  $15 \text{ mW/cm}^2$ ) for 2 min undergo already 19% and 25% of isomerization, respectively. After 10 min of illumination, both *trans*-to-*cis* and *cis*-to-*trans* isomerization reach a stationary state with *trans/cis* ratio of 60/40. The *trans*-isomer is in a little excess compared to *cis*- one, because the *trans*-PEG550-TPE-Chol is more photo-stable than the *cis* one and the *cis*-isomer has a faster isomerization rate than that of *trans*-isomer. No significant photo-cyclization was observed for both *cis* and *trans*-PEG550-TPE-Chol after 10 min of illumination (nearly no new  $^1\text{H}$  NMR signals appears at 6.7 -6.8 ppm).<sup>16,28</sup>

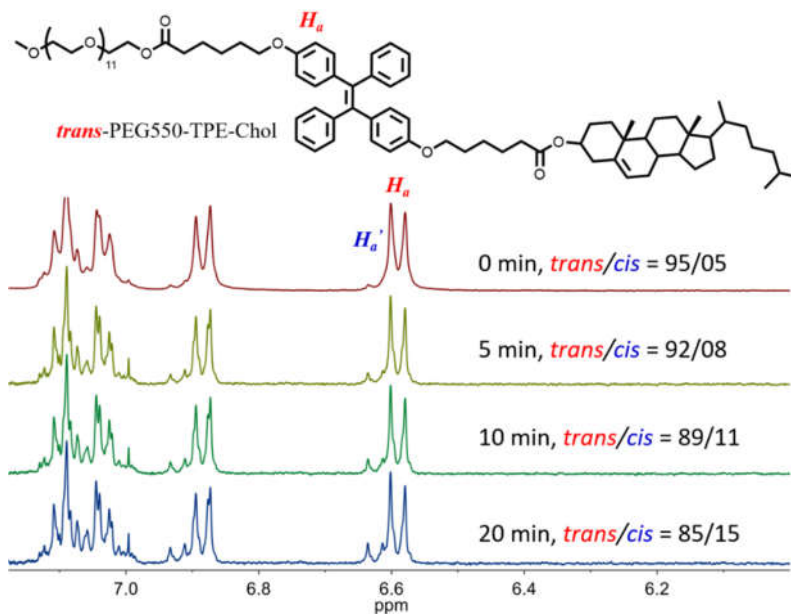


**Figure 2.15.** Chemical structure and partial  $^1\text{H}$  NMR spectra of *trans*-PEG550-TPE-Chol in  $\text{CDCl}_3$  upon weak UV light (365 nm,  $0.5 \text{ mW/cm}^2$ ) as a function of time.  $T = 25^\circ\text{C}$ . After 2 min of illumination, no photoisomerization can be detected. After 10 min of illumination, *trans*-PEG550-TPE-Chol undergo 6% of isomerization.

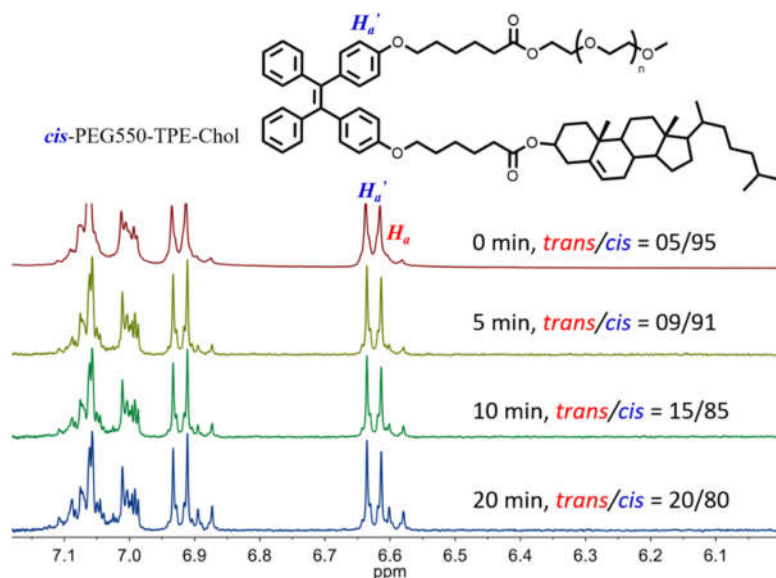


**Figure 2.16.** Chemical structure and partial  $^1H$  NMR spectra of *cis*-PEG550-TPE-Chol in  $CDCl_3$  upon weak UV light (365 nm, 0.5 mW/cm<sup>2</sup>) as a function of time. T= 25°C. After 2 min of illumination, no photoisomerization can be detected. After 10 min of illumination, *cis*-PEG550-TPE-Chol undergo 10% of isomerization, respectively.

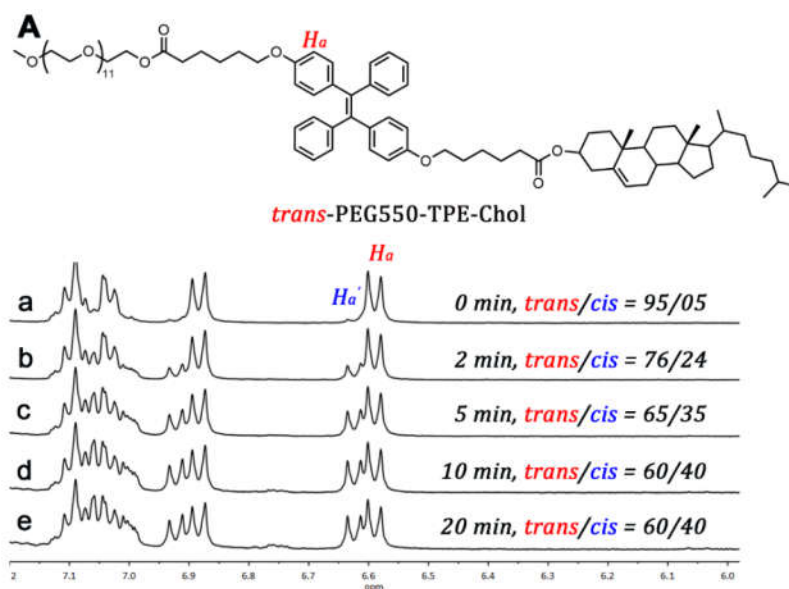


**Figure 2.17.** Chemical structure of *trans*-PEG550-TPE-Chol, and partial  $^1H$  NMR spectra of *trans*-PEG550-TPE-Chol in  $CDCl_3$  after UV irradiation (365 nm, 15 mW/cm<sup>2</sup>) with different duration: (a) t = 0 min, (b) t = 2 min, (c) t = 5 min, (d) t = 10 min, (e) t = 20 min.

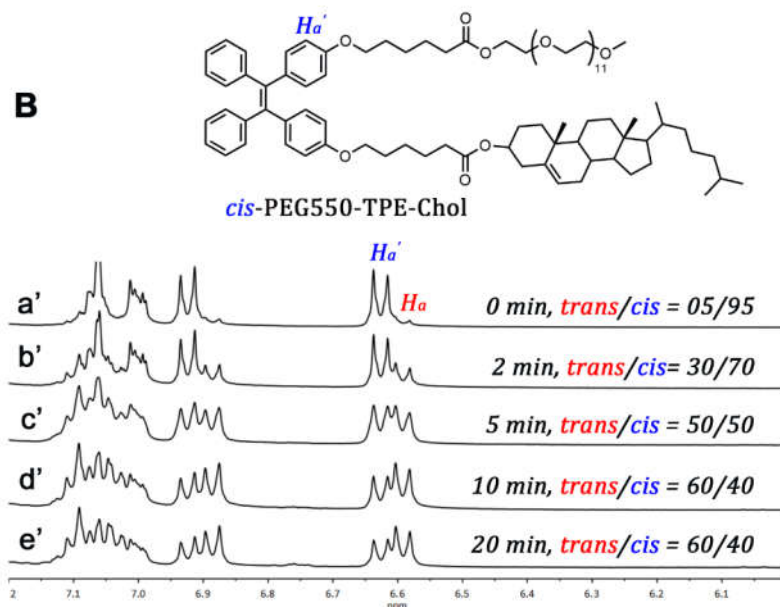


**Figure 2.18.** Chemical structure of *cis*-PEG550-TPE-Chol, and partial  $^1\text{H}$  NMR spectra of *cis*-PEG550-TPE-Chol in  $\text{CDCl}_3$  after UV irradiation (365 nm, 15  $\text{mW}/\text{cm}^2$ ) with different duration: (a')  $t = 0$  min, (b')  $t = 2$  min, (c')  $t = 5$  min, (d')  $t = 10$  min, (e')  $t = 20$  min. The abscises of all NMR spectra are scaled from 6.0 to 7.2 ppm for clarity.

### 2.3.3 Self-Assembly of *trans*- and *cis*-PEG550-TPE-Chol and their mixtures: vesicles, perforated vesicles and cylindrical micelles

Considering the molecular weight ( $M_n = 1510$  Da) of PEG550-TPE-Chol, which is higher than traditional small amphiphilic molecules like lipids, egg phosphatidylcholine or dihexadecylglycerophosphorylcholine, we prepared the vesicles using thin-film hydration method at high temperature ( $T = 65$  °C) to accelerate the sample hydration and polymer self-organization. Typically, the chloroform solution of PEG550-TPE-Chol or their stereoisomer (0.5 wt%) was uniformly deposited on the surface of a roughened Teflon plate, followed by drying in vacuum to remove all solvent and to get a thin polymer film. Then the thin film sample was hydrated with deionized water at 65 °C for 48 h in a sealed bottle. We have shown in the above section that the stereoisomers are stable at 70°C for at least 30 min of heating. Here a long heating duration (48h) being used, we first checked if there were any *trans-cis* isomerization of amphiphiles during the self-assembling process. For this purpose, the self-assemblies of *trans*- and *cis*-PEG550-TPE-Chol recovered by freeze-drying was dissolved in deuterated DMSO and analyzed by  $^1\text{H}$  NMR, respectively. As shown in Figure 2.19, the



*trans/cis* ratios of both *trans*- and *cis*-PEG550-TPE-Chol do not show any change and keep being 95/5 and 5/95, respectively, after the self-assembling process, which proved the absence of the isomerization.

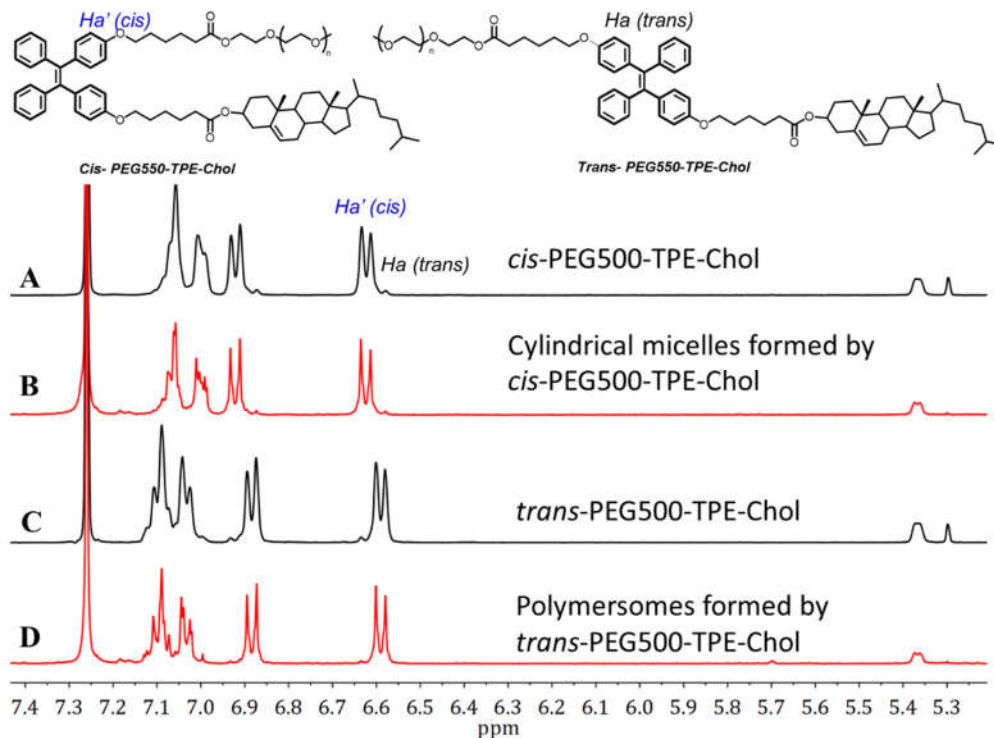


**Figure 2.19.** Partial  $^1\text{H}$  NMR spectra of *trans*- and *cis*-PEG550-TPE-Chol recovered from their self-assemblies, together with those of initial *trans*- and *cis*-PEG550-TPE-Chol polymers (400 MHz,  $\text{CDCl}_3$ ). (A) *cis*-PEG550-TPE-Chol; (B) polymer recovered from cylindrical micelles formed by *cis*-PEG550-TPE-Chol; (C) *trans*-PEG550-TPE-Chol; (D) polymer recovered from polymersomes formed by *trans*-PEG550-TPE-Chol. The self-assemblies were prepared by film hydration method at  $65^\circ\text{C}$  during 48h.

The morphologies and sizes of the self-assemblies were characterized by cryo-electron microscopy (cryo-EM) and dynamic light scattering (DLS). PEG550-TPE-Chol (*trans/cis* = 60/40) self-assembled into perforated vesicles, while *trans*-PEG550-TPE-Chol self-assembled into normal vesicles and *cis*-PEG550-TPE-Chol into cylindrical micelles (Figure 2.20-2.22). Their statistical sizes distributions by DLS are shown in Figure 2.23, which indicate multimodal size distributions, especially for vesicles of *trans*-isomer with sizes from 80 nm to 5  $\mu\text{m}$ . Indeed, different sizes of vesicles were observed as shown in Figure 2.21. Because the DLS analysis is based on spherical models and gives hydrodynamic diameters ( $D_h$ ) of



spherical particles, the data for *cis*-PEG550-TPE-Chol do not reflect the real size of long cylindrical micelles. The length of cylindrical micelles reaches several hundreds of nanometers until several micrometers, and some closed loops are also visible (see Figure 2.22).

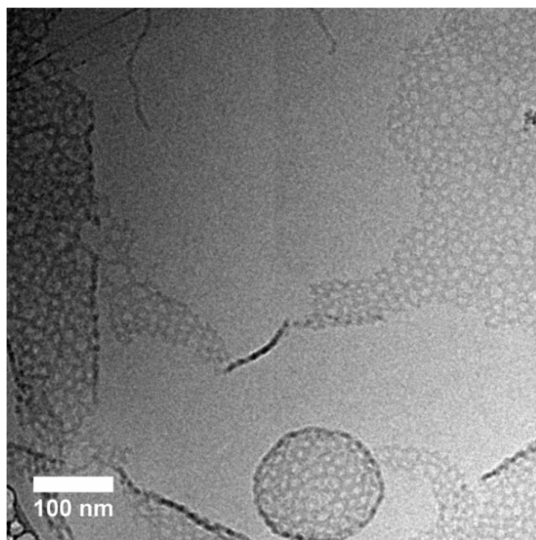


**Figure 2.20.** Supplemental cryo-EM images of self-assemblies in water of PEG550-TPE-Chol synthesized without stereoisomer separation containing isomers at inherent ratio of *trans/cis* = 60/40.

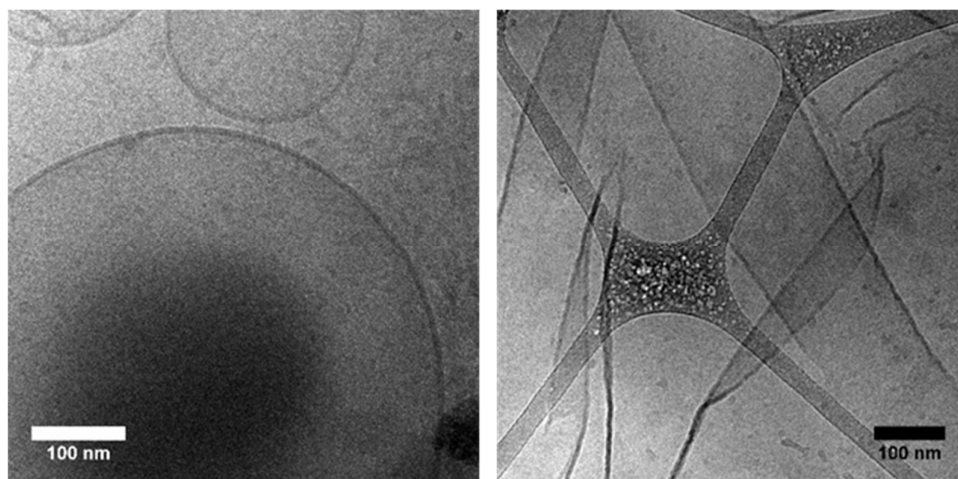


**Figure 2.21.** Supplemental cryo-EM images of *trans*-PEG550-TPE-Chol self-assemblies in water.

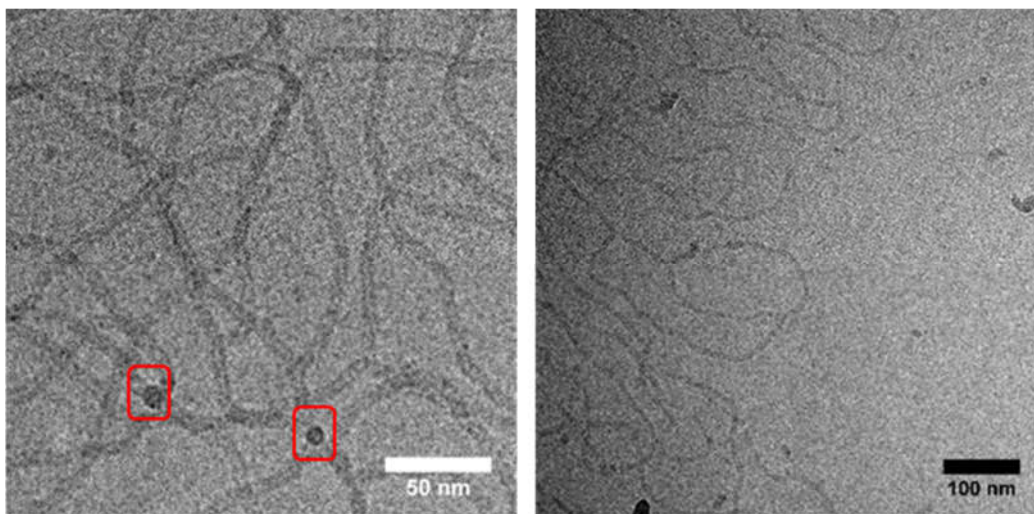


**Figure 2.22.** Supplemental cryo-EM images of *cis*-PEG550-TPE-Chol self-assemblies in water. The squares indicate the round ends of the cylindrical micelles.

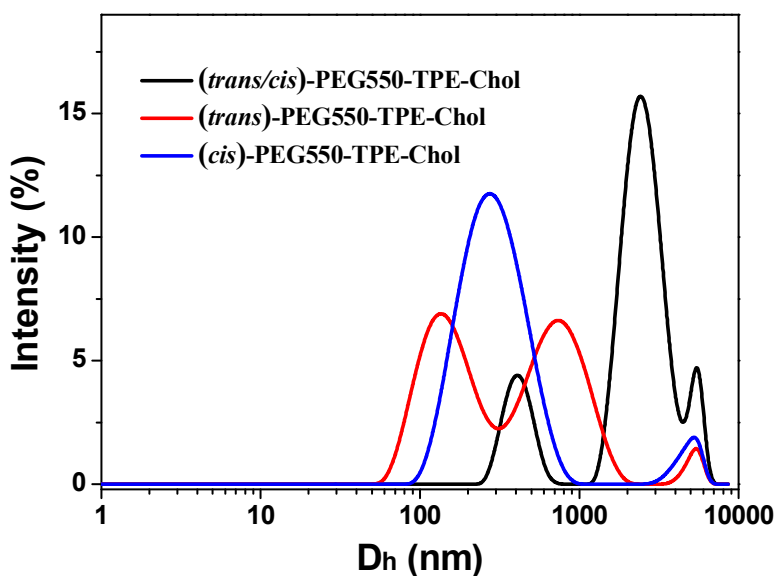


**Figure 2.23.** Distributions of hydrodynamic diameters measured by DLS for self-assemblies formed by PEG550-TPE-Chol, *trans*-PEG550-TPE-Chol and *cis*-PEG550-TPE-Chol with film hydration method.

Note that the trace amount of *cis*-isomer (5%) in the *trans*-PEG550-TPE-Chol did not influence the formation of vesicles, which represent the absolute majority of the morphologies. Meanwhile, *cis*-PEG550-TPE-Chol formed only cylindrical micelles despite the presence of 5% *trans*-isomer according to the collected cryo-EM images. The membrane thickness of vesicles and the diameter of cylindrical micelles were evaluated from the FWHM (Full Width

at Half Maximum) of the electronic density profile perpendicular to the membrane through statistical analysis of about 30 different vesicles in the cryo-EM images. The thickness of vesicle membrane for *trans*-PEG550-TPE-Chol was measured as  $7.5 \pm 0.5$  nm, the diameter of cylindrical micelles for *cis*-PEG550-TPE-Chol as  $6.5 \pm 0.5$  nm and the thickness of the membrane of perforated vesicles for PEG550-TPE-Chol as  $7.3 \pm 0.5$  nm.

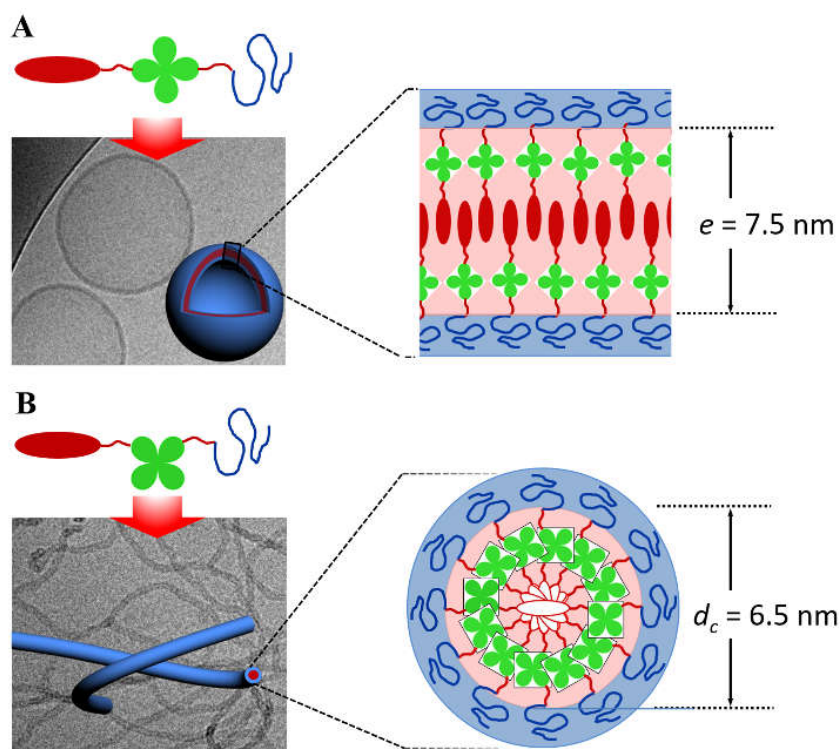


**Figure 2.24.** The morphologies models of polymersomes (A) and cylindrical micelles (B) formed by *trans*-isomer and *cis* isomer, respectively. The red ellipsoid represents the cholesterol moiety, and the green trefoil the TPE group. The red line represents the aliphatic spacer, and the blue line the PEG550 chain. In the cylindrical micelle model, empty red ellipsoids are used to represent the cholesterol moiety in order to highlight molecular organization along the cylinder long axis.

When the stereo-structure changes from *trans*- to *cis*-type, the morphological transition of self-assemblies from vesicles to cylindrical micelles should be driven by the minimization of the interfacial energy. Following qualitatively the theory of Israelachvili *et al.*<sup>29,30</sup>, the packing parameter  $p = v/al$  of *trans*-PEG550-TPE-Chol in aqueous solution should be around 1 for vesicle formation, while the  $p$  value of *cis*-PEG550-TPE-Chol should be smaller and approach

$l/2$  for cylindrical micelle formation (where  $v$  is the hydrophobic volume,  $a$  the optimal interfacial area, and  $l$  the length of the hydrophobic block normal to the interface). Here, the chemical structures are the same for both isomers, so their steric shapes dictate their packing parameter in the self-assemblies. A schematic representation of their self-assembly and packing is given in Figure 2.24.

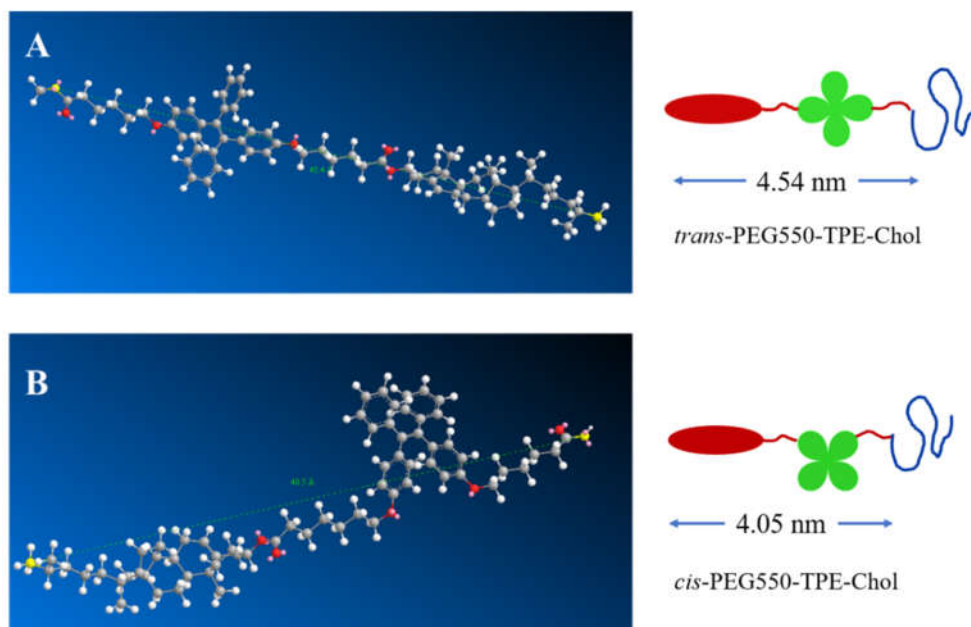


**Figure 2.25.** The plausible molecular models of the hydrophobic part proposed for (A) *trans*-PEG-TPE-Chol and (B) *cis*-PEG-TPE-Chol in the bilayer membranes and cylindrical micelles. The red ellipsoid represents the cholesterol moiety, and the green trefoil the TPE group. The red line represents the aliphatic spacer C6, and the blue line the PEG550 chain. The lengths of hydrophobic parts were estimated by Chem3D.

The plausible molecular models of the hydrophobic part for *trans*- and *cis*-PEG-TPE-Chol at extend state are illustrated in Figure 2.25, with the lengths of  $l_{trans} = 4.54$  nm and  $l_{cis} = 4.05$  nm. The thickness of vesicle membrane ( $e = 7.5$  nm) is between  $l_{trans}$  (4.54 nm) and  $2l_{trans}$  (9.08 nm), the diameter of cylindrical micelles ( $d_c = 6.5$  nm) is also between  $l_{cis}$  (4.05) and  $2l_{cis}$  (8.10 nm). Therefore, both *trans*- and *cis*-PEG-TPE-Chol in the bilayer membrane and in the cylindrical micelles should be packed in the interdigitated way as shown in Figure 2.24A and 2.24B. Cholesterol is a versatile building block which supports the formation of bilayer membranes<sup>31</sup> and fibril structures<sup>32,33</sup> due to its molecular rigidity, self-assembling nature, asymmetric carbons, *etc.* For the cylindrical micelles formed by *cis*-PEG-TPE-Chol, along the

cylindrical axis the cholesterol moieties turn around this axis to form the cylindrical micelles, whose cross-section is round as shown in squares in Figure 2.22.

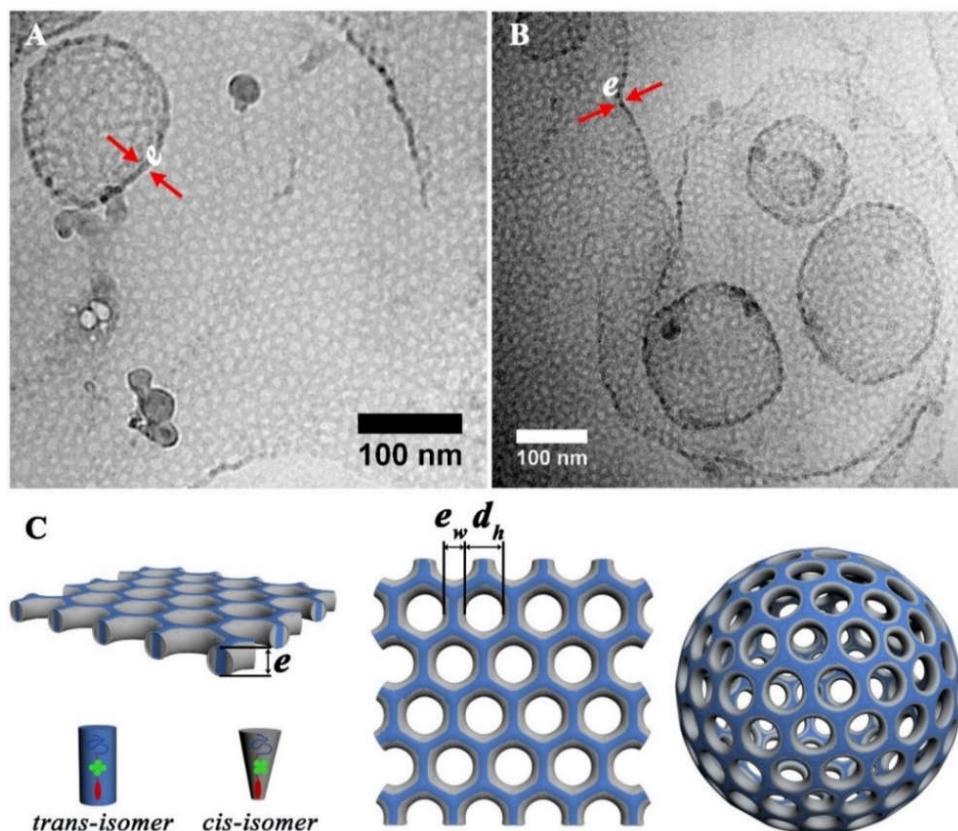


**Figure 2.26.** (A, B) Cryo-EM images of self-assemblies obtained from *trans*- and *cis*-PEG550-TPE-Chol mixtures intentionally prepared at the ratio  $trans/cis = 60/40$ . (C) Schematic representation of perforated membrane and nano-porous polymersomes. The blue cylinder represents the critical packing shape of membrane-forming *trans*-PEG550-TPE-Chol which are preferentially assembled in flatter areas in assemblies. The grey truncated cone refers to the critical packing shape of micelle-forming *cis*-PEG550-TPE-Chol which probably which are predominately aggregated at the edges of holes owing higher curvature.

Interestingly the PEG550-TPE-Chol forms perforated membranes and vesicles, similarly to the mixture of small molecular amphiphiles, e.g., C16TAC and EPC.<sup>3</sup> The novelty here is that PEG550-TPE-Chol is a stereoisomers-mixture synthesized as one compound, simply and inherently without the tedious separation of intermediates *trans*- and *cis*-isomers during the synthetic procedure. Further, we prepared artificially the mixtures of both stereoisomers to get

*trans/cis* ratio of 60/40, the same as inherently synthesized PEG550-TPE-Chol, and then performed the self-assembling by film hydration in the identical conditions. Figure 2.26 shows the representative morphologies of its self-assemblies observed by cryo-EM, which are the same as those obtained with inherently synthesized PEG550-TPE-Chol (Figure 2.19).

The scenario of porous membrane formation can be explained as follows. Micelle-forming *cis*-isomers in a bilayer membrane try to impose a positive curvature on the constituent monolayers (leaflets). The monolayers may remain united to a flat bilayer only up to a critical concentration of the micelle-forming *cis*-isomers. Above this critical point, edges may form, which would contain predominately the micelle-forming *cis*-isomers and assemble into hemicylindrical structures with a negative curvature (the holes). With *trans/cis* ratio of 60/40, the hole part and strand part have similar proportion in the mesh-like membrane. Table 2.1 summarizes the measured values for bilayer membrane thickness ( $e$ ), cylindrical micelle diameters ( $d_c$ ), pore diameter ( $d_h$ ) and the minimal wall thickness ( $e_w$ ) between two pores (see Figure 2.26 for the definition). We found  $e_w \geq d_c$ , which means the narrowest place of the wall is almost composed of the cross-section of two face-to-face hemicylinders.

**Table 2.1.** Size characterization of different morphologies of *trans/cis* isomers and mixtures by cryo-EM

Sample	Membrane thickness $e$ (nm)	Cylindrical micelle diameter $d_c$ (nm)	Pore diameter $d_h$ (nm)	Pore wall thickness $e_w$ (nm)
<i>trans</i> -PEG550-TPE-Chol ( <i>trans/cis</i> = 95/5)	$7.5 \pm 0.5$	-	-	-
Isomers mixture ( <i>trans/cis</i> = 60/40)	$7.3 \pm 0.5$	-	9.0 – 27.0	6.9 – 7.6
<i>cis</i> -PEG550-TPE-Chol ( <i>trans/cis</i> = 5/95)	-	$6.5 \pm 0.5$	-	-



### 2.3.4 AIE and photo-responsive properties of polymersomes, perforated polymersomes, and cylindrical micelles

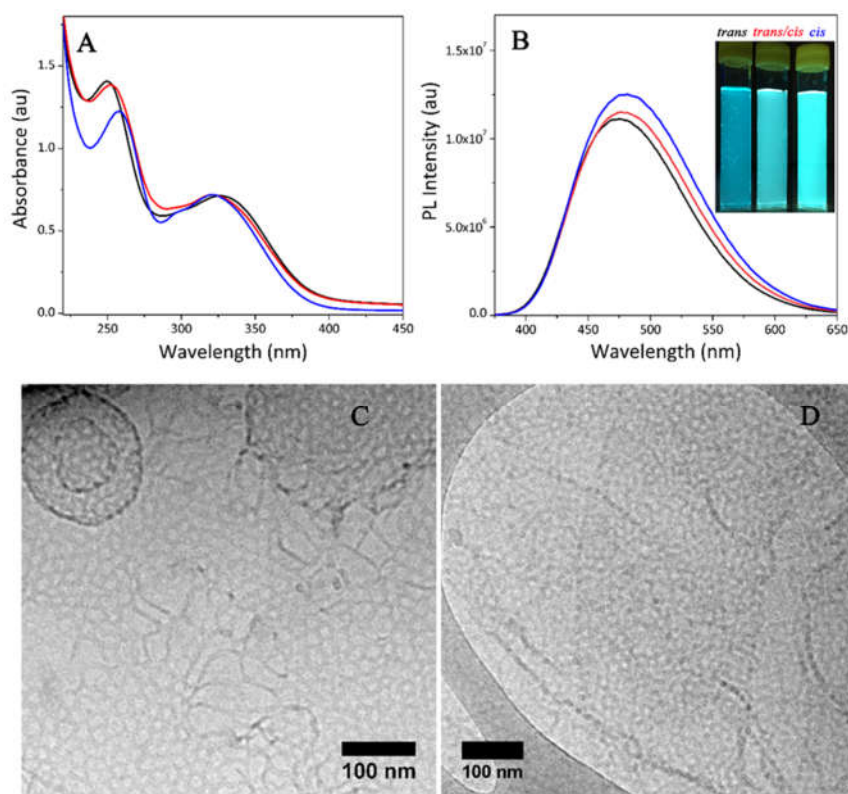


**Figure 2.27.** (A) The UV-visible absorption spectra of *trans* assemblies (black line), *cis* assemblies (blue line) and the assemblies formed by *trans/cis* mixtures (*trans/cis* = 60/40) (red line). (Concentration:  $6,7 \times 10^{-2}$  mg/ml). (B) The photoluminescence (PL) spectra of *trans* assemblies (black line), *cis* assemblies (blue line) and the assemblies formed by *trans/cis* mixtures (*trans/cis* = 60/40) (red line). (concentration:  $6.7 \times 10^{-2}$  mg/ml; excitation wavelength: 352 nm,  $0.5 \text{ mW/cm}^2$ ). The inset photos are the dispersions of self-assemblies taken under 365 nm UV light ( $0.5 \text{ mW/cm}^2$ ). (C) and (D) Cryo-EM images of perforated membranes and vesicles obtained by irradiation of vesicles of *trans*-PEG550-TPE-Chol (C) and of cylindrical micelles of *cis*-PEG550-TPE-Chol (D) after 30 min of irradiation by UV light ( $365 \text{ nm}$ ,  $15 \text{ mW/cm}^2$ ).

All self-assemblies of both *trans*- and *cis*-PEG550-TPE-Chol, as well as of their mixtures are fluorescent under UV light because of TPE moieties. Once the TPE self-assembled in hydrophobic domain of nanostructures, the physical constraints and space limitations enable to restrict the intramolecular rotation of phenyl groups around the single bonds in TPE. Under

UV illumination, the non-radiation decay of excited TPE is locked and the radiative decay channel turns on, consequently nanostructures become efficiently emissive. Their UV-visible absorption spectra and fluorescence spectra are shown in Figure 2.27. The quantum yields are 0.12 and 0.15 for *trans*- and *cis*-PEG550-TPE-Chol assemblies, respectively.

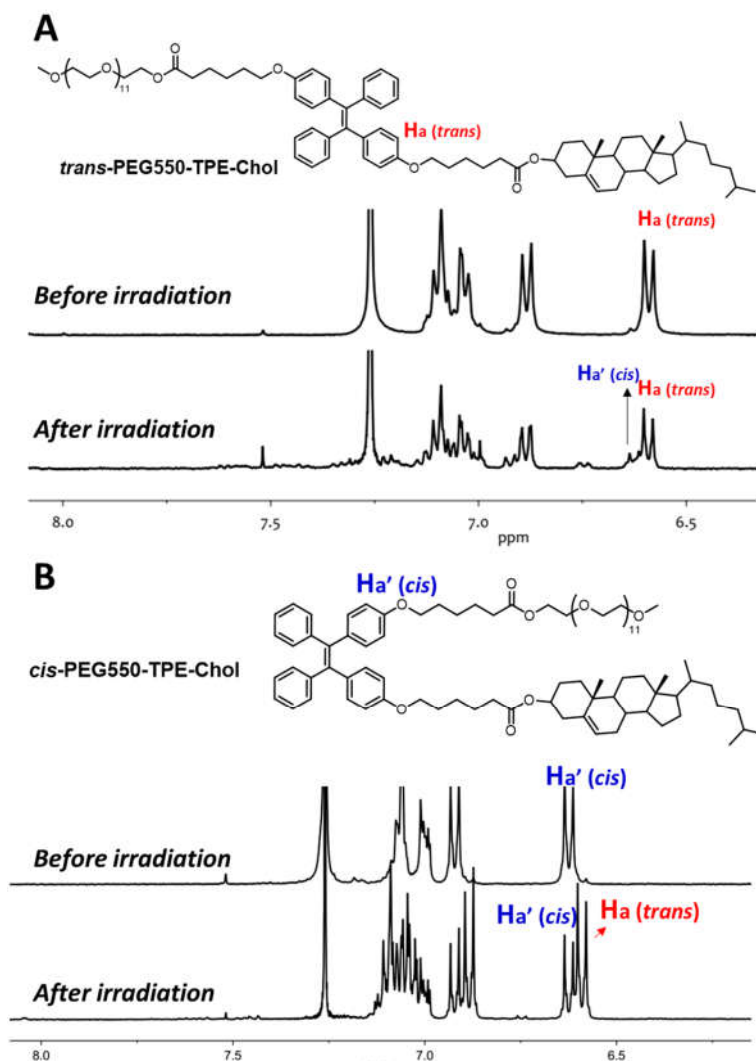


**Figure 2.28.**  $^1\text{H}$  NMR spectra of polymers recovered from polymersomes of *trans*-PEG-TPE-Chol (A) and from cylindrical micelles of *cis*-PEG-TPE-Chol (B) before and after irradiation under UV light (365 nm, 15 mW/cm<sup>2</sup>) for 30 min. The self-assemblies were freeze-dried and then solubilized in  $\text{CDCl}_3$  to recover the polymers.

Since both *trans*- and *cis*- isomers can undergo *trans*-to-*cis* and *cis*-to-*trans* isomerization under UV illumination, we have also studied the morphological transformation of their self-assemblies under UV light of higher intensity. Typically, the aqueous dispersions of self-



assemblies of *trans*- and *cis*-PEG550-TPE-Chol were exposed to UV light (365 nm, 15 mW.cm<sup>-2</sup>) for 30 min, respectively. One part of the irradiated sample was investigated by cryo-EM, and the rest was first freeze-dried and then solubilized in CDCl<sub>3</sub> for analysis by <sup>1</sup>H NMR. <sup>1</sup>H NMR spectra (Figure 2.28) show that after UV illumination, the *trans/cis* ratios in both samples become 60/40, in agreement with the results obtained in solution samples exposed to UV light (Figure 2.17 and 2.18).

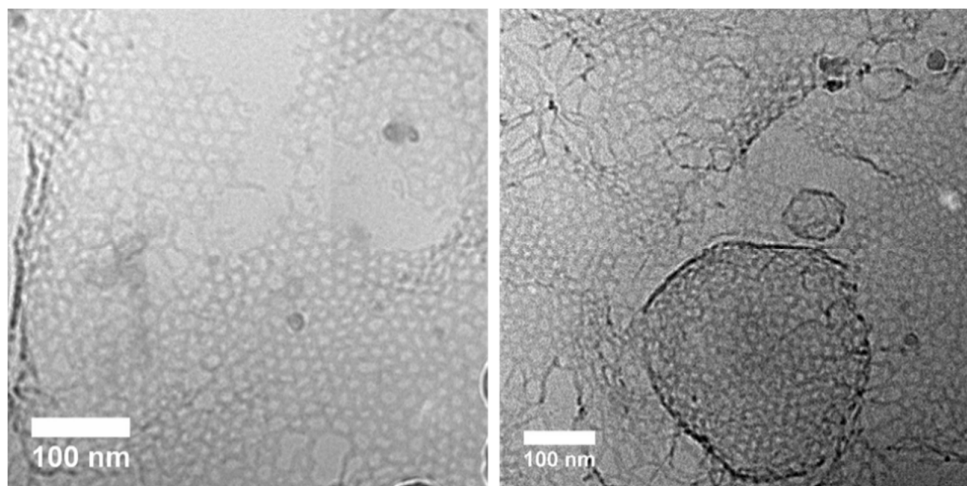


**Figure 2.29.** Supplemental cryo-EM images of polymersomes of *trans*-PEG550-TPE-Chol after 30 min of irradiation by UV light (365 nm, 15 mW/cm<sup>2</sup>).

It is also notable that photocyclization of TPE moiety begin to occur as a trace of new peak emerged at 6.7 -6.8 ppm for both *cis* and *trans*-PEG550-TPE-Chol after 30 min illumination (Figure 2.28). Cryo-EM images of both UV treated samples are shown in Figure 2.27C and 2.27D. More images are given in Figure 2.29 and 2.30. Polymersomes of *trans*-PEG550-TPE-Chol initially with homogeneous and smooth surface were perforated by the *cis*-isomers resulted from the photoisomerization, while cylindrical micelles of *cis*-PEG550-TPE-Chol under UV interweaved to form meshes and perforated membranes because of the appearance of *trans*-isomers. The perforated membranes obtained from cylindrical micelles were less structured (Figure 2.27D) than those from smooth vesicles, probably for the kinetic reason, *i.e.*, because of the slow rate of the fusion between separated cylindrical micelles. As expected, perforated polymersomes and membranes from *trans/cis* mixtures of PEG550-TPE-Chol did not show significant change upon UV light exposure (see cryo-EM images in Figure 2.31), because of simultaneous *trans*-to-*cis* and *cis*-to-*trans* isomerization.

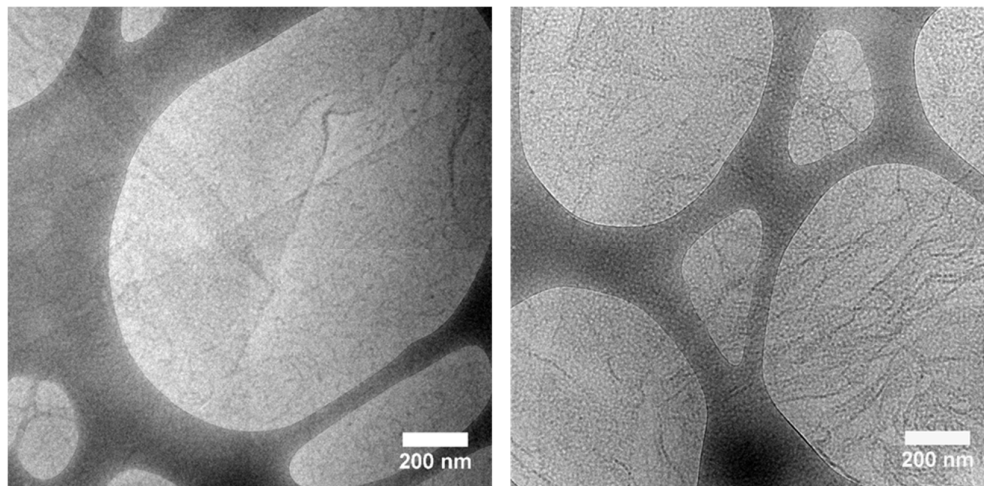


**Figure 2.30.** Supplemental cryo-EM images of cylindrical micelles of *cis*-PEG550-TPE-Chol after 30 min of irradiation by UV light (365 nm, 15 mW/cm<sup>2</sup>).

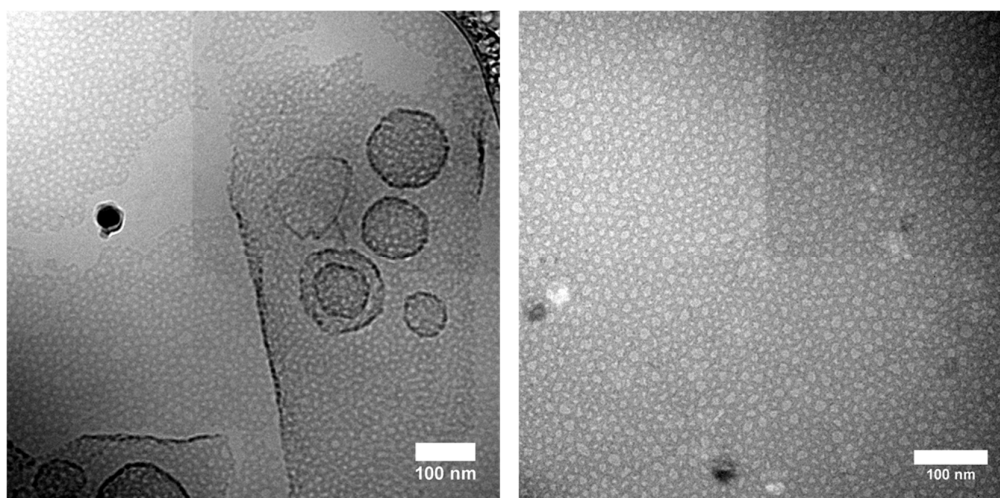


**Figure 2.31.** Cryo-EM images of perforated vesicles and membranes of *trans/cis* mixture of PEG550-TPE-Chol (*trans/cis* = 50/50) after 30 min of irradiation by UV light (365 nm, 15 mW/cm<sup>2</sup>).

The transition from the closed to open states (with pores of 9-27 nm diameters) for polymersomes formed by *trans*-PEG550-TPE-Chol, triggered by UV light, indicated that this kind of polymersomes could be used to encapsulate guest molecules of big sizes and release them in a controlled way. The tetramethylrhodamine isothiocyanate–dextran (TRITC-Dextran, MW = 4400 Da) was used as a model molecule for test. The details of encapsulation and release experiments were described Figure 2.32 demonstrates the release percentages after 0,

15 and 30 min of UV irradiation, 50% of TRITC-Dextran being released after 30 min of irradiation.

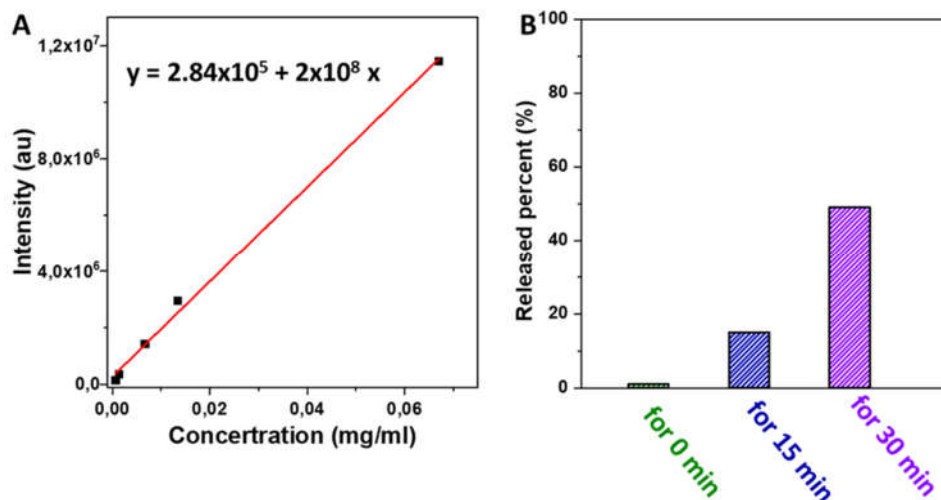


**Figure 2.32.** (A) The fluorescence intensity of TRITC-Dextran water solutions at 570 nm (excitation wavelength = 490 nm) as a function of TRITC-Dextran concentration. (B) The release percentage of TRITC-Dextran from *trans*-PEG550-TPE-Chol polymersomes as a function of irradiation time.

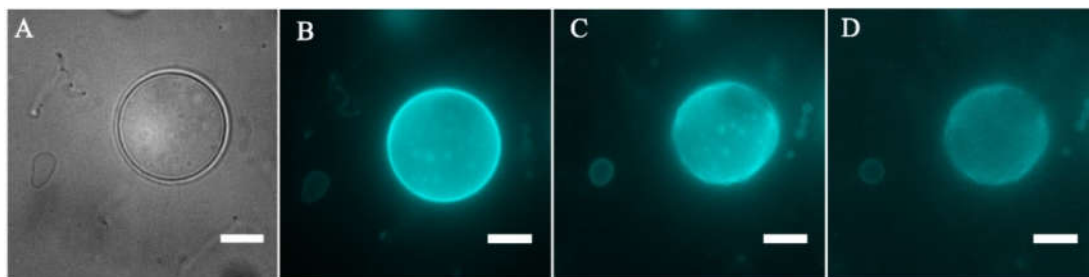


**Figure 2.33.** Epifluorescence optical microscopic images of giant vesicles of PEG550-TPE-Chol. (A) Bright field. (B-D) Fluorescence images under continuous UV illumination at  $t = 0$  (B),  $t = 40$  sec (C) and  $t = 60$  sec (D). The exposure time of each picture was 300  $\mu$ sec. Scale bar = 10  $\mu$ m. LED-UV (365 nm) was used for illumination. The focused intensity on the sample was 15 mW/cm<sup>2</sup>.

Big morphologies like giant vesicles and large membranes also co-existed with nanostructures in PEG550-TPE-Chol self-assemblies as shown in Figure 2.26. Cryo-EM allows to detect the nanostructures in detail, but it cannot visualize the giant structures wholly. Therefore, epifluorescence optical microscopy was also used for observation of the giant vesicles formed by PEG550-TPE-Chol (Figure 2.33). Under UV light, giant vesicles are cyan

fluorescent as shown in Figure 2.33. With the increase of UV illumination time, the membrane becomes fluctuating, probably because the hole parts and strand parts interchange continuously resulting from the simultaneous *trans-cis* and *cis-trans* isomerization in PEG550-TPE-Chol.

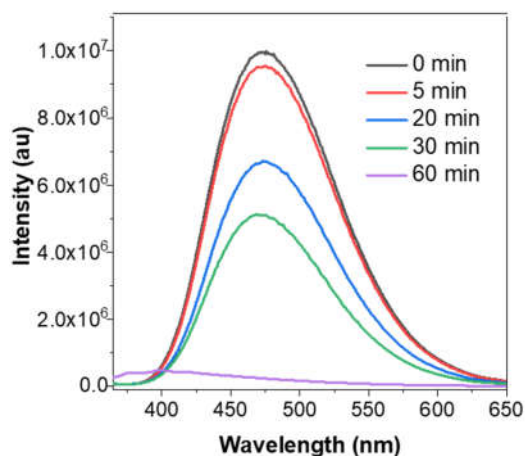


**Figure 2.34.** Photoluminescence spectra of polymersomes of PEG550-TPE-Chol before (black line) and after irradiation under UV light (365 nm, 15 mW/cm<sup>2</sup>) for different time.

Even with this high intensity UV of 15 mW/cm<sup>2</sup>, the fluorescence intensity only decreased, but not quenched, after 5 min of illumination (Figure 2.34), demonstrating good photostability of AIE polymersomes. Further, the fluorescence will be greatly decreased after 60 min illumination due to the cyclization<sup>21</sup> of the TPE moiety (Figure 2.34-2.36). TPE and its derivatives had been observed to undergo photo-cyclization both in solution and in the solid state upon irradiation by UV light (Figure 2.35). The cyclization further proved by the NMR spectra of assemblies as function of irradiation time. As shown in Figure 2.36, a new <sup>1</sup>H NMR signals appears at 6.7 -6.8 ppm after 30 min irradiation. Further irradiation the signal Ha totally disappear, indicating the fully cyclization of the TPE moiety in *trans*-TPE550-TPE-Chol after 60 min irradiation.

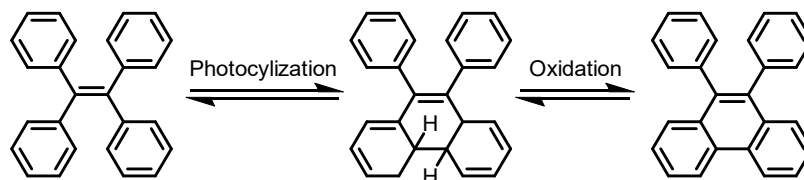


**Figure 2.35.** Typical photo-cyclization process of TPE.

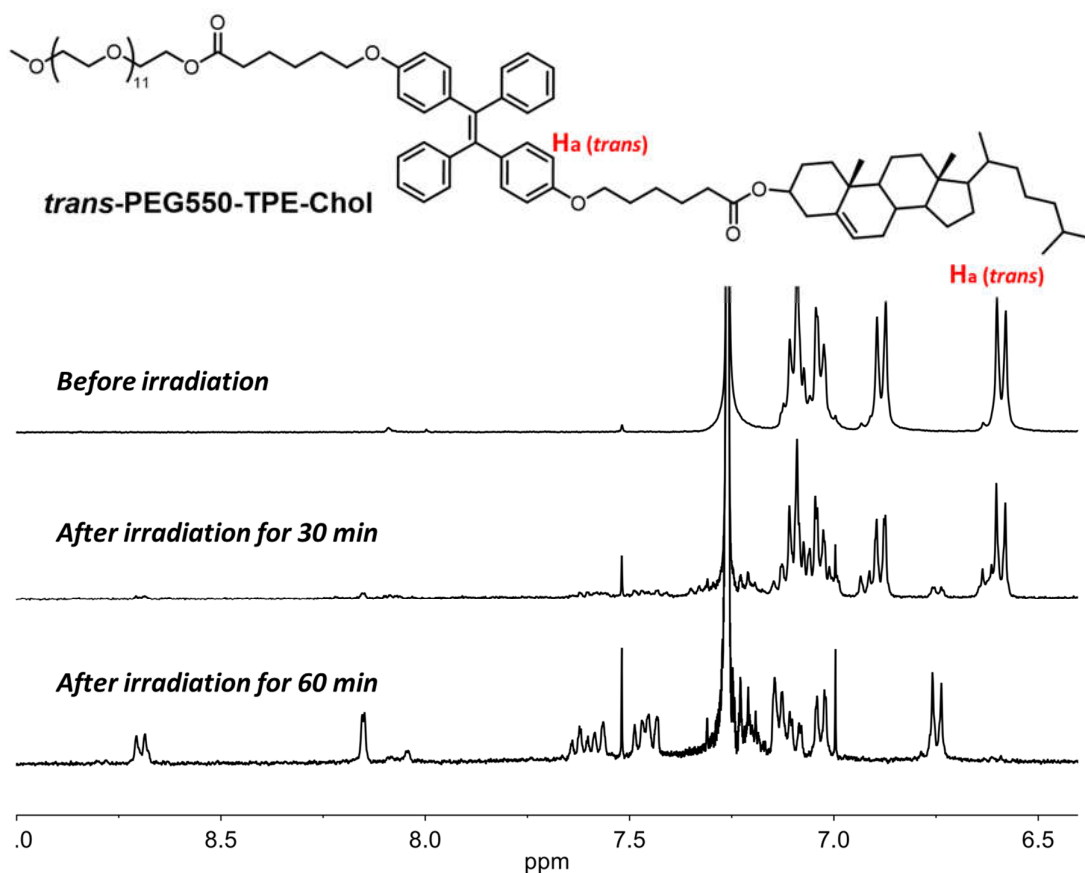


**Figure 2.36.**  $^1\text{H}$  NMR spectra of polymers recovered from polymersomes of *trans*-PEG-TPE-Chol before and after irradiation under UV light (365 nm, 15 mW/cm<sup>2</sup>) for 30 min and 60 min. The self-assemblies were freeze-dried and then solubilized in CDCl<sub>3</sub> to recover the polymers.

## 2.4 Conclusion

We have shown stereoisomer-directed self-assemblies: *trans*-PEG550-TPE-Chol formed normal vesicles, *cis*-PEG550-TPE-Chol formed cylindrical micelles, and PEG550-TPE-Chol synthesized without isomers' separation (*trans/cis* = 60/40) formed perforated vesicles and membranes with the pores size of 9 - 27 nm. Similar nano-porous vesicles were also obtained by self-assembling the artificial mixture of *trans*- and *cis*-PEG550-TPE-Chol in the ratio of *trans/cis* = 60/40.

All these self-assemblies exhibited AIE fluorescence under UV illumination of normal intensity for observation and imaging (typically < 0.5 mW/cm<sup>2</sup>). With stronger UV intensity (15 mW/cm<sup>2</sup>) and longer illumination time (2 - 30 min), photo-responsive features were recorded due to *trans*-to-*cis* and *cis*-to-*trans* photo-isomerization. Smooth vesicles of *trans*-

PEG550-TPE-Chol were perforated by the *cis*-isomers stemmed from the photoisomerization, while cylindrical micelles of *cis*-PEG550-TPE-Chol interweaved to form meshes and perforated membranes. Nano-porous vesicles of PEG550-TPE-Chol upon strong UV light exposure did not show significant change in nanoscale, but in micrometer scale membrane fluctuation was observed by epifluorescence microscopy.

The vesicles of *trans*-PEG550-TPE-Chol can be considered as light-gated polymersomes, where pores of 9-27 nm were generated under strong UV illumination ( $15 \text{ mW/cm}^2$ ). It can be used to perform traced transportation under weak UV light and controlled release of small molecules ( $< 30 \text{ nm}$ ) under stronger UV light. Nano-porous polymersomes and polymer membranes are also promising for applications that require nano-pores as channels for material transportation. We speculate that the nano-porous polymersomes may be used as capsules for the culture of multicellular spheroids which are considered as good *in-vitro* models of micro-tissues like tumors or neurons<sup>10,34</sup>. All nutrients (proteins and oxygen) required for cell division can diffuse freely through the capsule membrane and allow proliferation of the encapsulated cells. Meanwhile, since PEG is by nature cell-repellent, cells form cellular aggregates, *i.e.*, multicellular spheroids. Organ-on-chip tissue engineering may be possible using these nano-porous giant polymersomes.

## References

- 1 Angelescu, D. G. & Linse, P. Viruses as supramolecular self-assemblies: modelling of capsid formation and genome packaging. *Soft Matter* **4**, 1981-1990 (2008).
- 2 Myschik, J. *et al.* On the preparation, microscopic investigation and application of ISCOMs. *Micron* **37**, 724-734 (2006).
- 3 Edwards, K., Gustafsson, J., Almgren, M. & Karlsson, G. Solubilization of lecithin vesicles by a cationic surfactant: intermediate structures in the vesicle-micelle transition observed by cryo-transmission electron microscopy. *J. Colloid Interface Sci.* **161**, 299-309 (1993).
- 4 Almgren, M. Stomatosomes: perforated bilayer structures. *Soft Matter* **6**, 1383-1390 (2010).
- 5 Ljusberg-Wahren, H. *et al.* in *The Colloid Science of Lipids* 99-104 (Springer, 1998).
- 6 van Dam, L., Karlsson, G. & Edwards, K. Direct observation and characterization of DMPC/DHPC aggregates under conditions relevant for biological solution NMR. *BBA Biomembranes* **1664**, 241-256 (2004).
- 7 Kim, J. K., Lee, E., Lim, Y. b. & Lee, M. Supramolecular capsules with gated pores from an amphiphilic rod assembly. *Angew. Chem. Int. Ed.* **47**, 4662-4666 (2008).
- 8 Berlepsch, H. v. *et al.* Controlled self-assembly of stomatosomes by use of single-component fluorinated dendritic amphiphiles. *Soft matter* **14**, 5256-5269 (2018).

- 9 Alessandri, K. *et al.* A 3D printed microfluidic device for production of functionalized hydrogel microcapsules for culture and differentiation of human Neuronal Stem Cells (hNSC). *Lab on a Chip* **16**, 1593-1604 (2016).
- 10 Alessandri, K. *et al.* Cellular capsules as a tool for multicellular spheroid production and for investigating the mechanics of tumor progression in vitro. *Proceedings of the National Academy of Sciences* **110**, 14843-14848 (2013).
- 11 Piñol, R. *et al.* Self-assembly of PEG-b-liquid crystal polymer: the role of smectic order in the formation of nanofibers. *Macromolecules* **40**, 5625-5627 (2007).
- 12 Zhou, Y., Briand, V. A., Sharma, N., Ahn, S.-k. & Kasi, R. M. Polymers comprising cholesterol: synthesis, self-assembly, and applications. *Materials* **2**, 636-660 (2009).
- 13 Xie, Y. & Li, Z. Recent Advances in the Z/E Isomers of Tetraphenylethene Derivatives: Stereoselective Synthesis, AIE Mechanism, Photophysical Properties, and Application as Chemical Probes. *Chem. Asian J.* **14**, 2524-2541 (2019).
- 14 Peng, H.-Q. *et al.* Dramatic differences in aggregation-induced emission and supramolecular polymerizability of tetraphenylethene-based stereoisomers. *J. Am. Chem. Soc.* **139**, 10150-10156 (2017).
- 15 Peng, H. Q. *et al.* Visualizing the Initial Step of Self-Assembly and the Phase Transition by Stereogenic Amphiphiles with Aggregation-Induced Emission. *ACS Nano* **13**, 839-846 (2019).
- 16 Bunker, C. E., Hamilton, N. B. & Sun, Y. P. Quantitative application of principal component analysis and self-modeling spectral resolution to product analysis of tetraphenylethylene photochemical reactions. *Anal. Chem.* **65**, 3460-3465 (1993).
- 17 Mei, J. *et al.* Aggregation-induced emission: the whole is more brilliant than the parts. *Adv. Mater.* **26**, 5429-5479 (2014).
- 18 Mei, J., Leung, N. L., Kwok, R. T., Lam, J. W. & Tang, B. Z. Aggregation-induced emission: together we shine, united we soar! *Chem. Rev.* **115**, 11718-11940 (2015).
- 19 Li, J. *et al.* Supramolecular materials based on AIE luminogens (AIEgens): construction and applications. *Chem. Soc. Rev.* **49**, 1144-1172 (2020).
- 20 Yan, L., Zhang, Y., Xu, B. & Tian, W. Fluorescent nanoparticles based on AIE fluorogens for bioimaging. *Nanoscale* **8**, 2471-2487 (2016).
- 21 Feng, G. & Liu, B. Aggregation-Induced Emission (AIE) Dots: Emerging Theranostic Nanolights. *Acc. Chem. Res.* **51**, 1404-1414 (2018).
- 22 Mabrouk, E., Cuvelier, D., Brochard-Wyart, F., Nassoy, P. & Li, M.-H. Bursting of sensitive polymersomes induced by curling. *PNAS* **106**, 7294-7298 (2009).
- 23 del Barrio, J. *et al.* Self-Assembly of Linear-Dendritic Diblock Copolymers: From Nanofibers to Polymersomes. *J. Am. Chem. Soc.* **132**, 3762-3769 (2010).
- 24 Cui, Z.-K. *et al.* Nonphospholipid Fluid Liposomes with Switchable Photocontrolled Release. *Langmuir* **30**, 10818-10825 (2014).
- 25 Liu, D., Wang, S., Xu, S. & Liu, H. Photocontrollable Intermittent Release of Doxorubicin Hydrochloride from Liposomes Embedded by Azobenzene-Contained Glycolipid. *Langmuir* **33**, 1004-1012 (2017).

- 26 Li, L. *et al.* Smart azobenzene-containing tubular polymersomes: fabrication and multiple morphological tuning. *Chem. Commun.* **56**, 6237-6240 (2020).
- 27 Zhang, C. J. *et al.* Structure-Dependent cis/trans Isomerization of Tetraphenylethene Derivatives: Consequences for Aggregation-Induced Emission. *Angew. Chem. Int. Ed.* **128**, 6300-6304 (2016).
- 28 Zhu, L. *et al.* Aggregation-Induced Emission and Aggregation-Promoted Photo-oxidation in Thiophene-Substituted Tetraphenylethylene Derivative. *Chem. Asian J.* **11**, 2932-2937 (2016).
- 29 Antonietti, M. & Förster, S. Vesicles and liposomes: a self-assembly principle beyond lipids. *Advanced Materials* **15**, 1323-1333 (2003).
- 30 Israelachvili, J. N., Mitchell, D. J. & Ninham, B. W. Theory of self-assembly of hydrocarbon amphiphiles into micelles and bilayers. *Journal of the Chemical Society, Faraday Transactions 2: Molecular and Chemical Physics* **72**, 1525-1568 (1976).
- 31 Echegoyen, L. E. *et al.* The first evidence for aggregation behavior in a lipophilic [2.2.2]-cryptand and in 18-membered ring steroidal lariat ethers. *Tetrahedron letters* **29**, 4065-4068 (1988).
- 32 Murata, K. *et al.* Thermal and light control of the sol-gel phase transition in cholesterol-based organic gels. Novel helical aggregation modes as detected by circular dichroism and electron microscopic observation. *Journal of the American Chemical Society* **116**, 6664-6676 (1994).
- 33 Jung, J. H., Shinkai, S. & Shimizu, T. Nanometer-level sol-gel transcription of cholesterol assemblies into monodisperse inner helical hollows of the silica. *Chemistry of materials* **15**, 2141-2145 (2003).
- 34 Simkiss, K. & Wilbur, K. M. *Biomineralization*. (Elsevier, 2012).





## Chapter III. Polymersomes with Hexagonal Nano-Porous Structures in the Membrane

### 3.1 Introduction

Structuring pores into stable membrane of capsules and controlling their opening are extremely useful for applications that require nano-pores as channels for material exchange and transportation, such as organ-on-chip tissue engineering.<sup>1,2</sup> However, the number of experimental and theoretical researches in perforated vesicles is still limited. In the chapter II, we reported on the development of AIE polymersomes with randomly packed pores in the membrane from the self-assembly of *trans* and *cis* mixtures of PEG550-TPE-Chol (the isomer mixtures simply noted as PEG550-TPE-Chol). Here, we describe the preparation of AIE nanoporous polymersomes where the nanopores are structured in a hexagonal lattice instead of randomly packed state. They are self-assembled from a new amphiphilic copolymer of *trans* and *cis* mixture of PEG550-SS-TPE-SS-Chol (the isomer mixtures simply noted as PEG550-SS-TPE-SS-Chol), which is slightly different from PEG550-TPE-Chol described in the chapter II. In PEG550-SS-TPE-SS-Chol, the flexible spacers between PEG and TPE, and between Chol and TPE have one additional disulfide bond -S-S-, respectively (Figure 3.1). The PEG550-SS-TPE-SS-Chol synthesized naturally without the separation of stereoisomers contains *trans* and *cis* isomers in nearly equivalent molar ratio. They formed well-structured nanopores that self-organized into hexagonal superstructure in the membrane using thin-film hydration strategy. The hexagonal nano-porous vesicles exhibit reduction-responsive property due to the presence of disulfide bonds. The vesicles disappear after addition of dithiothreitol.

In order to have a close look on the formation mechanism of perforated membrane by *trans/cis* mixtures and the structuration of nanopores, we have studied the morphological evolution of amphiphilic polymers as function of the content of *cis* isomers. For the synthetical reason, we used *trans* and *cis*-PEG550-TPE-Chol instead of those of PEG550-SS-TPE-SS-Chol for this study (the synthesis of latter is more time consuming and I had no enough time to perform it during my thesis). A morphological evolution from vesicles, pseudo porous vesicles, porous vesicles, Y junctions, to cylindrical micelles with the increase of the *cis* proportion were observed. All the self-assemblies exhibited strong fluorescence. A few of local hexagonal organizations of the nanopores were detected in the *trans/cis* mixtures of PEG550-TPE-Chol with *trans/cis* ratio close to 50/50. We have tried to explain, from the point

of view of molecular structures, this random organization with some local hexagonal ones in the case of PEG550-TPE-Chol, and the perfect hexagonal organization in large scale in the case of PEG550-SS-TPE-SS-Chol.

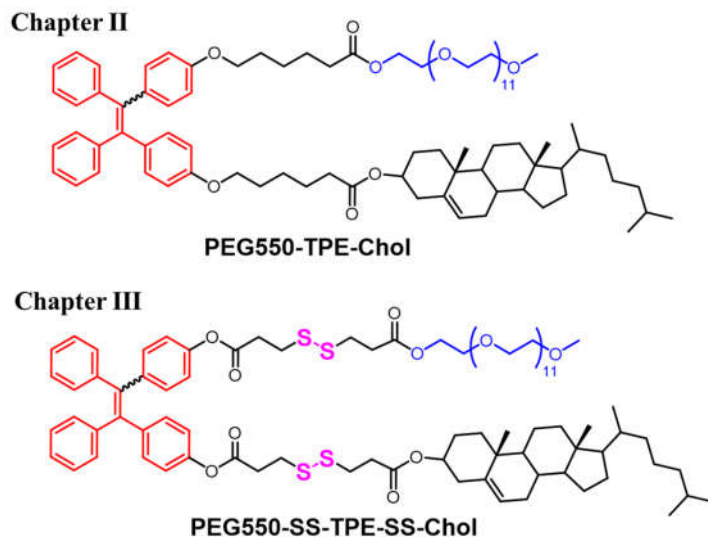


**Figure 3.1.** The chemical structure of PEG550-TPE-Chol and PEG550-SS-TPE-SS-Chol.

## 3.2 Experimental sections

### 3.2.1 Materials

4-Methoxybenzophenone ( $\geq 98\%$ ), Titanium tetrachloride ( $\text{TiCl}_4$ ,  $>98\%$ ), Boron tribromide ( $\text{BBr}_3$ ,  $>98\%$ ), 4-dimethylaminopyridine (DMAP,  $>99\%$ ), Zn Powder (2.5 cm,  $>99\%$ ), 1-(3-Dimethylaminopropyl)-3-ethylcarbodiimide hydrochloride (EDCI,  $>98\%$ ), Lithium hydroxide ( $\text{LiOH}$ ,  $\geq 98\%$ ), Cholesterol (Chol,  $>95\%$ ), Poly (ethylene glycol) methyl ether ( $\text{MeO-PEG}_n\text{-OH}$ ,  $n = 12$ ,  $M_n = 550$  Da,  $M_w/M_n = 1.01$ ) and 3,3'-Dithiodipropionic acid were purchased from Alfa Aesar. The chemical reagents were used as purchased without further purification.

### 3.2.2 Synthesis

The amphiphilic molecules PEG550-SS-TPE-SS-Chol with tetraphenylethene (TPE) at core were synthesized as shown in Scheme 3.1. The *trans/cis* -TPE-2OH were synthesized according to the literature,<sup>3</sup> and the details have already been described in Chapter II (2.3.1).

**Synthesis of TPE-SS-Chol-OH.** A mixture of TPE-2OH (2.75 mmol, 1.0 g), SS-Chol (2.60 mmol, 1.5 g), (3-dimethylaminopropyl)ethyl-carbodiimide monohydrochloride (EDCI, 3.30 mmol, 0.63 g) and 4-dimethylaminopyridine (DMAP, 3.30 mmol, 0.40 g) was dissolved in 50 mL of dichloromethane. Then the trimethylamine (11 mmol, 0.66 g) was added into the mixture. The resultant solution was stirred at room temperature for overnight. Then the organic phase was extracted with saturated NaCl aqueous for three times. The final product was purified by flash chromatography using petroleum ether and ethyl acetate (5:1 volume ratio) as eluent solvents.  $^1\text{H NMR}$  (400 MHz,  $\text{CDCl}_3$ ):  $\delta = 7.10- 6.98$  (m, 12H, *ArH*), 6.91- 6.81 (m, 4H, *ArH*), 6.57 (t, 2H,  $J(\text{H,H}) = 8.00$  Hz, *ArH*), 5.38 (s, 1H,  $\text{C}=\text{CH}$ ), 4.66 (m, 1H,  $\text{COOCH}$ ), 3.04- 2.91 (m, 6H,  $\text{CH}_2\text{CH}_2\text{SSCH}_2$ ), 2.71 (t, 2H,  $J(\text{H,H}) = 2.00$  Hz,  $\text{CH}_2\text{COO}$ ), 2.34 (d, 2H,  $J(\text{H,H}) = 8.00$  Hz,  $\text{CH}_2$ ), 2.02- 0.68 (m, 45H, alkane).

**Synthesis of HOOC-SS-TPE-SS-Chol.** A mixture of TPE-SS-Chol-OH (1.08 mmol, 1.00 g), 3,3'-dithiodipropionic acid (1.08 mmol, 0.23 g), (3-dimethylaminopropyl)ethyl-carbodiimide monohydrochloride (EDCI, 1.30 mmol, 0.20 g) and 4-dimethylaminopyridine (DMAP, 1.30 mmol, 0.16 g) was dissolved in 50 mL of dichloromethane. Then the trimethylamine (5.20 mmol, 0.31 g) was added into the mixture. The resultant solution was stirred at room temperature for overnight. Then the organic phase was extracted with saturated NaCl aqueous for three times. The product was purified by flash chromatography using petroleum ether and ethyl acetate (1:1 volume ratio) as eluent solvents.  $^1\text{H NMR}$  (400 MHz,  $\text{CDCl}_3$ ):  $\delta = 7.14- 7.00$  (m, 14H, *ArH*), 6.88- 6.83 (m, 4H, *ArH*), 5.38 (s, 1H,  $\text{C}=\text{CH}$ ), 4.66 (m, 1H,  $\text{COOCH}$ ), 3.02- 2.93 (m, 12H,  $\text{COOCH}_2\text{CH}_2\text{SSCH}_2$ ), 2.82 (t, 2H,  $J(\text{H,H}) = 8.00$  Hz,  $\text{CH}_2\text{COOH}$ ), 2.74- 2.70 (m, 2H,  $\text{CH}_2\text{COO}$ ), 2.34 (d, 2H,  $\text{CCH}_2\text{C}$ ), 2.05- 0.68 (m, 45H, alkane).

**Synthesis of PEG550-SS-TPE-SS-Chol.** To a 100 ml round flask, the TPE-SS-Chol, poly (ethylene glycol) methyl ether ( $\text{MeO-PEG}_n\text{-OH}$ ,  $M_n = 550$  Da,  $M_w/M_n = 1.01$ ), N-(3-Dimethylaminopropyl)-N-ethylcarbodiimide hydrochloride (EDCI), and 4-dimethylaminopyridine (DMAP) and 50 mL of dichloromethane was added. The solution was stirred at room temperature for overnight. Then the organic phase was extracted with 1 mol/L HCl aqueous, and then dried, filtered, evaporated. The product was purification by flash chromatography using dichloromethane and methanol (30:1 volume ratio) as eluent solvents:  $^1\text{H NMR}$  (400 MHz,  $\text{CDCl}_3$ ):  $\delta = 7.14- 6.97$  (m, 14H,*ArH*), 6.88- 6.81 (m, 4H, *ArH*), 5.37 (s, 1H,  $\text{C}=\text{CH}$ ), 4.67- 4.59 (m, 1H,  $\text{COOCH}$ ), 3.70- 3.53 (m, H for PEG), 3.37 (s, 3H,  $\text{OCH}_3$ )

3.01- 2.92 (m, 12H,  $\text{CH}_2\text{CH}_2\text{SSCH}_2$ ), 2.79- 2.69 (m, 4H,  $\text{CH}_2\text{COO}$ ), 2.33 (d, 2H,  $\text{CHCH}_2\text{C}$ ,  $J$  (H,H) = 8.00 Hz), 2.07- 0.67 (m, H for alkane).

### 3.2.3 Instruments

**Nuclear Magnetic Resonance (NMR).**  $^1\text{H}$  NMR and  $^{13}\text{C}$  NMR spectra were measured on a Bruker AV 400 and Bruker AV 500 spectrometers. Chemical shifts  $\delta$  are given in ppm and referenced to tetramethylsilane (TMS) in  $\text{CDCl}_3$  (0 ppm). High-resolution mass spectra (HRMS) were recorded on a GCT premier CAB048 mass spectrometer operating in MALDI-TOF mode.

**Size Exclusion Chromatography (SEC).** Number-average molecular weights ( $M_n$ ) of polymers were calculated by  $^1\text{H}$  NMR. Molecular weight distributions ( $M_w/M_n$ ) of polymers were estimated by size exclusion chromatography (SEC) using THF as eluent at a flow rate of 1 mL/min.

**UV-vis Spectroscopy.** UV spectra were measured on a Milton Ray Spectronic 3000 Array spectrophotometer.

**Fluorescence Emission Spectroscopy.** Photoluminescence (PL) spectra were recorded on a Horiba FluoroMax Spectrofluorometers. The sample solution in THF or acetone with concentrations of  $\sim 10^{-5}$  M was put in quartz cells with a pathlength of 1 cm.

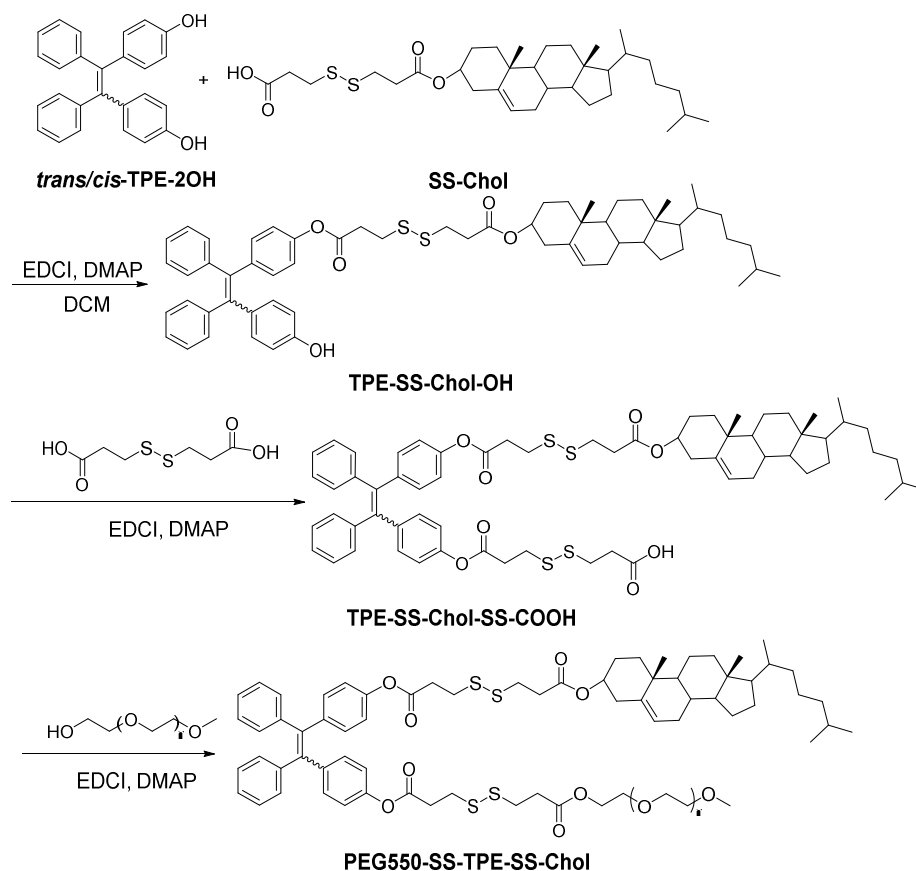
**Dynamic Light Scattering (DLS).** Hydrodynamic diameters of self-assemblies and their distributions in pure water were measured at 25 °C by dynamic light scattering (DLS, Malvern zetasizer 3000HS, UK) with a 633 nm laser. A 90° scattering angle was used for all measurements.

**Cryo-Electron Microscopy (Cryo-EM).** Self-assembled morphologies were studied by cryo-electron microscopy (cryo-EM) in Institut Curie (Orsay). Cryo-EM images were acquired on a JEOL 2200FS energy-filtered (20 eV slit) field emission gun electron microscope operating at 200 kV using a Gatan US1000 camera. For the sample preparation, a total of 5  $\mu\text{L}$  of samples were deposited onto a 200-mesh holey copper grid (Ted Pella Inc., U.S.A.) and flash-frozen in liquid ethane cooled down at liquid nitrogen temperature using a Leica EM-CPC system.

### 3.3 Results and Discussion

#### 3.3.1 Synthesis and characterization of PEG550-SS-TPE-SS-Chol

The synthesis of amphiphilic molecules PEG550-SS-TPE-SS-Chol was performed through the synthetic route as shown in Scheme 3.1. Initially, the AIEgen TPE-2OH with *trans* and *cis* isomers in nearly equivalent molar ratio were synthesized according to the literature.<sup>3</sup> The TPE-SS-Chol-OH was synthesized through an esterification reaction of TPE-2OH and SS-Chol in the presence of DMAP, EDCI and trimethylamine. With two further steps of esterification reaction, the final amphiphilic molecule PEG550-SS-TPE-SS-Chol was obtained. The Figure 3.2 indicates the <sup>1</sup>H NMR spectra of PEG550-SS-TPE-SS-Chol.



**Scheme 3.1.** The synthetic route to PEG550-SS-TPE-SS-Chol.

As no isomer separation was performed during the whole procedure to final amphiphilic molecules, the PEG550-SS-TPE-SS-Chol contains *trans* and *cis* isomers in nearly equivalent molar ratio, which was proved by the partial <sup>1</sup>H NMR spectra of PEG550-SS-TPE-SS-Chol as shown in Figure 3.3. Based on the result described in Chapter II, the double peaks at  $\delta =$

6.83 ppm correspond to *trans*- PEG550-SS-TPE-SS-Chol, while  $\delta = 6.86$  belong to its *cis* counterpart. The integral area of two resonance peak gave the ratio of *trans/cis* = 50/50.

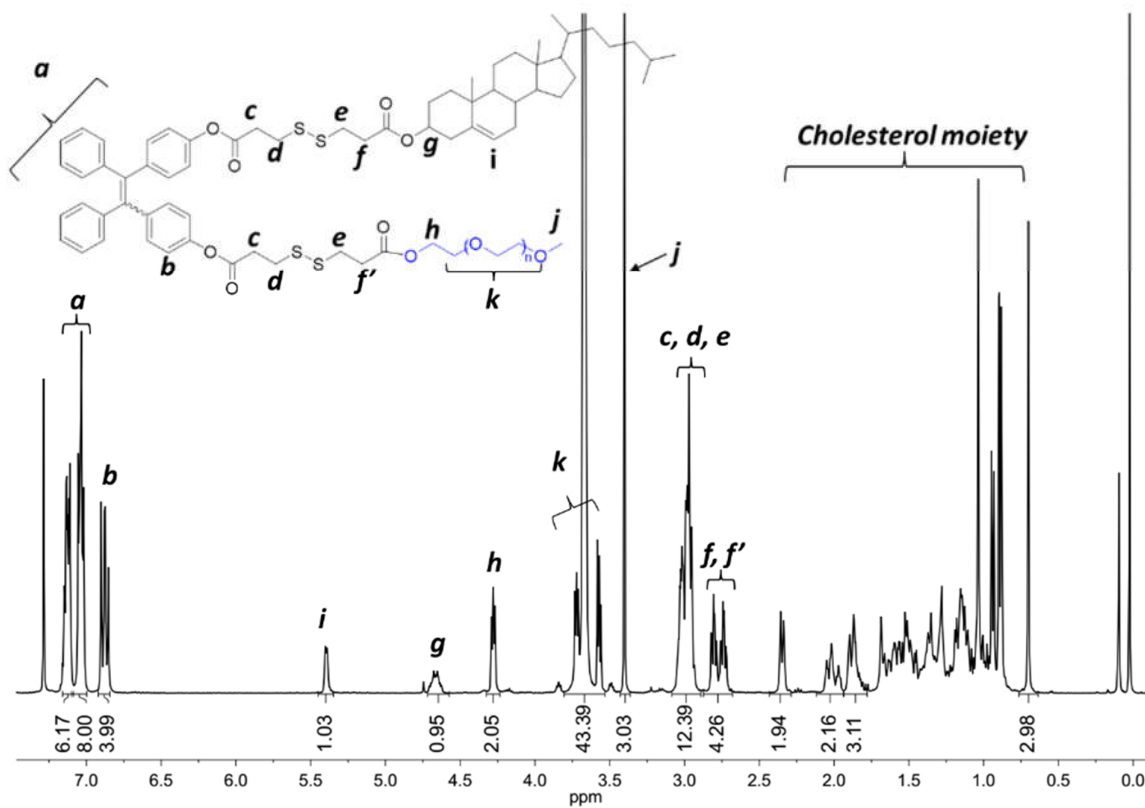


**Figure 3.2.** <sup>1</sup>H NMR spectra of PEG550-SS-TPE-SS-Chol (400 MHz, CDCl<sub>3</sub>).

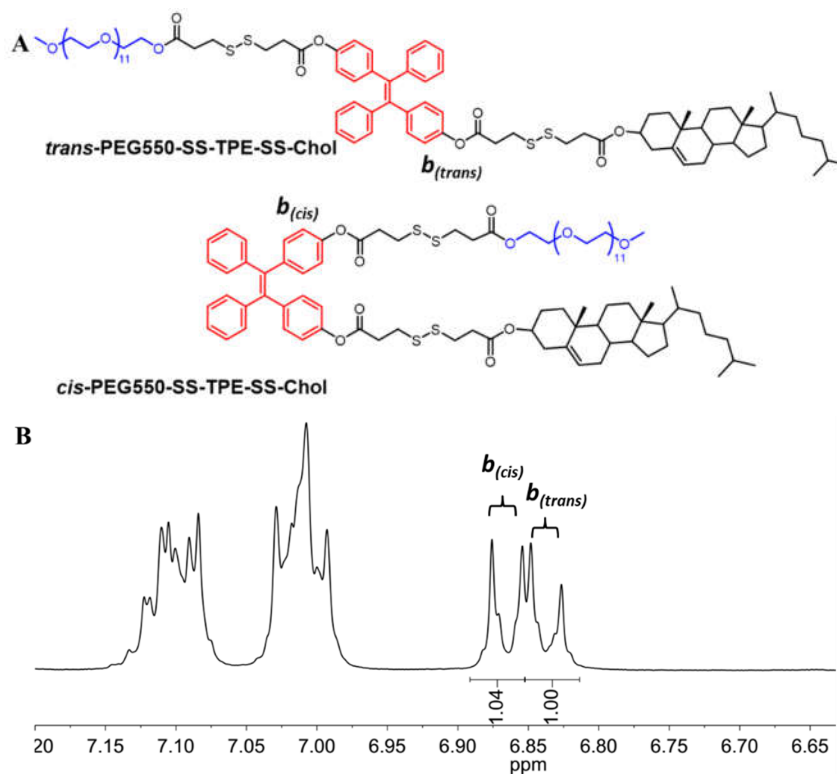


**Figure 3.3.** (A). The chemical structure of the *trans*- and *cis*-PEG550-SS-TPE-SS-Chol. (B) Partial <sup>1</sup>H NMR spectra of the *trans* and *cis* mixture of PEG550-SS-TPE-SS-Chol prepared without isomer separation (400 MHz, CDCl<sub>3</sub>).

### 3.3.2 Reduction-triggered degradation of PEG550-SS-TPE-SS-Chol

The reduction-triggered degradation of PEG550-SS-TPE-SS-Chol was studied. The PEG550-SS-TPE-SS-Chol was firstly dissolved in THF, to which the reducing agent dithiothreitol (DTT) with 10 equiv moles of disulfide bonds was added. DTT was chosen because it is a strong and cheap reducing agent. The polymer solutions were analyzed by SEC before and after addition of DTT. Their chromatogram (Figure 3.4) shows the elution peaks of copolymers shift toward the lower molecular weight side (with high elution time) after addition of the reducing agent. The original peak belongs to PEG550-SS-TPE-SS-Chol almost disappear after 24 h. This result was as expected and consistent with scission of the -S-S- link, between the PEG and the TPE, as well as between Chol and TPE due to reduction reaction.



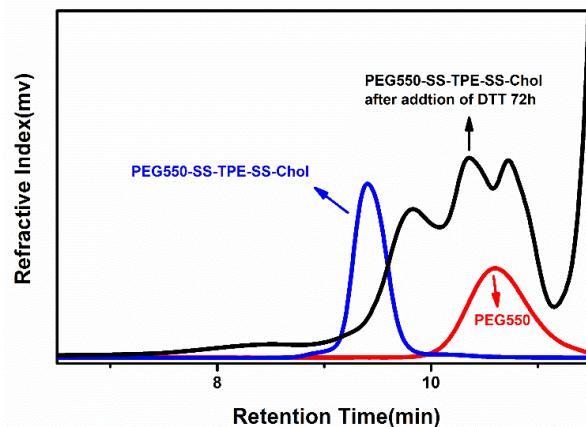


**Figure 3.4.** SEC chromatograms of PEG550 (red curve) and PEG550-SS-TPE-SS-Chol before (red curve) and after (black one) addition of DTT.

### 3.3.3 Self-assembly of PEG550-SS-TPE-SS-Chol in comparison with that of PEG550-TPE-Chol

Here, we also employed the thin-film hydration method to perform the self-assembly of PEG550-SS-TPE-SS-Chol. Typically, the chloroform solution of the amphiphilic oligomer (0.5 wt%) was uniformly deposited on the surface of a roughened Teflon plate, followed by drying in vacuum to remove all solvent and to get a thin film of amphiphilic molecules. Then the thin film sample was hydrated with deionized water at 65 °C for 48 h in a sealed bottle. The PEG550-SS-TPE-SS-Chol forms spontaneously vesicles with nanopores in the membrane. Very interestingly, the nanopores self-organize into nearly perfect hexagonal superstructure in the membrane and vesicles in large scale (Figure 3.5a-b), in contrast to the random pore organization with some local hexagonal patterns (inside red frame) in the case of PEG550-TPE-Chol (Figure 3.5c-d). More images of perforated membranes and vesicles of PEG550-SS-TPE-SS-Chol are shown in Figure 3.6-3.7. The insets with red and blue frame in Figure 3.6 are the FFT images for the red and blue rectangle parts, respectively, clearly indicating the pores in the membrane are hexagonally packed. This was further proved by the high-resolution cryo-EM images. As shown in Figure 3.7B, hexagonally packed pores could be observed. The software ImageJ was employed to deal with the high-resolution cryo-EM images. Hexagonally packed holes were clearly presented.

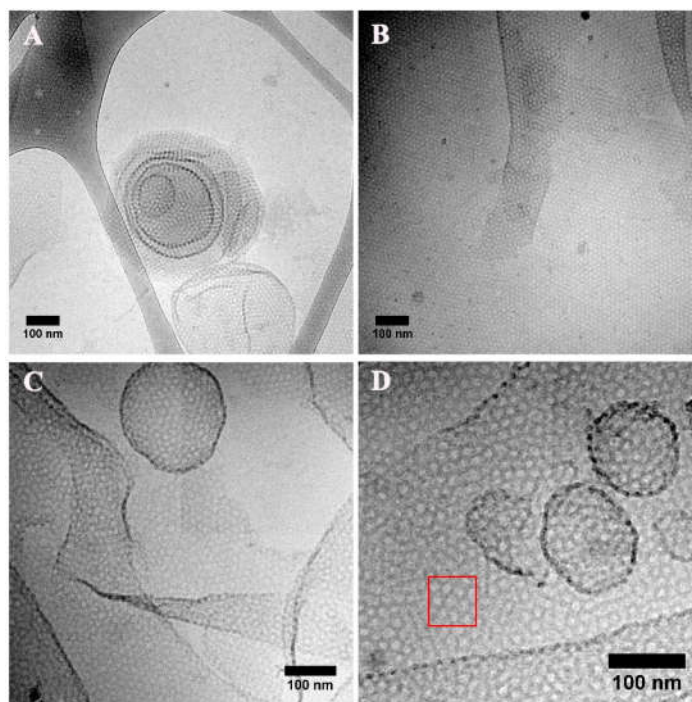


**Figure 3.5.** Cryo-EM images of membranes and vesicles formed by PEG550-SS-TPE-SS-Chol (A, B) and by PEG550-TPE-Chol (C, D). PEG550-SS-TPE-SS-Chol: *trans/cis* =50/ 50, PEG550-TPE-Chol: *trans/cis* =50/ 50.

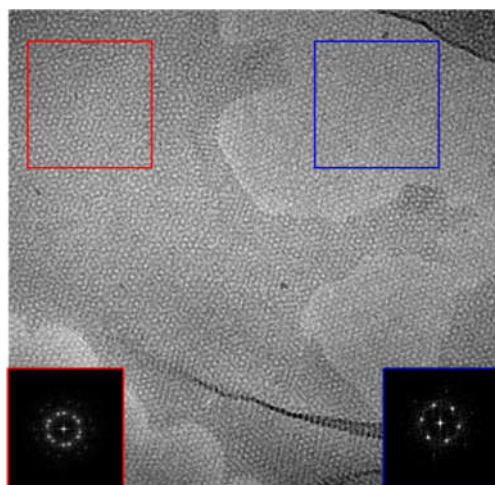


**Figure 3.6.** Cryo-EM images of PEG550-SS-TPE-SS-Chol. The inserted images with red and blue frame are the FFT for the red and blue rectangle parts, respectively. In the red part, two membranes superimposed on each other with an angle shift of a few degree ( $17\sim 21^\circ$ ) between their hexagonal lattices.

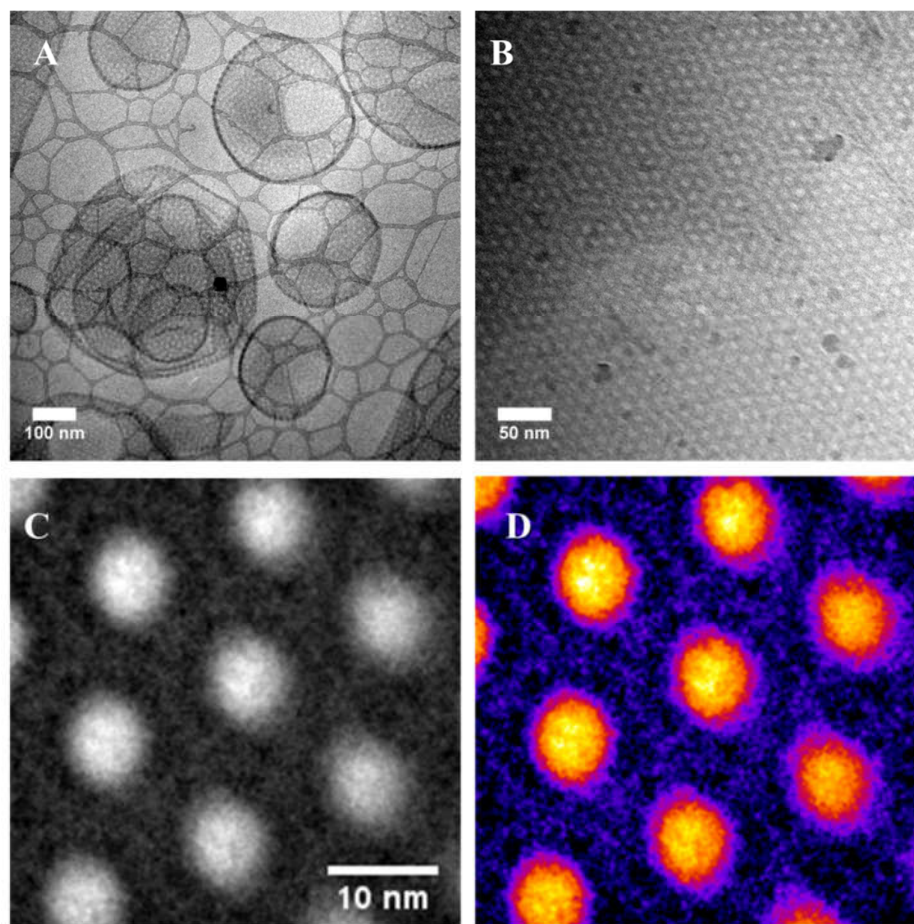


**Figure 3.7.** Cryo-EM images of self-assemblies obtained from PEG550-SS-TPE-SS-Chol with *trans/cis* ratio of 50/50. (A) and (B) are in high magnification images of 30k (A) and of 60k (B). (B) is an example of high-resolution images, which then treated with ImageJ (C, D), clearly showing the hexagonally packed pores in the membrane.

### 3.3.4 Self-assembly mechanism of nanoporous structures in the membrane

To understand the formation mechanism of perforated membrane by *trans* and *cis* mixtures, the interesting thing would be to synthesize separately *trans*- and *cis*-isomers, and then to study the self-assemblies of the mixtures of *trans*- and *cis*- isomers intentionally prepared with different relative ratios (like 25/75, 40/60, 50/50, 60/40, 75/25). For the synthetical reason, we used *trans* and *cis*-PEG550-TPE-Chol described in Chapter II for this study. The synthesis of *trans* and *cis* PEG550-SS-TPE-SS-Chol is more time consuming and I had not enough time to perform it during my thesis.

The self-assembly behaviors of *trans*-PEG550-TPE-Chol, *cis*-PEG550-TPE-Chol, and the mixtures of *trans*- and *cis*- isomers intentionally prepared with different relative ratios (25/75, 40/60, 50/50, 60/40, 75/25) are then studied carefully. The morphologies of the self-assemblies were characterized by cryo-electron microscopy (cryo-EM). As already described in Chapter II, the *trans*-PEG550-TPE-Chol self-assembled into normal vesicles and *cis*-PEG550-TPE-Chol into cylindrical micelles (Figure 3.8).

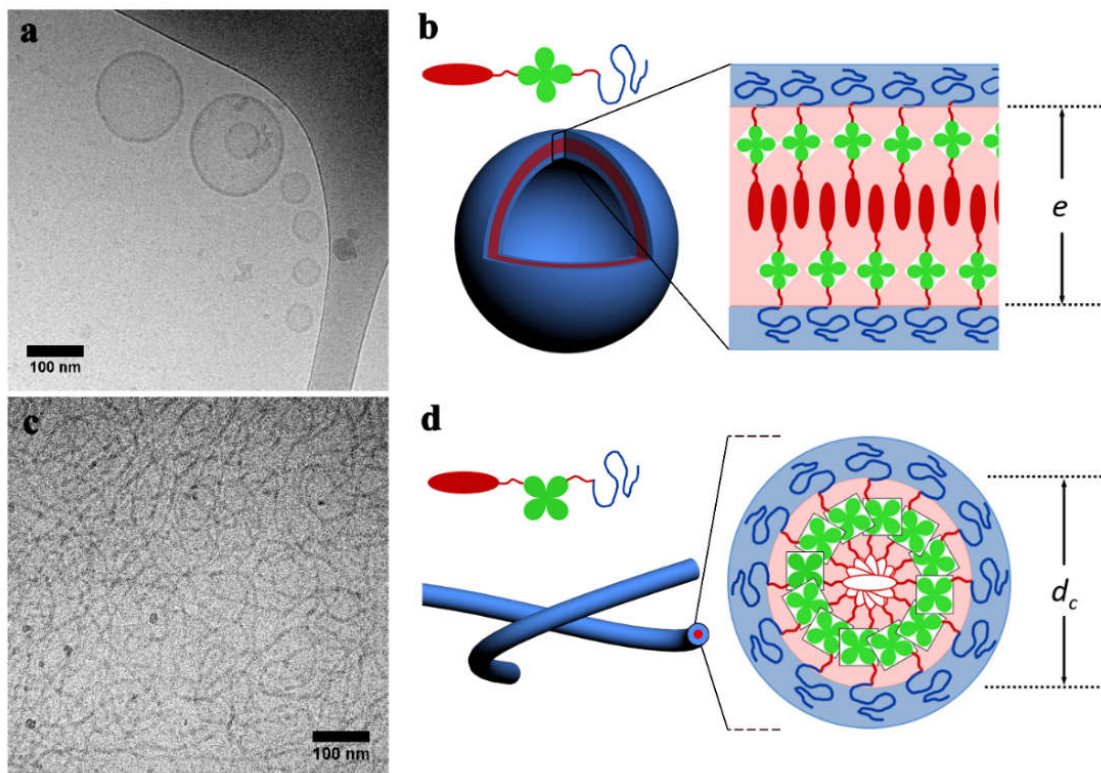


**Figure 3.8.** Cryo-EM images of nanostructures formed by *trans*-PEG550-TPE-Chol (a) and *cis*-PEG550-TPE-Chol (c). The method of thin-film hydration was used to perform the self-assembly. The molecular packing models of vesicles and cylindrical micelles are shown in b and d, respectively. The red ellipsoid represents the cholesterol moiety, and the green trefoil the TPE group. The red line represents the aliphatic spacer, and the blue line the PEG550 chain. In the cylindrical micelle model, empty red ellipsoids are used to represent the cholesterol moiety to highlight molecular organization along the cylinder long axis.

The morphological transition of self-assemblies from vesicles to cylindrical micelles should be driven by the minimization of the interfacial energy when stereo-structure changes from *trans*- to *cis*-type. Following qualitatively the theory of Israelachvili *et al.*<sup>4,5</sup>, the packing



parameter  $p = v/al$  of *trans*-PEG550-TPE-Chol in aqueous solution should be around 1 for vesicle formation, while the  $p$  value of *cis*-PEG550-TPE-Chol decreases and approaches 1/2 for cylindrical micelle formation (where  $v$  is the hydrophobic volume,  $a$  the optimal interfacial area, and  $l$  the length of the hydrophobic block normal to the interface).

Five mixtures I-V were prepared from *trans*- and *cis*-PEG550-TPE-Chol: I (*trans/cis* = 75/25), II (*trans/cis* = 60/40), III (*trans/cis* = 50/50, above-discussed), IV (*trans/cis* = 40/60), V (*trans/cis* = 25/75). Figure 3.9-3.12 shows the most representative morphologies of their self-assemblies observed by cryo-EM.

As shown in 3.9, the content of 25% of *cis*-isomer is already enough to introduce nano-pores in the membranes and vesicles, but the pore sizes are not homogeneous. 20% of pores have diameter < 7.0 nm, 55% of pores have diameter between 7.0 – 15 nm and 25% of pores have diameter >15 nm. More interestingly flat ribbons instead of cylindrical micelles and objects like octopus comprised of ribbon arms radiating from a single bilayer are evident in loose parts of meshes (see Figure 3.9B). Note that the ribbons with large side perpendicular to image plate appear blacker than those with large side parallel to image plate (see Figure 3.9B and its inset). It is clear that in the mixture of *trans/cis* = 75/25, *cis*-rich domains appear, which form the hemicylindrical structures of edges of interwoven ribbons and of the holes in porous vesicles (see inset of schematic illustration in Figure 3.9D).

When the contents of *trans*- and *cis*- isomers are more balanced, such as *trans/cis* = 60/40, 50/50 and 40/60, perforated membranes and vesicles (include small and giant ones) are the main morphologies (Figure 3.10). Interestingly, in the case of *trans/cis*=50/50, holes in the membrane tend to organize locally in hexagonal structure (see structure inside the red frames in Figure 3.11).

When *cis*- isomers become dominant like *trans/cis* = 25/75, we observed a lot of cylindrical micelles and a few of interwoven ribbons (meshes) (Figure 3.12). In this stage, since the curvature is low in the junctions of interwoven ribbons, there may be a gradual enrichment of vesicles-forming *trans* isomers at these points (see inset of schematic illustration in Figure 3.12D). Finally, in *cis*-isomer, only cylindrical micelles were observed (Figure 3.8B).

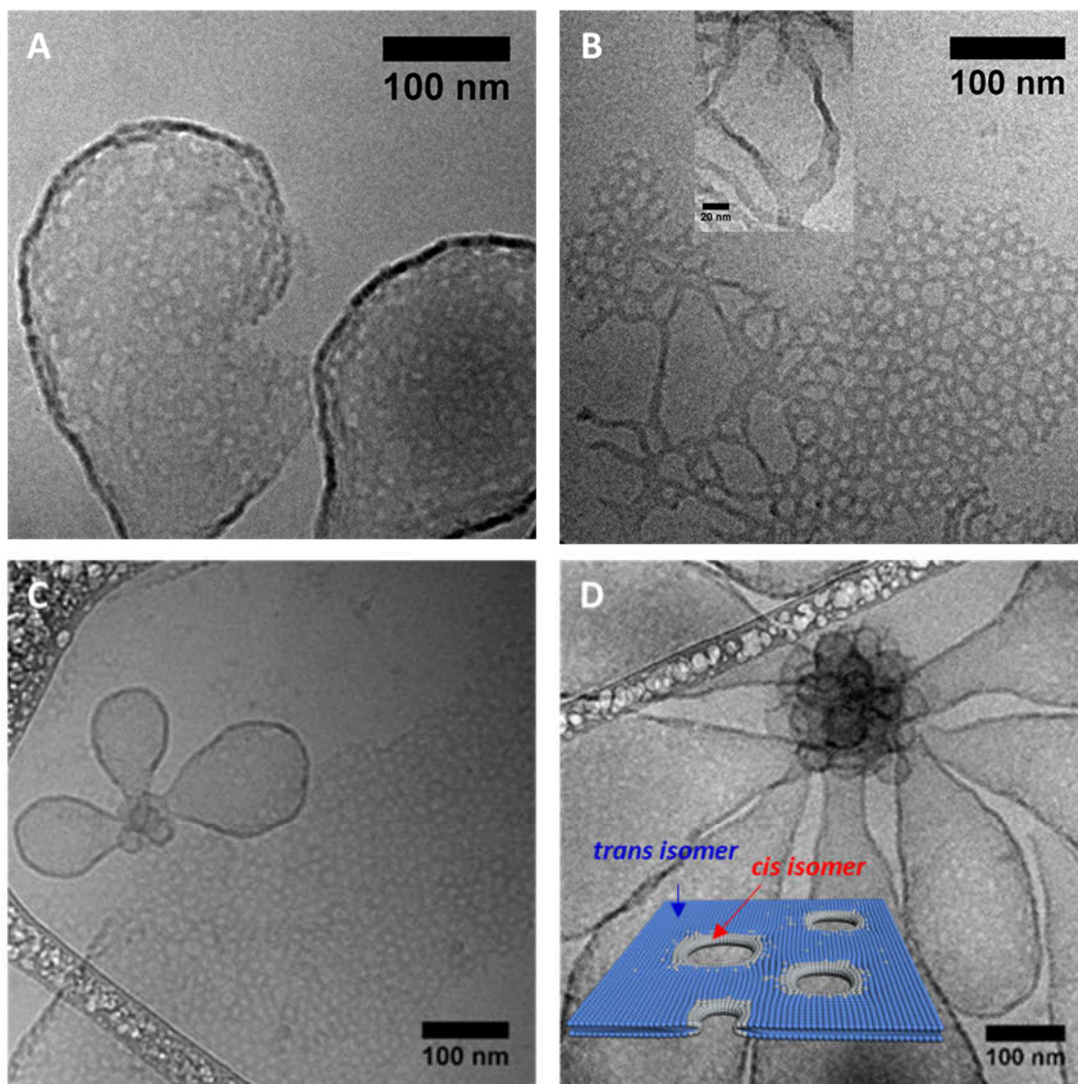


**Figure 3.9.** Cryo-EM images of the assemblies of Mixture I ( $trans/cis = 75/25$ ). The inset in D is the schematical illustration of porous membrane, indicating the possible position of different isomer within the assemblies. The blue dots represent the vesicles-forming *trans*-PEG550-TPE-Chol, which is preferably assembled in flatter areas with low curvature. The gray dots refer to the micelles-forming *cis*-PEG550-TPE-Chol, which are likely aggregated at the edges of holes with high curvature.

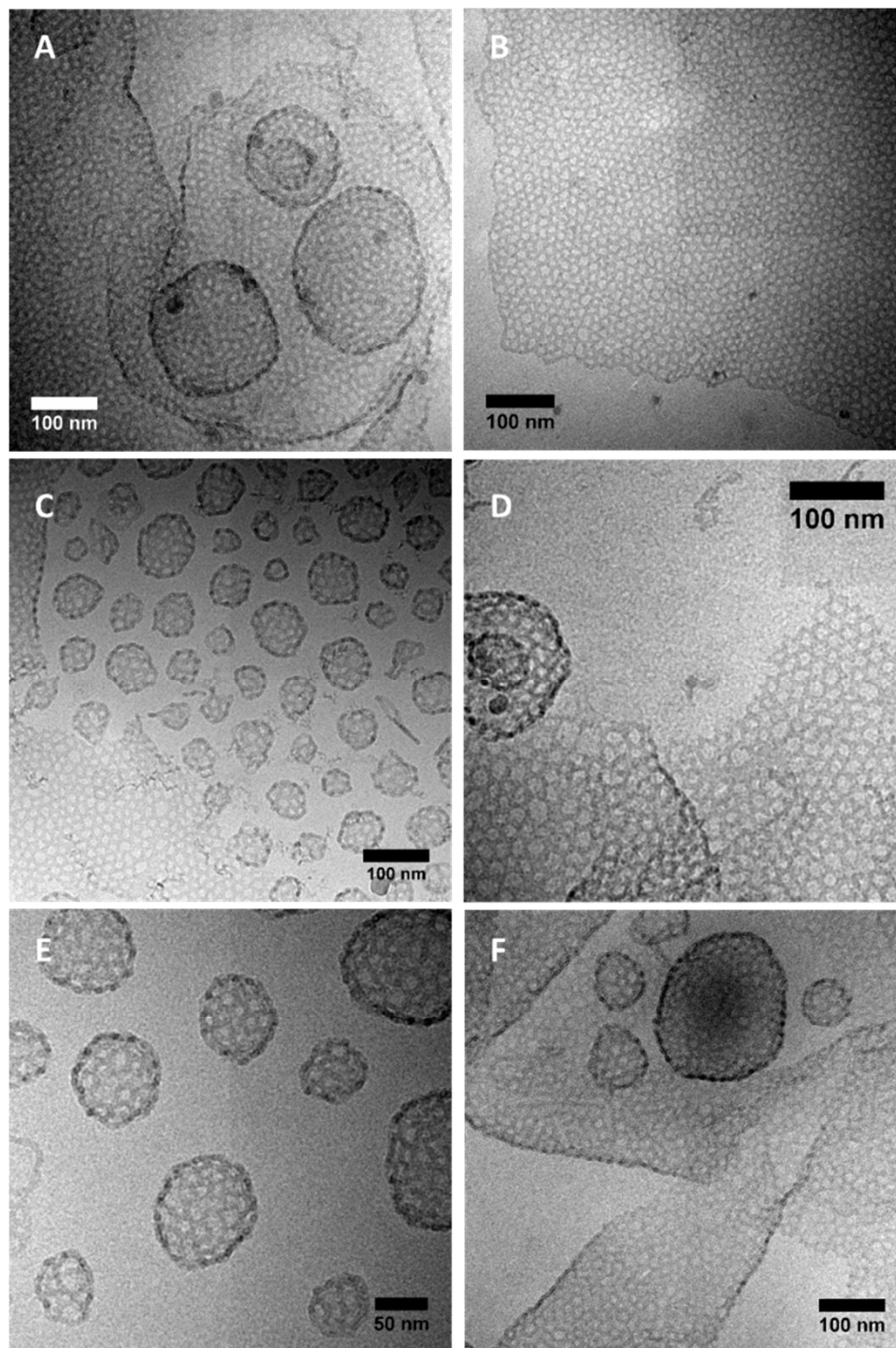


**Figure 3.10.** Cryo-EM images of the assemblies of (A, B) Mixture II (*trans/cis* = 60/40), (C, D) Mixture III (*trans/cis* = 50/50) and (E, F) Mixture IV (*trans/cis* = 40/60).

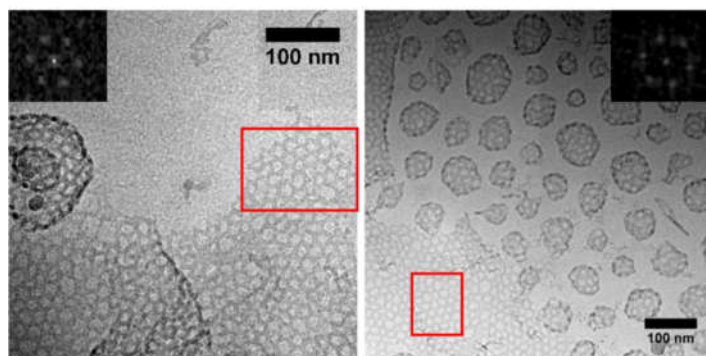


**Figure 3.11.** Cryo-EM images of the assemblies of Mixture III ( $trans/cis=50/50$ ). the inserted images are the FFT for the red rectangle parts, respectively.

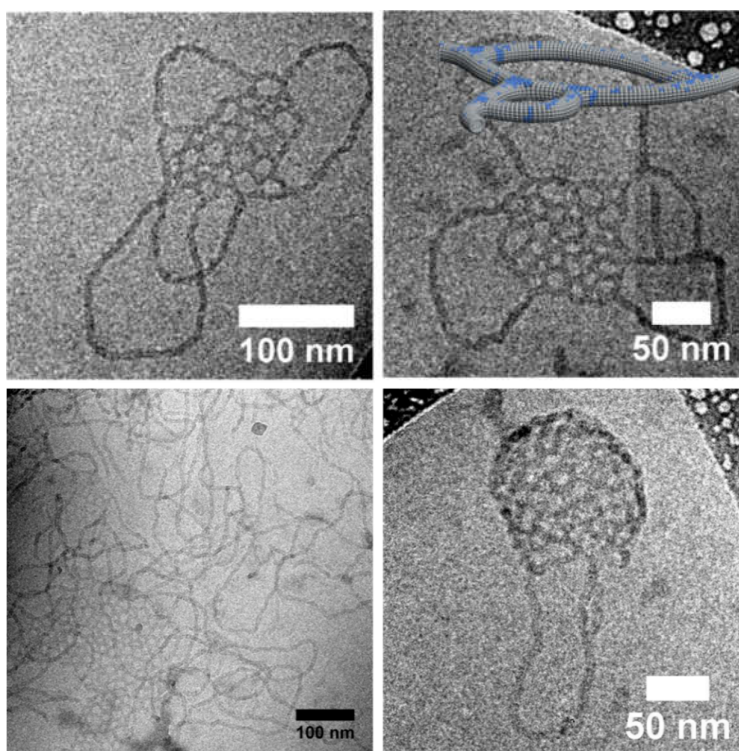


**Figure 3.12.** Cryo-EM images of self-assemblies obtained from Mixture V ( $trans/cis = 25/75$ ). The inset is the schematical illustration of interwoven ribbons, indicating the possible position of *trans* and *cis* isomer within the assemblies. The blue dots represent the vesicles-forming *trans*-PEG550-TPE-Chol, which is preferably assembled in flatter areas. The gray dots refer to the micelles-forming *cis*-PEG550-TPE-Chol, which are likely aggregated in the assemblies with higher curvature.



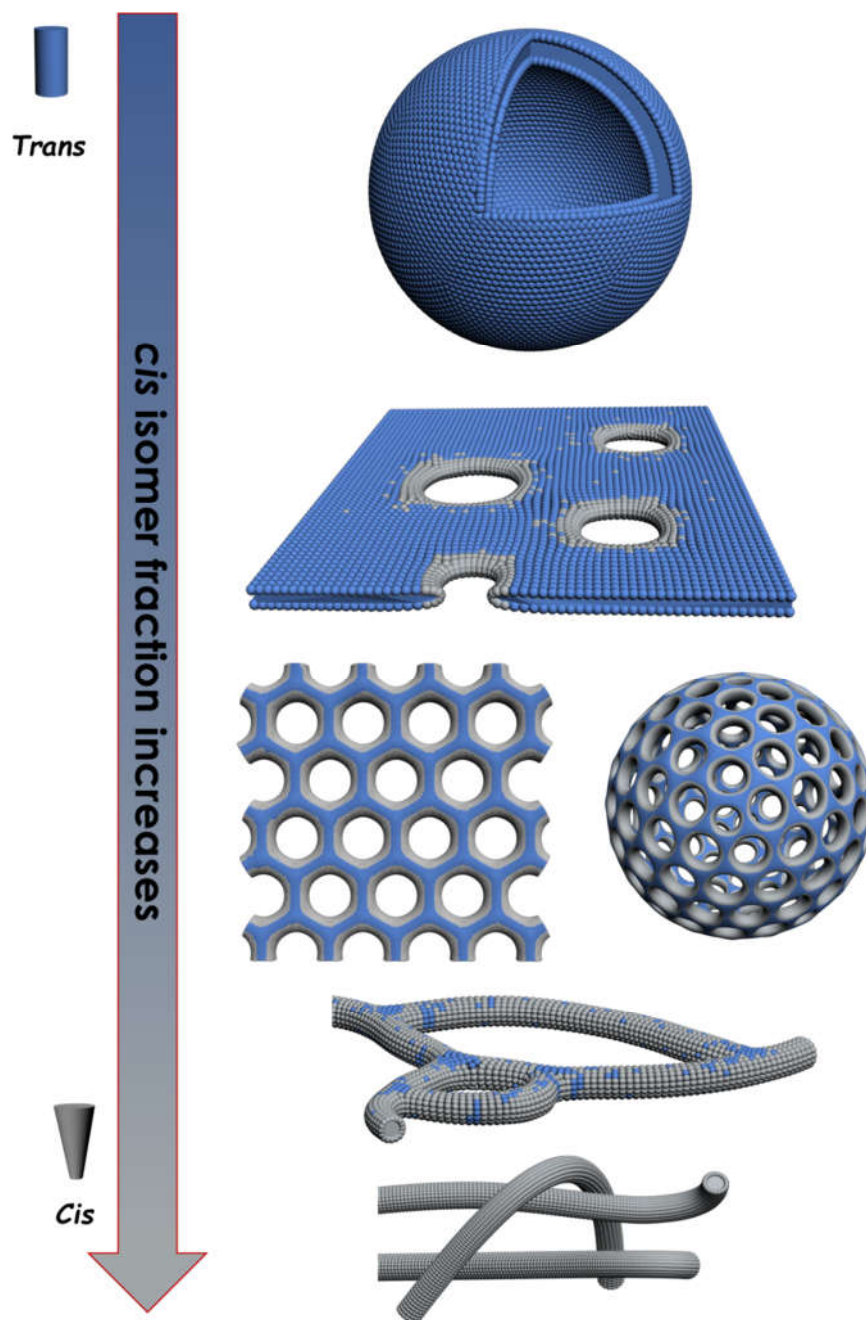


**Figure 3.13.** Schematic illustration of the representative morphological evolution of PEG550-TPE-Chol as a function of the *cis* fraction. The blue cylinder represents the *trans*-PEG550-TPE-Chol that is preferably assembled in flatter areas with low curvature. The gray cone represents the *cis*-PEG550-TPE-Chol that is likely aggregated at the edges of holes with high curvature. <sup>6</sup>.

The results indicate that the formation of porous structure by *trans* and *cis* mixtures of PEG550-TPE-Chol ascribes to the distinct packing parameter of *trans* and *cis* isomers. In the isomer mixture, the vesicle-forming *trans* isomer preferably self-assemble into flatter membrane with low curvature, while micelle forming *cis* isomer tend to impose a positive curvature on the constituent monolayers. The membrane may remain united under a critical concentration of the *cis* isomer. Above this point, the formation of edges may occur. The edges would contain more of micelles-forming *cis* isomer than the flatter membrane regions, leading to formation of hemicylindrical structures and then porous structures. Because of the remarkably similar structure of PEG550-TPE-Chol and PEG550-SS-TPE-SS-Chol, we can extrapolate this conclusion to the case of *trans* and *cis* mixtures of PEG550-SS-TPE-SS-Chol.

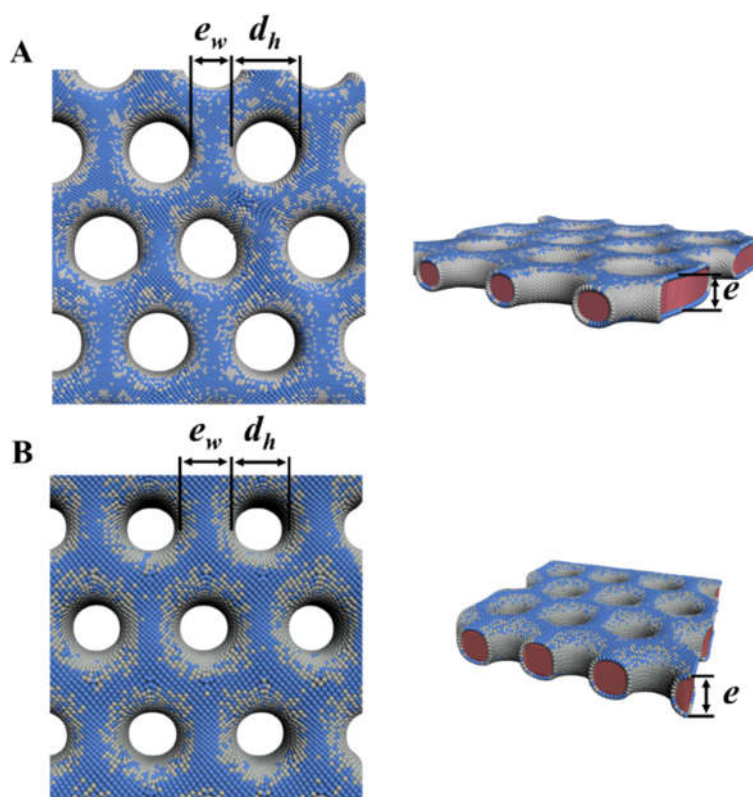


**Figure 3.14.** Schematic illustration perforated membrane formed by *trans/cis* mixtures of PEG550-TPE-Chol (A) and PEG550-SS-TPE-SS-Chol (B). The blue dots represent the vesicle-forming *trans*-PEG550-TPE-Chol, which is preferably assembled in flatter areas with low curvature. The gray dots refer to micelle-forming *cis*-PEG550-TPE-Chol, which are likely aggregated at the edges of holes with high curvature. The red area represents the hydrophobic domain.

Interestingly, the hexagonal superstructure of pores is present only locally in the membrane of PEG550-TPE-Chol (*trans/cis* = 50/50), while it is general and everywhere in the membrane of PEG550-SS-TPE-SS-Chol (*trans/cis* = 50/50) (Figure 3.14). Let us examine the membrane thickness, the nanopore size and the minimal thickness of the pore wall for both PEG550-TPE-Chol (different *trans/cis* ratios) and PEG550-SS-TPE-SS-Chol (*trans/cis* = 50/50) (see Table 3.1 and Table 3.2.) All values were measured by cryo-EM.

Table 3.1 summarizes the bilayer membrane thickness ( $e$ ), cylindrical micelle diameters ( $d_c$ ), pore diameter ( $d_h$ ) and the minimal wall thickness ( $e_w$ ) between two adjacent pores (see Figure 3.14 for the definition) of PEG550-TPE-Chol with different *trans/cis* ratios. We can notice that the membrane thickness decreases slightly with the increase of the *cis* content in the case of PEG550-TPE-Chol, and that the pore diameter and the minimal wall thickness of pore reach nearly stable values when *trans/cis* approaches 50/50 (including 60/40 and 40/60).

**Table 3.1.** Size characterization of different morphologies of *trans*-PEG550-TPE-Chol, *cis*-PEG550-TPE-Chol and their mixtures by cryo-EM.

Sample	Membrane thickness $e$ (nm)	Cylindrical micelle diameter $d_c$ (nm)	Pore diameter $d_h$ (nm)	Pore wall thickness $e_w$ (nm)
<i>trans</i> -PEG550-TPE-Chol	$7.5 \pm 0.5$	-	-	-
Mixture I ( <i>trans/cis</i> = 75/25)	$7.4 \pm 0.6$	-	$5.2 - 100^a$	-
Mixture II ( <i>trans/cis</i> = 60/40)	$7.2 \pm 0.5$	-	$13.0 \pm 1.7$	$6.9 \pm 0.7$
Mixture III ( <i>trans/cis</i> = 50/50)	$7.3 \pm 0.6$	-	$11.5 \pm 1.2$	$7.0 \pm 0.7$
Mixture IV ( <i>trans/cis</i> = 40/60)	$7.2 \pm 0.6$	-	$11.9 \pm 1.2$	$7.0 \pm 0.6$
Mixture V ( <i>trans/cis</i> = 25/75)	-	-	$11.3 \pm 3.0^a$	$6.8 \pm 0.6^b$
<i>cis</i> -PEG550-TPE-Chol	-	$6.5 \pm 0.5$	-	-

<sup>a</sup> The pore size is very heterogeneous. 5.2 nm is the lowest measurable values for the visible holes. Big holes until 100 nm are located in loose mesh parts.

<sup>b</sup> The pore sizes were measured in the parts of meshes.

Table 3.2 summarizes the values of  $e$ ,  $d_h$  and  $e_w$  of PEG550-SS-TPE-SS-Chol ( $trans/cis = 50/50$ ), together with those of PEG550-TPE-Chol ( $trans/cis = 50/50$ ) for comparison. In the case of PEG550-TPE-Chol ( $trans/cis = 50/50$ ), the membrane thickness,  $e = 7.3$  nm, is nearly the same as, but slightly lower than, that of classical membrane without pores of *trans*-isomer ( $e = 7.5$  nm). The minimal wall thickness,  $e_w = 7.0$  nm, is nearly the same as, but slightly higher than, the cylindrical diameter (in other words the addition of two hemicylinder radii,  $d_c = 6.5$  nm), which means between the hemicylindrical edges of two adjacent pores, there is few space for bilayer. In the case of PEG550-SS-TPE-SS-Chol ( $trans/cis = 50/50$ ), the membrane thickness ( $e = 8.4$  nm) and the minimal wall thickness ( $e_w = 7.9$  nm) are higher than those of PEG550-TPE-Chol ( $trans/cis = 50/50$ ). This is easy to understand because PEG550-SS-TPE-SS-Chol has longer spacers with two disulfides bonds (-S-S-) inserted in the middle. The counter lengths of hydrophobic parts become  $l_{trans} = 5.26$  nm and  $l_{cis} = 4.77$  nm for PEG-SS-TPE-SS-Chol, which are higher than those of PEG550-TPE-Chol ( $l_{trans} = 4.54$  nm and  $l_{cis} = 4.05$  nm). The interesting observation is that the longer PEG550-SS-TPE-SS-Chol has the smaller pore diameter ( $d_h = 7.0$  nm) with more homogeneous size distribution ( $d_h = 7.0 \pm 0.7$  nm), while the shorter PEG550-TPE-Chol has bigger pore diameter with less homogeneous size distribution ( $d_h = 11.5 \pm 1.5$  nm).

**Table 3.2.** Size characterization of perforated membranes of TPE550-SS-TPE-SS-Chol ( $trans/cis = 50/50$ ) and PEG550-TPE-Chol ( $trans/cis = 50/50$ ) measured by cryo-EM.

Stereoisomers` s mixture ( $trans/cis = 50/50$ )	Membrane thickness $e$ (nm)	Pore diameter $d_h$ (nm)	Pore wall thickness $e_w$ (nm)
PEG550-SS-TPE-SS-Chol	$8.4 \pm 0.5$	$7.0 \pm 0.7$	$7.9 \pm 0.5$
PEG550-TPE-Chol	$7.3 \pm 0.5$	$11.5 \pm 1.5$	$7.0 \pm 0.5$

Basically, PEG550-TPE-Chol ( $trans/cis = 50/50$ ) and PEG550-SS-TPE-SS-Chol ( $trans/cis = 50/50$ ) have similar chemical structures. Nevertheless, the following differences should be emphasized. First, the molecule of PEG550-SS-TPE-SS-Chol, with two disulfide bonds inserted in the spacers at both sides of TPE, is longer than PEG550-TPE-Chol, the bond lengths of C-C, C-S and S-S being 0.154, 0.182, 0.207 nm, respectively. Secondly, the rotational energies of S-S and C-S bonds are lower than that of C-C bond. Consequently, PEG550-SS-TPE-SS-Chol is “softer” than PEG550-TPE-Chol. This softness may facilitate

the molecular movements in the case of PEG550-SS-TPE-SS-Chol and drive the arrangement of the pores into perfect hexagonal superstructures.

### 3.3.5 Reduction responsive property of PEG550-SS-TPE-SS-Chol self-assemblies

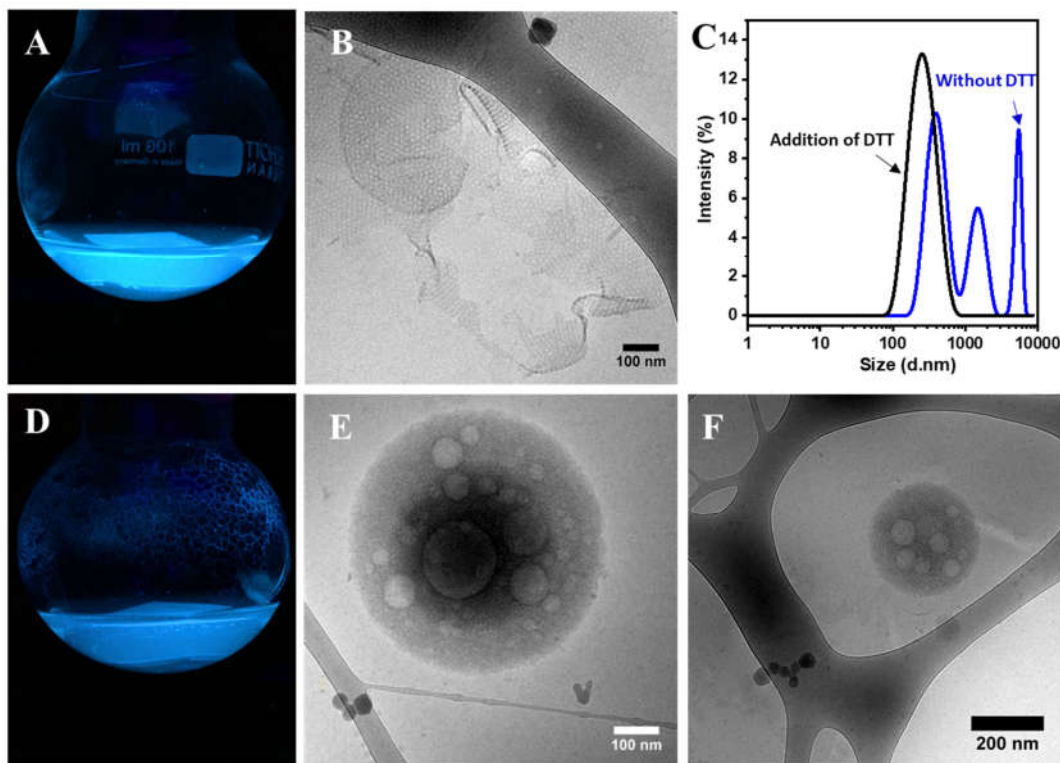


**Figure 3.15.** The characterization of the self-assemblies of PEG550-SS-TPE-SS-Chol before (A, B) and after (D-F) addition of DTT. (A, D) The images taken under UV 365 lamp. (B, E, F) The cryo-EM images of assemblies. (C) The DLS profile of self-assemblies of PEG550-SS-TPE-SS-Chol before and after addition of DTT.

The reduction-responsive property of PEG550-SS-TPE-SS-Chol self-assemblies was also examined. The reducing agent DTT (10 equivalent moles of disulfide bonds) was added into the water dispersion of self-assemblies. Initially, the dispersion exhibits strong fluorescence under UV lamp (Figure 3.15A) The fluorescence intensity seems to decrease after treating with DTT for 72 h (Figure 3.15D). DLS result indicated that porous structures with large diameter transform to assemblies with small size. The morphologies of resultant self-assemblies were characterized by cryo-EM. The porous membrane structures disappear and transform to “exotic” morphology with a lot of huge holes (Figure3.15E-F).

### 3.4 Conclusion

We have confirmed stereoisomer-directed self-assemblies: *trans* and *cis* mixtures of PEG550-TPE-Chol with increasing content of *cis*-isomers (5, 25, 40, 50, 60, 75 and 95%) exhibit the morphological transformation from normal vesicles (bilayer membranes), perforated vesicles (bilayer membranes), interwoven ribbons, and cylindrical micelles. *Trans*-isomer constructs the flat parts of the nanoporous membrane, while *cis*-isomer builds the pore wall. We extrapolate this conclusion to the PEG550-SS-TPE-SS-Chol with *trans/cis* ratio of 50/50 synthesized inherently without isomer separation.

PEG550-SS-TPE-SS-Chol (*trans/cis* = 50/50) with longer and softer spacers forms perforated membranes and vesicles, in which the nanopores with homogeneous size self-organized into nearly perfect hexagonal superstructure of pores in large scale. However, shorter PEG550-TPE-Chol (*trans/cis* = 50/50) without disulfide bonds in the spacers exhibits only local hexagonal arrangement of pores whose sizes are less homogeneous.

The vesicles and membranes with hexagonally organized nanopores are fascinating. The delicate molecular conditions for their formation need to be studied further, for example, by theoretical simulation. The potential applications of these reduction-responsive nanoporous membranes can be explored in the future.

### References

- 1 Alessandri, K. *et al.* A 3D printed microfluidic device for production of functionalized hydrogel microcapsules for culture and differentiation of human Neuronal Stem Cells (hNSC). *Lab on a Chip* **16**, 1593-1604 (2016).
- 2 Alessandri, K. *et al.* Cellular capsules as a tool for multicellular spheroid production and for investigating the mechanics of tumor progression in vitro. *Proceedings of the National Academy of Sciences* **110**, 14843-14848 (2013).
- 3 Duan, X.-F., Zeng, J., Lü, J.-W. & Zhang, Z.-B. Insights into the General and Efficient Cross McMurry Reactions between Ketones. *The Journal of Organic Chemistry* **71**, 9873-9876 (2006).
- 4 Antonietti, M. & Förster, S. Vesicles and liposomes: a self-assembly principle beyond lipids. *Advanced Materials* **15**, 1323-1333 (2003).
- 5 Israelachvili, J. N., Mitchell, D. J. & Ninham, B. W. Theory of self-assembly of hydrocarbon amphiphiles into micelles and bilayers. *Journal of the Chemical Society, Faraday Transactions 2: Molecular and Chemical Physics* **72**, 1525-1568 (1976).
- 6 Almgren, M. Stomatosomes: perforated bilayer structures. *Soft Matter* **6**, 1383-1390 (2010).



## Chapter IV. Fluorescent Cubosomes and Hexosomes with Aggregation-Induced Emission Characteristic

### 4.1 Introduction

Amphiphilic block copolymers (ABCs) can self-assemble in a selective solvent (water being the mostly used) into various forms of colloids like spherical micelles, cylindrical micelles, vesicles, cubosomes and hexosomes, depending on the overall shape of the ABCs in solution.<sup>1-5</sup> This shape, by analogy with low-molecular-weight surfactants, can be described with the packing parameter  $p$  in the first approximation,  $p=v/al$ , where  $v$  is the volume of the core segment,  $l$  its length, and  $a$  the equilibrium area at the core/corona interface.<sup>6</sup> Most efforts have long since been dedicated to exploring polymer micelles and polymer vesicles (polymersomes) with  $p < 1$ , which belong to the normal (oil-in-water) self-assembled nanostructures (Figure 4.1). Very recently, polymer cubosomes and hexosomes with  $p > 1$ , which belong to the inverted (water-in-oil) self-assembled nanostructures, have attracted more and more attention.<sup>7</sup> Compared to polymer spherical/cylindrical micelles and vesicles, these colloids with inverted morphologies present numerous advantages due to their uniform, tunable and highly ordered porous structure, such as higher loading volume for both hydrophilic and hydrophobic substances, larger specific surface areas, and much better colloidal, chemical and mechanical stability.<sup>8,9</sup> Moreover, because of the high molecular weight of polymers, polymer cubosomes and hexosomes present the lattice parameters of at least one order of magnitude higher than lipid cubosomes and hexosomes, and their pore size can be adjusted from  $10^1$  to  $10^2$  nm by regulating the molecular weight of polymers. Therefore, the polymer cubosomes and hexosomes are interesting candidates as functional materials for gated uptake, release, separation, catalysts, electrodes, and photonics, *etc.*<sup>7,10,11</sup> Since the first report on polymer hexosomes, which was named at that time as hexagonally packed hollow hoops (HHH),<sup>12</sup> polymer cubosomes and hexosomes are now rationalized as part of morphological diagram of ABCP in the selective solvent.<sup>3,7</sup> Nevertheless, this field is still in its infancy, with many remaining challenges and exciting opportunities.



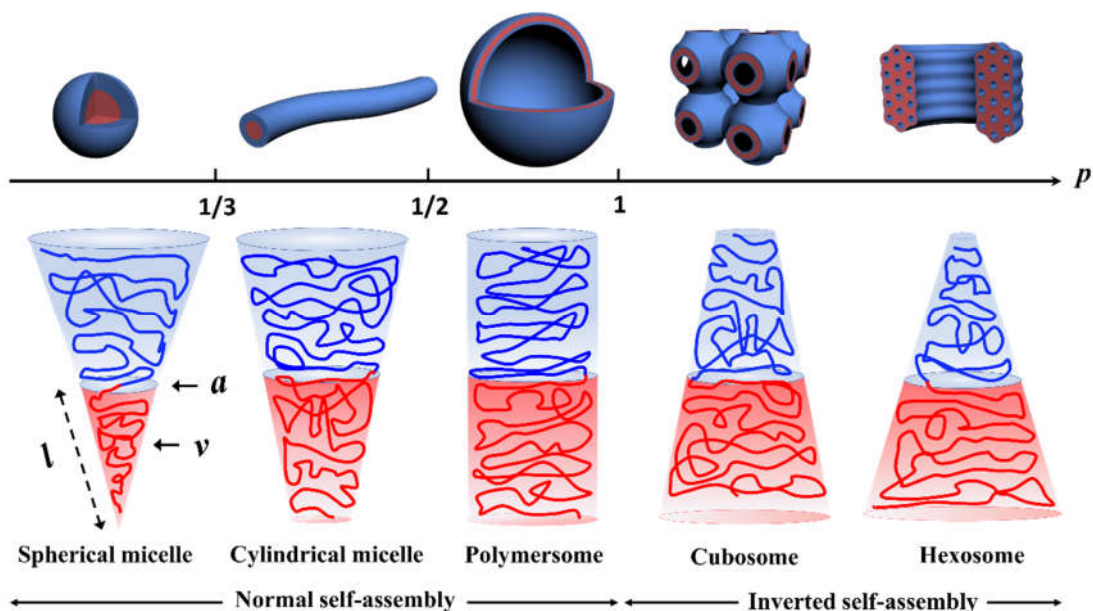


**Figure 4.1** Self-assembling of amphiphilic block copolymers into morphologies from polymersomes, lamellae to inverted morphologies (cubosomes and hexosomes) with the increase of their packing parameter  $p = v/al$ , where  $v$  is the hydrophobic chain volume,  $a$  is the interfacial area per chain and  $l$  is the hydrophobic chain length.

The polymer cubosomes and hexosomes reported in the literature include the following categories according to the architectures of the ABCP used: (1) linear diblock;<sup>13-22</sup> (2) side-chain diblock copolymers<sup>23-33</sup> where the side-chains exhibit special features (crystalline,<sup>23-28</sup> liquid crystalline,<sup>29</sup> nucleobase-pair interaction,<sup>30</sup> halogen bonding interaction,<sup>31</sup> *etc*); (3) diblock copolymers with dendrimers as blocks.<sup>34-40</sup> The most used hydrophilic blocks are poly(acrylic acid) (PAA) and poly(ethylene glycol) (including linear PEG, dendrimers with oligomer OEG branches, or polymethacrylate or polynorbornene with OEG side-chains). In case of PAA as hydrophilic block, the negatively charged pores and channels of cubosomes made from PAA-*b*-Polystyren (PS), were used to encapsulate positively charged proteins with high loading capacity, and the pore size could be adjusted by pH variation for sustained release.<sup>16</sup> The variety of hydrophobic blocks also remains limited and are based mainly on the repeating units of styrene,<sup>16-21,29,31,34-40</sup> methacrylate<sup>15,24-28,30</sup> and norbornene.<sup>32,33</sup> The most studied ones are amorphous polymers like PS<sup>16-21</sup> and poly(*n*-butyl methacrylate) (PBMA),<sup>15</sup> and crystalline polymers like poly(*n*-octadecyl methacrylate) (PODMA)<sup>24-27</sup> and poly(*n*-docosyl methacrylate) (PDSMA).<sup>28</sup> The melting point of the crystalline block was employed to perform the thermally controlled release of ibuprofen previously encapsulated in

cubosomes.<sup>28</sup> Driven by the increasing research interest in polymer cubosomes and hexosomes, the development of new ABCP systems for the controllable preparation of cubosomes and hexosomes with innovative potential applications are highly desirable.

In chapter II and III we explored the so-called “crew-cut” regime at  $1/3 < p \leq 1$ , in which polymeric cylinders and vesicles with positive curvature were afforded by self-assembling of AIEgen-containing amphiphilic polymers. In this chapter, we tend to go beyond this “crew-cut” regime and design amphiphilic block copolymers with large hydrophobic blocks to enter the regime of  $p > 1$  to synthesize the cubosomes and hexosomes. Amphiphilic block copolymers PEG-*b*-PTPEMA with a hydrophobic block PTPEMA much larger than its corresponding hydrophilic PEG block were designed and synthesized. The hydrophobic block PTPEMA was a polymethacrylate with the bulky AIE moiety, tetraphenylethene (TPE), as the side group. Four highly asymmetric block copolymers with hydrophilic block weight ratio  $f_{\text{PEG}} \leq 20\%$  were synthesized. Cubosomes or hexosomes with strong fluorescence were obtained through the self-assembly of polymers with  $f_{\text{PEG}} < 9\%$  in dioxane/water and THF/water systems using nanoprecipitation strategy. Their ordered internal structures were studied by electron microscopy (cryo-EM, SEM and TEM) and X-ray scattering technique (SAXS). To elucidate their formation mechanisms, other parameters influencing the morphologies, like the water content during the self-assembly and the organic solvent composition, were also investigated. This study not only inspires people to design novel building blocks for the preparation of functional cubosomes and hexosomes, but also present the first AIE fluorescent polymer cubosomes and hexosomes with potential applications in bio-related fields.

## 4.2 Experimental sections

### 4.2.1 Materials

Diphenylmethane (99%, Alfa Aesar), 4-methoxybenzophenone (97%, Acros), *n*-butyllithium (2.5 M in hexane, Sigma-Aldrich), *p*-toluenesulfonic acid monohydrate (97%, Alfa Aesar), boron tribromide (BBr<sub>3</sub>, 1.0 M in dichloromethane, Sigma-Aldrich), 3-bromo-1-propanol (97%, Alfa Aesar), potassium carbonate (K<sub>2</sub>CO<sub>3</sub>, 99%, Sigma-Aldrich), methacryloyl chloride (97%, Sigma-Aldrich), triethylamine (99%, Alfa Aesar), *n*-dodecylthiol (98%, Sigma-Aldrich), sodium hydride (60% dispersion in mineral oil, Sigma-Aldrich), carbon disulfide (99%, Sigma-Aldrich), iodine (99%, Sigma-Aldrich), 4,4'-azobis(4-cyanopentanoic acid) (98%, Alfa Aesar), *N,N'*-dicyclohexylcarbodiimide (99%, Sigma-Aldrich) and 4-(dimethylamino)pyridine (99%, Sigma-Aldrich) were used as received. Poly(ethylene glycol)

monomethyl ether (mPEG-OH,  $M_n = 2000$  Da) was purchased from Fluka and purified by precipitation in diethyl ether for three times before using. 2,2'-azobis(isobutyronitrile) (AIBN) was recrystallized from ethanol for three times before using.

#### 4.2.2 Synthesis

##### **Synthesis of monomer TPEMA and RAFT agent mPEG<sub>45</sub>-CTA.**

The monomer TPEMA and RAFT agent mPEG<sub>45</sub>-CTA were synthesized according to the previous report.<sup>41</sup>

##### **Synthesis of polymer PEG<sub>45</sub>-*b*-PTPEMA<sub>n</sub>.**

All polymerizations were performed using Schlenk technique. Taking the synthesis of PEG<sub>45</sub>-*b*-PTPEMA<sub>16</sub> as an example, the typical RAFT polymerization process was described as follows: TPEMA (237 mg, 0.5 mmol), mPEG-CTA (60 mg, 0.025 mmol) and AIBN (0.9 mg, 0.005 mmol) were added into a 15 mL Schlenk tube equipped with a Teflon coated stirring bar. Then 1.5 mL dry THF was added. After the solution was clear, the Schlenk tube was degassed by three freeze-pump-thaw cycles and then immersed into an oil bath of 70 °C. The mixture was stirred at 70 °C for 16 h. The polymerization was terminated by freezing the resultant mixture in liquid nitrogen. The mixture was then poured drop-by-drop into cold isopropanol to precipitate the crude PEG-*b*-PTPEMA. The precipitate was collected by centrifugation. After being re-dissolved in THF and reprecipitated in cold isopropanol twice more and then dried under vacuum at room temperature for 24 h, the pure polymer was obtained as a white solid.

##### **Synthesis of PEG<sub>45</sub>-*b*-PTPEMA<sub>n</sub> assemblies.**

Nanoprecipitation method was used to prepare the PEG<sub>45</sub>-*b*-PTPEMA<sub>n</sub> assemblies. The general procedure was described as follows: Typically, the copolymer (2.5 mg) was dissolved in 2 mL of dioxane. The mixture was stirred for 1h at room temperature. Then 5ml of Milli-Q water was added into the organic solvent with the addition rate of 1ml/h under stirring. After the addition, the resultant mixture was dialyzed against a large amount of pure water to remove the organic solvent. The aggregates were obtained by centrifugation at 5000 r.p.m. for 10 min, and then dispersed in the water again for characterizations.

#### 4.2.3 Instruments

**Nuclear Magnetic Resonance (NMR).** <sup>1</sup>H NMR and <sup>13</sup>C NMR spectra were recorded on

Bruker Avance III HD 400 MHz spectrometer at 298 K. Deuterated chloroform ( $\text{CDCl}_3$ ) was used as the solvent. NMR chemical shifts were recorded in parts per million referenced to the residual solvent proton ( $\delta = 7.26$  ppm) for  $^1\text{H}$  NMR and carbon ( $\delta = 77.1$  ppm) for  $^{13}\text{C}$  NMR.

**Size Exclusion Chromatography (SEC).** Molecular weights (MWs) and molecular weight distributions ( $\mathcal{D}$ ) were determined by size exclusion chromatography (SEC) which consisted of a Waters 1515 isocratic high-performance liquid chromatograph pump, two Styragel HR 5E columns and a refractive index (RI) detector. DMF containing 0.01 mol/L LiBr was used as the eluent with a flow rate of 1.0 mL/min at 60 °C. Commercial monodispersed polystyrenes (PS) were used as the calibration standards.

**Fluorescence Emission Spectroscopy.** The fluorescence emission spectroscopy characterization was carried out on a FluoroMax spectrofluorometer. Samples were added to a 1cm quartz cuvette with all flanks transparent.

**Dynamic Light Scattering (DLS).** Hydrodynamic diameters ( $D_h$ ) of the self-assemblies of amphiphilic PEG-*b*-PTPEMA block copolymers and their size distributions in deionized water were measured at 25 °C by dynamic light scattering (DLS, Malvern zetasizer 3000HS, UK) with a 633 nm laser. All measurements were performed with a 90° scattering angle. The sample solution in the scattering cell was equilibrated for 2 min before measurement.

**Cryo-Electron Microscopy (Cryo-EM).** Morphologies of the copolymer colloids were characterized by cryo-EM. Images were acquired on a JEOL 2200FS energy-filtered (20 eV) field emission gun electron microscopy operating at 200 kV using a Gatan ssCCD 2048 × 2048 pixels. Samples were prepared by deposition of 5  $\mu\text{L}$  sample solution onto a 200 mesh holey copper grid (Ted Pella Inc., U.S.A.) and the samples were flash-frozen in liquid ethane which were cooled down at liquid nitrogen temperature.

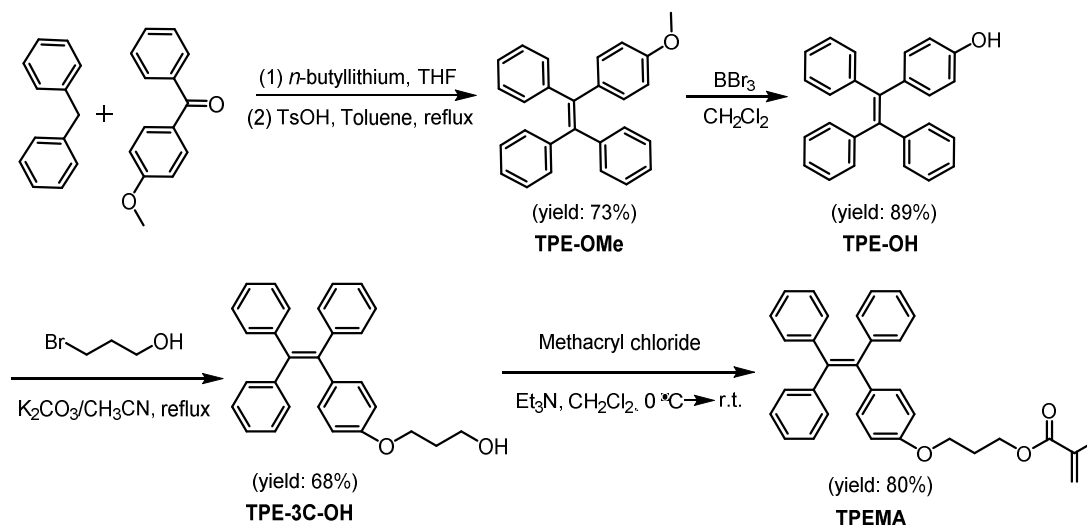
**Scanning electron microscope (SEM).** Morphologies of the polymer cubosomes and hexosomes were characterized by SEM. The images were acquired on a Zeiss Leo 1530 FEG-SEM. Samples were prepared by depositing of 5  $\mu\text{L}$  sample solution onto silicon wafer, followed by a freeze drying to remove the water. Then the samples were observed by the SEM. As for the broken polymer cubosomes and hexosomes, a clean silicon wafer was putted on the surface of the silicon with samples to slightly crush the samples.

**Small-Angle X-ray Scattering (SAXS).** SAXS experiments were carried out on the Xeuss 2.0 apparatus of Laboratoire Léon Brillouin installed in the SWAXS Lab (CEA Saclay, France). The instrument uses a micro-focused Cu  $K\alpha$  source (wavelength of 1.54 Å, 8 keV) and a Pilatus3 1M detector (Dectris, Switzerland). One configuration was chosen to cover the broad

q range, from 0.09 to 4 nm<sup>-1</sup>, with the sample to detector distance was 1.18m, a collimated beam size of 1\*1 mm<sup>2</sup> (entrance) and an aperture of 0.6 × 0.6 mm<sup>2</sup> (exit). The powder sample was placed in a cell made of two square (5mm\*5mm) silicon nitride windows separated by a 1mm-thick spacer. The thickness of each window was 200 nm. The scattering intensity of the empty cell, bare beam and dark were measured and subtracted from the scattering intensity of the powder sample according to standard protocols.<sup>42</sup> Since the amount of powder in the beam was not really controlled, intensity is in arbitrary units.

## 4.3 Results and Discussion

### 4.3.1 Synthesis and characterizations of monomer TPEMA



**Scheme 4.1** The synthetic route to TPEMA monomer.

The target AIE amphiphilic block copolymers could be achieved by the polymerization of appropriate monomers bearing AIE luminogens. Here we chose tetraphenylethene as the AIE luminogens because of its ready synthetic accessibility and great structural tenability. A TPE furnished methacrylate (TEMA) were synthesized as show in Scheme 4.1 according to our previous report.<sup>41</sup> Firstly, the TPE-OMe was synthesized by coupling reaction of diphenylmethane with 4-methoxybenzophenone, followed by acid-catalyzed dehydration in the presence of a catalytic amount of *p*-toluenesulfonic acid (TsOH). TPE-OH was then obtained with a yield of 89% by treatment of TPE-OMe with boron tribromide (BBr<sub>3</sub>). After that, TPE-OH reacted with 3-bromo-1-propanol to produce TPE-3C-OH. The reaction between TPE-3C-OH and methacryloyl chloride led to the formation of TPEMA with a yield

of 80%. TPEMA has been examined by NMR. The  $^1\text{H}$  NMR and  $^{13}\text{C}$  NMR spectra of TPEMA are shown in Figure 4.2 and Figure 4.3. All the NMR signals could be assigned to the corresponding protons or carbons of TPEMA, indicating that pure TPEMA was prepared.

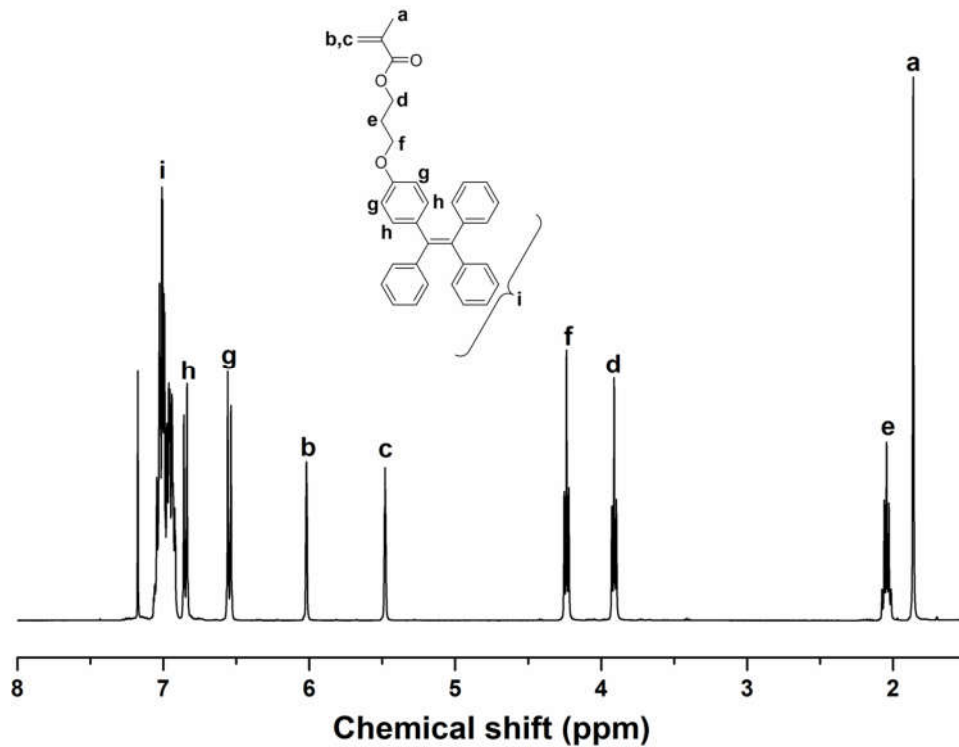


**Figure 4.2**  $^1\text{H}$  NMR and  $^{13}\text{C}$  NMR spectra of TPEMA.  $\text{CDCl}_3$ , 400 MHz, 297 K.

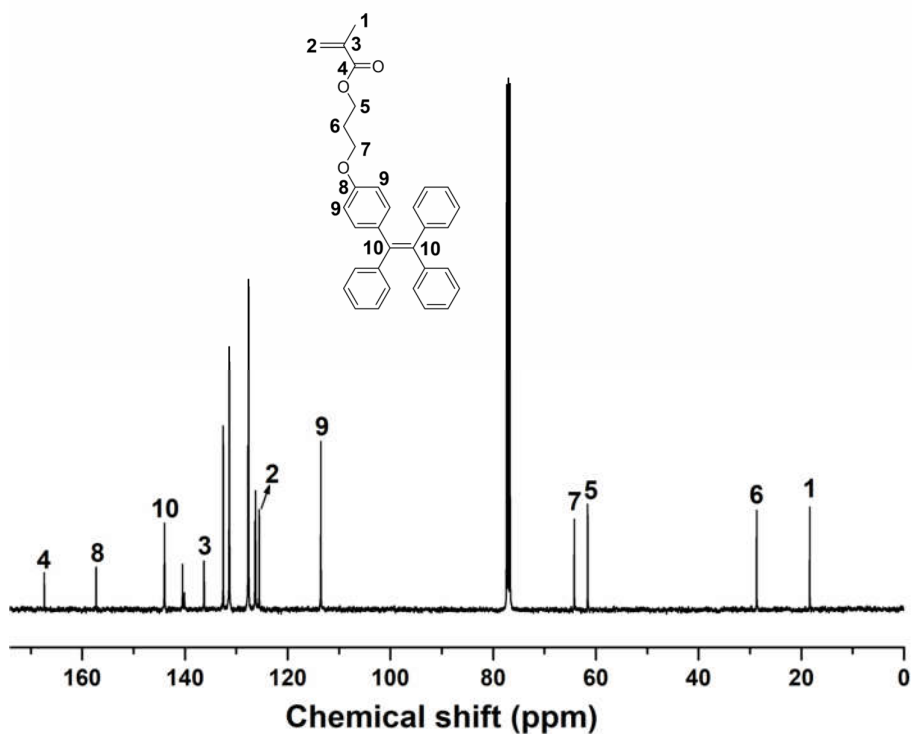
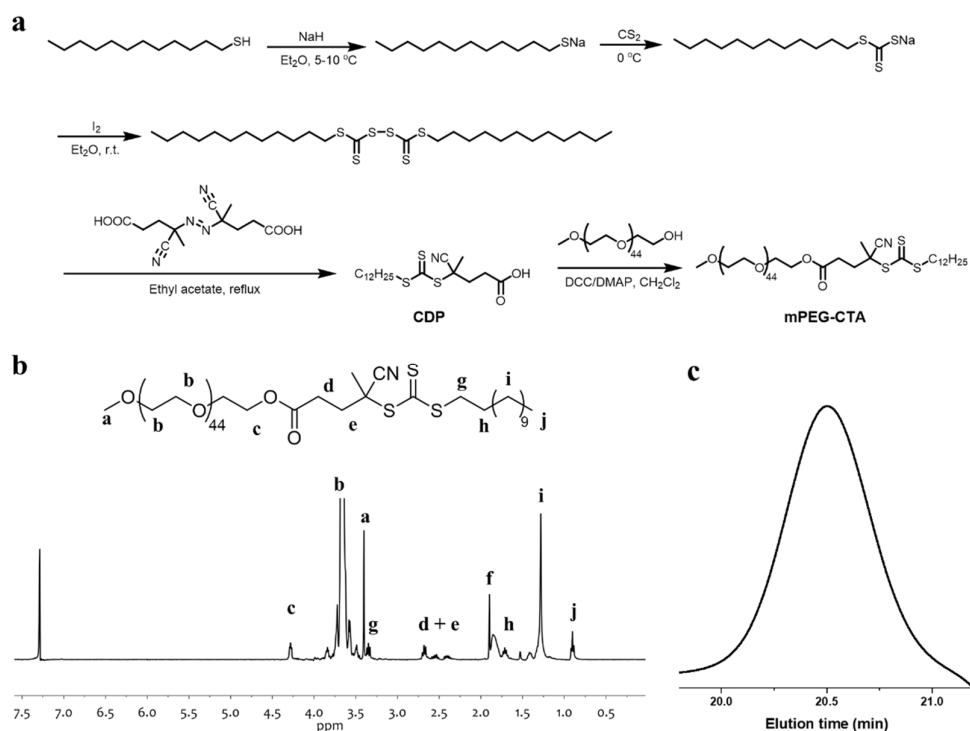


**Figure 4.3** <sup>13</sup>C NMR spectra of TPEMA. CDCl<sub>3</sub>, 100 MHz, 297 K.

#### 4.3.2 Synthesis and characterizations of mPEG-CTA

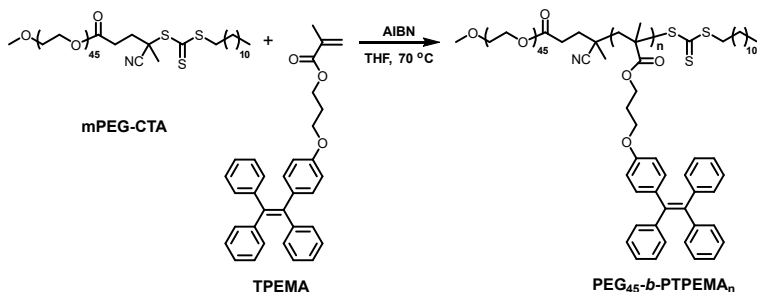
The macroinitiator mPEG-CTA was synthesized according to the synthetic route as shown in Scheme 4.2a. In brief, the n-dodecylthiol firstly reacted with the sodium hydride (NaH) to form sodium thiododecylate, which was then treated with carbon disulfide (CS<sub>2</sub>) to afford the sodium S-dodecyl trithiocarbonate. After that, the bis-(dodecylsulfanylthiocarbonyl) disulfide was produced by the reaction of S-dodecyl trithiocarbonate and solid iodine (I<sub>2</sub>). Followed by a reaction with 4,4'-azobis(4-cyanopentanoic acid), the CDP was obtained. Through a esterification reaction, mPEG-OH (poly(ethylene glycol) monomethyl ether was attached to the CDP to yield the macroinitiator mPEG-CTA. The mPEG-CTA was carefully characterized by <sup>1</sup>H NMR and SEC (Scheme 4.2b-c). From the <sup>1</sup>H NMR spectrum, we can see that all the proton signals could be assigned to the corresponding protons or carbons of mPEG-CTA. SEC curve of mPEG-CTA gave a unimodal peak with a narrow PDI (1.11). All these results indicated that pure mPEG-CTA was obtained.



**Scheme 4.2.** (a) The synthetic route to mPEG-CTA; (b) the <sup>1</sup>H NMR spectrum of mPEG-CTA (CDCl<sub>3</sub>, 400 MHz); (c) the SEC curve of mPEG-CTA with DMF as the eluent.

### 4.3.3 Synthesis and characterizations of PEG<sub>45</sub>-*b*-PTPEMA

The amphiphilic block copolymer PEG-*b*-PTPEMA were synthesized by reversible addition-fragmentation chain transfer (RAFT) polymerization of monomer TPPEMA in presence of the macro-chain transfer agent of mPEG<sub>45</sub>-CTA (M<sub>n</sub> = 2400 Da) and the initiator of 2,2'-azobis(isobutyronitrile) (AIBN). Scheme 4.3 illustrated the synthetic route to PEG-*b*-PTPEMA.



**Scheme 4.3** Synthetic route to amphiphilic diblock copolymer PEG-*b*-PTPEMA by RAFT polymerization.



One of the prerequisites for the formation of bicontinuous cubic phases (primitive  $Im\bar{3}m$ , double diamond  $Pn\bar{3}m$ , gyroid  $Ia\bar{3}d$ ) or hexagonal phase ( $P6mm$ ) is to construct the highly asymmetric ABCP with low hydrophilic block weight ratio. To realize this goal, we performed four RAFT polymerizations using relatively low mPEG-CTA/TPEMA ratio in THF at 70 °C. The estimated hydrophilic block weight ratios ( $f_{\text{PEG}}$ ) are designed ranging from 16.8 % to 3.1% (Table 4.1). After 16 h of polymerization, the conversions of TPEMA monomers were all high than 80% confirmed by the  $^1\text{H}$  NMR spectra of resultant reaction mixture. The polymerization was terminated by freezing the resultant mixture in liquid nitrogen. The mixture was then poured drop-by-drop into cold isopropanol to precipitate the crude PEG-*b*-PTPEMA. The precipitate was collected by centrifugation. After being re-dissolved in THF and reprecipitated in cold isopropanol twice more and then dried under vacuum at room temperature for 24 h, the pure polymer was obtained as a white solid. Then the obtained pure polymer was characterized carefully by NMR (Figure 4.4) and SEC (Figure 4.5).

**Table 4.1** Synthesis of amphiphilic PEG-*b*-PTPEMA block copolymers.

Sample <sup>[a]</sup>	[mPEG-CTA]/[TPEMA]/[AIBN]	yield	$M_n$ <sup>[b]</sup>	$D$ <sup>[c]</sup>	Estimated $f_{\text{PEG,wt\%}}$ <sup>[d]</sup>	$f_{\text{PEG,wt\%}}$ <sup>[e]</sup>
PEG <sub>45</sub> - <i>b</i> -PTPEMA <sub>16</sub>	1:20:0.2	65 %	9900	1.10	16.8%	20%
PEG <sub>45</sub> - <i>b</i> -PTPEMA <sub>29</sub>	1:35:0.2	61 %	17500	1.10	10.5%	12.3%
PEG <sub>45</sub> - <i>b</i> -PTPEMA <sub>42</sub>	1:50:0.2	60 %	22300	1.11	7.7 %	8.9 %
PEG <sub>45</sub> - <i>b</i> -PTPEMA <sub>122</sub>	1:130:0.2	65 %	60200	1.17	3.1%	3.3%

[a] All polymer samples were prepared by RAFT using mPEG-CTA ( $M_n = 2400$  Da, PDI = 1.11) as the macro chain transfer agent in THF at 70 °C. [b]  $M_n$  was calculated by  $^1\text{H}$  NMR; [c] Obtained by SEC in 0.01 M LiBr/DMF, with elution rate at 1 mL/min, PS as standard. [d] Calculated by the feeding ratio of [mPEG-CTA]/[TPEMA]. [e] Calculated by DP obtained with  $^1\text{H}$  NMR data.

The  $^1\text{H}$  NMR spectrum of PEG<sub>45</sub>-*b*-PTPEMA<sub>m</sub> copolymer showed all the proton signals of the polymer structure, which confirmed the synthesis of the target block copolymer. The DP

of TPPEMA units were calculated by comparing the integrated areas of the proton peaks from TPE moiety (peak a for TPPEMA) and that from the methyl group at the end of PEG block (peak d) in the  $^1\text{H}$  NMR spectrum. For example, the DP of the  $\text{PEG}_{45}\text{-}b\text{-PTPEMA}_m$  shown in Figure 4.4 was calculated as 16. The  $M_n$  of the block copolymer could then be calculated after knowing the DP of each repeating unit on the polymer chain. The SEC trace of the obtained four block copolymer showed unimodal peaks with low polydispersity index of  $\mathcal{D} = 1.1\text{-}1.2$  (Figure 4.5). The detailed information about their composition, molecular weights, molecular weight distributions and hydrophilic ratios are listed in Table 4.1. In addition, the hydrophobic block TPPEMA exhibited a high glassy temperature  $T_g = 93^\circ\text{C}$  as measured in  $\text{PEG}_{45}\text{-}b\text{-PTPEMA}_{122}$  (Figure 4.6).

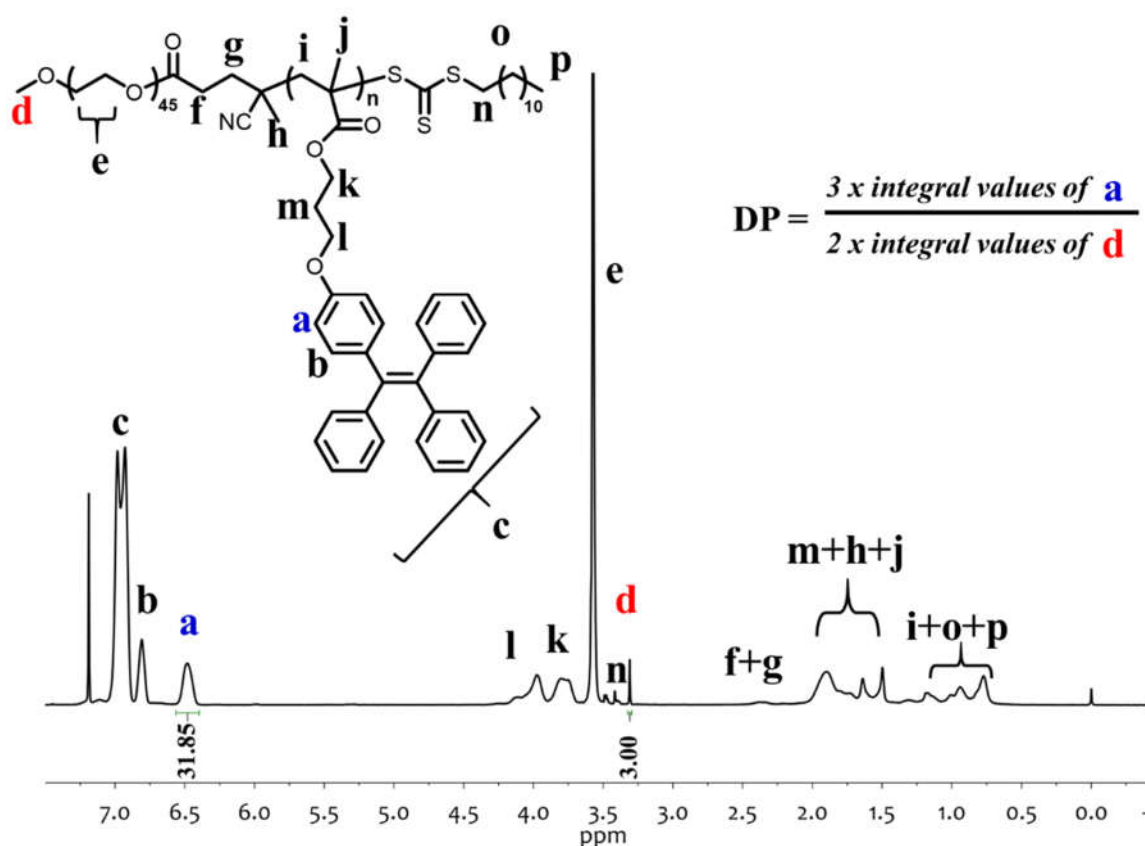


**Figure 4.4**  $^1\text{H}$  NMR spectrum of  $\text{PEG}_{45}\text{-}b\text{-PTPEMA}_{16}$  copolymer. ( $\text{CDCl}_3$ , 400 MHz, 298 K)

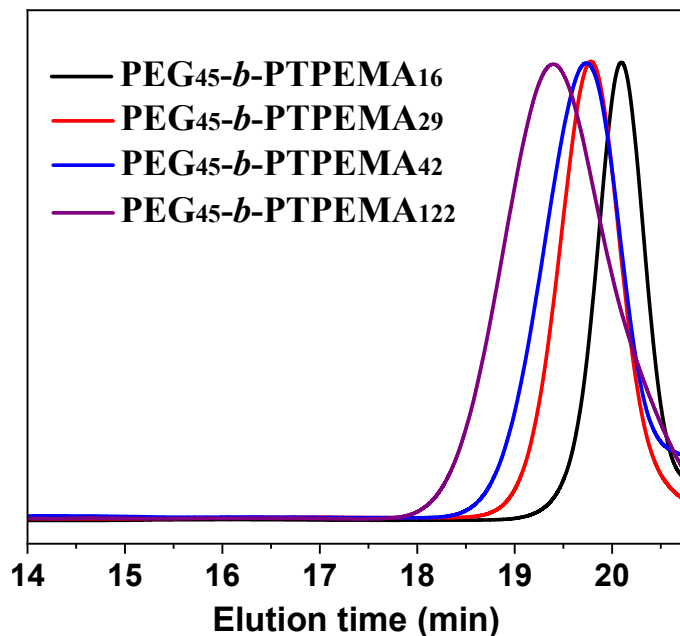


Figure 4.5. SEC traces of PEG-*b*-PTPEMA copolymers with DMF as the eluent.

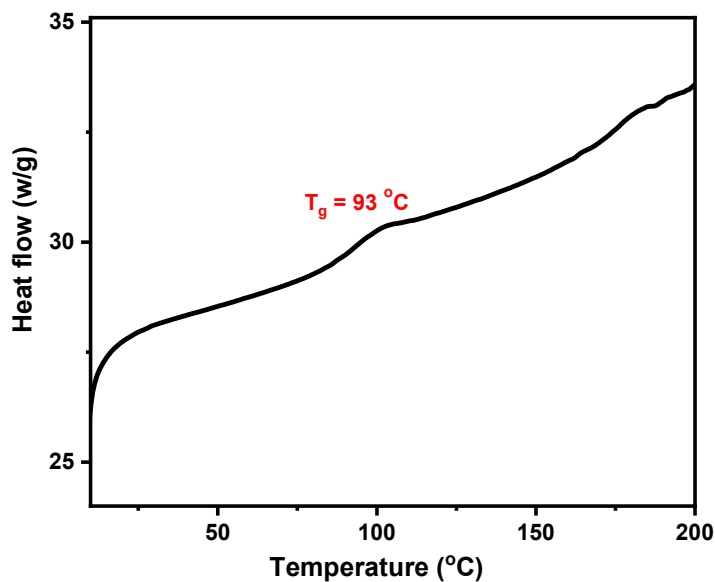
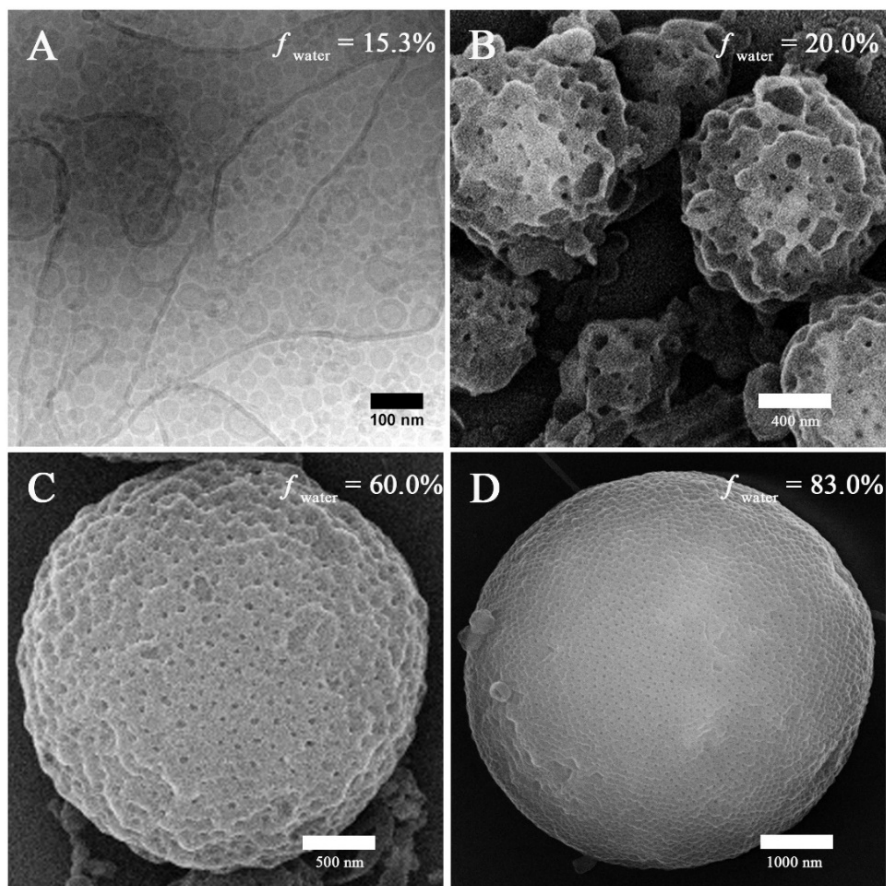


Figure 4.6 DSC thermogram of PEG<sub>45</sub>-*b*-PTPEMA<sub>122</sub> from 0 to 200 °C at 10 °C/min (2<sup>nd</sup> heating scan).

#### 4.3.4 Hexosomes, primitive cubosomes and polymersomes formed in dioxane/water system

The self-assembly of PEG<sub>45</sub>-*b*-PTPEMA<sub>n</sub> was performed through nanoprecipitation method using firstly dioxane as the cosolvent. Typically, a solution of copolymer at a concentration of

0.25 wt% was prepared in dioxane, and then water was added progressively into the solution until the volume content of water  $f_{\text{water}}$  reaches 83%. The final self-assemblies were obtained by dialyzing the mixture against a large volume of water (refreshing 3 times the water) to remove all organic solvent. Taking PEG<sub>45</sub>-*b*-PTPEMA<sub>42</sub> ( $f_{\text{PEG}} = 8.9\%$ ) as an example, we started to study the intermediate morphologies of self-assemblies formed at different water content during the nanoprecipitation, and then the final morphology in pure water.



**Figure 4.7** The intermediate morphologies of particles obtained at different  $f_{\text{water}}$  in the self-assembling process of PEG<sub>45</sub>-*b*-PTPEMA<sub>42</sub> by nanoprecipitation in dioxane/water. (A) cryo-EM image (B-D) SEM images.

At  $f_{\text{water}} = 15, 20, 60, 83\%$ , small aliquots (10  $\mu\text{L}$ ) were withdrawn from the self-assembly mixture, respectively. Each aliquot was immediately injected into a large excess of water ( $\sim 1$  mL) to quench the self-assembly. The obtained nano/micro-particles were then examined by scanning electron microscope (SEM), transmission electron microscopy (TEM) and cryo-electron microscopy (cryo-EM). The cryo-EM images clearly illustrate spherical

polymersomes and irregular giant polymersomes at  $f_{\text{water}} = 15\%$  (Figure 4.7). Increasing  $f_{\text{water}}$  from 15% to 20%, large compound vesicles (LCVs) are observed as shown in Figure 4.7B, presumably due to coalescence of polymersomes. Upon further increase of  $f_{\text{water}}$  from 20% to 60%, these LCVs undergo structural refinement, forming sponge-like particles (Figure 4.7C). Subsequently, the sponge structures tend to rearrange into spherical cubosomes with rather regular pores on the surface, as shown in Figure 4.7D, for  $f_{\text{water}} = 83\%$  (the cubic phase structures will be discussed in detail below). All these observations reveal the pathway of morphological evolution from polymersomes, to sponge particles and to cubosomes, which indicates the formation mechanism of cubosomes (hexosomes) and guides us for their preparation.

The final self-assemblies of PEG<sub>45</sub>-*b*-PTPEMA<sub>n</sub> ( $n = 16, 29, 42$  and  $122$ ) were then prepared using above-discussed nanoprecipitation until added water reaching  $f_{\text{water}} = 83\%$  and then dialyzed against large quantity of water. Their morphologies of PEG<sub>45</sub>-*b*-PTPEMA<sub>n</sub> ( $n = 16, 29, 42$  and  $122$ ) were studied by DLS, cryo-EM, TEM and SEM as shown in Figure 4.8-4.11. In brief, PEG<sub>45</sub>-*b*-PTPEMA<sub>n</sub> with  $n = 16, 29, 42$  and  $122$  formed polymersomes, sponge structures, cubosomes, and hexosomes, respectively.

Specifically, spherical vesicles of PEG<sub>45</sub>-*b*-PTPEMA<sub>16</sub> are clearly revealed by the cryo-EM image (Figure 4.8A) and confirmed by SEM image showing broken empty spheres (Figure 4.8B). The membrane thickness (hydrophobic part) of polymersomes is  $8.5 \pm 0.5$  nm, measured by statistical analysis of 30 different polymersomes from the collected cryo-EM images. On the other hand, the length of the stretched hydrophobic part PTPEMA<sub>16</sub> was about 6.5 nm (calculated by Chem3D software). A perfect tail-to-tail bilayer should have the membrane thickness of 13.0 nm which is higher than the measured one. It indicated that the conformation of the hydrophobic chain PTPEMA<sub>16</sub> should be coil-like in the membrane and the chain entanglement would also be possible between two leaflets. The average hydrodynamic diameter of polymersomes is 160 nm measured by DLS (Figure 4.8C).

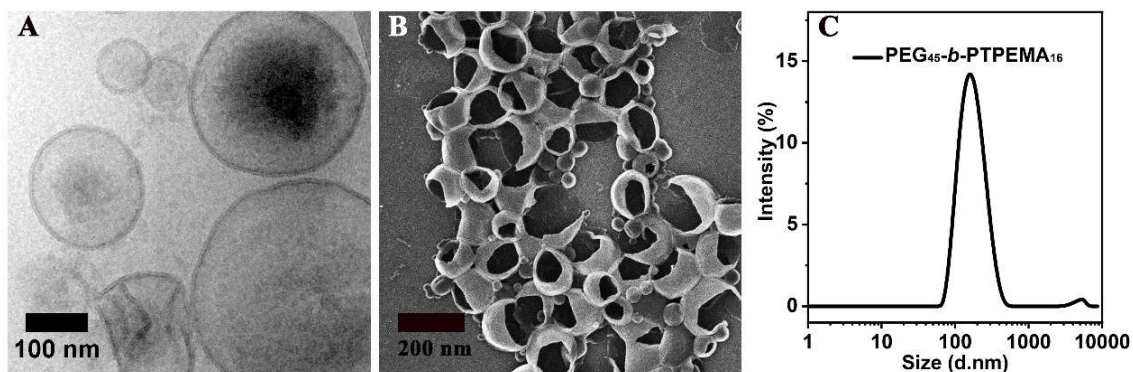


**Figure 4.8** Characterizations of polymersomes formed by PEG<sub>45</sub>-*b*-PTPEMA<sub>16</sub> using dioxane as the cosolvent with initial concentration of 0.25wt%. (A) Cryo-EM. (B) SEM and (C) DLS profile.

When the length of the hydrophobic block PTPEMA<sub>n</sub> increases to  $n = 29$ , sponge-like nanoparticles with disordered porous structures, together with polymersomes, appear as shown by TEM and SEM images (Figure 4.9A and 4.9B).

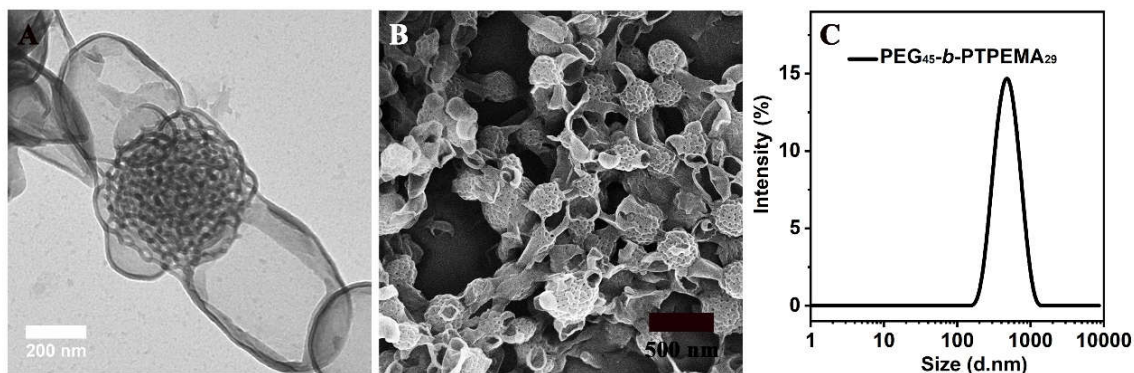


**Figure 4.9** Characterizations of spongy structure formed by PEG<sub>45</sub>-*b*-PTPEMA<sub>29</sub> using dioxane as the cosolvent with initial concentration of 0.25wt%. (A) TEM. (B) SEM and (C) DLS profile.

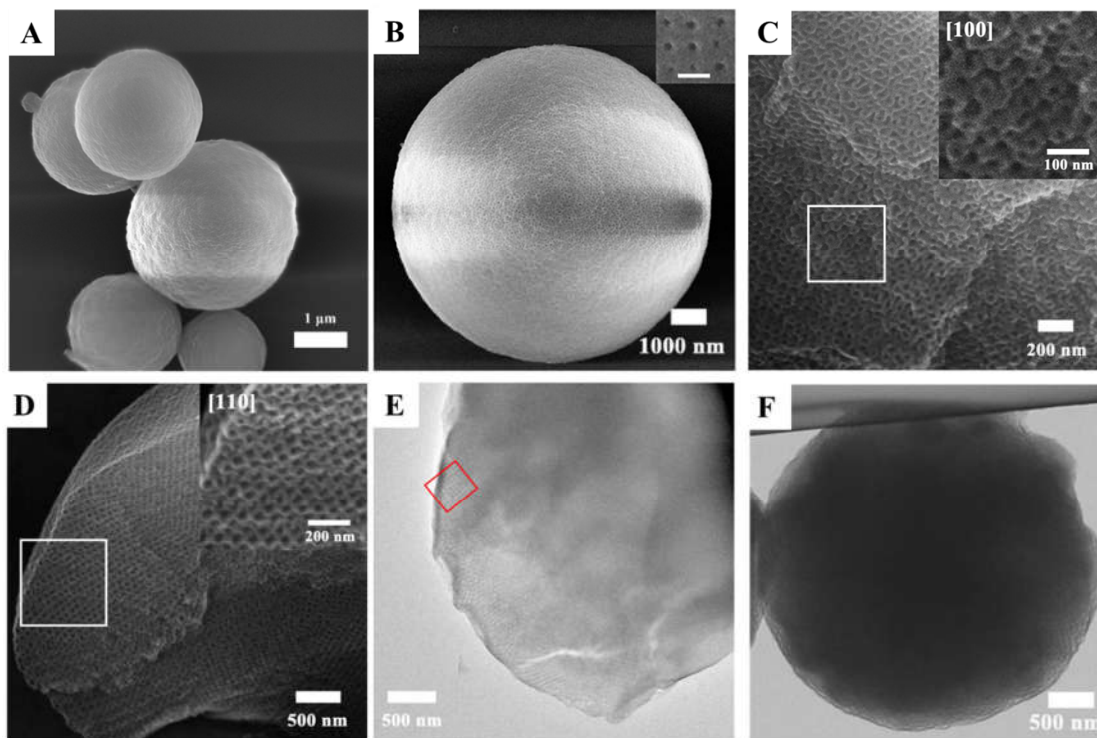
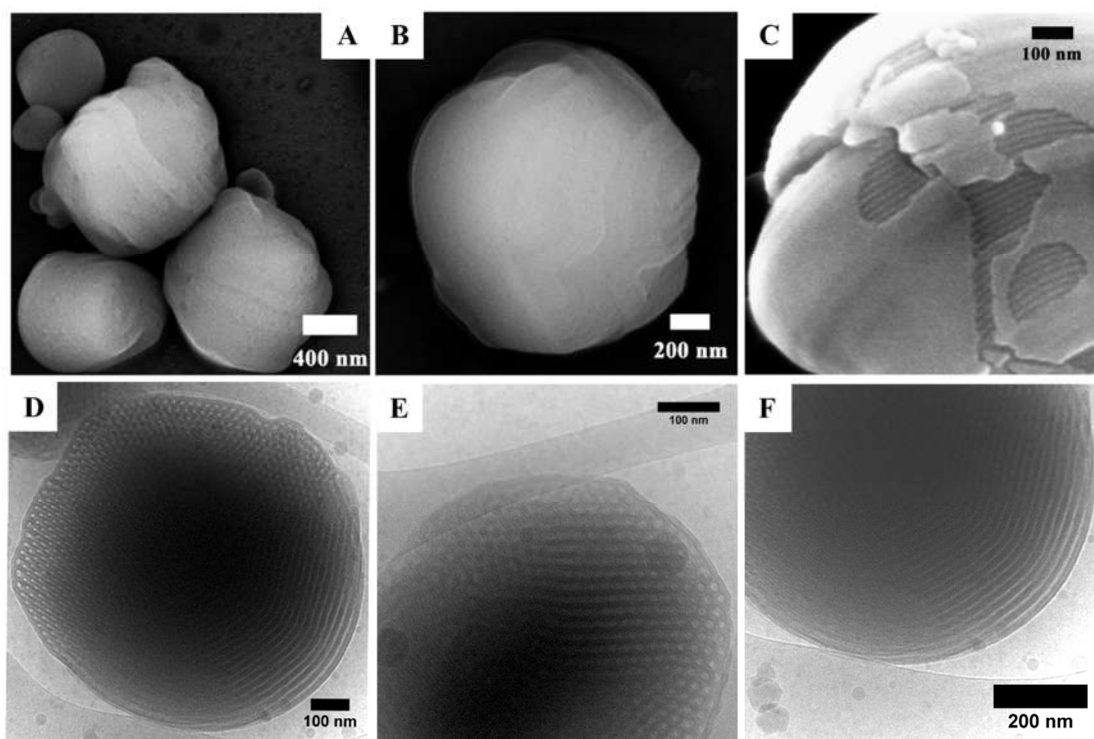


**Figure 4.10** Characterizations of self-assemblies formed by PEG<sub>45</sub>-*b*-PTPEMA<sub>42</sub> using dioxane as the cosolvent with initial concentration of 0.25wt%. (A-D) SEM images. The inset in B shows the amplified images of a part of surface (Scale bar: 100 nm). The insets in C and D are the SEM images of  $Im\bar{3}m$  cubosomes in the [100] and [110] directions, respectively. (E-F) TEM images. The red rectangle in E displaying the typical contrasts of the [100] direction of primitive cubosomes. The dark regions in the cubosome are present because of the inherent large size of the cubosome which cause the scattering of the electrons before reaching the TEM camera.

Further increasing the hydrophobic block length to  $n = 42$  and 122, the PEG<sub>45</sub>-*b*-PTPEMA<sub>42</sub> and PEG<sub>45</sub>-*b*-PTPEMA<sub>122</sub> self-assembled into cubosomes (Figure 4.10) and hexosomes (Figure 4.11), respectively. The inset in Figure 4.10B (SEM) shows that the cubosome has tetragonal pores on its surface. The Figure 4.10C and 4.10D show SEM images of cubosomes of PEG<sub>45</sub>-*b*-PTPEMA<sub>42</sub> broken by liquid nitrogen freezing during the sample preparation, where their ordered internal domains along the [100] and [110] direction are exposed (insets in Figure 4.10C and 4.10D respectively). TEM was also applied to examine the internal structure of cubosomes (Figure 4.10E-F). The thin places of the cubosome display the



organization along [100] direction of the primitive cubic phase (Figure 4.10E). The average unit cell size of primitive cubic structure was measured as  $a_p = 45$  nm from the TEM image.



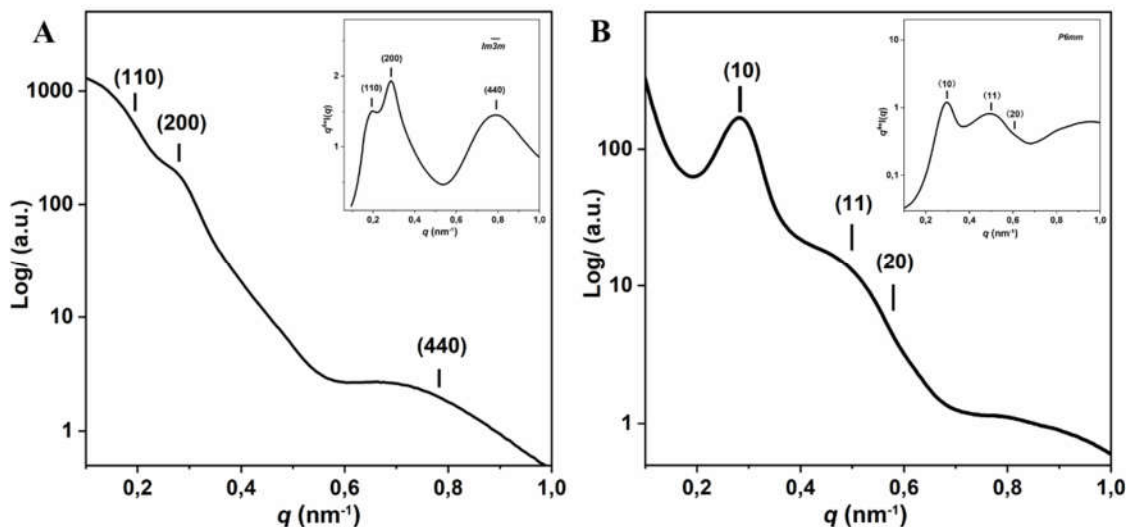
**Figure 4.11** Characterizations of self-assemblies formed by PEG<sub>45</sub>-*b*-PTPEMA<sub>112</sub> using dioxane as the cosolvent with initial concentration of 0.25wt%. (A-C) SEM images. C shows the broken hexosomes. (D-F) cryo-EM images.

Figure 4.11A-C and 4.11D-F show SEM and cryo-EM images of hexosomes of PEG<sub>45</sub>-*b*-PTPEMA<sub>122</sub>, respectively. Figure 4.10A-B (SEM) displays a non-spherical morphology with packed cylinders. The SEM image in Figure 4.11C displays one hexosomes with surface defects, which clearly reveals the tightly packed cylindrical channels. These typical curved cylinders of hexosomes were clearly observed by cryo-EM (Figure 4.11C). The hexagonal packing of these cylinders is visible in cryo-EM images (Figure 4.11E) in the regions of cross sections. The average unit cell parameter of the  $P6mm$  structure was measured as  $a_H = 24$  nm from the cryo-EM image.

SAXS profile of PEG<sub>45</sub>-*b*-PTPEMA<sub>42</sub> cubosomes (Figure 4.12A-B) displays characteristic ratios of 2:4:32 for the square of scattering vector ( $q^2$ ), which correspond to (110), (200), and (440) reflections of primitive cubic structure  $Im\bar{3}m$ . SAXS profile of PEG<sub>45</sub>-*b*-PTPEMA<sub>122</sub>



hexosomes (Figure 4.12C-D) gives  $q^2$  ratios of 1:3:4 corresponding to (10), (11), and (20) reflections of hexagonal structure  $P6mm$ . The lattice parameters deduced from these SAXS profiles were  $a_P = 46$  nm for  $Im\bar{3}m$  cubosomes and  $a_H = 25$  nm for the  $P6mm$  hexagonal structure, which are all in good agreement with that evaluated by TEM.



**Figure 4.12** SAXS profile of (A)  $Im\bar{3}m$  cubosomes of  $PEG_{45}-b-PTPEMA_{42}$  and (B) hexosomes of  $PEG_{45}-b-PTPEMA_{122}$ . The insets in A and B show their SAXS profiles presented in  $q^4 \cdot I(q)$  vs  $q$ , clearly showing the (110), (200) and (440) reflections of the primitive cubic structure  $Im\bar{3}m$  (inset in A), and the (10), (11) and (20) reflections of the hexagonal structure  $p6mm$  (inset in B).

The tendency of the formation of polymersomes, cubosomes and hexosomes with the gradual decrease of hydrophilic ratio  $f_{PEG}$  (from 20% to 3.3%) and the increase of the hydrophobic block length is in agreement with the classical phase diagram according to packing parameter  $p$  changing from  $p \leq 1$  for normal vesicular structures to  $p > 1$  for inverse cubic phase and hexagonal phase (Figure 4.13).<sup>[1c]</sup>

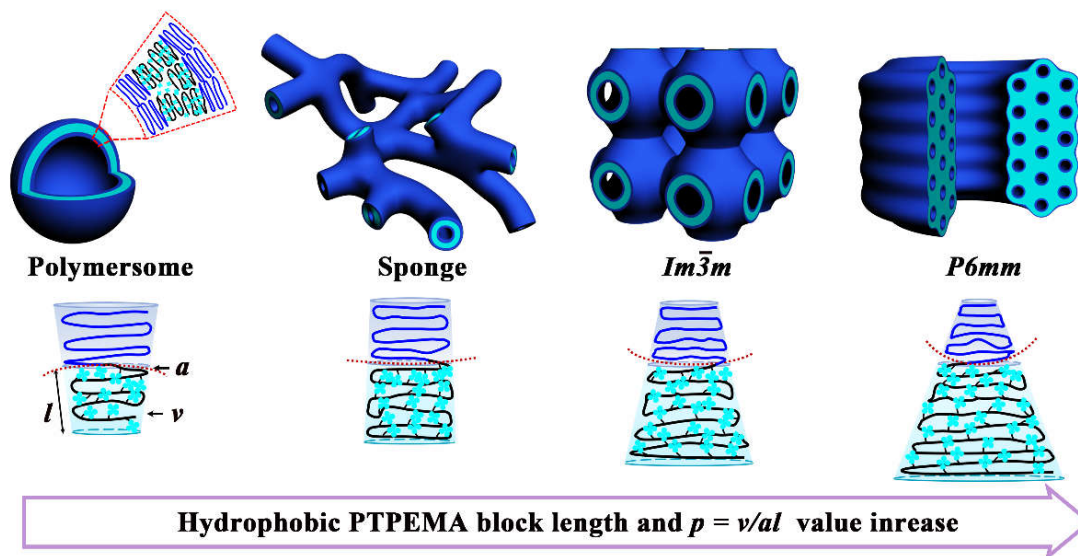


**Figure 4.13** Schematic illustration of morphological transformation of  $\text{PEG}_{45}\text{-}b\text{-PTPEMA}_n$  assemblies with the length increase of the hydrophilic block PTPEMA which corresponds to the increase of packing parameter  $p$ .

Further, the effect of the initial concentration on the self-assembly behavior was examined taking  $\text{PEG}_{45}\text{-}b\text{-PTPEMA}_{122}$  in dioxane/water system as an example with higher initial concentrations  $c_0 = 0.4 \text{ wt\%}$  and  $2 \text{ wt\%}$  in dioxane, respectively. When  $c_0 = 0.4 \text{ wt\%}$ ,  $Pn\bar{3}m$  and  $P6mm$  phase structures coexist in most of colloids particles as revealed by SEM images in Figure 4.14A and 4.14B.<sup>21</sup> A few of particles with  $Im\bar{3}m$  structure showing tetragonal pores on the surface were also observed (Figure 4.14C and 4.14D). Further increasing the concentration to  $c_0 = 2 \text{ wt\%}$ , polymersomes and particles with sponge structure were obtained (Figure 4.15). We conclude that the low initial concentration  $c_0 = 0.25 \text{ wt\%}$  is the most favorable one for cubosomes and hexosomes preparation of our copolymers.

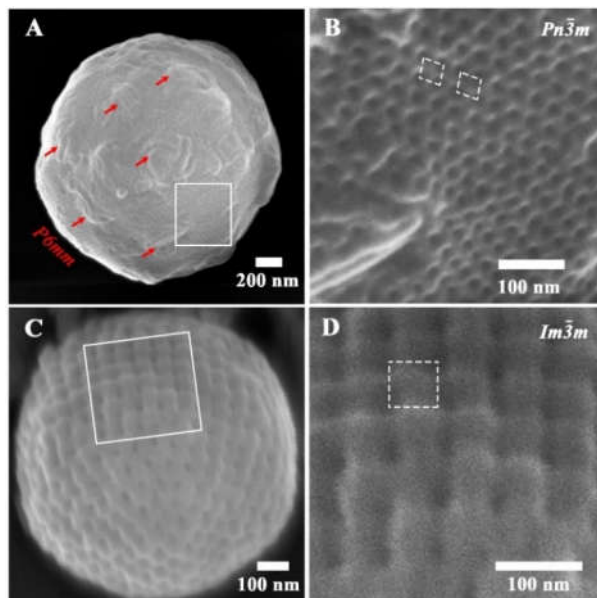


**Figure 4.14.** The SEM images of PEG<sub>45</sub>-*b*-PTPEMA<sub>122</sub> assemblies using dioxane as cosolvent at the initial polymer concentration of 0.4 wt%. (A) The assemblies with the coexistence of  $Pn\bar{3}m$  and  $P6mm$  structures (The red arrows indicating the cylindrical channels of  $P6mm$ ). (B) The amplification image of the white rectangle part in A, showing the diamond-shaped packing of pores on the surface (indicated by white diamonds). (C) The  $Im\bar{3}m$  particles. (D) The amplification image of the white rectangle part in C, showing tetragonal pores on the surface (indicate by dotted line square).

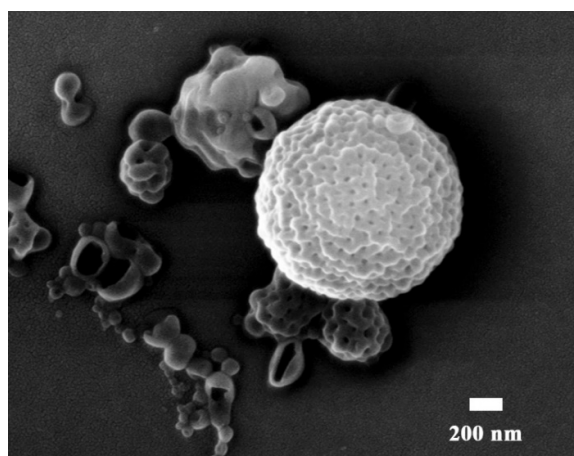


**Figure 4.15** The SEM images of PEG<sub>45</sub>-*b*-PTPEMA<sub>122</sub> aggregates using dioxane as cosolvent at the initial polymer concentration of 2 wt%.

### 4.3.5 Hexosomes and polymersomes formed in THF/water system

The effect of co-solvent on the self-assembly was also studied. Instead of dioxane, tetrahydrofuran (THF) was then used as co-solvent to prepare particles of PEG<sub>45</sub>-*b*-PTPEMA<sub>*n*</sub> with initial concentration of 0.25wt%. Figure 4.16-4.19 shows cryo-EM, TEM and SEM images of self-assemblies of PEG<sub>45</sub>-*b*-PTPEMA<sub>*n*</sub> (*n* = 16, 29, 42, 122) formed in THF/H<sub>2</sub>O systems.

As in the case of dioxane/ H<sub>2</sub>O system, the PEG<sub>45</sub>-*b*-PTPEMA<sub>16</sub> forms also spherical vesicles, as displayed by the cryo-EM image (Figure 4.16B) and confirmed by SEM image showing broken open capsules (Figure 4.16A). The membrane thickness of polymersomes is  $e = 11.0 \pm 0.5$  nm, measured by cryo-EM, and the average hydrodynamic diameter of polymersomes is of  $D_h = 250$  nm measured by DLS (Figure 4.16C). Interestingly, the thickness  $e = 11.0$  nm here is still lower but remarkably close to the membrane thickness of 13.0 nm for a perfect tail-to-tail bilayer. These characteristic values ( $e$  and  $D_h$ ) of polymersomes PEG<sub>45</sub>-*b*-PTPEMA<sub>16</sub> obtained in THF/water are larger than those obtained in dioxane/water where  $e = 8.5 \pm 0.5$  nm and  $D_h = 160$  nm. That means the PTPEMA chain are more extended when self-assemble in THF/water. Indeed, thicker bilayer will bend less easily, and the vesicles obtained have lower curvature and larger diameter as in the case of polymersomes in THF/water. The reason is that THF is a better solvent for PTPEMA than dioxane (see the section “Self-assembly in Dioxane/THF/water system” below for detailed discussion).

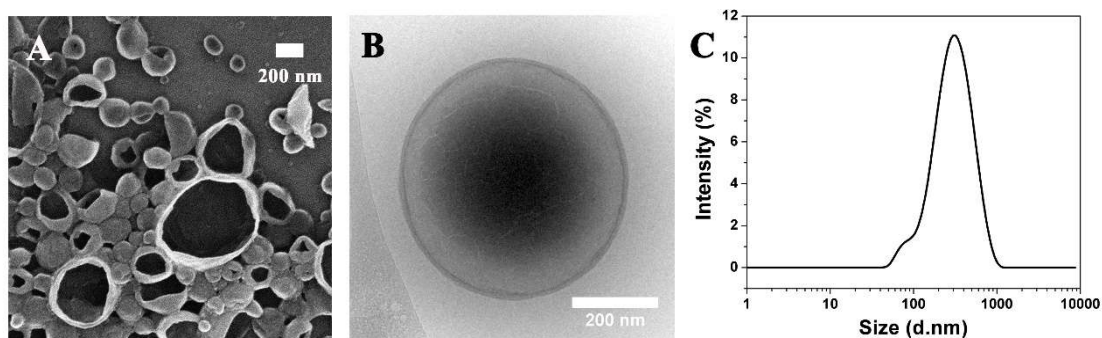


**Figure 4.16** Characterizations of polymersomes formed by PEG<sub>45</sub>-*b*-PTPEMA<sub>16</sub> using THF as the cosolvent with initial concentration of 0.25wt%. (A) SEM, (B) cryo-EM and (C) DLS profile.

Increasing the hydrophobic block length to  $n = 29$ , polymersomes are still the dominant species based on the SEM and TEM images (Figure 4.17A and 4.17B). However, in THF/H<sub>2</sub>O

systems, sponge-like structure and inverse cubic phase do not occur anymore. The hexosomes directly appear co-existing with polymersomes (see red circle in Figure 4.17A).

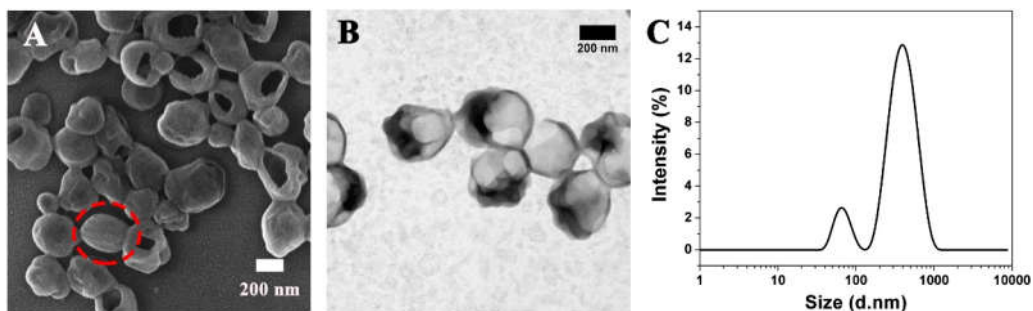


**Figure 4.17** Characterizations of polymersomes formed by PEG<sub>45</sub>-*b*-PTPEMA<sub>29</sub> using THF as the cosolvent with initial concentration of 0.25wt%. (A) SEM, (B) TEM and (C) DLS profile. The red circles in A indicate the hexosomes.

Further increasing the hydrophobic block length to  $n = 42$ , the hexosomes become the major structure (Figure 4.18), with an average hydrodynamic diameter of 220 nm and narrow dispersity of PDI = 0.2 as measured by DLS (Figure 4.18C). Cryo-EM images (Figure 4.18B) reveal their internal structures with hexagonally packed cross-section. The average unit cell parameter of the  $P6mm$  structure was measured as  $a_H = 26$  nm based on cryo-EM images. This hexagonal structure of PEG<sub>45</sub>-*b*-PTPEMA<sub>42</sub> when prepared in THF/water was confirmed by the analysis of the SAXS profile, showing peaks with  $q^2$  ratios of 1:3:4, assigned to the (10), (11), and (20) reflections of the hexagonal structure with  $a_H = 29$  nm as lattice parameter (Figure 4.18D).

Finally, when the hydrophobic block length increases to  $n = 122$ , solid particles with dense structure are obtained according to their cryo-EM and SEM images (Figure 4.19A and B).

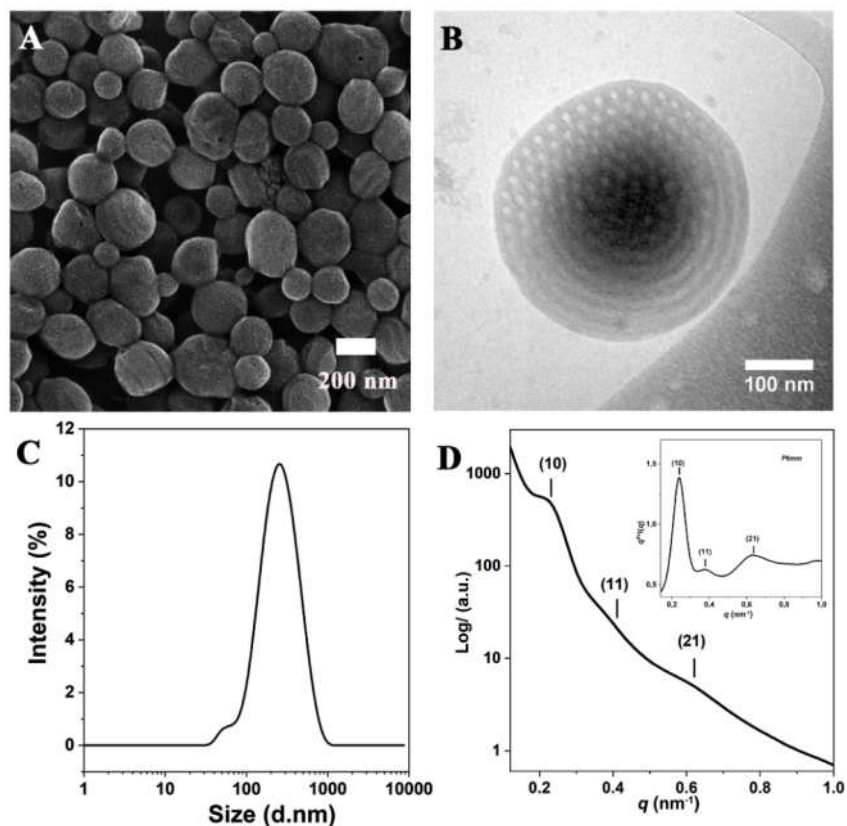


**Figure 4.18** Characterizations of hexosomes formed by PEG<sub>45</sub>-*b*-PTPEMA<sub>42</sub> using THF as the cosolvent with initial concentration of 0.25wt%. (A) SEM, (B) cryo-EM, (C) DLS profile and (D) SAXS profiles. Inset in D shows the SAXS curve presented in  $q^4 \cdot I(q)$  vs  $q$ , clearly demonstrating the (10), (11) and (21) reflections of hexagonal structure  $p6mm$ .

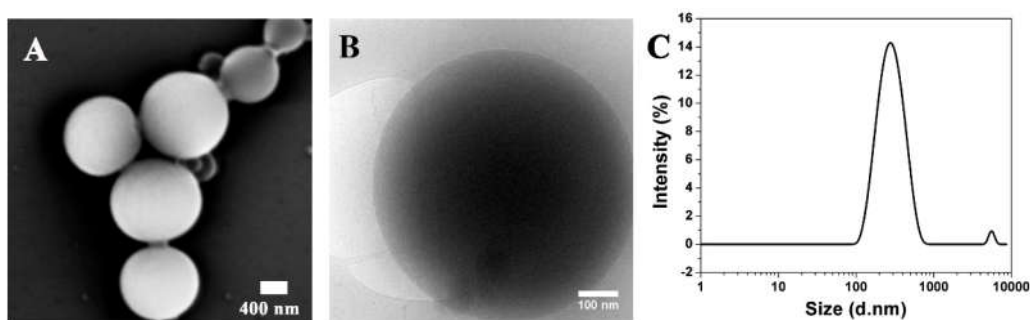


**Figure 4.19** Characterizations of solid particles formed by PEG<sub>45</sub>-*b*-PTPEMA<sub>122</sub> using THF as the cosolvent with initial concentration of 0.25wt%. (A) SEM, (B) Cryo-EM and (C) DLS profile.



#### 4.3.6 Effects of co-solvent on the morphology of self-assembly

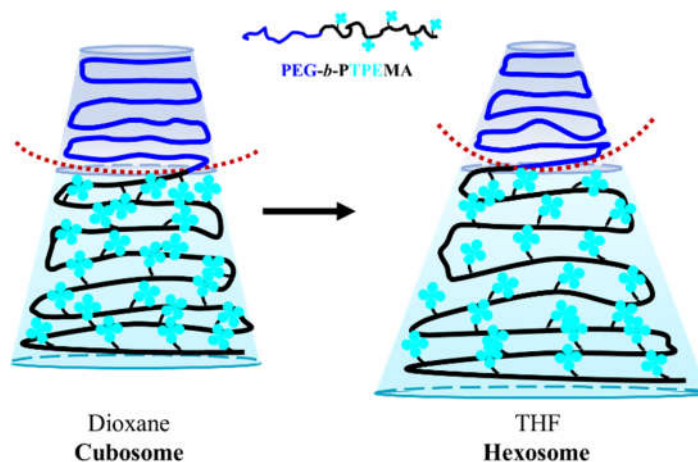


**Figure 4.20** Schematic representation of the molecular shapes of PEG<sub>45</sub>-*b*-PTPEMA<sub>42</sub> in dioxane/water and THF/water system, which result in cubosome and hexosome, respectively.

The above-discussed results suggest that the nature of co-solvent has significant influence on the nanostructure of the colloidal particles. This is expected because the co-solvent with different solubility parameter directly affects the dimensions of both hydrophilic and hydrophobic domains during the self-assembling process.<sup>43</sup> The solubility parameters ( $\delta$ ) of THF, dioxane, and the repeat unit of PEG are  $\delta_{\text{THF}} = 18.6$ ,  $\delta_{\text{dioxane}} = 20.5$ , and  $\delta_{\text{PEG}} = 20.2$  MPa<sup>1/2</sup>, respectively. For PTPEMA block,  $\delta_{\text{PTPEMA}} = 18.9$  MPa<sup>1/2</sup> is calculated using a group contribution method.<sup>44</sup> Typically, the closer are the  $\delta$  values of the polymer and the solvent, the better is the solubility of the polymer in the solvent. Therefore, PEG is more soluble in dioxane than in THF, while PTPEMA is more soluble in THF than in dioxane. The initial shapes of PEG<sub>45</sub>-*b*-PTPEMA<sub>42</sub>, for example, are different in dioxane/water and THF/water systems, as shown in Figure 4.20. Thus, the inverse curvature toward the PEG interface is higher in THF case than in dioxane case. Indeed, PEG<sub>45</sub>-*b*-PTPEMA<sub>42</sub> self-assembled into cubosomes with lower negative interface curvature in dioxane/water, but into hexosomes with higher negative curvature in THF/water system. Moreover, for shorter PTPEMA block, PEG<sub>45</sub>-*b*-PTPEMA<sub>29</sub> formed polymersomes with positive curvature together with sponge structure in dioxane/water system, while it formed polymersomes and hexosomes with high negative curvature in THF/water system. As the solvent in PEG part is progressively replaced by water (a good solvent for PEG but not miscible at all with PTPEMA), the swollen shape of PTPEMA in THF or in dioxane is the key parameter during the self-assembling process.

**Table 4.2** Summary of the thickness of the hydrophobic part of bilayer membrane ( $e$ ) for

different PEG-*b*-PTPEMA morphologies. <sup>[a]</sup>

Sample	Dioxane/water system	THF/water system
PEG <sub>45</sub> - <i>b</i> -PTPEMA <sub>16</sub>	8.5±0.5 nm ( <i>polymersomes</i> )	11.0±0.5 nm ( <i>polymersomes</i> )
PEG <sub>45</sub> - <i>b</i> -PTPEMA <sub>29</sub>	11.0±0.5 nm ( <i>sponges</i> )	12.1±0.5 nm ( <i>polymersomes and hexosomes</i> )
PEG <sub>45</sub> - <i>b</i> -PTPEMA <sub>42</sub>	11.7±0.5 nm ( <i>cubosomes</i> )	13.2±1.0 nm ( <i>hexosomes</i> )
PEG <sub>45</sub> - <i>b</i> -PTPEMA <sub>122</sub>	13.2±1.0 nm ( <i>hexosomes</i> )	-

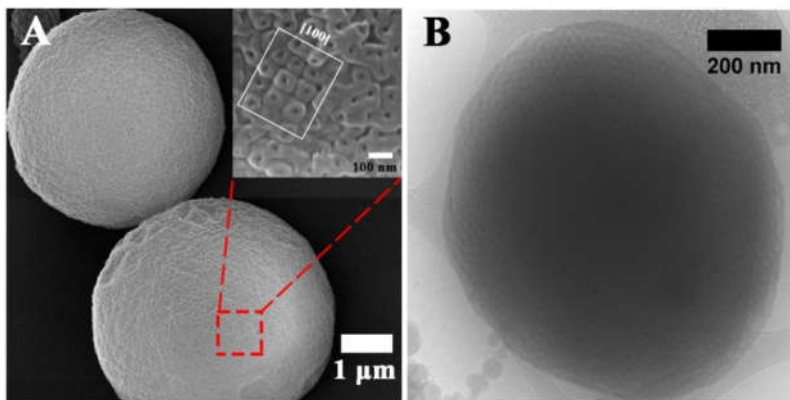
[a] Thickness measured from the FWHM of the electronic density profile perpendicular to the bilayer membrane through statistical analysis of about 30 different assemblies in the cryo-EM images.

**Table 4.3** Solubility Parameters of the Binary Solvents.

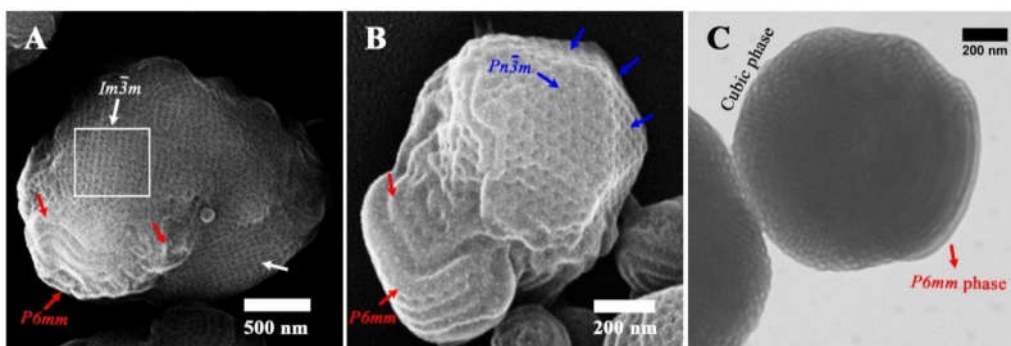
$v_{\text{THF}}/(v_{\text{THF}} + v_{\text{dioxane}})$	Solubility parameters of the mixed solvents (MPa <sup>-1/2</sup> )
0%	20.5
25 %	20.1
40%	19.7
50 %	19.5
100%	18.6

Table 4.2 lists the thickness of the hydrophobic part of bilayer membrane in different morphologies. In general, PEG<sub>45</sub>-*b*-PTPEMA<sub>n</sub> assemblies formed in THF/water system have thicker membrane than those constructed in dioxane/water system, implying that the PTPEMA chain is more extended in THF/water than in dioxane/water system during the self-assembling. Above results suggest that a cosolvent with higher affinity for the hydrophobic block tends to facilitate the formation of nanostructures with higher negative curvature. This was further proved by the self-assembly behavior of PEG<sub>45</sub>-*b*-PTPEMA<sub>42</sub> in dioxane/THF/water system. Mixtures of organic solvents dioxane/THF with THF content of 25%, 40% and 50% were used to prepare the PEG<sub>45</sub>-*b*-PTPEMA<sub>42</sub> solution with initial concentration  $c_0 = 0.25$  wt%. As shown in Table 4.3, with the increase of the THF content, the solubility parameter of the binary cosolvent approach to that of the hydrophobic block PTPEMA. At the THF content of 25% ( $\delta = 20.1$ ), the PEG<sub>45</sub>-*b*-PTPEMA<sub>42</sub> preferably self-assembled into the spherical  $Im\bar{3}m$  cubosomes (Figure 4.21), showing tetragonal pores on its surface (Figure 4.21A). Their ordered internal domains along the [100] direction was also observed (Figure 4.21A).





**Figure 4.21.** The SEM (A) and cryo-EM (B) images of PEG<sub>45</sub>-*b*-PTPEMA<sub>42</sub> cubosomes formed in dioxane/THF/water system with THF content of 25%.



**Figure 4.22** The SEM (A-B) and cryo-EM (C) images of PEG<sub>45</sub>-*b*-PTPEMA<sub>42</sub> aggregates formed in dioxane/THF/water system with THF content of 40%. (A) The intermediate morphologies composed of  $Im\bar{3}m$  and  $P6mm$  structures. The tetragonal pores (in white rectangle) correspond to  $Im\bar{3}m$  structure, while the cylindrical channels (the red arrows) ascribe to  $p6mm$  structure. (B) The intermediate morphologies composed of  $Pn\bar{3}m$  and  $P6mm$  structures. The polyhedral surfaces (the blue arrows) are the characteristic of  $Pn\bar{3}m$  cubosomes. The cylindrical channels (the red arrows) belong to  $p6mm$  structure. (C) The intermediate morphologies showing the cubic and  $P6mm$  phase.

When the THF fraction increased to 40% ( $\delta = 19.7$ ), non-spherical particles were formed displaying both regular pores and tightly packed channels on its surface, as shown in Figure 4.22A. The tetragonal pores correspond to  $Im\bar{3}m$  structure, while the cylindrical channels belong to  $P6mm$  structure. Interestingly, the particles with mixed structure of  $Pn\bar{3}m$  and  $P6mm$  phase also was observed as shown in Figure 4.22B, where in addition to the tightly packed

channels, characteristic polyhedral surfaces of  $Pn\bar{3}m$  cubosome were observed. The cryo-EM images further confirmed the internal structure of the aggregate, showing cubic and  $P6mm$  phases (Figure 4.22C). These intermediate mixture structures provide the evidence for morphology evolution from cubosomes to hexosomes. Further increasing the proportions of THF to 50% ( $\delta = 19.5$ ), only hexosomes were observed according to the collected SEM and TEM images (Figures 4.23A and 4.23B).

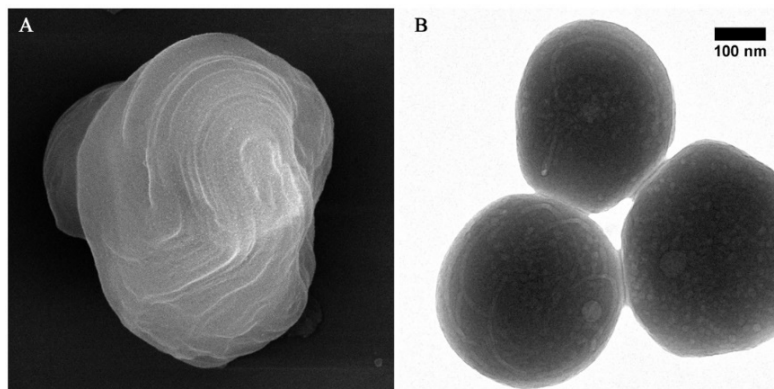


**Figure 4.23.** The SEM (A) and TEM (B) images of  $PEG_{45}\text{-}b\text{-}PTPEMA_{42}$  hexosomes in dioxane/THF/water system with THF content of 50%.

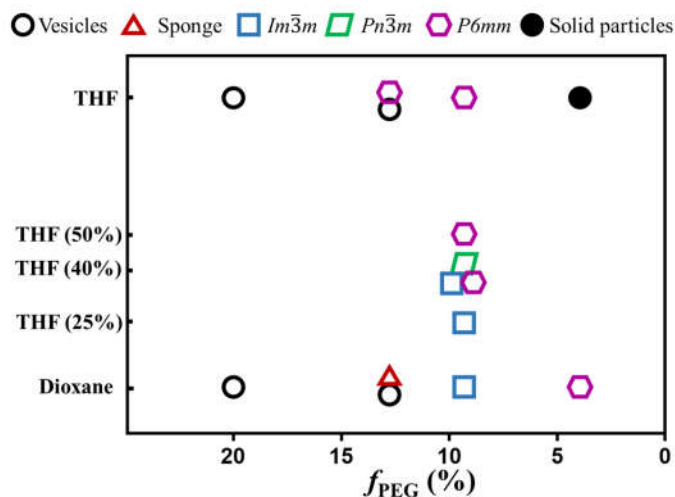


**Figure 4. 24** Morphological phase diagrams of the self-assemblies of  $PEG_{45}\text{-}b\text{-}PTPEMA_n$  with different  $f_{PEG}$  fraction and using different organic co-solvent.

In conclusion, a phase transformation of the self-assembled structure of  $PEG_{45}\text{-}b\text{-}PTPEMA_{42}$  from  $Im\bar{3}m$ ,  $Pn\bar{3}m$  (cubosomes) to  $P6mm$  (hexosome) was observed with the increase of the

affinity between the cosolvent and hydrophobic block by adjusting the content of THF in the mixed solvent of dioxane/THF. Together with the morphological transformation discussed before upon the increasing of the hydrophobic length (the decreasing of the  $f_{\text{PEG}}$  fraction) of PEG<sub>45</sub>-*b*-PTPEMA<sub>n</sub> in pure dioxane and THF, a phase diagram is drawn in Figure 4.24.

#### 4.3.7 AIE fluorescence of PEG<sub>45</sub>-*b*-PTPEMA<sub>n</sub> self-assemblies

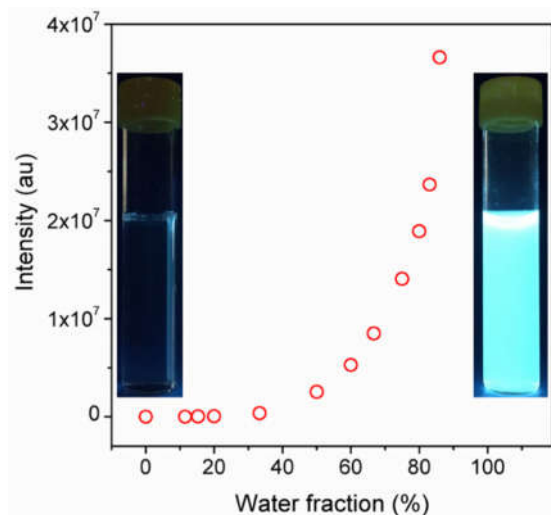


**Figure 4.25** The evolution of fluorescence intensity as a function of water content during the nanoprecipitation of PEG<sub>45</sub>-*b*-PTPEMA<sub>42</sub> in dioxane/water system. The insets are the photos taken under UV light of 365 nm for PEG<sub>45</sub>-*b*-PTPEMA<sub>42</sub> in dioxane solution (left) and its cubosomes in water after dialysis (right).

The fluorescence evolution during the self-assembly process by nanoprecipitation was first studied taking PEG<sub>45</sub>-*b*-PTPEMA<sub>42</sub> in dioxane/water as an example. As shown in Figure 4.25, a slight increase of fluorescence intensity is observed after the addition of water to  $f_{\text{water}} = 15\%$ , indicating the PEG<sub>45</sub>-*b*-PTPEMA<sub>42</sub> begins to form assemblies. Then the fluorescence intensity keeps a slow increase rate until  $\sim 50\%$  of water content. At this stage, the mobility of the hydrophobic chains and TPE moieties in the aggregates is still high because of the plasticizing effect of the organic solvent, leading to the low growth rate of fluorescence. Further increasing the water content, an exponential augmentation of fluorescence intensity is observed, probably due to the removal of the organic solvent from the hydrophobic domains driven by the high osmotic pressure between the outside and the inside of these domains. This solvent removal effectively reduces the mobility of PTPEMA chain and block the intermolecular rotation of

TPE units, resulting in a rapidly growth of the fluorescence intensity. These assemblies with strong fluorescence also correspond to the organization of the nanostructure into sponge phase (~ 60%) and cubic phase (~80%) as discussed above (Figure 4.25). These observations show clearly the AIE property of the self-assemblies (the insets in Figure 4.25).

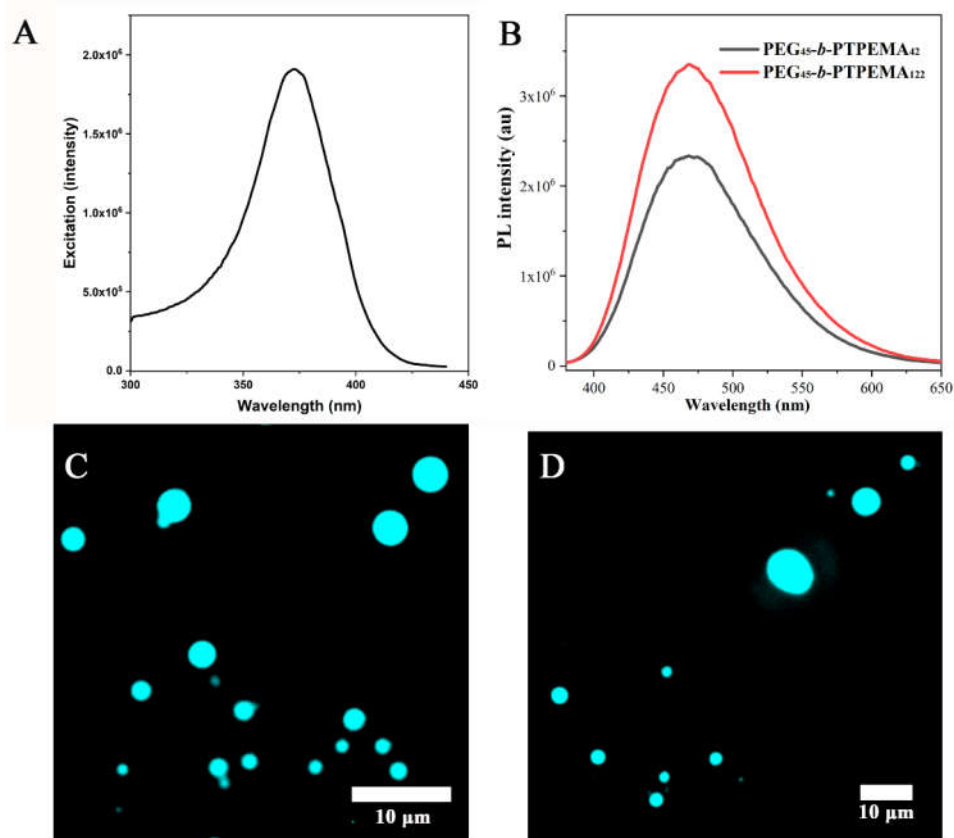


**Figure 4.26** (A) The excitation spectra of the PEG<sub>45</sub>-*b*-PTPEMA<sub>42</sub> cubosomes. (Concentration: about 0.2 mg. mL<sup>-1</sup>, emission: 480 nm). Photoluminescence spectra of the PEG<sub>45</sub>-*b*-PTPEMA<sub>42</sub> cubosomes and PEG<sub>45</sub>-*b*-PTPEMA<sub>122</sub> hexosomes (concentration: 0.4 mg mL<sup>-1</sup>; excitation wavelength:  $\lambda = 370$  nm). (C, D) The images of PEG<sub>45</sub>-*b*-PTPEMA<sub>42</sub> cubosomes (C) and PEG<sub>45</sub>-*b*-PTPEMA<sub>122</sub> hexosomes (D) taken with epifluorescence microscope (illumination wavelength:  $\lambda = 365$  nm). The self-assembly was performed in dioxane/water system.

The final colloidal dispersions of PEG<sub>45</sub>-*b*-PTPEMA<sub>42</sub> and of PEG<sub>45</sub>-*b*-PTPEMA<sub>122</sub> in water were then characterized by fluorospectrometer and fluorescence microscopy. PEG<sub>45</sub>-*b*-PTPEMA<sub>42</sub> cubosomes and PEG<sub>45</sub>-*b*-PTPEMA<sub>122</sub> hexosomes exhibit high fluorescence

(Figure 4.26B) with maximal emission at wavelengths of 468 nm and 469 nm, respectively, under the excitation at wavelength of 370 nm, which corresponds to the maximal wavelength in the excitation spectrum (Figure 4.26A). Observed by epifluorescence microscopy, the colloids (cubosomes and hexosomes) emit bright cyan fluorescence under the illumination of UV light ( $\lambda_{\text{ex}} = 365 \text{ nm}$ ) as shown in Figure 4.26C-D. The quantum yields of PEG<sub>45</sub>-*b*-PTPEMA<sub>42</sub> cubosomes and PEG<sub>45</sub>-*b*-PTPEMA<sub>122</sub> hexosomes were measured as 17% and 23%, respectively, using the integrating sphere method.

#### 4.4 Conclusion

A series of amphiphilic block copolymers PEG<sub>45</sub>-*b*-PTPEMA<sub>n</sub> with the bulky AIE moiety TPE as side group and with high asymmetry in block lengths ( $f_{\text{PEG}} = 20, 12.3, 8.9, 3.3 \%$ ) have been synthesized. These ABCPs could form polymersomes, sponge structures, and colloids with inverse ordered structures including primitive cubosomes and hexosomes by increasing the length of hydrophobic block (decreasing the hydrophilic ratio  $f_{\text{PEG}}$ ). In addition to  $f_{\text{PEG}}$ , other parameters influencing the self-assembly like the initial polymer concentration, the water content added before the final dialysis, and the solvent were studied in detail. The demonstration of the morphologic evolution pathway from polymersomes, large complex vesicles, sponge structures to primitive cubosomes and hexosomes upon the addition of water allows us to understand the formation mechanism of cubosomes and hexosomes. The study on the effect of organic co-solvent guides us to control the final internal structure of colloids by appropriate choice of solvent. These polymer cubosomes and hexosomes are extremely stable colloids with  $T_g$  around 90°C for the hydrophobic part, which can be kept stable for months in ambient conditions. Moreover, in contrast to polymersomes, they can be freeze-dried and re-dispersed in water without structural change. Therefore, this research provides a platform for a better comprehension of the formation of inverted morphologies and enriches the examples of ABCPs to form cubosomes and hexosomes. All polymer cubosomes and hexosomes in this work exhibit bright cyan fluorescence. Here, TPE that emit blue light when excited in UV light was used for the proof of concept of AIE inverted colloids. Other AIEgens excitable at longer wavelength or AIE photosensitizers can be introduced in the hydrophobic part of cubosomes and hexosomes, which may have potential applications in bioimaging and nanomedicine.

## 4.5 References

- 1 Antonietti, M. & Förster, S. Vesicles and Liposomes: A Self-Assembly Principle Beyond Lipids. *Adv. Mater.* **15**, 1323-1333 (2003).
- 2 Blanz, A., Armes, S. P. & Ryan, A. J. Self-Assembled Block Copolymer Aggregates: From Micelles to Vesicles and their Biological Applications. *Macromol. Rapid Commun.* **30**, 267-277 (2009).
- 3 Gröschel, A. H. & Walther, A. Block Copolymer Micelles with Inverted Morphologies. *Angew. Chem. Int. Ed.* **56**, 10992-10994 (2017).
- 4 Mai, Y. & Eisenberg, A. Self-assembly of block copolymers. *Chem. Soc. Rev.* **41**, 5969-5985 (2012).
- 5 Wong, C. K., Qiang, X., Müller, A. H. E. & Gröschel, A. H. Self-Assembly of block copolymers into internally ordered microparticles. *Prog. Polym. Sci.* **102**, 101211 (2020).
- 6 Israelachvili, J. N., Mitchell, D. J. & Ninham, B. W. Theory of self-assembly of hydrocarbon amphiphiles into micelles and bilayers. *J. Chem. Soc. Faraday Trans.* **72**, 1525-1568 (1976).
- 7 Allen, S. D., Bobbala, S., Karabin, N. B. & Scott, E. A. On the advancement of polymeric bicontinuous nanospheres toward biomedical applications. *Nanoscale Horiz.* **4**, 258-272 (2019).
- 8 Yaghmur, A., Rappolt, M. & Larsen, S. W. In situ forming drug delivery systems based on lyotropic liquid crystalline phases: structural characterization and release properties. *J. Drug Deliv. Sci. Technol.* **23**, 325-332 (2013).
- 9 de Campo, L. *et al.* Reversible Phase Transitions in Emulsified Nanostructured Lipid Systems. *Langmuir* **20**, 5254-5261 (2004).
- 10 Li, C. *et al.* Self-assembly of block copolymers towards mesoporous materials for energy storage and conversion systems. *Chem. Soc. Rev.* **49**, 4681-4736 (2020).
- 11 Barriga, H. M. G., Holme, M. N. & Stevens, M. M. Cubosomes: The Next Generation of Smart Lipid Nanoparticles? *Angew. Chem. Int. Ed.* **58**, 2958-2978 (2019).
- 12 Zhang, L., Bartels, C., Yu, Y., Shen, H. & Eisenberg, A. Mesosized Crystal-like Structure of Hexagonally Packed Hollow Hoops by Solution Self-Assembly of Diblock Copolymers. *Phys. Rev. Lett.* **79**, 5034-5037 (1997).
- 13 Haluska, C. K., Gózdź, W. T., Döbereiner, H.-G., Förster, S. & Gompper, G. Giant hexagonal superstructures in diblock-copolymer membranes. *Phys. Rev. Lett.* **89**, 238302 (2002).
- 14 Chen, Y. *et al.* Perforated block copolymer vesicles with a highly folded membrane. *Macromolecules* **40**, 4389-4392 (2007).
- 15 McKenzie, B. E. *et al.* Bicontinuous nanospheres from simple amorphous amphiphilic diblock copolymers. *Macromolecules* **46**, 9845-9848 (2013).
- 16 Yu, H., Qiu, X., Nunes, S. P. & Peinemann, K.-V. Biomimetic block copolymer particles with gated nanopores and ultrahigh protein sorption capacity. *Nat. Commun.* **5**, 1-10 (2014).

- 17 Zhang, W. J., Hong, C. Y. & Pan, C. Y. Formation of hexagonally packed hollow hoops and morphology transition in RAFT ethanol dispersion polymerization. *Macromol. Rapid Commun.* **36**, 1428-1436 (2015).
- 18 Ding, Z., Gao, C., Wang, S., Liu, H. & Zhang, W. Macro-RAFT agent mediated dispersion polymerization: the monomer concentration effect on the morphology of the in situ synthesized block copolymer nano-objects. *Polym. Chem.* **6**, 8003-8011 (2015).
- 19 Ku, K. H. *et al.* Particles with tunable porosity and morphology by controlling interfacial instability in block copolymer emulsions. *ACS nano* **10**, 5243-5251 (2016).
- 20 He, H. *et al.* Cubosomes from hierarchical self-assembly of poly (ionic liquid) block copolymers. *Nat. Commun.* **8**, 1-8 (2017).
- 21 Lin, Z. *et al.* Tunable Self-Assembly of Diblock Copolymers into Colloidal Particles with Triply Periodic Minimal Surfaces. *Angew. Chem. Int. Ed.* **56**, 7135-7140 (2017).
- 22 Allen, S. D., Bobbala, S., Karabin, N. B., Modak, M. & Scott, E. A. Benchmarking Bicontinuous Nanospheres against Polymersomes for in Vivo Biodistribution and Dual Intracellular Delivery of Lipophilic and Water-Soluble Payloads. *ACS Appl. Mater.* **10**, 33857-33866 (2018).
- 23 Presa-Soto, D., Carriedo, G. A., de la Campa, R. & Presa Soto, A. Formation and Reversible Morphological Transition of Bicontinuous Nanospheres and Toroidal Micelles by the Self-Assembly of a Crystalline-b-Coil Diblock Copolymer. *Angew. Chem. Int. Ed.* **55**, 10102-10107 (2016).
- 24 McKenzie, B. E., Nudelman, F., Bomans, P. H., Holder, S. J. & Sommerdijk, N. A. Temperature-responsive nanospheres with bicontinuous internal structures from a semicrystalline amphiphilic block copolymer. *J. Am. Chem. Soc.* **132**, 10256-10259 (2010).
- 25 Holder, S. J., Woodward, G., McKenzie, B. & Sommerdijk, N. A. Semi-crystalline block copolymer bicontinuous nanospheres for thermoresponsive controlled release. *RSC Adv.* **4**, 26354-26358 (2014).
- 26 McKenzie, B. E. *et al.* The evolution of bicontinuous polymeric nanospheres in aqueous solution. *Soft Matter* **12**, 4113-4122 (2016).
- 27 McKenzie, B. E. *et al.* Controlling internal pore sizes in bicontinuous polymeric nanospheres. *Angew. Chem. Int. Ed.* **54**, 2457-2461 (2015).
- 28 Monaghan, O., Bomans, P., Sommerdijk, N. A. & Holder, S. J. Controlling the melting transition of semi-crystalline self-assembled block copolymer aggregates: controlling release rates of ibuprofen. *Polym. Chem.* **8**, 5303-5316 (2017).
- 29 Lyu, X. *et al.* Head-tail asymmetry as the determining factor in the formation of polymer cubosomes or hexosomes in a rod-coil amphiphilic block copolymer. *Angew. Chem. Int. Ed.* **57**, 10132-10136 (2018).
- 30 Kang, Y. *et al.* Use of complementary nucleobase-containing synthetic polymers to prepare complex self-assembled morphologies in water. *Polym. Chem.* **7**, 2836-2846 (2016).

- 31 Vanderkooy, A., Pfefferkorn, P. & Taylor, M. S. Self-assembly of polymer nanostructures through halogen bonding interactions of an iodoperfluoroarene-functionalized polystyrene derivative. *Macromolecules* **50**, 3807-3817 (2017).
- 32 Parry, A. L., Bomans, P. H., Holder, S. J., Sommerdijk, N. A. & Biagini, S. C. Cryo electron tomography reveals confined complex morphologies of tripeptide-containing amphiphilic double-comb diblock copolymers. *Angew. Chem. Int. Ed.* **47**, 8859-8862 (2008).
- 33 Barnhill, S. A., Bell, N. C., Patterson, J. P., Olds, D. P. & Gianneschi, N. C. Phase diagrams of polynorbornene amphiphilic block copolymers in solution. *Macromolecules* **48**, 1152-1161 (2015).
- 34 La, Y. *et al.* Colloidal inverse bicontinuous cubic membranes of block copolymers with tunable surface functional groups. *Nat. Chem.* **6**, 534-541 (2014).
- 35 Park, C. *et al.* Mesoporous monoliths of inverse bicontinuous cubic phases of block copolymer bilayers. *Nat. Commun.* **6**, 1-9 (2015).
- 36 An, T. H. *et al.* Solution self-assembly of block copolymers containing a branched hydrophilic block into inverse bicontinuous cubic mesophases. *ACS nano* **9**, 3084-3096 (2015).
- 37 Cho, A. *et al.* Mix-and-match assembly of block copolymer blends in solution. *Macromolecules* **50**, 3234-3243 (2017).
- 38 Cho, A., La, Y., Shin, T. J., Park, C. & Kim, K. T. Structural requirements of block copolymers for self-assembly into inverse bicontinuous cubic mesophases in solution. *Macromolecules* **49**, 4510-4519 (2016).
- 39 Jeong, M. G. & Kim, K. T. Covalent Stabilization of Inverse Bicontinuous Cubic Structures of Block Copolymer Bilayers by Photodimerization of Indene Pendant Groups of Polystyrene Hydrophobic Blocks. *Macromolecules* **50**, 223-234 (2017).
- 40 La, Y. *et al.* Templated synthesis of cubic crystalline single networks having large open-space lattices by polymer cubosomes. *Nat. Commun.* **9**, 5327 (2018).
- 41 Zhang, D., Fan, Y., Chen, H., Trepout, S. & Li, M. H. CO<sub>2</sub>-Activated Reversible Transition between Polymersomes and Micelles with AIE Fluorescence. *Angew. Chem. Int. Ed.* **58**, 10260-10265 (2019).
- 42 Brûlet, A., Lairez, D., Lapp, A. & Cotton, J.-P. Improvement of data treatment in small-angle neutron scattering. *J. Appl. Crystallogr.* **40**, 165-177 (2007).
- 43 McKenzie, B. E. *et al.* Bicontinuous Nanospheres from Simple Amorphous Amphiphilic Diblock Copolymers. *Macromolecules* **46**, 9845-9848 (2013).
- 44 Brandrup, J., Immergut, E. H., Grulke, E. A., Abe, A. & Bloch, D. R. *Polymer handbook*. Vol. 7 (Wiley New York etc, 1989).





---

## Chapter V. General Conclusions and Perspectives

### 5.1 General conclusions

The thesis describes the preparation and characterization of several AIE polymer self-assemblies including polymersomes, porous polymersomes, polymer cubosomes and hexosomes through the self-assembly of AIEgen-containing amphiphilic copolymers. These copolymers include amphiphilic copolymers with TPE as stereocenter and linear amphiphilic block copolymers with TPE as pendants in the hydrophobic block. The main results of these works are summarized as three papers submitted or to submit for publications.

#### (1) Light-gated nano-porous polymersomes from stereoisomer-directed self-assemblies

In this work, we firstly prepare two amphiphilic stereoisomers with the TPE as the stereocenter, namely *trans*-PEG550-TPE-Chol and *cis*-PEG550-TPE-Chol by post-modification of the poly(ethylene glycol) (PEG) block, in which the PEG is the hydrophilic block and TPE together with the cholesterol serve as the hydrophobic component. These two amphiphilic stereoisomers present the same hydrophilic ratio of  $f_{\text{PEG}} = 37\%$ , but distinct spatial configuration. They are thermally stable. However, the isomerization of these two stereoisomers can be activated by UV illumination ( $15 \text{ mW}\cdot\text{cm}^{-2}$ ). Both isomers reach a stationary state with *trans/cis* ratio of 60/40 after 20 min illumination.

These two amphiphilic stereoisomers exhibit distinct self-assemble behaviors: the *trans*-PEG550-TPE-Chol prefers to form normal vesicles, the *cis*-PEG550-TPE-Chol tends to construct the cylindrical micelles. Interestingly, PEG550-TPE-Chol synthesized without isomers' separation (*trans/cis* = 60/40) forms perforated vesicles and membranes with the pores size ranging from 9 to 27 nm. All these self-assemblies show strong fluorescence.

The smooth vesicles formed by *trans*-PEG550-TPE-Chol can be perforated under UV illumination due to the generation of its *cis* counterpart stemmed from the isomerization. This transition from “closed” to “open” state for the vesicle allows to release the encapsulated substance in a controlled way. In addition, the cylindrical micelles prepared from *cis*-PEG550-TPE-Chol tend to interweave to construct perforated membranes. There is no significant morphological change for porous polymersomes self-assembled by *trans/cis* mixture of PEG550-TPE-chol after UV illumination, but membrane fluctuation in micrometer scale can be observed by epifluorescence microscopy.

## (2) Polymersomes with hexagonal nano-porous structures in the membrane

In this part, we report on AIE nano-porous polymersomes where the nanopores are structured in a hexagonal lattice. They are self-assembled from amphiphilic copolymer PEG550-SS-TPE-SS-Chol, that is slightly different from PEG550-TPE-Chol described in first work. In PEG550-SS-TPE-SS-Chol, the flexible spacers between PEG and TPE, and between Chol and TPE have one additional disulfide bond -S-S-, respectively. Moreover, PEG550-SS-TPE-SS-Chol synthesized naturally without the separation of stereoisomers contains *trans* and *cis* isomers in nearly equivalent molar ratio. PEG550-SS-TPE-SS-Chol forms spontaneously vesicles with nanopores in the membrane. Interestingly, these nanopores self-organize into hexagonal superstructure in contrast to the random nanopores in the case of PEG550-TPE-Chol. The hexagonal nano-porous vesicles exhibit reduction-responsive property due to the presence of disulfide bonds. The vesicles disappear after addition of dithiothreitol.

To understand the formation mechanism of perforated membrane by *trans/cis* mixtures and the structuration of nanopores, both situations of PEG550-SS-TPE-SS-Chol and PEG550-TPE-Chol are compared. Especially, morphological evolution of *trans/cis* mixture of PEG550-TPE-Chol as function of the *cis* proportion was studied, and an evolution from vesicles, pseudo porous vesicles, porous vesicles, Y junctions, to cylindrical micelles are observed.

## (3) Fluorescent polymer cubosomes and hexosomes with AIE characteristics

In this work, we report for the first time AIE cubosomes and hexosomes from new amphiphilic block copolymer PEG-*b*-PTPEMA, in which the hydrophobic block PTPEMA was a polymethacrylate with TPE as side group. Four highly asymmetric block copolymers with a hydrophobic block much larger than its corresponding hydrophilic block were synthesized by RAFT polymerization, leading to copolymers with  $f_{\text{PEG}} (\text{wt}\%) = 20, 12.3, 8.9, 3.3 \%$ , respectively.

These block copolymers self-assemble into AIE polymersomes, sponge-like particles,  $Im\bar{3}m$  cubosomes, and  $P6mm$  hexosomes, respectively, through nanoprecipitation in water using dioxane as co-solvent. The inverse morphologies are confirmed by cryo-EM, SEM TEM and SAXS techniques. When THF is used as co-solvent, these copolymers form AIE polymersomes, mixture of polymersomes and hexosomes, hexosomes and spherical solid colloid, respectively. The co-solvent effect on the morphologies was studied by using the

solvent mixture between dioxane and THF with different ratio. The increase of the affinity between the cosolvent and hydrophobic block would result in the formation of inverse morphologies with higher inverted curvatures. Moreover, the morphologic evolution pathway from vesicles, large complex vesicles, spongy structures to cubosomes upon the addition of water during the self-assembling, allows us to understand the formation mechanism of cubosomes.

## 5.2 Perspectives

In the present manuscript, we have synthesized two families of AIE amphiphilic copolymers by integrating the AIEgens, TPE, into their molecular structures, and then constructed various AIE nano and microparticles including AIE polymersomes, porous AIE polymersomes, AIE polymer cubosomes and hexosomes. For future studies, more experimental works could be done to get deeper insight into the self-assembly behavior of these AIE amphiphilic copolymers and to explore their potential applications.

For example, for PEG550-SS-TPE-SS-Chol and PEG550-TPE-Chol, the self-assembly was performed only by thin-film hydration method. The drawback of this method is the low encapsulation efficiency for water-soluble molecules, which may limit their applications as the carrier. Thus, other techniques, like double emulsion and nanoprecipitation methods, could be employed to study their assembly behaviors. For amphiphilic copolymers PEG-*b*-PTPEMA, it is interesting to synthesize polymers with  $f_{\text{PEG}}$  ranging from 8.9 to 12.3%, and study their self-assembly behavior in the THF/water system, since no cubosomes phase was recorded in THF/water system with the four copolymers studied already.

To explore the potential application of AIE self-assembled morphologies, the porous hexagonal membrane may be constructed by the fusion of the hexagonal vesicles and be studied to separate substances or nanoparticles with different sizes. The cubosomes and hexosomes could be used as the template to synthesize inorganic particles with order internal structures for application of energy storage.

Further, lots of opportunities reside in the design of new AIE amphiphilic copolymers and novel AIE self-assembled materials. For example, different stimuli including chemical and physical stimuli can be integrated into AIE polymersomes and cubosomes to realize the release of encapsulated substance in a controllable way. Physical stimuli, such as light or magnetic field, which show obvious advantage with the possibility of remote and precise control, are

worthy of attention. Targeting moieties could be introduced into the surface of polymersomes and polymer cubosomes/hexosomes to realize the targeted binding of tissue/cell, specific labelling, and targeted drug release. Especially, AIE polymersomes and cubosomes/hexosomes which are excited and emit in visible/NIR range with narrow band emission and high fluorescence quantum efficiency are highly desirable because they can avoid the harmful effects on the tissue/cells and can operate with deep penetration in biological tissue. In addition, some of NIR-red AIEgens that can produce reactive oxygen species (ROS) could be used to construct AIE particles capable of photodynamic therapy (PDT) under white light illumination. We believe that AIE polymersomes and AIE polymer cubosomes/hexosomes may serve as the promising platform for drug delivery, bioimaging, diagnostics, theranostics, and biosensors.

---

## List of publications and conference abstracts

### Publications

- **H. Chen**, Y. Fan, X. Yu, V. Semetey, S. Trépout, and M.-H. Li. Light-Gated Nano-Porous Capsules from Stereoisomer-Directed Self-Assemblies, *ACS nano*, doi.org/10.1021/acsnano.0c07400.
- **H. Chen** and M.-H. Li, Recent Progress in Fluorescent Vesicles with Aggregation-Induced Emission, *Chin. J. Polym. Sci.*, **2019**, *37*, 352- 371.
- **H. Chen**,<sup>#</sup> L. Zhou,<sup>#</sup> X. Shi, J. Hu, J. Guo, P.-A. Albouy and M.-H. Li, AIE Fluorescent Gelators with Thermo-, Mechano- and Vapo-Chromic Properties, *Chem. Asian J.*, **2019**, *14*, 781 -788. (<sup>#</sup> equal contribution)
- B. Ni,<sup>#</sup> **H. Chen**,<sup>#</sup> M. Zhang, P. Keller, M. Tatoulian and M.-H. Li, Thermo-Mechanical and Photo-Luminescence Properties of Micro-Actuators Made of Liquid Crystal Elastomers with Cyano-oligo(p-phenylene vinylene) Crosslinking Bridges, *Mater. Chem. Front.* **2019**, *3*, 2499-2506. (<sup>#</sup> equal contribution)
- X. Yu,<sup>#</sup> **H. Chen**,<sup>#</sup> X. Shi, P.-A. Albouy, J. Guo, J. Hu and M.-H. Li, Liquid Crystal Gelators with Photo-Responsive and AIE Properties, *Mater. Chem. Front.*, **2018**, *2*, 2245-2253. (# equal contribution)
- N. Zhang,<sup>#</sup> **H. Chen**,<sup>#</sup> Y. Fan,<sup>#</sup> L. Zhou, S. Trépout, J. Guo and M.-H. Li, Fluorescent Polymersomes with Aggregation-Induced Emission, *ACS Nano*, **2018**, *12*, 4025 -4035. (<sup>#</sup> equal contribution)
- Y. Deng, **H. Chen**, X. Tao, S. Trépout, J. Ling and M.-H. Li, Synthesis and Self-assembly of Poly(ethylene glycol)-block-poly(N-3-(methylthio)propyl glycine) and Their Oxidation-Sensitive Polymersomes, *Chin. Chem. Lett.*, **2020**, *31*, 1931- 1935.
- X. Tao, **H. Chen**, S. Trépout, J. Cen, J. Ling and M.-H. Li, Polymersomes with Aggregation-Induced Emission Based on Amphiphilic Block Copolypeptoids, *Chem. Comm.*, **2019**, *55*, 13530- 13533.
- Y. Deng, **H. Chen**, X. Tao, F. Cao, S. Trépout, J. Ling and M.-H. Li, Oxidation-Sensitive Polymersomes Based on Amphiphilic Diblock Copolypeptoids, *Biomacromolecules*, **2019**, *20*, 3435 – 3444.
- D. Zhang, Y. Fan, **H. Chen**, S. Trépout and M.-H. Li, CO<sub>2</sub> -Activated Reversible Transition between Polymersomes and Micelles with AIE Fluorescence, *Angew. Chem. Int. Ed.*, **2019**, *58*, 10260-10265.

- **H. Chen**, M.-H. Li, Chapter of “AIE Fluorescent Polymersomes” in book “Handbook of Aggregation-Induced Emission”, *forthcoming*.
- **H. Chen**, Y. Fan, N. Zhang, S. Trépout, P. Bergam, A. Brûlet, B. Z. Tang, M.-H. Li. Fluorescent Polymersomes, Cubosomes and Hexosomes with Aggregation-Induced Emission. *Submitted*.
- **H. Chen**, Y. Fan, X. Yu, S. Trépout and M.-H. Li. Hexagonal Nano-porous Structures in Amphiphilic Rod-Coil Oligomer Membranes. *In preparation*.

#### **Conference abstracts**

- **H. Chen**, Y. Fan, X. Yu, V. Semetey, S. Trépout, and M.-H. Li, Stereodirecting Self-assemblies of Amphiphilic Tetraphenylethene-Cored Polymers, IUPAC, Paris, France **2019**.
- **H. Chen**, Y. Fan, X. Yu, V. Semetey, S. Trépout, and M.-H. Li, Self-Assembled Nanostructures with Morphological Control, Aggregation-Induced Emission and Photo-Responsive Property Based on Stereoisomers of Tetraphenylethene-containing Amphiphilic Polyme, E-MRS Spring Meeting and Exhibit, Strasbourg, France **2018**.





## RÉSUMÉ

---

L'émission induite par l'agrégation (AIE) fait référence à un phénomène photophysique anormal présenté par un groupe de luminogènes spécifiques qui ne sont pas émissifs en solution mais deviennent hautement luminescents à l'état agrégé. Il fournit un moyen simple de s'attaquer aux problèmes de l'extinction de fluorescence provoqués par l'agrégation (ACQ) qui se produisent avec la plupart des fluorogènes organiques conventionnels. La combinaison de luminogènes AIE (AIEgens) avec des assemblages polymères présente un intérêt particulier et peut ouvrir une nouvelle voie pour préparer des matériaux luminescents hautement efficaces avec des applications potentielles dans le domaine biomédical. Parmi les divers assemblages de polymères AIE, les polymersomes AIE et les particules AIE avec des morphologies inverses (comme les cubosomes et les hexosomes) sont particulièrement attractifs car ils peuvent être utilisés comme outils de bioimagerie pour imager en temps réel l'administration de substances thérapeutiques, et pour le diagnostic et la théranostique. Cependant, le nombre de travaux sur les polymersomes AIE est encore très limité, et aucun cubosome et hexosome de polymère AIE n'a été décrit dans la littérature. Les objectifs de cette thèse sont de préparer de nouveaux polymersomes AIE et de développer les premiers cubosomes et hexosomes polymères AIE.

Les travaux de la recherche de cette thèse sont présentés en trois chapitres (II, III et IV) après une introduction générale (Chapitre I) et avant la conclusion et les perspectives (Chapitre V). Les polymersomes AIE et les polymersomes AIE nanoporeux auto-assemblés respectivement à partir du stéréoisomère *trans* de PEG550-TPE-Chol et des mélanges *trans* et *cis* de PEG550-TPE-Chol sont étudiés (Chapitres II et III). Des polymersomes AIE formée par PEG550-SS-TPE-SS-Chol, qui possèdent des nanopores organisés en structure hexagonale dans la membrane, sont décrits (Chapitre III). Enfin, les premiers cubosomes et hexosomes AIE sont préparés avec succès à partir des copolymères à blocs PEG-*b*-PTPEMA hautement asymétriques, et présentés dans le Chapitre IV.

## MOTS CLÉS

---

Polymersomes, Cubosomes, Hexosomes, Emission Induite par l'Agrégation

## ABSTRACT

---

Aggregation-induced emission (AIE) refers to an unusual photophysical phenomenon shown by a group of specific luminogens that are non-emissive in solution but become highly luminescent in aggregated state. It provides a straightforward way to tackle the aggregation caused fluorescence quenching (ACQ) problems that happen to most conventional organic fluorogens. The combination of AIE luminogens (AIEgens) with polymer assemblies present particular interest and may open a novel way to prepare highly efficient luminescent materials with potential applications in bio-medical field. Among various AIE polymer assemblies, AIE polymersomes and AIE particles with inverse morphologies (like cubosomes and hexosomes) are especially attractive since they may be used as bioimaging tools for real-time imaging of therapeutic substances delivery, and for diagnostic and theranostics. However, the number of works on AIE polymersomes is still very limited, and no AIE polymer cubosome and hexosome have been reported in the literature. The objectives of the present thesis are to prepare new AIE polymersomes and to develop the first AIE polymer cubosomes and hexosomes.

The research contents are presented in three chapters (II, III and IV) after a general introduction (Chapter I) and before the conclusion and perspectives (Chapter V). AIE polymersomes and nanoporous polymersomes self-assembled, respectively, from the *trans*-stereoisomer of PEG550-TPE-Chol and the *trans* and *cis* mixtures of PEG550-TPE-Chol are investigated (Chapter II and III). AIE polymersomes with hexagonally packed nanopores in the membrane formed by PEG550-SS-TPE-SS-Chol are described (Chapter III). Finally, the first AIE cubosomes and hexosomes are successfully prepared from the highly asymmetric block copolymers PEG-*b*-PTPEMA and presented in Chapter IV.

## KEYWORDS

---

Polymersomes, Cubosomes, Hexosomes, Aggregation-Induced Emission

